Engineering Parallel Transmit/Receive Radio-Frequency Coil Arrays for Human Brain MRI at 7 Tesla

Thèse N° 9555

Présentée le 24 juin 2019

à la Faculté des sciences de base
Laboratoire Leenaards-Jeantet d’imagerie fonctionnelle et métabolique
Programme doctoral en physique

pour l’obtention du grade de Docteur ès Sciences

par

Jérémie Daniel CLÉMENT

Acceptée sur proposition du jury

Prof. F. Mila, président du jury
Prof. R. Gruetter, Ö. Ipek, directeurs de thèse
Prof. A. Webb, rapporteur
Prof. A. Raaijmakers, rapporteur
Prof. G. Boero, rapporteur

2019

ÉCOLE POLYTECHNIQUE
FÉDÉRALE DE LAUSANNE

Abstract

Magnetic resonance imaging is widely used in medical diagnosis to obtain anatomical details of the human body in a non-invasive way. Clinical MR scanners typically operate at a static magnetic field strength (B_0) of 1.5T or 3T. However, going to higher field is of great interest since the signal to noise ratio is proportional to B_0. Therefore, higher image resolution and better contrast between the human tissues could be achieved.

Nevertheless, new challenges arise when increasing B_0. The wavelength associated with the radio-frequency field B_1^+ has smaller dimensions - approx. 12 cm for human brain tissues - than the human brain itself (20 cm in length), the organ of interest in this thesis. The main consequence is that the transmit field distribution pattern (B_1^+) is subject to constructive or destructive interferences which are visible in the final MR images as bright and dark signal spots, respectively. These effects prevent ultra-high field MR scanners ($\geqslant$ 7T) from being used for routine clinical diagnosis. Parallel-transmit is one approach to address these new challenges. Instead of using an RF coil connected to a single power input as is commonly done at lower magnetic fields, multiple RF coils are used with independent power inputs. The subsequent distinct RF signals can be manipulated separately, which provides an additional degree of freedom to generate homogeneous B_1^+-field distributions over large or specific regions in the human body.

This thesis is about the design and construction of innovative RF coils for human brain MR at 7T.

The first project was to construct a transmit/receive RF coil array optimized for whole-brain MR imaging. Because of the inherent inhomogeneities of RF volume coils, it is usually quite challenging to get a homogeneous RF signal in both the cerebral cortex and the cerebellum simultaneously. To address these difficulties, an 8-channel RF coil array was built with dipoles since they could provide a large longitudinal (vertical axis - head to neck) coverage and high transmit field efficiency. To maximize the RF signal, they were geometrically arranged in a tight configuration around the human head, and this resulted in complete coverage of the human brain, with particularly high homogeneity over the cerebellum.

However, since the receive sensitivity over large fields-of-view is related to the number of channels available to detect the NMR signal, the next step was to add a 32-channel receive loop coil array to the transmit coil array. The geometrical combination of the two coil arrays was performed with special care to limit the interactions, given the tight configuration of the design. The results demonstrate the feasibility of the combination between a tight-fitting transmit-only dipole coil array and a dense receive-only loop coil array. The complete coverage of the human brain was reflected in the substantial increase in signal-to-noise compared to the transmit/receive dipole coil array alone. Moreover, acquisition time was shortened since higher acceleration factors could be used.

To optimize the individual RF fields and generate constructive B_1^+-field interferences, a method was developed making use of the particle-swarm algorithm. The aim was to determine the best combination between all the channel to produce a high and homogeneous transmit B_1^+-field. The algorithm was implemented with a graphical-user interface so that it would be straightforward to use. The results demonstrated that good homogeneity could be achieved over the whole-brain using the optimized weights on the 8-channel transmit/32-channel receive dipole coil array. Moreover, the optimization was shown to be robust across multiple subjects.

The last project was focused on the single transmit system. As noted above, local volume coils present pronounced transmit field inhomogeneities in specific regions of the human brain such as the temporal lobes. A widely-used approach to address these challenges locally is to add dielectric pads inside the volume coils in close proximity to the human body. These dielectric pads enhance the local transmit field efficiency. It was demonstrated in this thesis that constructing dedicated surface coils is a valuable alternative to the dielectric pads in terms of transmit field efficiency and MR spectroscopy results. Two RF coil setups were developed for the temporal and frontal lobes of the human brain, respectively.

This thesis provides extensive insight on MR engineering of RF coils at ultra-high field and the potential of parallel-transmit to address the future needs in clinical applications.

Keywords:
ultra-high field, phased array, center-shortened dipoles, parallel imaging, parallel transmission, RF phase shimming, particle-swarm algorithm, surface coils, 7T, whole-brain imaging, cerebellum, radio-frequency coil array.

Résumé

De nos jours, l'imagerie par résonance magnétique est largement utilisée dans les diagnostics médicaux afin d'obtenir des détails anatomiques du corps humain via une méthode qui est non-invasive. Les scanners IRM disponibles en milieu hospitalier ont des valeurs typiques de champ magnétique statique (B_0) comprises entre 1.5T et 4T. Cependant, il existe un grand intérêt à aller à plus haut champ étant donné que le rapport signal-sur-bruit est proportionnel à B_0. En conséquence, des images à plus haute résolution et de meilleurs contrastes entre les tissus pourraient être obtenus.

Néanmoins, l'augmentation du champ B_0 s'accompagne de nouveaux défis. La longueur d'onde associée au champ radio-fréquence B_1^+ est réduite (environ 12 cm dans les tissus du cerveau humain) et devient de l'ordre de grandeur du cerveau humain (20 cm en longueur) qui était l'organe d'intérêt dans le cadre de cette thèse. La principale conséquence est que la distribution spatiale du champ de transmission (B_1^+) est sujette à des interférences dites constructives ou destructives qui peuvent être observées dans l'image finale sous la forme de régions où le signal est respectivement puissant ou faible. Ces effets ont jusqu'à présent empêché les scanners IRM dits à ultra-haut champ ($\geqslant$ 7T) d'être utilisés pour du diagnostic médical. Les méthodes de transmission en parallèle sont une approche possible pour relever les défis présents à 7T. Au lieu d'utiliser une antenne radio-fréquence connectée à une seule entrée de puissance comme c'est généralement fait à plus bas champ magnétique, de multiples antennes radio-fréquence sont utilisées avec chacune une entrée de puissance indépendante. En conséquence de quoi, les signaux radio-fréquence de chaque antenne peuvent être manipulés afin de générer des interférences constructives sur des régions soit grandes soit spécifiques du corps humain.

Le but de cette thèse est d'imaginer et de construire des designs innovants d'antennes radio-fréquence pour l'imagerie par résonance magnétique à 7T.

Le premier projet a été la construction d'un réseau d'antennes RF utilisables en transmission et réception et qui serait optimisé pour l'IRM du cerveau dans son entier. En particulier, il est habituellement difficile d'obtenir un signal RF homogène à la fois dans le cortex cérébral et dans le cervelet à cause des inhomogénéités inhérentes aux antennes RF de volume. Pour relever ces défis, un réseau d'antennes à 8 canaux a été construit avec des dipoles sachant qu'ils présentent une bonne couverture selon l'axe longitudinal (axe vertical - de la tête au cou) combinée avec une haute efficacité en terme de champ transmis (B_1^+). Afin de maximiser le signal RF, ils ont été géométriquement placés de manière rapprochée autour de la tête. Les résultats ont démontré une couverture totale du cerveau humain et particulièrement homogène au niveau du cervelet.

Cependant, la sensibilité en réception étant liée au nombre de canaux disponible pour détecter le signal, l'étape suivante dans le travail présenté ici a été d'inclure un réseau d'antennes à 32 canaux dédiés à la réception à l'intérieur du réseau d'antennes dipoles à 8 canaux utilisé pour la transmission du signal RF. L'imbriquement des deux réseaux d'antennes a été effectué avec précaution afin de limiter les possible interactions étant donné l'ajustement serré du réseau d'antennes de transmission autour de la tête. Une couverture totale du cerveau humain a été démontrée avec également une augmentation significative du rapport signal-sur-bruit en comparaison de la situation où seulement le réseau d'antennes dipoles à 8 canaux était utilisé en transmission et en réception. De plus, le temps d'acquisition a pu être raccourci en utilisant des coefficient d'accélération plus élevés.

Afin d'optimiser les champs radio-fréquence individuels et générer des interférences constructives en B_1^+, une méthode a été développée en utilisant un algorithme d'optimisation par essaims particulaires. L'objectif était de déterminer la meilleure combinaison possible entre tous les canaux afin de produire un champ de transmission B_1^+ homogène et de haute intensité. L'algorithm a été implementé via une interface graphique afin qu'il soit aisé à utiliser. Les résultats ont démontré qu'une bonne homogénéité pouvait être obtenue sur tout le cerveau en utilisant les coefficient optimaux avec le réseau d'antennes à 8 canaux en transmission et 32 canaux en réception. De plus, l'optimisation s'est révelée robuste à travers de multiples volontaires.

Le dernier projet de cette thèse s'est concentré sur le système de transmission via un seul canal. Comme mentionné précédemment, les antennes RF de volume présentent des inhomogénéités marquées du champ de transmission dans différentes régions du cerveau humain, dont les lobes temporaux. Une approche largement utilisée pour répondre à ce défi consiste à ajouter des blocs diélectriques à l'intérieur de l'antenne de volume, proche du corps humain. Ces bloc diélectriques améliorent localement l'efficacité du champ de transmission B_1^+. Dans cette thèse, il a été démontré que construire des antennes de surfaces dédiées pour ces régions est une alternative valable aux blocs diélectriques en terme d'efficacité de champ B_1^+ et au niveau des résultats en spectroscopie. Pour ce faire, deux ensemble d'antennes de surfaces ont été développés pour les lobes temporaux et frontaux du cerveau humain.

Cette thèse donne un aperçu détaillé des méthodes d'ingéniérie d'antennes radio-fréquence en résonance magnétique à ultra-haut champ et du potentiel de la transmission en parallèle pour répondre aux besoins futurs en applications cliniques.

Mots-clés:
ultra-hau champ, antenne réseau à commande de phase, dipoles , imagerie en parallèle, transmission en parallèle, homogénéisation de champ radio-fréquence, optimisation par essaims particulaires, antennes de surface, 7T, imagerie du cerveau en entier, cervelet, réseau d'antennes radio-fréquence.

There is a time for everything, and a season for every activity under the heavens [...] He has made everything beautiful in its time.

Ecclesiastes 3: 1 & 11

Sola Gratia

Contents

Abstract iii
Résumé v
Table of Contents xi
List of Figures xv
List of Tables xvii

Outline of the thesis **2**

1. Introduction **3**
- 1.1. Historical background 3
- 1.2. Physics of NMR 4
  - 1.2.1. The NMR quantum approach 4
  - 1.2.2. The NMR classical approach 6
- 1.3. RF Hardware and Methods 15
  - 1.3.1. NMR probes 15
  - 1.3.2. Scattering parameters S_{ii} and S_{ij} 17
  - 1.3.3. Surface Coils 18
  - 1.3.4. Volume Coils 24
- 1.4. Electromagnetic field simulations 26
  - 1.4.1. FDTD simulations 27
  - 1.4.2. Specific absorption rate 28
- 1.5. Parallel transmit at 7T 30
  - 1.5.1. Fundamental principle 30
  - 1.5.2. User procedure 31
  - 1.5.3. Hardware implementation 32
  - 1.5.4. Characterization of transmit-receive head RF coil arrays at 7T 33
  - 1.5.5. Decoupling strategies for transmit/receive coil arrays at 7T 34
  - 1.5.6. Transmit-receive head RF coil arrays at 7T 37
- 1.6. Receive coil arrays at 7T 38
  - 1.6.1. Preamplifier decoupling 40
  - 1.6.2. Noise correlation matrix 41
  - 1.6.3. SENSE method and g-factor 42
  - 1.6.4. SNR calculation 43

2. A whole-brain dipole coil array at 7T **49**
- 2.1. Introduction 52
- 2.2. Methods 53
  - 2.2.1. Single dipole design 53

    - 2.2.2. Coil array design 54
    - 2.2.3. Electromagnetic field simulations 54
    - 2.2.4. Coil array construction 55
    - 2.2.5. MR Experiments 56
  - 2.3. Results 59
  - 2.4. Discussion 63
  - 2.5. Conclusion 70

3. A combined 32-channel loop coil receive array with a 8-channel transmit dipole array 71
  - 3.1. Introduction 74
  - 3.2. Methods 75
    - 3.2.1. Receive Array 75
    - 3.2.2. Transmit Array 77
    - 3.2.3. Electromagnetic field simulations 77
    - 3.2.4. MR Experiments 79
  - 3.3. Results 80
  - 3.4. Discussion 82
  - 3.5. Conclusion 89

4. Particle-swarm algorithm for RF phases optimization at 7T 91
  - 4.1. Introduction 94
  - 4.2. Methods 96
    - 4.2.1. Particle-swarm algorithm theory 96
    - 4.2.2. The Matlab GUI interface for B_1^+ optimization 97
    - 4.2.3. Characterization of the algorithm performances 102
  - 4.3. Results 102
  - 4.4. Discussion 106
  - 4.5. Conclusion 112

5. Dedicated surface coils for the temporal and the frontal lobes of the human brain 113
  - 5.1. Introduction 116
  - 5.2. Methods 117
    - 5.2.1. Coil design and construction 117
    - 5.2.2. TR switch design for the ETE Loops 119
    - 5.2.3. Electromagnetic field simulations 119
    - 5.2.4. MR Experiments 122
  - 5.3. Results 124
  - 5.4. Discussion 127
  - 5.5. Conclusion 130

6. General conclusion and outlook **133**
6.1. Main conclusions 133
6.2. Outlook 134

List of Symbols **137**

List of Abbreviations **139**

References **156**

Publications **157**

Curriculum vitae **159**

Acknowledgments **161**

List of Figures

1.1. Zeeman Effect and bulk magnetization 5
1.2. Precession of a spinning top 7
1.3. Magnetization in laboratory and rotating reference frames 10
1.4. T_2, T_2^* and T_1 relaxation curves 11
1.5. Transverse relaxation phenomenon 11
1.6. Evolution of the magnetization for two consecutives T_R 14
1.7. GRE signal with respect to the flip angle 14
1.8. Impedance Curves 17
1.9. Dipoles - Magnetic and electric fields 19
1.10. Microstrip design 20
1.11. Loops - Magnetic and electric fields 21
1.12. Dipole and Loops orientations 22
1.13. Radiation Losses - Voltage Division 23
1.14. Birdcage Coil - Theoretical principle 25
1.15. Birdcage Coil - Transmit field maps 26
1.16. EM simulations - Yee Cell 27
1.17. Birdcage Coil - Transmit field maps 32
1.18. Capacitive/Inductive decoupling 35
1.19. Dipoles - Working principle for decoupling 36
1.20. Coil Arrays - Pictures 39
1.21. Overlapping Method 40
1.22. Preamplifier decoupling schematic 41
1.23. Reconstruction pipeline in SNR units 43
1.24. Parallel imaging principle 45
1.25. Receive Array - Pictures 47

2.1. 8Tx/Rx - Photos of the design 57
2.2. 8Tx/Rx - Simulation Model 58
2.3. 8Tx/Rx - Single center-shortened/fractionated dipoles 60
2.4. 8Tx/Rx - Comparison center-shortened/Fractionated dipoles 61
2.5. 8Tx/Rx - Scattering Matrices 62
2.6. 8Tx/Rx - Individual transmit field maps 62
2.7. 8Tx/Rx - Whole-brain RF shimmed maps 64
2.8. 8Tx/Rx - SAR maps 65
2.9. 8Tx/Rx - GRE images 66
2.10. 8Tx/Rx - Cerebellum RF shimmed Maps 67
2.11. 8Tx/Rx - Comparison with Nova coil 68

3.1. 8Tx/32Rx - Photos of the design 78
3.2. 8Tx/32Rx - Noise Correlation Matrices 81
3.3. 8Tx/32Rx - Scattering Matrices and B_1^+ maps 82
3.4. 8Tx/32Rx - Comparison of flip angle maps with the commercial 1Tx/32Rx coil 83
3.5. 8Tx/32Rx - SAR_{10g} maps for the cerebellum optimized RF phases 84
3.6. 8Tx/32Rx - 3D-GRE images 85
3.7. 8Tx/32Rx - SNR and g-factor maps 86
3.8. 8Tx/32Rx - Multi-slice GRE images 86
3.9. 8Tx/32Rx - SNR maps on the cerebellum 87
3.10. 8Tx/32Rx - High-resolution MR images of the cerebellum 87
3.11. 8Tx/32Rx - High-resolution MP2RAGE images of the whole-brain 88

4.1. PSO Algorithm 96
4.2. GUI interface for the PSO algorithm 98
4.3. Simulated RF shimmed B_1^+ maps and results for the 8Tx/Rx dipole coil arrays 104
4.4. Computed transmit sensitivities optimized with the PSO algorithm and the mean method 105
4.5. Computed transmit sensitivities optimized with the PSO algorithm on a single reference volunteer 106
4.6. Measured B_1^+ maps for RF phases optimized with the PSO algorithm on a single volunteer 107
4.7. Measured B_1^+ maps for RF phases optimized with the gaussian and double region cost functions 108
4.8. Calculated, Measured and Simulated B_1^+ maps for optimized RF phases . . . 109
4.9. SAR_{10g} maps for optimized RF phases 110

5.1. Design of the Ear-to-Ear Loops 118
5.2. Design of the frontal-region operating Loops 118
5.3. TR Switch Circuit - Overall View 120
5.4. TR Switch Circuit - Unilateral Mode 121
5.5. TR Switch Circuit - Bilateral Mode 121
5.6. Simulation model for the comercial birdcage coil 123
5.7. Simulation model for the ETE and FRO loops 123
5.8. Attenuation coefficients of the TR switch 124
5.9. Attenuation coefficients of the TR switch with the quadrature ETE loops . . . 125
5.10. Simulation model for the ETE and FRO loops 126
5.11. Experimentally measured B_1^+ maps for the quadrature ETE loops 126
5.12. Measured and simulated B_1^+ maps with the dielectric pad in-place 127
5.13. SAR_{10g} maps for the ETE, FRO and the commercial birdcage coils 128
5.14. RO loops/commercial birdcage - MR spectra from the VOI 128

5.15. FRO loops/commercial birdcage - Metabolites concentrations in the VOI . . . 129
5.16. ETE Loops - MR spectrum and anatomical images 129

List of Tables

1.1. Coil Arrays - Main Results 37
1.2. Receive Array - Pictures 45

4.1. Gaussian optimization - Parameters 101
4.2. Optimized RF phases and corresponding $SAR_{10g,max}$ values 109

Outline of the thesis

The overall goal of this thesis was to investigate innovative radio-frequency coil designs for parallel-transmit whole-brain magnetic resonance (MR) at 7T. To achieve this goal, one particular RF coil design, the dipole antenna, was widely investigated. A transmit/receive RF coil array was built using center-shortened dipoles with a specific geometrical arrangement that enabled whole-brain coverage, including the cerebellum. Current RF coil designs at 7T are well suited for cerebral cortex MR imaging, but often lack signal in the lower areas of the brain. In parallel with the construction of the dipole coil array, a MATLAB graphical user interface (GUI) was developed together with the implementation of a particle-swarm optimization (PSO) method to determine the optimal RF weights of the individual channels in the dipole coil array. To further push the investigation on dipole coil arrays, an independent 32-channel receive loop coil array was built and combined with the transmit dipole coil array. The purpose was to increase sensitivity to the nuclear magnetic resonance (NMR) signal and to enable higher acceleration rates for image acquisition. The combination of a transmit-only dipole coil array with a dense receive-only loop coil array had not been reported when the work described in this thesis began. Therefore, investigation of the nature of the interactions between the two coil arrays was a key point of this work. In particular, the receive coil array geometry needed to be adapted compared to the common approaches due to the specific constraints when combined with a dipole transmit coil array. The thesis also aimed to investigate the benefits and challenges in using dedicated surface RF coils to get enhanced transmit field efficiency in regions usually presenting low intensities.

Most parts of this thesis were adapted from peer-reviewed articles (two published) or conference proceedings. In the next subsections, a brief description of each chapter is given.

Chapter 1 introduces first the theoretical concepts underlying nuclear magnetic resonance with both a quantum and classical approach. It continues with an extensive description of the hardware aspects of magnetic resonance relevant to the different RF coil designs and the quantities to evaluate their performances. The fundamental principles for parallel-transmit are described together with an overview on the RF infrastructure. The methods used throughout the thesis to evaluate the transmit and receive arrays performances are explained. The chapter concludes with a detailed review of transmit/receive and transmit-only/receive-only RF coil arrays developed for the human head magnetic resonance at 7T.

Chapter 2 presents the construction of the 8-channel transmit/receive dipole coil array. The transmit field efficiency, in challenging regions such as the cerebellum, was specifically investigated. The chapter introduces the topic with a brief review of the existing RF coil designs for head imaging at 7T and the justification of the choices made for this study. Thereafter, the methods are detailed and the main results are presented.

Chapter 3 describes the construction of the 32-channel receive-only loop coil array. The relevant design aspects are pointed out. A comparison is done with a commercial 32-channel receive coil array available at our lab to state more clearly the performances of the RF coil design proposed in this thesis. Different criteria as the signal-to-noise ratio, noise correlation matrix and g-factor maps were evaluated.

Chapter 4 presents an extensive description of the Matlab GUI and methods developed for RF phase shimming in parallel-transmit systems at 7T. The precedent optimization methods and the method used (the particle-swarm algorithm) are reviewed in detail. A theoretical insight is given about the particle-swarm-optimization (PSO) algorithm, and the way to compute the individual transmit field sensitivities is described. The performance of the algorithm is evaluated by its ability to provide efficient whole-brain coverage in terms of transmit field.

Chapter 5 introduces the construction of dedicated surface coils for MR spectroscopy in the temporal and frontal lobes of the human head at 7T. It also describes the design of a dedicated transmit-receive (TR) switch to enable unilateral or bilateral transmit modes depending on the particular need. The results were compared in terms of transmit field efficiency to a commercial birdcage coil with an additional dielectric pad used to enhance the transmit field.

The thesis concludes with a summary of the main achievements of the work, along with an outlook on what could be the next steps.

1

Introduction

1.1 Historical background

Nuclear magnetic resonance (NMR) spectroscopy and magnetic resonance imaging (MRI) are essential methods in contemporary science and medicine. The non-invasive nature of MRI and the multiple possibilities offered in terms of anatomical visualization and tissue contrast make this technique among the most widely used in radiology ($\approx$ 600,000 MR examinations in 2016 in Switzerland). In the fields of chemistry and biology, the NMR is an important tool for determining molecular structure and understanding metabolism and biological processes. The following lines provide a brief look back on the theoretical and experimental foundations of NMR.

The NMR story starts in the second quarter of the 20th century when Rabi characterized it for the first time in molecular beams of LiCl [1]. Inspired by the experiment performed by Otto Stern and Walter Gerlach 16 years earlier which found evidence of the quantum nature of the nuclei angular momentum was exposed [2], and further by the mathematical description of the nuclear spin given by Pauli in 1927 [3], Rabi introduced a *resonance method for recording the magnetic properties of atomic nuclei* for which he received in the 1944 Nobel Prize in Physics. Two years later, a major realization in NMR was achieved when Bloch et al. [4] and Purcell et al. [5] discovered the nuclear magnetic moment in liquids and solids, respectively. Like Rabi they observed that nuclei placed in a magnetic field could absorb RF energy at a specific frequency. This phenomenon characterizes **resonance**. Bloch and Purcell were awarded for their discovery in 1952 with the Nobel Prize in Physics.

The path to modern NMR was opened by such scientists as Hahn, Ernst and Anderson. In 1950, Hahn presented the first free induction decay (FID), a result of his experiments with pulsed NMR (short RF excitation pulses) [6]. The same year, he demonstrated the possibility to reverse the loss of phase coherence following a short RF excitation pulse by applying a second RF pulse that would refocus the signal [7]. Ernst and Anderson introduced the Fourier transform approach to determine the frequency response of an FID acquired after exciting a broad range of frequencies. These achievements led to the development of magnetic resonance imaging. In 1973, Lauterbur applied the reconstruction method of computed tomography to NMR. A 2D image was reconstructed with the acquisition of multiple 1D profiles acquired along different radial directions by using magnetic field gradients [8]. Mansfield provided a mathematical framework with the k-space formalism and 2D-Fourier transformation to reconstruct an image, giving rise to modern MRI methods. They were awarded with the Nobel Prize in Medicine or Physiology in 2003 for their *discoveries concerning magnetic resonance imaging*.

1.2 Physics of NMR

In this section an introduction to the underlying physics of NMR is given. The concepts of nuclear spin, macroscopic magnetization and interactions with the RF field are reviewed. The Bloch equations which describe the temporal evolution of the NMR signal will be introduced.

1.2.1 The NMR quantum approach

1.2.1.1 Nuclear spin

The foundations of NMR rest on an intrinsic property of the particles constituting matter, **nuclear spin, I**. It characterizes a particle the same way as mass, charge or size do. The particles can be categorized according to their spin property. Indeed, depending on the internal composition of the particle (protons, neutrons which are composed of quarks) the spin value can be either half-integer, integer or null. Particles with a half-integer value (like protons and electrons) are called **fermions** and obey Fermi-Dirac statistics to describe their distribution over energy states. As fermions, they are subject to Pauli's exclusion principle which states that two identical fermions cannot occupy the same quantum state simultaneously. Particles with an integer spin value (like photons, mesons) are called **bosons** and obey the Bose-Einstein statistics. The total spin value of a particle depends on the number of protons and neutrons. When there is an even number of both (like ^{12}C, ^{16}O), the total spin is 0. However, only non-zero spin particles are useful for MR experiments. A non-zero spin particle can be seen as a spinning charge sphere although the particle is not physically rotating. Nevertheless, it is a helpful description to understand the following concepts.
Like a macroscopic object in rotation, the particle spin is characterized by a **spin angular momentum** $\vec{S}$ (analogous to the angular momentum) that is directly associated with the spin I of the particle. The direction of $\vec{S}$ can be modified by external forces (such as a magnetic field) and the magnitude is given by Equation 1.1:

$$\left|\vec{S}\right| = \hbar \sqrt{I(I+1)} \tag{1.1}$$

where $\hbar$ is the Planck constant h divided by 2π. The discrete energy states accessible for a particle with spin are characterized by the quantum number $\mathbf{m_I}$ which can take 2I + 1 values (Equation 1.2).

$$m_I = -I, -I+1, ..., I-1, I \tag{1.2}$$

For spins 1/2 like proton, there are therefore two energy states available characterized by m_I = 1/2 and m_I = -1/2. An other important property to mention is the magnetic moment $\vec{\mu}$ that is linked to $\vec{S}$ via the so-called **gyromagnetic ratio**, γ, which is specific to a nucleus (Equation 1.3).

$$\vec{\mu} = \gamma \vec{S} \tag{1.3}$$

Various nuclei can be investigated in NMR experiments, including carbon ^{13}C, phosphorus ^{31}P or sodium ^{23}Na. They are used to get metabolic information. Nevertheless, the scope of this thesis is centered on proton NMR, which is the most often used for human measurements because of the high natural abundance of water (H_2O) in the human body. The γ-value for proton is about 42.58 MHz/T.

1.2.1.2 The quantum NMR

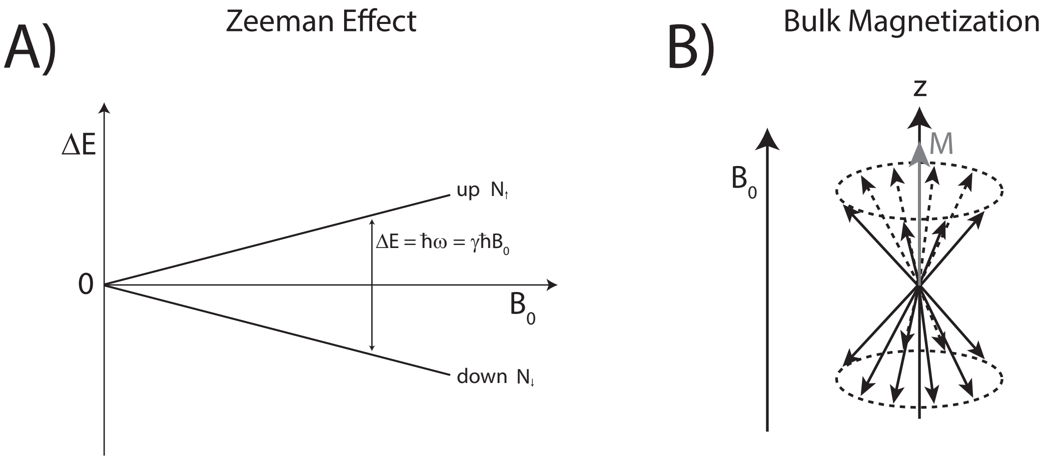

Figure 1.1: *A) Zeeman effect: the energy difference between the two spin states is linear with the main magnetic field* B_0*. B) Bulk magnetization seen as the sum of the individual magnetic moments.*

In presence of an external magnetic fiel, $\vec{B}_0$, (aligned along $\hat{z}$ by convention), the spins (through the magnetic moment) will tend to orient in certain directions associated to the energy levels described previously. In the case of proton NMR, the two available spin states are referred as the anti-parallel (spin "down") or parallel (spin "up") with respect to the direction of $\vec{B}_0$. However, the spins are not totally aligned with $\vec{B}_0$ and rotate along the z-axis at the Larmor frequency which will be defined later. The energy associated to these states are given by equation 1.4 where μ_z is the projection of the magnetic moment μ along the z-axis and $S_z = \hbar m_I$. This separation between the two energy states in presence of $\vec{B}_0$ is known as the **Zeeman splitting effect** (Figure 1.1A).

$$E_{m=\pm\frac{1}{2}} = -\mu_z B_0 = -\gamma S_z B_0 = \mp\frac{1}{2}\gamma\hbar B_0 \tag{1.4}$$

The difference between the two energy levels is proportional to the B_0 field strength, and given by equation 1.5.

$$\Delta E = E_{m=-\frac{1}{2}} - E_{m=+\frac{1}{2}} = \gamma\hbar B_0 \tag{1.5}$$

The transition between the two energy states therefore involves the absorption and emission of electromagnetic radiation. By Planck's relation, the difference of energy between the two states is associated with the electromagnetic radiation frequency (Equation 1.6).

$$\Delta E = \hbar\omega \Rightarrow \omega = \gamma B_0 \tag{1.6}$$

The frequency ω is known in NMR as the **Larmor frequency** ω_L. At 7T, it is approximately equal to 297 MHz for the proton. The two energy levels are almost equally populated at room temperature (T = 300K), and using the Boltzmann distribution the ratio between the two states (spin-up and spin-down) can be calculated (Equation 1.7):

$$\frac{N_\uparrow}{N_\downarrow} = \exp\left(\frac{\Delta E}{k_B T}\right) \tag{1.7}$$

where k_B is the Boltzmann constant, T is the temperature in Kelvin and ΔE is the difference in energy states (Equation 1.5). At 7T and room temperature the difference in population is almost negligible (8 per 1 million). Nevertheless, without this difference, no NMR signal could be measured. Such negligible differences are balanced by the very large number of protons contained in the human body tissues (approximately 60% of the body is water).

1.2.2 The NMR classical approach

In the classical approach of NMR, the spins are no longer considered individually at a macroscopic scale. Since the spins are additive quantities, a bulk magnetization, $\vec{M}$, can be calculated as the sum of the individual magnetic moments (Equation 1.8). Since there are slightly more spins parallel to B_0 than anti-parallel, the bulk magnetization is oriented along $\hat{z}$ and is defined by equation 1.9 (Figure 1.1B).

$$\vec{M} = \sum \vec{\mu} = \left(N_\uparrow - N_\downarrow\right)\mu_z \tag{1.8}$$

$$M_z = \frac{N\gamma^2\hbar^2 B_0}{4k_B T} \equiv M_0 \tag{1.9}$$

In equation 1.9, N corresponds to the total number of spins per unit volume. The NMR signal is directly proportional to the bulk magnetization (Equation 1.29) which depends on the square of the gyromagnetic ratio and is linear with B_0. Therefore, increasing the B_0 field results in increased sensitivity similarly as considering nuclei with high gyromagnetic ratio.

1.2.2.1 Precession

In classical mechanics, precession is a well-known phenomenon. For example, a spinning top with a certain angular moment will undergo a circular motion at a frequency Ω around the vertical axis z. According to the Newton's second law for rotations, the variation in angular momentum is equal to the torque applied to the system (Equation 1.10).

$$\frac{d\vec{L}}{dt} = \vec{\tau} \tag{1.10}$$

For the spinning top, torque is produced by gravity and the position of the angular momentum of the object varies according to equation 1.11 where $\vec{L}$ is the angular momentum and $\vec{\Omega}$ is the precession frequency.

$$\frac{d\vec{L}}{dt} = \vec{\Omega} \times \vec{L} \tag{1.11}$$

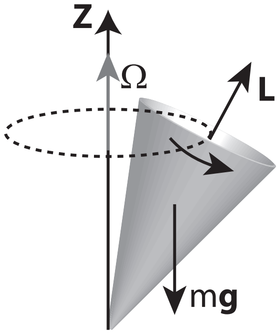

Figure 1.2: *Visual representation of a spinning top. The gravitational force (m$\vec{g}$ produces a torque which modifies the direction of angular momentum $\vec{L}$ giving rise to the precession motion about the z-axis with frequency Ω. Analogously the nuclei can be see as the spinning top. The precession is driven by the external magnetic field $\vec{B_0}$ and $\vec{S}$ is identified to the angular momentum for the spinning top.*

Similarly to the spinning top, the magnetic moment of a spin will undergo a torque defined by $\vec{\tau} = \vec{\mu} \times \vec{B_0}$, when subject to the $\vec{B_0}$ field. Since $\vec{S}$ is the spin angular momentum, equation is equivalent to equation 1.10 for a spin.

$$\frac{d\vec{S}}{dt} = \vec{\mu} \times \vec{B} \tag{1.12}$$

By identification with equations 1.3 and 1.11, it results that the spin magnetic moment precesses around $\vec{B_0}$ at a frequency $\omega = -\gamma \vec{B_0}$ which actually corresponds to the electromagnetic radiation frequency required to induce a transition between the two spin states. The sum over the magnetic moments therefore gives:

$$\frac{d\vec{M}}{dt} = -\gamma \vec{B_0} \times \vec{M} \tag{1.13}$$

At this point, a change in referential frame is done to describe in a simpler way the evolution of the magnetization $\vec{M}$ under RF excitation. The idea is to use a so-called **rotating frame** that rotates around $\vec{B_0}$ at the Larmor frequency (Equation 1.6) instead of the fixed reference frame of the lab. In the rotating frame, the temporal evolution of bulk magnetization is described by equation 1.14 where $\vec{\omega} = \vec{\omega_L}$ is the Larmor frequency.

$$\left(\frac{d\vec{M}}{dt}\right)_{rot} = \left(\frac{d\vec{M}}{dt}\right)_{lab} - \vec{\omega} \times \vec{M} \tag{1.14}$$

Combined with equation 1.13 in the case where only $\vec{B_0}$ is applied, it results that:

$$\left(\frac{d\vec{M}}{dt}\right)_{rot} = -\gamma \vec{B_0} \times \vec{M} - \vec{\omega} \times \vec{M} = -\gamma \left(\vec{B_0} + \frac{\vec{\omega_L}}{\gamma}\right) \times \vec{M} \tag{1.15}$$

The change to a rotating frame results with an additional fictitious field term $\vec{\omega_L}/\gamma$ to the main magnetic field $\vec{B_0}$. This new field, referred as the **effective** $\vec{B_{eff}}$-field is equal to zero when there is only $\vec{B_0}$, and therefore $\vec{M}$ is stationary. While this simplification may not appear very essential in this situation where there is only the main magnetic field, it is important to point out that in this configuration ($\vec{M}$ aligned with $\vec{B_0}$) no NMR signal can be measured. Indeed the main magnetic field is several orders of magnitude stronger than the bulk magnetization. To measure a signal, $\vec{M}$ has to be moved out of its equilibrium position along $\vec{B_0}$. In the next section, details are given about the method.

1.2.2.2 Excitation of the magnetization

The idea to create a detectable signal is to bring the magnetization $\vec{M}$ into the transverse plane (x-y plane). This is achieved by applying a radio-frequency magnetic field $\vec{B_1}$ oscillating in transverse plane (Figure 1.3A). Such magnetic field is produced by an RF coil according to Ampere's law (Equation 1.27). The so-called **transmit field** can be decomposed into two counter-rotating components $\vec{B_1^+}$ and $\vec{B_1^-}$:

$$\vec{B}_1 = \vec{B}_1^+ + \vec{B}_1^- \quad with \quad \vec{B}_1^+ = \frac{1}{2} B_{1,max} \left[\cos(\omega t + \varphi)\hat{x} - \sin(\omega t + \varphi)\hat{y}\right] \tag{1.16}$$

$$\vec{B}_1^- = \frac{1}{2} B_{1,max} \left[\cos(\omega t + \varphi)\hat{x} + \sin(\omega t + \varphi)\hat{y}\right] \tag{1.17}$$

where $B_{1,max}$ is the amplitude of the RF field produced by the coil, ω is the frequency, and ϕ is the initial phase. Only the $\vec{B}_1^+$ component of the transmit field rotating in the same direction as the magnetization (counter-clockwise) will interact with the spins. It means that half of the RF energy is "lost" . However, it is important to note that by the principle of reciprocity (see 1.3.1.1), the signal received in the RF coil is proportional to the $\vec{B}_1^-$ component of the RF field.

It is interesting at this point to see how the rotating frame defined in a previous section is useful to describe the displacement of $\vec{M}$. Assuming the system is considered in the reference frame of the lab, then according to equation 1.13 the total magnetic field would be $\vec{B}_{tot} = \vec{B}_0 + \vec{B}_1$ instead of only $\vec{B}_0$. Therefore, the magnetization precesses around both fields and follows a helicoidal trajectory (Figure 1.3A). This kind of representation is not very practical to use. As mentioned previously, in the rotating frame of reference the $\vec{B}_0$ is "canceled". Assuming the $\vec{B}_1$-field is emitted in the x-direction, and oscillating at Larmor frequency it will appear as stationary in the rotating frame of reference and oriented along x′ (Figure 1.3B).

Equation 1.13 in the rotating frame can therefore be re-written as:

$$\left(\frac{d\vec{M}}{dt}\right) = -\gamma \vec{B}_1 \times \vec{M} \tag{1.18}$$

The equation 1.18 describes the temporal evolution of the magnetization in the rotating frame of reference when the RF field $\vec{B}_1$ is emitted. The magnetization will precess around $\vec{B}_1$ at an angular frequency defined by equation 1.19.

$$\vec{\omega}_1(t) = -\gamma \vec{B}_1(t) \tag{1.19}$$

Depending on how long the RF field was applied, the final angle between the z-axis and the magnetization can be varied. If the RF amplitude of the $\vec{B}_1$-field is kept constant all along the RF transmission, the RF signal is called a hard-pulse. By integration of equation 1.19 over time (from 0 to a given time-length τ) the so-called **flip angle** can be calculated (Equation 1.20).

$$\alpha = \int_0^\tau \vec{\omega}_1(t)dt = \gamma \int_0^\tau \gamma B_1 dt = \gamma B_1 \tau \tag{1.20}$$

In the flip angle equation (Equation 1.20), the B_1 refers to the counter-clockwise compo-

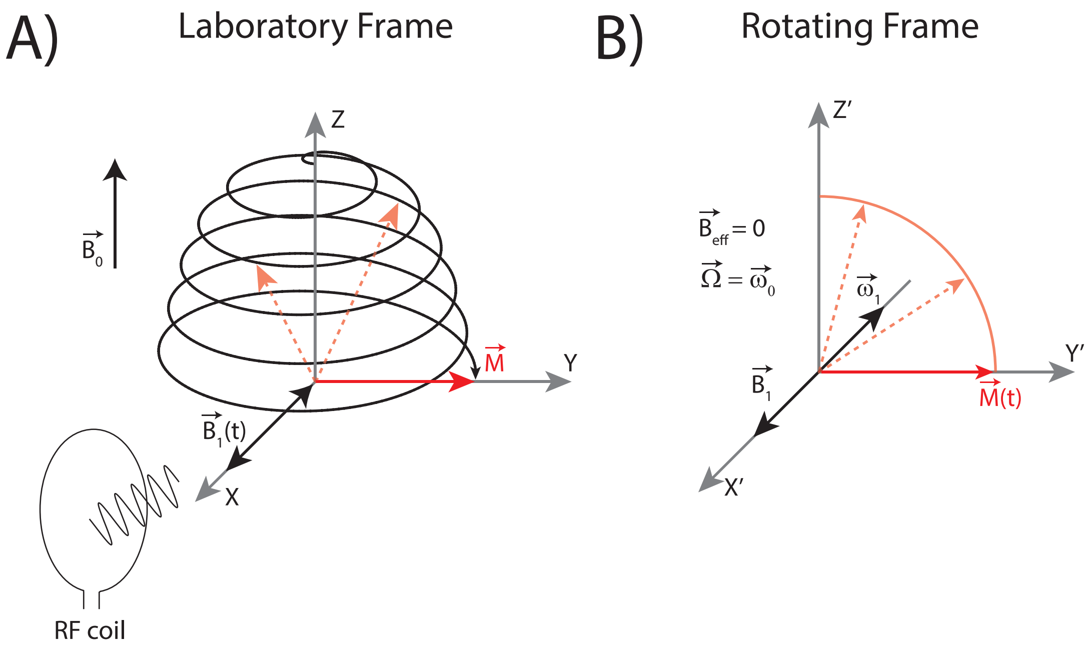

Figure 1.3: *A) In the laboratory frame: the RF excitation $\vec{B}_1(t)$ is time-varying along the x-direction, and the magnetization follows a helicoidal trajectory. B) In the rotating frame: the $\vec{B}_1$ excitation is stationary along x′ and the magnetization rotates around it.*

nent of the $\vec{B}_1$ field since it was previously described that only this component will induce a rotation of the magnetization. In Figure 1.3B, a 90°flip angle is shown. The magnetization lies down in the x′-y′ plane with no component along z′. Since it is related to the transmit field, the flip angle value for a given pulse length is an essential quantity for assessment of the RF coil efficiency (see 1.5.4.1).

1.2.2.3 Relaxation of the magnetization

After the RF pulse, the magnetization is completely in the transverse plane (assuming a 90°flip angle). At this point, two mechanisms take place. The **transverse relaxation** process describes the decay of the transverse component M_{xy} of the magnetization while **longitudinal relaxation** relates to the growth of longitudinal component M_z as magnetization returns to its equilibrium position along $\vec{B}_0$.

To describe the NMR phenomenon, the bulk magnetization was considered. However, to understand the decay of M_{xy} it is useful to consider again the magnetization as a sum of small magnetic moments. Right after the RF excitation, they are all in phase and precess around $\vec{B}_0$ (Figure 1.5) at the Larmor frequency. However, due to the inherent motion of the atoms in living tissues (Brownian motion) or vibrations, the interactions between e.g two individual magnetic moments may cause a very localized variation in the $\vec{B}_0$. One of the

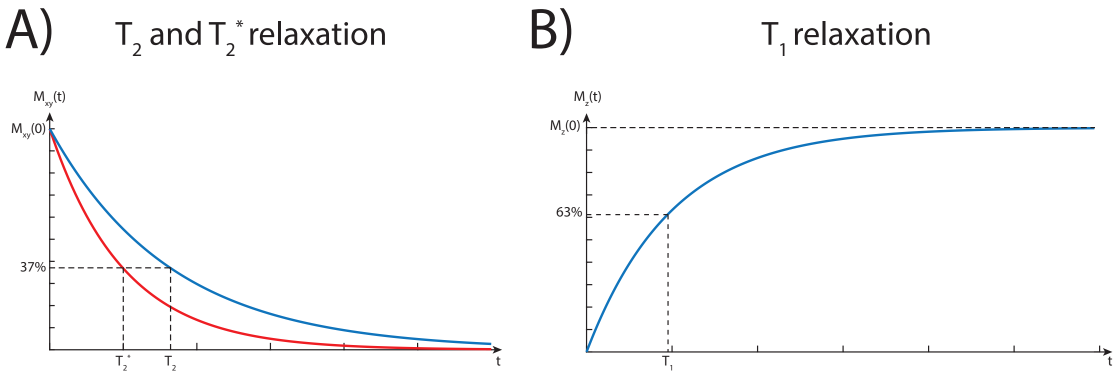

Figure 1.4: *A) T_2 (blue curve) and T_2^* decay curves. The characteristic times T_2 and T_2^* correspond to 37% remaining magnetization in the transverse plane. B) T_1 relaxation curve. The characteristic time T_1 corresponds to a 63% recovery of the initial magnetization (at equilibrium).*

two nuclei will experience a slightly stronger magnetic field while it will be opposite for the second nucleus. This phenomenon is called the **spin-spin interaction**. It results that they will precess at frequencies slightly different from the Larmor frequency. The first nucleus (experiencing a stronger magnetic field) will precess at a higher frequency and will gain phase while the second will lose phase with respect to the nuclei precessing at the Larmor frequency. When they are separated, they return to the original precessing frequency but the phase gain or loss remains. Since many of these interactions happen in the tissues (or any matter), it ends up with a complete loss of coherence in the transverse plane (Figure 1.5).

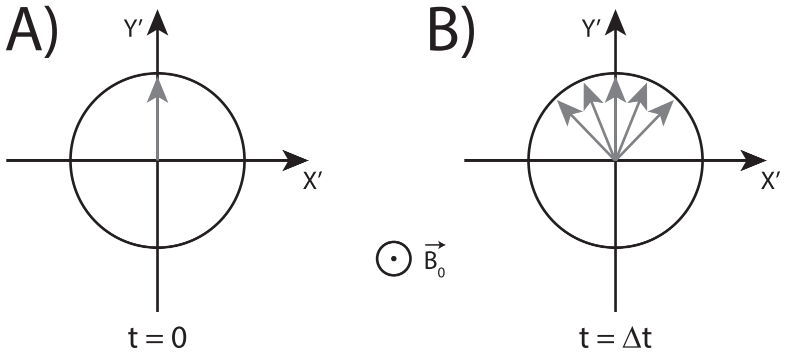

Figure 1.5: *(A) At t=0, the individual magnetic moments are in phase and give the maximal signal. B) After a short Δt interval, the magnetic moment have lost phase coherence because of the spin-spin interactions. The total transverse magnetization decays.*

The transverse magnetization decays according to equation 1.21 where T_2 is specific to a tissue and characterizes the time at which 37% of the original transverse magnetization $M_{xy}(0)$ is still measurable.

$$\frac{dM_{xy}}{dt} = -\frac{M_{xy}}{T_2} \Rightarrow M_{xy}(t) = M_{xy}(0)\exp(-t/T_2) \tag{1.21}$$

In human brain tissue, the T_2 values are on the order of tens of ms. While at the microscopic level the loss of phase coherence between the magnetic moments is attributed to the spin-spin interaction, large B_0 inhomogeneities due, for example, to air-tissue boundaries can also disturb the spin system in a same way. The field variations will induce a faster dephasing of the magnetic moments and thus the loss of coherence. The T_2 corrected for ΔB_0 fluctuations is called T_2^* and is defined by equation 1.22.

$$\frac{1}{T_2^*} = \frac{1}{T_2} + \gamma \Delta B_0 \tag{1.22}$$

Transverse relaxation describes the loss of phase coherence due to spin-spin interaction between the individual magnetic moments. However, this phenomenon does not induce a variation in the net energy of the system. **Longitudinal relaxation** concerns the recovery of the magnetization M_z component due to energy transfer from the spin system to the surrounding environment. This phenomenon is called the **spin-lattice interaction**, since at the beginning of NMR in solids the external environment was a crystalline lattice. The RF excitation of the spins induces transitions between low (spin-up orientation) to high (spin-down) energy states. However, statistically the spins "favor" the lower energy states. Therefore, during T_1-relaxation there is energy leaving the spin system. This energy is transferred to the nearby atoms and molecules through collisions or electromagnetic interactions. Transitions between the two energy states for a given nucleus are stimulated by fluctuating magnetic fields (near to the Larmor frequency) in the transverse plane and originating from nearby molecular motion. The evolution of longitudinal magnetization is described by :

$$\frac{dM_z}{dt} = \frac{M_0 - M_z}{T_1} \Rightarrow M_z(t) = M_0 + (M_z(0) - M_0)\exp(-t/T_1) \tag{1.23}$$

where M_0 is the initial magnetization (at equilibrium), $M_z(0)$ is the longitudinal magnetization after the RF excitation ($M_z(0) = 0$ for a 90°flip angle) and T_1 is the characteristic time at which 63% of the original magnetization is recovered (Figure 1.4B). T_1-relaxation is almost always longer than the T_2 and T_2^* processes, with typical T_1 values on the order of a hundred to a thousand of ms.

1.2.2.4 Bloch Equations

The relaxation parameters are added to the equation 1.13 which describes the evolution of the magnetization in the reference frame of the lab (stationary):

$$\frac{\vec{M}}{dt} = -\gamma \vec{B} \times \vec{M} - \frac{M_x \hat{e}_x + M_y \hat{e}_y}{T_2} - \frac{(M_z - M_0)\hat{e}_z}{T_1} \tag{1.24}$$

Since the longitudinal component of the magnetization is decoupled from the transverse components in the absence of a B_1-field (after RF excitation), it can be solved independently, and the temporal evolution of $M_z(t)$ corresponds to equation 1.23. Similarly, the system of equations for M_x and M_y results in the following equations to describe their temporal evolution:

$$\begin{aligned} M_x(t) &= M_0 \sin(\omega_0 t) \exp(-t/T_2) \\ M_y(t) &= M_0 \cos(\omega_0 t) \exp(-t/T_2) \end{aligned} \tag{1.25}$$

where T_2 is the characteristic relaxation time for transverse loss of phase coherence and ω_0 is the Larmor frequency (Equation 1.6).

1.2.2.5 Ernst angle or the optimum flip angle

According to the description of the magnetization, the maximal NMR signal is achieved when the magnetization is completely lying down in the transverse plane. Therefore, the ideal flip angle for any experiment would be 90°. However, this assumption is generally inaccurate because of the relaxation processes. Indeed, in order to get an MR image the same pulse (thus the same flip angle) has to be applied several times to get the required information for image reconstruction. As described in subsection 1.2.2.3, after the magnetization is flipped it will undergo a relaxation process to return to its equilibrium position along the main magnetic field $\vec{B}_0$. The associated longitudinal relaxation time T_1 is characteristic for every human tissue. The duration between two RF excitation pulses is known as the **repetition time** T_R.
In case of a 90°flip angle, the magnetization is totally in the transverse plane after the first RF pulse. During the delay T_R the longitudinal relaxation takes place. Unless to wait for a long time, it is presumable that a full longitudinal relaxation is not achieved at the end of the first T_R. Therefore, since the NMR signal is proportional to the effective magnetization available on the transverse plane it is foreseeable that a second 90°RF pulse may result in a loss of signal (Figure 1.6).

The optimal flip angle to maximize the signal intensity for a spoiled (transverse coherences are disrupted) gradient-echo sequence was defined [9] with equation 1.26 where T_R is the repetition time of the sequence and T_1 is the longitudinal relaxation time of e.g the human tissues.

$$\alpha_E = \arccos\left(\exp(-T_R/T_1)\right) \tag{1.26}$$

From this equation it is clear that for an infinite repetition time, the optimal flip angle is 90°. The signal intensity with respect to the flip angle is shown for a spoiled-GRE sequence (T_R = 500 ms, T_E = 30 ms) with the white matter (T_1 = 1000 ms, T_2^* = 28 ms) and the gray matter (T_1 = 1650 ms, T_2^* = 33 ms) at 7T (Figure 1.7). The optimal flip angle (maximum of the signal intensity curve) is significantly lower than 90°. Nevertheless, the best contrast

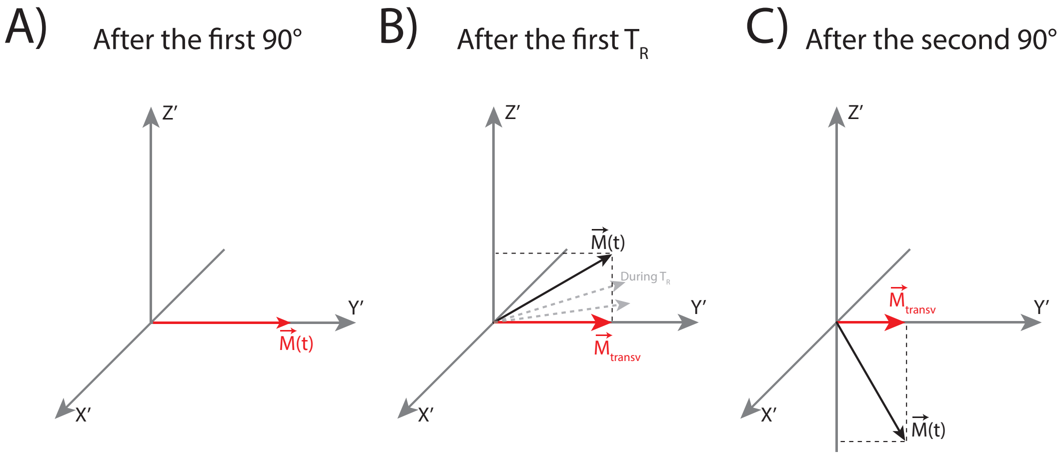

Figure 1.6: *A) Magnetization after the first 90° RF pulse is in x′-y′ plane and gives the maximal NMR signal. B) During* T_R *the longitudinal relaxation takes place (grey arrows) and after* T_R *the magnetization is not fully relaxed. C) The second 90° RF pulse brings into transverse plane x′-y′ the longitudinal projection of the magnetization present in B). By considering the effective transverse magnetization* $\vec{M}_{transv}$ *(red arrow), the loss of signal is clearly visible.*

between the two tissues is not achieved at one or the other Ernst angle but for a 80° flip angle (Figure 1.7, black double-arrow). The optimal flip angle for MR imaging is therefore often a balance between the optimal value for tissue contrast′ and the theoretical Ernst angle for maximal signal.

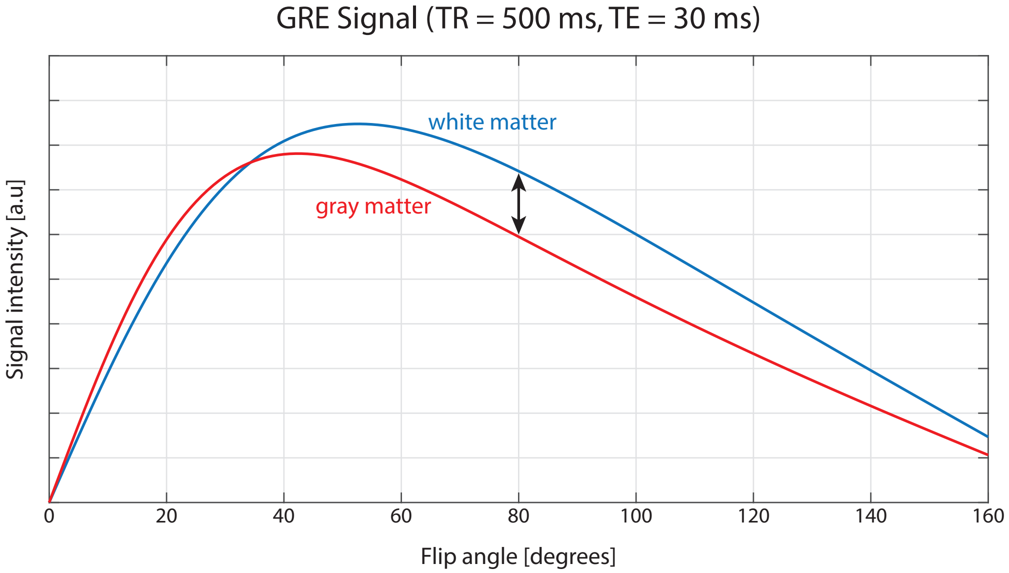

Figure 1.7: *GRE signal plotted for gray and white matter according to equation 4.3 for* T_R *= 500 ms and* T_E *= 30 ms. The optimal flip angle (equation 1.26 is lower than 90°. However, the best contrast between the two tissues (black double-arrow) is achieved at a different optimal flip angle (around 80°)*

1.3 RF Hardware and Methods

1.3.1 NMR probes

The NMR probe is a crucial component in MR systems. It is responsible for emitting the transverse magnetic field B_1 which tips the macroscopic magnetization M_0 (defined in section 1.2.2) in the plane orthogonal to the main magnetic field B_0. The NMR probe is also used to detect the MR signal incoming from the sample which is then transferred to the receive line and processed. The **reciprocity principle** is the fundamental theoretical concept used to understand the NMR probes and was stated by Hoult and Richards in 1976 [10]. In the next subsection it is briefly introduced.

1.3.1.1 The reciprocity principle

A NMR probe basically consists of an electrical circuit that is fed by a current I. By Ampere's law (Equation 1.27), a current density $\vec{J}$ through a surface S will induce a magnetic field $\vec{B}$.

$$\oint_C \vec{B} \cdot \vec{dl} = \mu_0 \iint_S \vec{J} \cdot \vec{dS} = \mu_0 I \tag{1.27}$$

In equation 1.27, $\oint_C$ is the closed integral, and $\iint_S$ the surface integral enclosed by C. The magnetic field induced by I in the NMR probe will interact with the spins in the sample. During reception, The MR signal received by the NMR probe is determined with Faraday's law of induction, which predicts the rise of an electromotive force ζ (a voltage difference) when a time-varying magnetic field flux goes through a surface enclosed by a path C (Equation 1.28).

$$\zeta = \oint_C \vec{E} \cdot \vec{dl} = -\iint_S \frac{d\vec{B}}{dt} \cdot \vec{dS} \tag{1.28}$$

In equation 1.28, $\vec{E}$ is the electric field and $\vec{B}$ the magnetic field. The principle of reciprocity states that the sensitivity at any point in space during signal reception ($\propto \zeta$, Equation 1.28) is proportional to the B_1 RF field strength produced at the same point while unit current is applied to the probe during transmission (Equation 1.27). The electromotive force is defined [10] by equation 1.29 where M_0 is the sample magnetization and B_1 is the magnetic field produced by the RF probe.

$$\zeta = -\frac{\partial}{\partial t}\{\vec{B_1} \cdot \vec{m}\} = \omega_0 B_1 M_0 \tag{1.29}$$

The transmit field B_1 can be calculated according to the specific design of the RF probe [11]. For the RF loop coil, which is widely used in NMR, it can be calculated with the Bio-Savart law for a current I flowing inside the loop given that the loop radius is small compared to the wavelength of the RF signal.

$$\vec{B}(z,R) = \frac{\mu_0 I}{2} \cdot \frac{R^2}{(z^2+R^2)^{3/2})} \tag{1.30}$$

In equation 1.30, the z-term corresponds to the penetration depth and R to the radius of the coil. At a given depth, there is one optimal radius that maximizes the transmit field B_1. The relationship between depth and optimal radius can be deduced from the derivative of equation 1.30 and is given by $R = \sqrt{2} \times z$.

1.3.1.2 RF probe circuits and matching

To understand the RF probes working principle, a brief introduction to the LC (inductor, capacitor) circuit is given. The electrical design consists of an inductor in parallel with a capacitor. Inductors will store the incoming energy in the form of magnetic fields while for a capacitor it will be as an electric field (between the two plates). Analogous to a mechanical oscillator, the circuit possesses an inherent resonance frequency where the energy will oscillate between the inductor (L) and the capacitor (C). In absence of any dissipation, the oscillations could last forever. Nevertheless, the internal resistance (R) of the components will dissipate the energy just as air friction does for a mechanical oscillator.
To describe the characteristics of these components, the concept of impedance is introduced (Z = R + iX) where R and X are respectively the **resistive** and the **reactive** parts. The impedances for the inductor, capacitor and resistor are given in equations 1.31,1.32, 1.33.

$$\begin{aligned} Z_R &= R \quad (1.31)\\ Z_L &= j\omega L \quad (1.32)\\ Z_C &= \frac{1}{i\omega C} = -\frac{i}{\omega C} \quad (1.33)\end{aligned}$$

The inductors and capacitors have an impedance that depends on the frequency. At high frequencies a capacitor will have a low impedance and an alternating current (AC) will easily go through it, while at high frequencies or high inductance value L, the inductor will block the RF signal. This is why in RF circuits for MR applications, high-inductance inductors (known as RF chokes) are often placed to isolate an electric path from RF currents. When the capacitor is placed in parallel with the inductor, a resonant circuit is created as described before. The total impedance is therefore given by equation 1.34 where $X_C = \frac{1}{\omega C}$ and $X_L = \omega L$.

$$\frac{1}{Z_A} = \frac{1}{r+i\omega L} + i\omega C \Rightarrow Z_{AB} = \frac{rX_C^2}{r^2+(X_L-X_C)^2} - iX_C\frac{r^2+X_L(X_L-X_C)}{r^2+(X_L-X_C)^2} \tag{1.34}$$

A resonance is achieved when the imaginary part of Z_{AB} is canceled. This is equivalent to:

$$LC\omega_r^2 = 1 - \frac{r^2C}{L} \approx 1 \tag{1.35}$$

where the term $\frac{r^2C}{L}$ can be neglected since the circuit resistance is usually small at the frequency of interest (a few ohms). The resistive component of the impedance is maximized at the same frequency (Figure 1.8A).

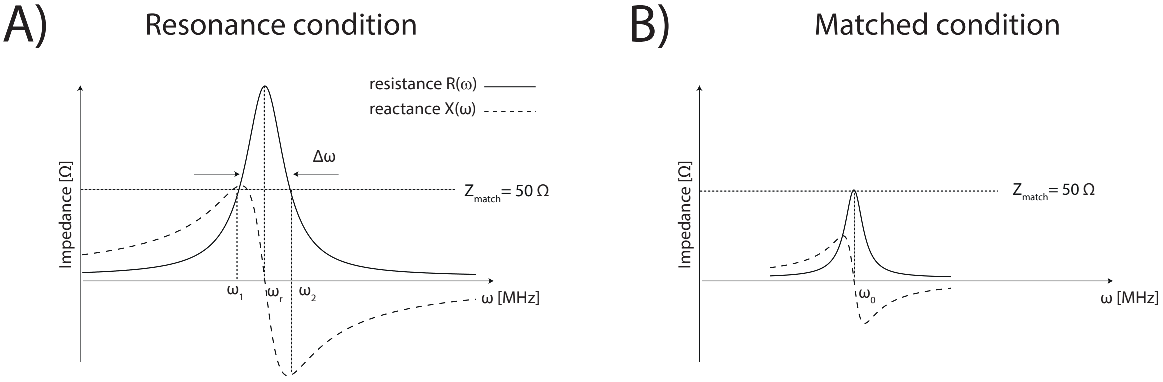

Figure 1.8: *A) Impedance curves when no matching is done. At resonance ω_r the reactive component is canceled while the resistive part is maximal. B) To match the resonance at 50 Ohms, ω_r has to be lowered or increased to match with ω_1 or ω_2*

To efficiently transfer the power from the RF amplifier to the RF coil, the circuit's impedance must be equal to the source impedance, which is usually 50 Ohms. The tuning and matching procedure consists therefore of adjusting the circuit such as it is matched to the RF amplifier impedance. The first step called **tuning** consists of adjusting the resonance frequency ω_r to ω_1 or ω_2, which should correspond to the Larmor's frequency of interest (Figure 1.8B). However, at these frequencies the reactive part of the total impedance (Equation 1.34) is non-zero. The second step called **matching** consists of adding a reactive element (capacitor or inductor) to cancel the reactive component (X_{tot}). At $\omega_r = \omega_1$, X_{tot} is positive, which corresponds to an inductive over-match, and a capacitor can be added in series, while at $\omega_r = \omega_2$, X_{tot} is negative, which corresponds to a capacitive over-match, and a series inductor is added. Nevertheless, since inductors are lossy components, it is usually preferred to use capacitors.

1.3.2 Scattering parameters S_{ii} and S_{ij}

The scattering parameter S_{ii} or **matching coefficient** is defined by equation 1.36 and characterizes the reflected power, for example, at the input port of a NMR probe, due to impedance mismatches. At S_{11} = -10 dB, 90% of the incoming power is delivered to the coil and 99% for S_{11} = -20 dB. It is therefore often unnecessary to go beyond -20 dB when tuning/matching a NMR probe since it will not produce a significant gain in terms of transmitted power. The second term defined in equation 1.36 is the **coupling coefficient**. It characterizes the power transmitted between two separated ports. It is commonly used to measure the coupling between RF coils, for example, in an array. This quantity is critical since the coupled power is not delivered to the human body tissue and thus it is lost power. For human head transmit coil arrays at 7T, the S_{12} value should be typically lower than -15 dB as it represents only 3% of coupled power.

$$\begin{aligned} S_{ii} &= 20 \times \log \left(\left| \frac{Z_i - Z_0}{Z_i + Z_0} \right| \right) \\ S_{ij} &= 10 \times \log \left(\left| \frac{P_{ij}}{P_{ii}} \right| \right) \end{aligned} \tag{1.36}$$

In equation 1.36 Z_i and Z_0 are respectively the impedance at input port of the RF probe and of the coaxial cable (typically 50 Ohms) used to transmit the RF power from the plug to the RF coil. The term P_{ij} corresponds to the power measured at port j when port i is active (P_{ii}).

1.3.3 Surface Coils

1.3.3.1 Dipole antennas

The dipole antenna has been used as a transmitter since the beginning of radio-telecommunication. The primary design is simple and consists of two separate identical conductive elements, with the signal received or transmitted in the gap between the two rods. The total length of the dipole is usually equal to the half-wavelength of the desired resonant frequency. The current distribution, and consequently the magnetic field, is therefore almost sinusoidal with a node at each end of the dipole and a maximum value at the center, where the feeding line is connected. The RF dipole design was first proposed for magnetic resonance applications in 2011 by Raaijmakers et al. [12]. At ultra-high field ($\geqslant$ 7T), deeply-located regions such as the prostate are challenging to access, since the RF power attenuation in the body is increased. Compared to other previous RF coil designs, the dipole antenna presents the distinct advantage of being usable as a far-field emitter. This means that the electromagnetic wave propagates into nearby media with higher efficiency, especially when the Poynting vector (Equation 1.37) is oriented toward the target location. The vector magnetic (H) and electric (E) fields for a dipole aligned in the z-direction are shown in Figure 1.9B-C. When the sample is placed below the dipole, the Poynting vector orientation will be favorable for deeply located targets [13].

$$\vec{S} = \vec{E} \times \vec{H} \tag{1.37}$$

The original design, namely the single-side-adapted dipole antenna (SSAD antenna), in-

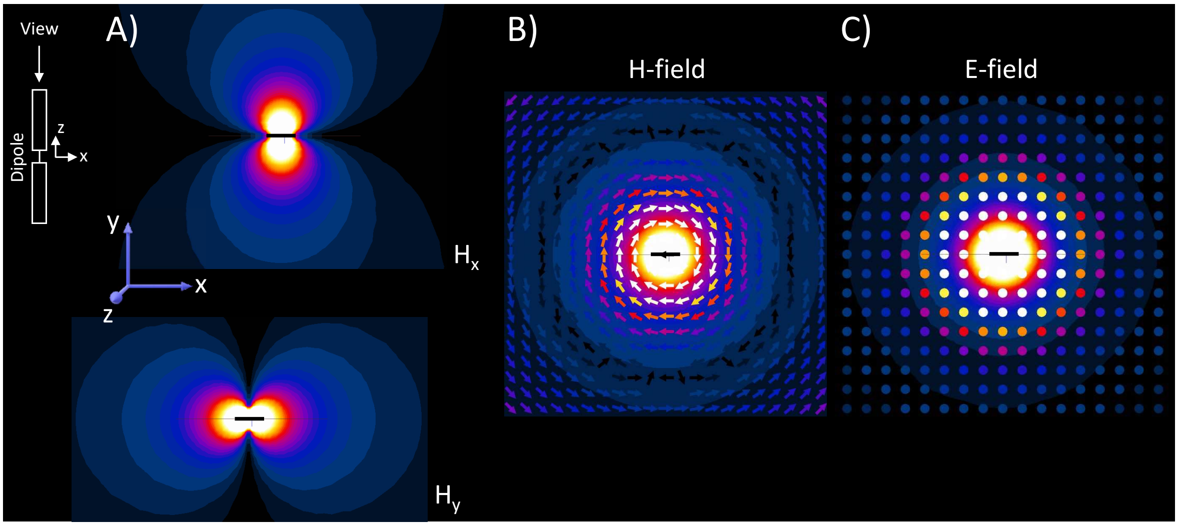

Figure 1.9: *For a simulated single-dipole without dielectric spacer and sample loading: A) X (upper image) and Y (bottom image) projections of the vector magnetic H-field. B) Root-mean-square magnitude and vectors for the magnetic H-field. C) Similar quantities as B) for the electric E-field.*

cluded a dielectric spacer placed between the dipole antenna and the human body tissues. It aimed to keep the electric field outside of the body and provided a dielectric matching from the antenna to the tissue. Nevertheless, it was therefore demonstrated that high coupling to the tissues is achieved without the dielectric material, as long as the dipole is placed close to the body [13]. Compared to loop coils, dipoles provide a better transmit field efficiency (defined as the B_1^+ field over the square root of specific absorption rate $SAR_{10g,max}$, see 1.4.2) in-depth, and the transmit field uniformity is increased.

1.3.3.2 Microstrip Coils

Microstrip RF coils were proposed as an alternative to loop coils [14] and can be understood as a transmission line. The RF coil design consists of a thin strip conductor that is separated from a ground-plane by a low-loss dielectric spacer (Figure 1.10). By nature it therefore works as a distributed capacitor in series. Moreover, the ground plane behaves as an RF shield which decreases the radiation losses (see 1.3.3.4). Thus, they could provide a better quality (Q)-factor compared to conventional loop coils [14]. Nevertheless, the SAR levels are generally higher compared to loops or dipoles [12].

The current distribution on a microstrip at resonance is identical to the dipoles with a maximal current at middle of the microstrip and with a primary resonant mode corresponding to half-wavelength of the resonant frequency. However, unlike a dipole surrounded only by air, the wavelength on a microstrip is dependent on the dielectric substrate properties and dimensions (Figure 1.10). It is reduced as shown in equation 1.38 [14]:

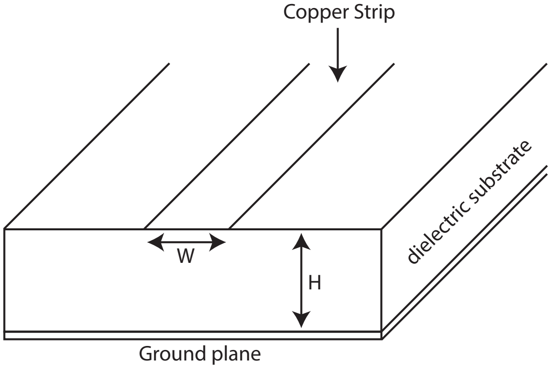

Figure 1.10: *Schematic of the microstrip RF coil design.*

$$\lambda = \frac{\lambda_0}{\sqrt{\epsilon_{eff}}} \tag{1.38}$$

where λ is the microstrip's wavelength, λ_0 is the vacuum wavelength and ϵ_{eff} is the effective dielectric constant defined as [14]:

$$\epsilon_{eff} = \frac{\epsilon_r + 1}{2} + \frac{\epsilon_r - 1}{2\sqrt{1 + \frac{12H}{W}}} \tag{1.39}$$

where ϵ_r is the relative permittivity of the dielectric substrate, W is the width of the microstrip and H the distance between the strip and the ground plane. For NMR, only the first resonant mode is interesting since it produces the more homogeneous transmit field along the microstrip length and the better sensitivity [14]. In terms of RF coil design, it requires L = $\lambda/2$, where L is the electrical length of the microstrip and λ is the effective wavelength defined in equation 1.38. Therefore the first resonant mode can be calculated with equation 1.40, where c is the speed of light in free space and the other parameters are as defined before.

$$f = \frac{c}{2L\sqrt{\epsilon_{eff}}} \tag{1.40}$$

The resonant frequency can be adapted by adding capacitors to the ends of the microstrip to adjust the electrical length of the coil or by modifying the distance between the ground plane and the strip to change the effective permittivity.

1.3.3.3 Loop Coils

Loop coils generally consist of a conductive wire that is bent to create a current loop fed at the input port by the sinusoidal RF signal from the MR scanner. The magnetic field created by a loop has been previously described (Equation 1.30). In this subsection, the same quantities displayed for a dipole (Figure 1.9) are shown for a loop coil to point out the differences between the two designs (Figure 1.11).

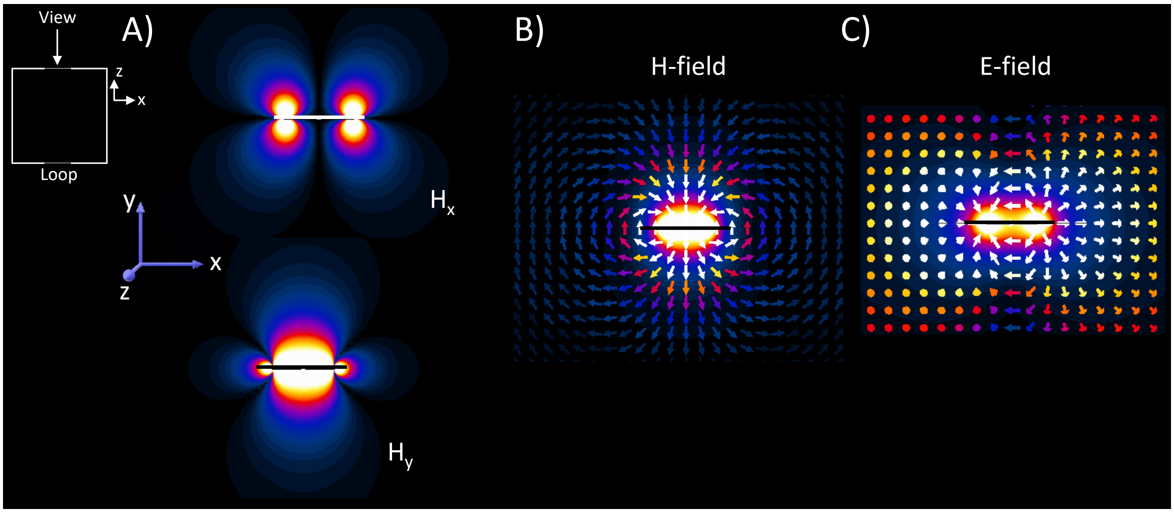

Figure 1.11: *For a simulated single-loop without sample loading: A) X (upper image) and Y (bottom image) projections of the vector magnetic H-field. B) Root-mean-square magnitude and vectors for the magnetic H-field. C) Similar quantities than B) for the electric E-field.*

In terms of H_x and H_y projections of the H-field, the main contribution to the magnetic field is in y-direction for the loop coil while for dipoles it is equally distributed. The vector field distribution of the magnetic field is directed towards the sample while for dipoles they were tangential. Therefore, a loop coil that would be placed perpendicular to the main magnetic field B_0 will not produce an efficient B_1-field while dipoles were shown to produce high transmit field [15]. Moreover loop coils present a Poynting (Equation 1.37) vector oriented in the z-direction. The energy flux of the electromagnetic field is therefore not oriented towards the sample which impairs the in-depth efficiency of the loop coil compared to the dipole antenna [13]. In Figure 1.12, various possible orientations of dipoles and loops are shown with indications on how efficient these orientations are in terms of transmit field efficiency. Nevertheless, while some of the orientations shown in Figure 1.12 are non-optimal for transmit purposes, they can provide significant improvements in terms of signal-to-noise ratio during reception of the MR signal [16].

1.3.3.4 Q-factor

The so-called Q-factor stands for quality factor and is an essential parameter for evaluating the sensitivity of, for example, a loop coil. It is defined by equation

$$Q = \omega_0 \frac{\text{total stored energy}}{\text{power loss}} = 2\pi \frac{\omega_0 L}{r} = 2\pi \frac{\omega_0}{\Delta\omega_0} \tag{1.41}$$

where ω_0 is the Larmor frequency, $\Delta\omega_0$ is the full width at half maximum (FWHM), L is

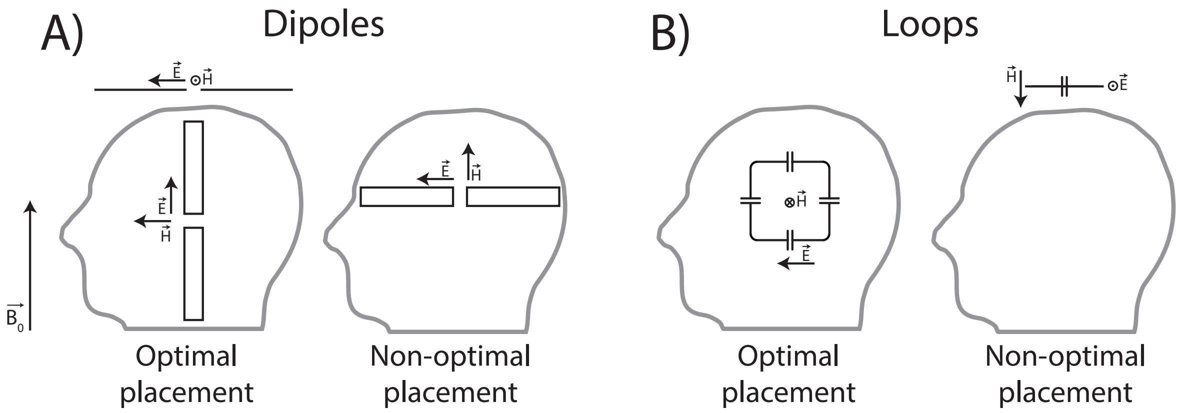

Figure 1.12: *For A) dipoles and B) loop coils. Left: optimal placements in terms of transmit field, right: non-optimal placement. A schematic of the head in sagittal orientation is represented (gray solid lines).*

the inductance of the coil and r is the equivalent resistance of the probe. The total energy in the loop coil is stored as for an inductor, which is defined by $\frac{1}{2}LI^2$. Similarly, the power dissipated per cycle is defined by the ohmic losses as in equation 1.42.

$$P = \frac{1}{2} r I^2 \tag{1.42}$$

Therefore, a high Q-factor means that the energy stored in the resonator takes longer to decay. In MRI, the voltage measured at the terminals of the RF probe during reception is directly proportional to the Q-factor of the coil and the electromotive force [17]. Thus, a high Q-factor contributes to a better detection of the signal. However, since the noise is amplified the same way, it does not imply a higher signal-to-noise ratio. It is then more critical to consider the RF losses when evaluating the performance of a loop coil. They originate from different sources which can be classified into three categories: ohmic resistance R_p, radiation loss R_r and coupled tissue losses R_s [18].

Ohmic losses They are common to any conductive element carrying a current I. The joule effect dissipate the power P through heating of the component or wire ($P = R_p I^2$). The resistance is specific to the conductive material and is proportional to the square root of the frequency ($\propto \sqrt{\omega}$) [18]. However, these losses are usually quite small compared to the other loss sources. For example, the ceramic capacitors used to adjust the tuning of the coils typically present a resistance lower than 1 Ω at 300 MHz. Moreover, while copper is predominantly used as coil conductor, other materials such as silver could be employed since they present a slightly higher conductivity.

Radiation loss Some of the energy contained inside the RF circuit will be lost through radiation into the far-field region of the coil. This phenomenon is more pronounced when the electrical length of the circuit approaches the half-wavelength of the RF signal frequency

[18]. The coil will then behave more as a RF field radiator (like a dipole antenna placed in the air, see subsection 1.3.3.1) with high voltages generated at the nodes of the circuit. The radiation losses are inversely proportional to the wavelength λ^4 (and therefore $\propto \omega^4$) and increase with the square of the area S, which is defined as a unit cross-section of the coil (Equation 1.43) [18].

$$R_r \approx 31200 \left(\frac{S}{\lambda^2} \right)^2 \tag{1.43}$$

One approach to address the radiation losses is to use additional series capacitors to divide the voltage nodes and decrease the electrical length of the conductive element (Figure 1.13). Since the series resistance of the capacitors is quite low, no large RF losses will be induced by these additional components.

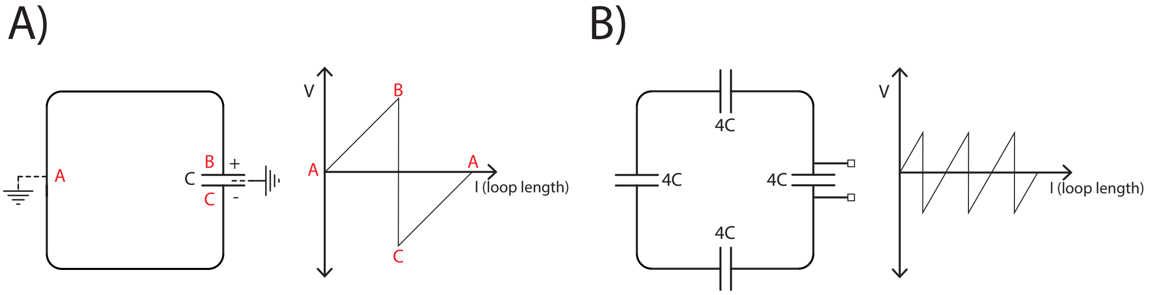

Figure 1.13: *A) Left: Single RF coil represented for only one series capacitor. The virtual grounds are shown. Right: voltage distribution along the path of the loop. B) Left: Single RF coil divided with 4 series capacitors. Right: voltage distribution along the path of the loop.*

Sample loss They are the most crucial losses for MRI and relate to the power dissipated in tissues when the RF coil is loaded by a sample. The losses are due to two different mechanisms, **conduction currents** and **displacement currents**, also known as **dielectric losses**. Conduction currents or **eddy currents** are induced in the sample (like the human head) by the oscillating magnetic field B_1 produced by the RF coil. The associated losses are approximately proportional to ω and are responsible for the temperature increase of the tissues. The dielectric losses correspond to the dissipation of energy through the fast changes in dielectric polarization of the tissue due to the alternating electric fields produced by the RF coil. These losses are proportional to ω^2. As with the radiation losses, decreasing the electric length can diminish this effect. Indeed the penetration of the electric field lines into the volume surrounding the coil is minimized by separating the RF coil with series capacitors (Figure 1.13B, voltage division). The sample losses are included in the equivalent resistance to calculate the Q-factor (Equation 1.43) when the RF coil is placed over a sample. Therefore, the measure of loaded and unloaded Q-factor gives an idea on how much power is dissipated inside the sample [19]. Since part of the power lost in tissues is used to excite the spin system, the measure of unloaded-to-loaded Q-factor ratio is an important quality assessment of the RF probe (should typically be ⩾ 3-4). Analogous to the electronic noise in electrical circuits that is generated by the thermal agitations of the charge carriers, the human body generates thermal noise due to the ionic nature of tissues and fluids. The corresponding noise voltage was established by Johnson and Nyquist [20, 21] and is defined by the following equation:

$$\mathrm{V} = \sqrt{4kTR\Delta f} \tag{1.44}$$

where k is the Boltzmann constant, T the body temperature, R the internal resistance and Δf the bandwidth over which the noise is measured. This noise voltage is part of the MR signal received by the NMR probe and will impair the ability to detect small signals.

1.3.4 Volume Coils

The volume coils were designed to transmit the RF signal homogeneously over large volumes such as the human body. However, while they are extensively used at magnetic fields up to 4T, new challenges arise at ultra-high field notably for RF homogeneity [22]. The following subsection presents the basis for birdcage volume coils and a description of the pros and cons at ultra-high field (⩾ 7T).

1.3.4.1 Birdcage Coils

The so-called birdcage coil was introduced in 1985 by Hayes et al. [23] as an alternative to saddle coils to provide higher RF homogeneity at 1.5T. The underlying principle is that a homogeneous rotating field can be created in the transverse plane of a conducting cylinder if the current distribution around its surface varies sinusoidally. If the conducting cylinder is approximated by a finite number (N) of rods arranged in cylindrical shape, the rotating transmit field is therefore achieved when the current on each rod is phase-shifted by $2\pi/\mathrm{N}$ with respect to the previous element. As an example, a 4-leg birdcage coil is shown in Figure 1.14B to demonstrate how the circularly-polarized transmit field is produced. This principle is extendable to N elements as described by Hayes et al. [23]. The elementary equivalent lumped element circuit (inductors and capacitors) is repeated N times with each time a phase-shift of $\Delta\phi(\omega)$. Since the total structure can be described as a closed loop, periodic boundary conditions apply and the total phase shift must be an integer multiple of 2π. The N successive phase shifts must therefore fulfill the condition given in equation 1.45, where M is an integer.

$$N\Delta\phi(\omega) = 2\pi M \tag{1.45}$$

The resonant frequencies ω can be derived from equation 1.45 and are given by equation 1.46, where $1 \leqslant \mathrm{M} \leqslant \mathrm{N}/2$. The highest B_1^+ field homogeneity is achieved for M = 1 since it generates currents in the rods proportional to $\sin\theta$, where θ is the cylindrical coordinate azimuthal angle.

$$\omega = \frac{2}{\sqrt{L_1 C}} \sin\frac{\pi M}{N} \tag{1.46}$$

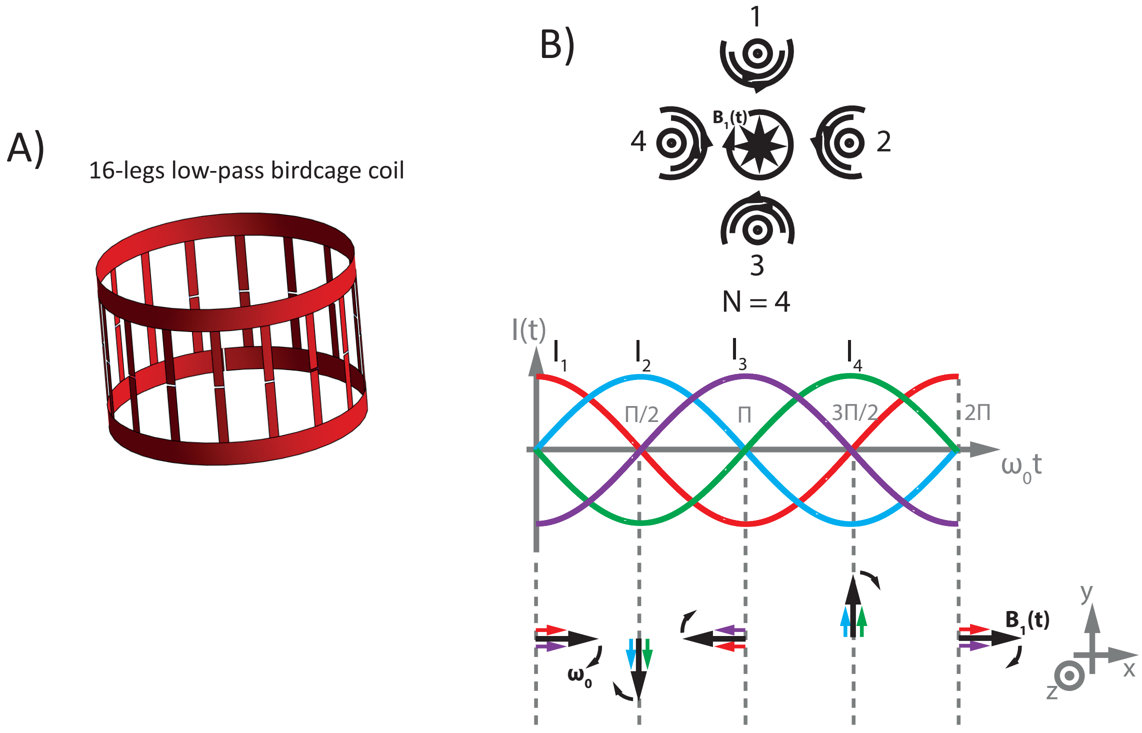

Eggenschwiler, 2015

Figure 1.14: *A) Overall view of the birdcage coil design. B) Visual representation of the working principle for a 4-leg birdcage coil.*

While at lower magnetic fields (1.5T to 3T) birdcage coils provide a homogeneous transmit field within the whole-head volume, at stronger magnetic fields ($\geqslant$ 7T) the transmit field pattern is typically altered and B_1^+-field inhomogeneities are observed inside the brain (Figure 1.15) [22]. The so-called *central brightening effect* was originally attributed to dielectric resonances in the media of propagation [24]. Such resonance occurs when the sample is excited at a frequency close to one of its natural resonant modes, which depends on the geometry and electrical properties of the sample. However, it was shown that the transmit field patterns observed at ultra-high field are most likely caused by wavelength effects leading to constructive or destructive interferences in the sample and the multiple carrying-current elements [25]. Indeed, central brightening patterns were observed even when the sample was excited at frequencies far from the dielectric resonance condition.

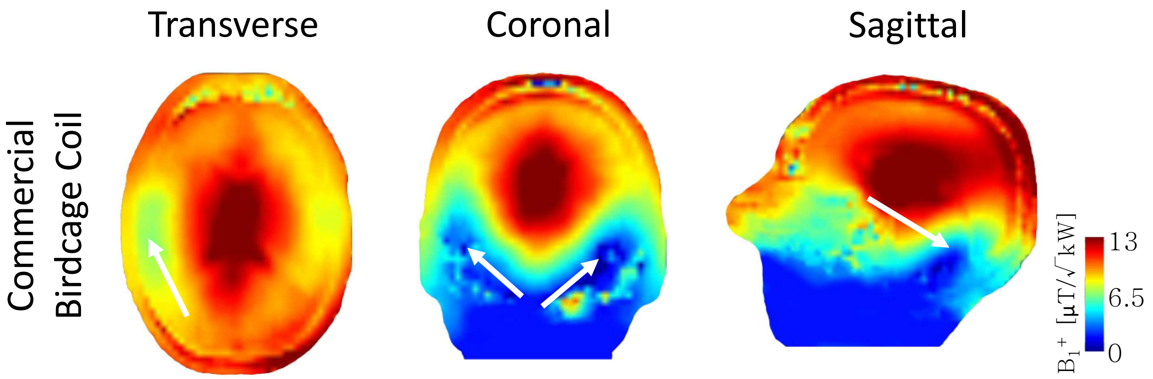

Figure 1.15: *For a commercial birdcage coil: experimentally measured* B_1^+ *maps normalized to 1 kW input peak-power, and shown in the three main orientations. The white arrows indicate the positions of transmit field drops.*

1.3.4.2 TEM Coil

To address these inhomogeneities, the transverse electromagnetic (TEM) resonator was proposed [18, 26]. It differs from the birdcage coil by two main points. First, the TEM is built with microstrips instead of rods that are placed on a non-conductive cylinder. Secondly, the outer surface is a slotted metallic shield which is connected via capacitors to the microstrips, while in birdcage coils, the RF shield is independent from the coil itself. Therefore, the TEM RF coil can be seen as a cavity resonator, which is by definition a *space which is normally bounded by an electrically conducting surface and in which oscillating electromagnetic energy is stored; the resonant frequency is determined by the geometry of the enclosure* [18]. Indeed, the RF shield in TEM RF coils serves as a return path for the currents circulating on the microstrips of the inner cylinder keeping the electromagnetic fields inside the volume of excitation and eliminating radiation losses. TEM RF coils usually produce a slightly better transmit field homogeneity at ultra-high fields compared to the birdcage coils [27].

1.4 Electromagnetic field simulations

Electromagnetic field simulations are an essential tool to estimate the characteristics (e.g transmit field efficiency, coverage, RF safety) of any RF coil prior to its construction. By solving the Maxwell equations (Equation 1.47), the complete temporal and spatial behavior of the electric and magnetic fields can be found. In the next sub-section an introduction to the FDTD method is given since it was used throughout this work with Sim4Life (ZMT AG, Switzerland).

$$
\begin{aligned}
\vec{\nabla}.\vec{E} &= \frac{\rho}{\epsilon_0} \\
\vec{\nabla} \times \vec{E} &= -\frac{\partial \vec{B}}{\partial t} \\
\vec{\nabla}.\vec{B} &= 0 \\
c^2 \vec{\nabla} \times \vec{B} &= \frac{\vec{j}}{\epsilon_0} + \frac{\partial \vec{E}}{\partial t} \qquad (1.47)
\end{aligned}
$$

In Equation 1.47, $\vec{E}$ and $\vec{B}$ are respectively the electric and magnetic fields, ρ and $\vec{j}$ are the charge and current densities, c is the speed of light and ϵ_0 is the vacuum permittivity.

1.4.1 FDTD simulations

The Finite-Difference Time-Domain method (or FDTD) is an algorithm developed and presented in the 60's to solve Maxwell's equations (Equation 1.47) in curl form [28]. The electric and magnetic field components are allocated in space on a 3D-grid with a Cartesian coordinate system. The boundary conditions for each voxel in the 3D-grid are defined with the properties of perfect conductors except for the ones located at the limits of the simulation space which are defined as an absorbing medium to avoid reflected waves. For the inner voxels (not located at the limits) it therefore implies that the tangential component of the electric field and normal component of the magnetic field vanishes on the surfaces [28]. This leads to the following cell in Figure 1.16, named the Yee-cell, where the fields are evaluated.

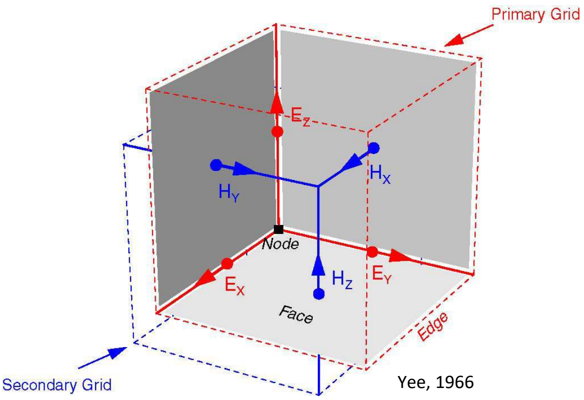

Figure 1.16: *Visual representation of the Yee cell. The magnetic and electric fields are respectively computed at the center-face and along the edges of the cell.*

The electric field is evaluated on the edges of the cell and the magnetic field at the center-faces of the cell. Numerical stability is ensured by limiting the time step to the Courant-Friedrich-Levy criterion (Equation 1.48). The time step has to be smaller than the time needed for the wave to propagate from one node to the other. Or expressed differently, the grid size must be higher than the distance traveled by the wave during the step time. Therefore, simulation time scales up with decreasing excitation frequencies.

$$\Delta t \leq \frac{1}{c\sqrt{\frac{1}{(\Delta x)^2}+\frac{1}{(\Delta y)^2}+\frac{1}{(\Delta z)^2}}} \tag{1.48}$$

1.4.2 Specific absorption rate

One of the most important challenges in terms of RF safety at ultra-high field is the temperature rise of the human tissues due to the conduction (also known as eddy currents) and displacement currents induced by the RF coils (see 1.3.3.4). The specific absorption rate (SAR) was defined as a measure of the rate at which energy is absorbed by human tissues when exposed to a radio frequency field. An accurate evaluation of SAR is not only important in MRI, but also e.g. in telecommunications, particularly with mobile phones, since they are usually placed close to the body. SAR is expressed in [W/kg] and is calculated with Equation 1.49, where $\sigma(\vec{r})$ corresponds to the spatial electric conductivity and $\rho(\vec{r})$ is the density distribution.

$$\mathrm{SAR} = \frac{1}{V}\int_{VOI} \frac{\sigma(\vec{r})\left|\vec{E}(\vec{r})\right|^2}{2\rho(\vec{r})}d\vec{r} \tag{1.49}$$

The integral is taken over a predefined volume-of-interest (VOI) and normalized to the total volume V. The factor 2 in the denominator stands for the root-mean-square value of the E-fields. However, the measurement of the electric fields in MR scanners is very complicated. Therefore, electromagnetic field simulations are performed to estimate the E-fields associated with a given RF coil geometry on a full-human tissue model and thus to compute SAR and establish safe operation limits. However, the variability in shape and size between subjects has to be accounted [29]. Therefore, different human models (women, men, children), including several tissues with their respective dielectric properties at various frequencies were developed either whole-body [30–35] or for specific body parts [36–38] to get higher confidence in the established power deposition limits when a subject whose σ, ρ are unknown is scanned. In Sim4Life, the virtual family 3.0 [35] is available for electromagnetic field simulations.

1.4.2.1 Global and local SAR

There are two main ways to evaluate SAR. The **global SAR** refers to the averaged deposited power over the exposed body part. The RF power limits are derived from the simulations on a voxel-basis to make sure the safe SAR values established by the IEC 60601-2-33 standard are respected. For head, SAR should not exceed 3.2 W/kg over a 6 min duration. The RF power is monitored by the MR scanner under the global RF supervision in both single and parallel transmit modes (see section 1.5). However, the computed global SAR is usually high since it is based on a voxel-wise evaluation and does not account for heat diffusion inside the tissues. This is why the **local SAR** was defined as the SAR averaged over a local region of the body. In MRI it is usual to average the SAR over 10g tissue volume. This quantity will be therefore further referred as the SAR_{10g}. The IEC guidelines recommend not to exceed 10 W/kg averaged over 6 minutes and 20 W/kg over 10 seconds in normal operating mode for the head.

1.4.2.2 SAR in parallel-transmit mode

The RF power limits can usually be determined in a straightforward way when operating in single-transmit mode. Indeed, a single-channel surface or volume RF coil (e.g. a birdcage coil) produces a specific electromagnetic field pattern, and the electric component of this field can be precisely simulated (with fixed RF amplitude and phase). In parallel-transmit operating mode, the electric fields have to be computed every time the individual RF phases of the coil array elements are manipulated to counteract the transmit field inhomogeneities (see section 1.5.1). Therefore, the interactions with tissues will depend on how the electric field generated by the individual coil array elements will add up or cancel each other. A common approach to ensure safe operation is to compute what is called the **worst-case scenario**. The RF power limits are derived from a situation where the electric fields are combined in the worst possible way at every position (constructive interferences). However, this procedure results in largely overestimated limits since the worst-case scenario RF phases are not likely to be used as they do not produce an efficient transmit mode in terms B_1^+-field distribution pattern. Nevertheless, this approach is required since the global RF supervision only accounts for the forward and reflected power on each channel and not for the phase relations between the channels. Therefore, MR experiments within the SAR limits typically require lowering the transmit voltage to sub-optimal values which affect, for example, the image quality of the MR measurements.

For a SAR calculation method that would be valid for any RF waveform and phases, the first step is to compute the so-called Q-matrices, which are defined by Equation 1.50, for each voxel or averaged volume in the human body (e.g. the 10g tissue volume) [39, 40]. In Equation 1.50 $\mathbf{S}_E$ stands for the electric field sensitivity (3 x C matrix, where C is the number of coils), without any specific RF waveform.

$$\mathbf{Q}(\vec{r}) = \frac{1}{V}\int_{VOI} \frac{\sigma(\vec{r})\mathbf{S}_E^H(\vec{r}).\mathbf{S}_E(\vec{r})}{2\rho(\vec{r})} d\vec{r} \tag{1.50}$$

$$\mathrm{SAR}(\vec{r_m}) = \frac{1}{T_{scan}}\int_t \vec{w}^H(t').\mathbf{Q}(\vec{r_m}).\vec{w}(t')dt' \tag{1.51}$$

The SAR model for each position is then calculated with Equation 1.51, where $\vec{w}$(t) stands for the RF waveform and channel weights. However, such calculations are computationally intensive since a large number of sub-volumes are investigated (typically m $\approx$ 300,000). The elegant **Virtual Observation Points** (VOP) method was proposed to decrease the computation time by reducing the number of sub-volumes investigated while keeping a conservative estimation of the local SAR [40]. Without considering the body structures, the idea was to cluster the Q-matrices such that the maximal SAR value among all the matrices is always lower than the maximal value calculated over the clusters. It is described by Equation 1.52, where A_j corresponds to the matrix associated with the cluster, or more explicitly to the VOP (j = 1,...,N).

$$\max_{\vec{r}=\vec{r}_1,\vec{r}_2,\ldots,\vec{r}_m} \frac{1}{T_{scan}} \int_t \vec{w}^H(t').\mathbf{Q}(\vec{r}).\vec{w}(t')dt' \leqslant \max_{j=1,2,\ldots,N} \frac{1}{T_{scan}} \int_t \vec{w}^H(t').\mathbf{A}_j.\vec{w}(t')dt' \tag{1.52}$$

Depending on the size and complexity of the body model, VOP compression can reduce the volumes to investigate to a few hundred. This makes possible the online supervision of the local SAR_{10g} or global SAR (depending on how the Q-matrices were calculated) at low computational cost.

1.5 Parallel transmit at 7T

1.5.1 Fundamental principle

Because of the inherent transmit field inhomogeneities, it is challenging to achieve a large homogeneous volume excitation at ultra-high fields ($\geqslant$ 7T). To overcome these limitations, individual surface coils can be combined into an array and geometrically arranged around the brain or any other region of interest. Each array element being individually controlled, the total B_1^+ field distribution can be modulated to increase the homogeneity across the brain. The fundamental principle parallel transmit relies on is called the **superposition principle**. It states that the total transmit field produced by an array of N transmitting channels is the sum over the complex individual $\mathrm{B}_{1,\mathrm{n}}^+$ field profiles (Equation 1.53).

$$\mathrm{B}_{1,\mathrm{tot}}^+(\vec{\mathrm{r}}) = \sum_{n=1}^{N} \mathrm{B}_{1,\mathrm{n}}^+(\vec{\mathrm{r}}) \tag{1.53}$$

with the individual $\mathrm{B}_{1,\mathrm{n}}^+$ defined as in equation 1.54.

$$\mathrm{B}_{1,\mathrm{n}}^+(\vec{\mathrm{r}}) = |\mathrm{B}_{1,\mathrm{n}}^+|\mathrm{e}^{\mathrm{i}\phi(\vec{\mathrm{r}})} \tag{1.54}$$

The term $\phi(\vec{\mathrm{r}})$ corresponds to the transmit field phase at the given position $\vec{\mathrm{r}}$. The methods to compute the individual transmit field maps and to perform B_1^+ field optimization are described in chapter 4. When the phases at a given point are equal, the combination is said to be **additive** (constructive interference) and results in a bright B_1^+-field spot. Conversely, the combination is said to be **substractive** when the phases combination lead to destructive interference and generates dark spots.

1.5.2 User procedure

To use a scanner's parallel-transmit capabilities, the user needs first to switch the system to the appropriate mode (parallel-transmit on step 2.3 Siemens Magnetom 7T MRI scanner versus single transmit). At this point only the master channel is active. Then, the slave channels are activated via a script which checks the proper functioning of the measurement control units. Afterwards, unlike a single-transmit system, a few quality and safety checks are done to ensure that the MR scanner can be used properly. The first test, called **phase adjustment**, aims to determine the RF phase of all modulators (Figure 1.17) relative to one receiver and conversely. This step is performed to ensure that there are no initial phase differences at the coil plug. Then, three other tests are performed to check the functioning of the safety procedures. The **VOP shutdown test** verifies the effective disabling of RF transmission when the local SAR (see 1.4.2) limits are exceeded by using the virtual observation points method [40]. However, this capability was not used in this thesis. The **RF monitor function test** checks if the results of the local SAR monitor and the result of the global RF power monitor are within specifications. The last safety check, the **PALI shutdown test**, is only related to the global RF power supervision. It verifies that RF transmission is disabled when the global limits are exceeded. This measurement relies on the difference between forward and reflected powers, which are measured by the MR scanner for each transmit line (see 1.5.3).

After doing the main quality and safety check, a subject can enter the scanner and be positioned inside the coil array. The basic calibrations (B_0 shimming and frequency adjustment) are done prior to any measurement. Then a dedicated single-slice 2D-GRE sequence is run (FA=25°, TR/TE = 100/10 ms, 2.3 x 2.3 mm^2, slice thickness = 5 mm, matrix = 128 x 128, TA = 1 min 42s) to compute the complex individual transmit field sensitivities required for RF phase shimming. A detailed description of the calculations is given in chapter 4, but essentially, the sequence is programmed such that the selected slice is acquired 8 times with only one active transmit channel at each time. In terms of hardware, the RF power amplifiers (see 1.5.3) are sequentially turned off. The individual transmit field sensitivity maps are processed with the dedicated GUI described in chapter 4 to optimize the RF phases over a user-drawn region-of-interest. Once this is done, a configuration file containing the information about amplitude and phase shifts is generated and loaded into the MR scanner software. The calculated optimal parameters are sent to the scanner's phase shifters and the RF signal goes through the 8 transmit paths with the appropriate phase shift between channels.

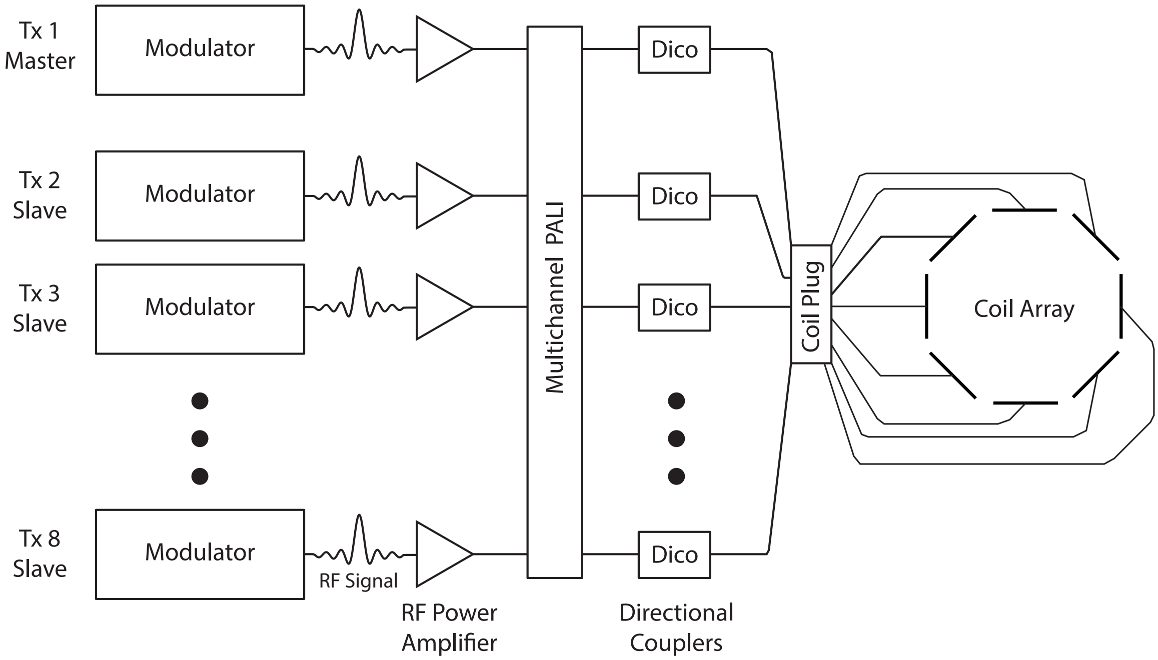
Tx 1
Master
Modulator
Tx 2
Slave
Modulator
Tx 3
Slave
Modulator
Tx 8
Slave
Modulator
RF Signal
RF Power
Amplifier
Multichannel PALI
Dico
Dico
Dico
Dico
Directional
Couplers
Coil Plug
Coil Array

Figure 1.17: *Parallel transmit infrastructure for the Magnetom 7T head-only MR scanner.*

1.5.3 Hardware implementation

To transmit through multiple coils, a dedicated RF infrastructure is available for the Magnetom 7T MR scanner (Siemens, Erlangen, Germany). The parallel transmit system is separated into 7 slaves and 1 master channel. Before starting the measurements, the sequence is prepared for each slave which then waits for the start signal from the master channel. All the channels are synchronized to transmit simultaneously with the 8 RF lines. Figure 1.17 displays the most important components on the transmit path from the signal generation to the coil array. In the next paragraphs, they are briefly introduced.

Modulator The modulator is responsible for generating the excitation pulses at the desired frequency. At the output of the modulator, the final RF signal is sent to the 8 channels, and to the RF amplifiers.

RF amplifier At this stage, the RF pulse from the modulator enters the RF power amplifier (RFPA) to amplify the RF signal such that the power is sufficient to get the needed field strength for the appropriate flip angle. Each RFPA is able to deliver up to 1 kW each (approximately 226 V). In single-transmit mode, internal losses in the cables and combiner limit the maximal achievable RF power to 7.5 kW (approximately 612 V). A circulator is installed in each RFPA to prevent high reflected power from going back into the line.

Multi-channel PALI and DICOs These two systems work together and are crucial to ensure the safety of subjects inside the scanner. DICOs stands for directional couplers which are placed on each transmit line to detect forward and reflected RF signals. The measurement for each channel is performed by the TALES (Transmit Antenna Level Sensor) unit which is the hardware sub-unit of the PALI (Power Absorption LImiter) software system that computes online (during the MR scan) the sum power over all channels. The peak power (per channel) and the sliding mean power (summed over all the channels) averaged over 10 s and 6 min are calculated. The values are compared to the user defined limits, which are derived from the specific-absorption-rate (SAR) levels calculated by electromagnetic field simulation (see 1.4.2.2). If the limit for any of the two averaging stages is exceeded, the PALI system shuts down the RF amplifier within 10 μs.

From here, the 8 independent transmit lines go through the phase shifters, which give the phase differences required for RF shimming. The system is then linked to a socket-plug interface where the transmit coil array can be connected, and each coil array element is fed through the associated individual transmit paths.

1.5.4 Characterization of transmit-receive head RF coil arrays at 7T

1.5.4.1 B_1^+-field and SAR normalization

All the B_1^+ maps were calculated for a 90°flip angle with a 500 μs hard pulse. According to Equation 1.20, this corresponds to a B_1^+ value of 11.7 μT. The transmit field efficiency was defined as in equation 1.56, and given in $\left[\mu T/\sqrt{kW}\right]$. The total power$_{90deg}$ was computed as in Equation 1.55 and the multiplicative term $\sqrt{1000}$ is used to normalize the result to 1 kW total input peak-power. In this thesis, the transmit field efficiency has been either normalized to 1 kW or 8 kW total input peak-power. Similarly, the transmit field efficiency can be expressed in [nT/V] (Equation 1.57), where total voltage$_{90deg}$ is calculated as the square root of 8 multiplied by the input voltage per transmit channel.

$$\mathrm{Power}_{90deg} = 8 \cdot \frac{(\mathrm{Voltage}_{channel})^2}{50} \tag{1.55}$$

$$B_{1,eff}\left[\frac{\mu T}{\sqrt{kW}}\right] = \frac{11.7}{\sqrt{\mathrm{Power}_{90deg}}} \cdot \sqrt{1000} \tag{1.56}$$

$$B_{1,eff}\left[\frac{nT}{V}\right] = \frac{11700}{\mathrm{Voltage}_{90deg}} \tag{1.57}$$

The RF losses from the RF amplifiers to the coil plug (Figure 1.17) were included in the initial calibration of the MR scanner so that the power/voltage used in the Equations 1.56 and 1.57 corresponds to the input at coil plug. However, it does not correspond to the true

delivered power/voltage to the coil since additional RF losses will occur from the coil plug to the coil array elements (typically $\leqslant$ 1 dB loss). Furthermore, failure or mistuning of one or multiple coil array elements may impair the accurate evaluation of the delivered power to the coil array. The total power/voltage used in the normalization of B_1^+-field did not account for these additional losses.
The local SAR_{10g} maps presented in this thesis were all computed for 1W total input power, without including the RF losses from the coil plug to the array nor internal RF losses of the coil array elements.

1.5.5 Decoupling strategies for transmit/receive coil arrays at 7T

The main challenge to address when combining RF coils is the inter-element coupling. When two loop coils are closely placed, the magnetic field created by the current I_2 in loop 2 will induce an electromotive force (emf) ζ_{12} in loop 1. The complete emf is therefore given by equation 1.58.

$$\zeta_{tot} = \zeta_1 + \zeta_{12} = -L_1 \frac{dI_1}{dt} - M_{12} \frac{dI_2}{dt} = i\omega L_1 I_1 + i\omega M_{12} I_2 \tag{1.58}$$

where M_{12} is the mutual inductance coefficient defined by equation 1.59, μ_0 is the free space permeability, C_i and C_j correspond to the closed curves of the RF coil, dl_i and dl_j are infinitesimally small elements of the circuits i and j and r_{ij} is the distance between two points.

$$\mathrm{M_{i,j}} = \frac{\mu_0}{4\pi} \oint_{C_i} \oint_{C_j} \frac{dl_i \cdot dl_j}{|r_{ij}|} \tag{1.59}$$

When two identical loops tuned to the same frequency f_0 are closely placed, this mutual inductance will cause a splitting of the resonances. This phenomenon impacts the efficiency of the coils as the signal and noise are transferred from one coil to another through mutual inductance, which results in a loss of sensitivity.

Overlap decoupling is the simplest approach to reduce the mutual coupling of two coupled loops [41]. When the center of the two loops are separated by approximately 75% of their diameter for circular loops, and 90% for square loops, the mutual inductance is canceled by the flux passing through the overlapping area and the splitting of resonance is eliminated.

Capacitive decoupling methods were introduced in 2004 as a method to decouple closely placed loops without overlapping them [42]. A capacitor is connected in between the adjacent loop coils. The working principle is depicted on Figure 1.18A. Together with the capacitors C_5 and C_6, the decoupling capacitor C_D form a small loop which counteract the mutual coupling between the two loops. Similarly, in the **inductive decoupling** method two small inductors are connected in series with the RF loop coil and placed in front of the inductor belonging to an other loop (Figure 1.18B) [43, 44]. The coupling between the two RF loop coils is canceled by the mutual coupling between the two small inductors. In this sense, it is a "through-air" decoupling method which constrains a bit less the coil array geometry compared to capacitive decoupling. However, inductors are lossy components; therefore, the inductive decoupling method is not often used.

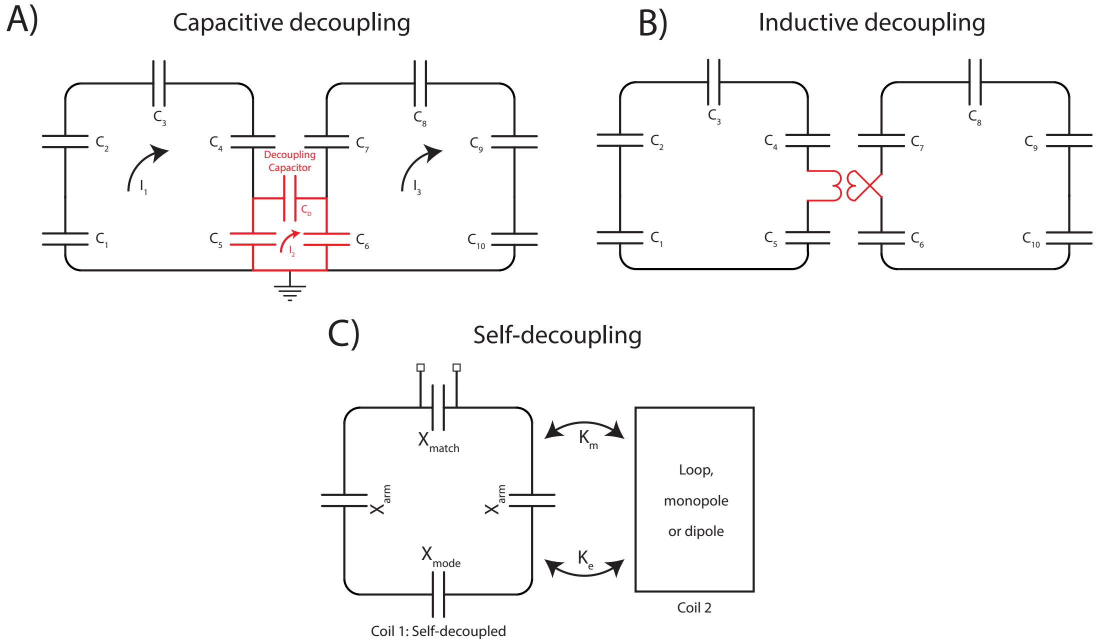
A)
Capacitive decoupling
C3
C2
C4
Decoupling Capacitor
C7
C8
C9
I1
CD
I3
C1
C5
I2
C6
C10
B)
Inductive decoupling
C3
C2
C4
C7
C8
C9
C1
C5
C6
C10
C)
Self-decoupling
Xmatch
Km
Xarm
Xarm
Loop,
monopole
or dipole
Xmode
Ke
Coil 2
Coil 1: Self-decoupled

Figure 1.18: *Schematics of A) the capacitive and B) the inductive decoupling methods. C) Self-decoupling method*

The passive shield decoupling method was presented in 2010 to efficiently decouple the coils in an array while enabling better flexibility in terms of geometrical arrangement compared to the capacitive or overlapping methods [45]. While most of the decoupling approaches rely on the capability to cancel or correct the mutual inductance between neighbors, the passive shield method consists on a copper shield surrounding each of the coils elements to interrupt any magnetic flux between the two RF coils.

The induced current elimination (ICE) method introduced in 2011, consists of placing an independent decoupling element in between two separate RF coils [46–48]. Similarly to the passive shield method, it enables higher flexibility in RF coil array designs since the individual elements are not physically connected. The induced currents between two RF coils are compensated by the induced currents from decoupling elements.

Passive scatterer for dipole decoupling When two dipoles are closely placed, mutual coupling decreases the overall efficiency of the setup. This aspect is particularly critical when designing dipole coil arrays for head imaging, since the tight geometrical configuration and consequent coupling impairs an efficient placement of the dipoles. While the capacitive or overlapping decoupling methods work efficiently on loop coils, they cannot be applied to dipoles because of their intrinsic geometry. Therefore, the magnetic wall approaches described in the previous paragraphs were investigated for dipoles [49, 50]. However, although the working principle is very similar to the ICE decoupling method the implementation and the practical aspects are slightly different. The method was theoretically investigated [51], and in the following paragraph a short description is given.

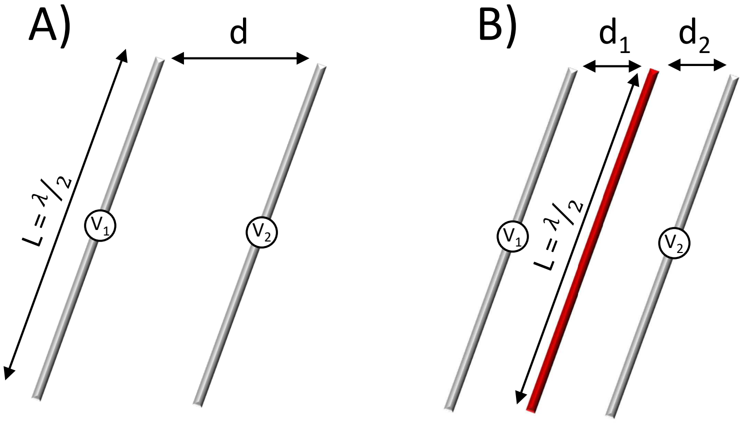

Figure 1.19: *A) Representation of two dipoles separated by a distance d and fed with voltage sources V_1 and V_2, respectively. B) The same two dipoles with the addition of a scatterer-dipole (in red) placed in between the two.*

The main principle behind decoupling is to cancel the electromotive force induced by a dipole in the others dipoles (Figure 1.19A). The idea is to place a scatterer-dipole in between the two coupled elements. It has to be placed at equal distance, have the same length and be on the same plane as the two dipoles to decouple such that the current induced in the scatterer-dipole by both dipoles is equivalent ($d_1 = d_2$ in Figure 1.19B). With the appropriate placement, any electromotive force induced in one antenna by the other is compensated by a part of the electromotive force induced in them by the scatterer-dipole. In our study, this method was empirically implemented to decouple adjacent dipoles in a coil array. Although all the elements had different lengths and planar orientations, quite high decoupling was achieved (see chapter 2, Figure 2.5). Nevertheless, since the working principle involves coupling to the scatterer, it is foreseeable that some RF losses may occur. Moreover the matching band of the dipole (meaning the bandwidth for $S_{11} \leqslant 20$ dB) was observed to be reduced by an order of magnitude when the scatterer-dipole was present [51]. Therefore, the dipole array may be more sensitive to the loading and the antenna efficiency may be decreased when the transmit bandwidth is wide.

The self-decoupling method is an elegant approach which provides high decoupling between adjacent coils without any additional circuitry (no shared capacitors or passive scatterer) [52]. Typically, a loop coil is segmented with capacitors that should have similar impedance to avoid unbalanced currents and radiation losses (antenna effect, see 1.3.3.4). The basic principle of the self-decoupling approach is to replace one capacitor on the loop coils (the one opposite to the feed port) with a high impedance (Figure 1.18C, X_{mode}). This creates a dual-mode behavior where the loop coils will act both as a loop and folded dipole. The associated magnetic and electric couplings between adjacent coils have opposite signs and can therefore cancel each other if the right balance between the two modes is found by adjusting the X_{mode} impedance (Figure 1.18C).

1.5.6 Transmit-receive head RF coil arrays at 7T

Table 1.1: *For the different Tx/Rx head coil arrays at 7T shown in the second column: power and voltage required to get a 90 °flip angle at center of the brain (3^{rd} column) and over the thalamus axial slice (4^{th} column). The last column indicates the decoupling strategy employed for the head coil arrays.*

Authors	Coil Design	Required power / voltage for a 90° at the center of the brain	Required power / voltage for a 90° averaged over the thalamus axial slice	Decoupling strategy
Adriany et al. 2005	8-channel transmission lines	2610 W / 361 V	-	Capacitive
Adriany et al. 2008	16-channel transmission lines	950 W / 218 V	-	Capacitive
Avdievich et al. 2011	8-channel loop coils	-	1111 W / 236 V	Inductive
Gilbert et al. 2011	15-channel loop coils	260 W / 114 V	-	Capacitive
Gilbert et al. 2012	16-channel loop coils	-	920 W / 215 V	Passive shield
Chen et al. 2014	8-channel meander ends dipoles	1617 W / 284 V	-	-
Zang et al. 2017	8-channel flexible dipoles	3803 W / 436 V	-	-
Clément et al. 2018	8-channel center-shortened dipoles	1130 W / 238 V	2035 W / 319 V	Passive scatterer

Seven transmit/receive (transmit and receive through the same channels) coil arrays built for human brain magnetic resonance at 7T were reviewed, and Table 1.1 gives a summary of the main results. The first column of the table indicates the first author and the year of the publication, while the second column gives a brief description of the coil array design. The third and fourth columns indicate the required peak power and total input voltage to get a 90°flip angle at the center of the brain, and/or averaged over the thalamus axial slice. All further quantification was evaluated according to the methods described in section 1.5.4.1. The last column gives the decoupling strategy employed as described in section 1.5.5.

To our knowledge, the first 7T Tx/Rx RF coil array was introduced in 2005 by Adriany et al. [53] and consisted of 8 strip transmission lines. The array elements were arranged on an elliptical former and the phase increment between neighboring coils was set to 45°(Figure 1.20A). As long as the coil array geometry is approximately circular, the resulting transmit field is close to the CP mode observed with the birdcage or TEM volume coils. When fed with a single 4 kW RF amplifier, the power was equally distributed through an 8-way splitter to the 8-channel microstrip elements. At the center of the brain, the 8-channel microstrip coil array produced a B_1^+ field of 7.24 $\mu T/\sqrt{kW}$ (32.4 nT/V), which was 38% stronger compared to the 8-channel loop coil array presented in the same study. The design was further extended to a 16-channel microstrip coil array [54] (Figure 1.20B), and the B_1^+ field efficiency was increased to 12 $\mu T/\sqrt{kW}$ (53.7 nT/V). Loop coil array designs were extensively investigated by Avdievich et al. [44, 55]. An 8-channel single-row loop coil array was built (Figure 1.20C), and a mean transmit field efficiency of 11.1 $\mu T/\sqrt{kW}$ (49.6 nT/V) was achieved over an axial slice centered on the thalamus for optimized RF phases (different from the CP-like mode). However, the longitudinal field-of-view was limited and did not cover the whole cerebral cortex or the cerebellum. Multiple-row coil arrays were therefore introduced to enlarge the field-of-view [44, 56, 57]. The 15-channel loop coils designed by Gilbert et al. [56] were arranged on three row (Figure 1.20D) on a circular former with a diameter of 279 mm. At the center of the brain, a B_1^+ field efficiency of 23 $\mu T/\sqrt{kW}$ (102.6 nT/V) was achieved, which represents a large gain compared to any other coil array previously reported. However, no further results were shown with this coil array. Subsequently, a 16-channel conformal loop coil array was proposed to improve the transmit-field uniformity over the whole brain [57] (Figure 1.20E). Over the thalamus axial slice, a mean B_1^+ field efficiency of 12.2 $\mu T/\sqrt{kW}$ (54.4 nT/V) was measured, and 8.9 $\mu T/\sqrt{kW}$ (39.8 nT/V) over the whole brain.

While all the designs introduced relied either on microstrips or loop coils, dipole antennas could be an alternative to these coils since they have been shown to have better RF signal penetration depth and field symmetry at 7T MRI [12, 58]. For head imaging at 7T, an 8-channel coil array was proposed in 2014 by Chen et al. [59] and built with meander-end dipoles arranged on a circular support with a diameter of 279 mm (Figure 1.20F). A B_1^+ field efficiency of 9.2 $\mu T/\sqrt{kW}$ (41.2 nT/V) was measured at center of the brain. Similarly, an 8-channel flexible dipole array, originally proposed for body imaging [60] was used in combination with a 29-channel receive-only dipole array on the human head at 7T [61]. The transmit array diameter was approximately of 250 mm (Figure 1.20G). At the center of the brain, a B_1^+ field efficiency of 6.0 $\mu T/\sqrt{kW}$ (26.8 nT/V) was achieved. For comparison, the values obtained with the 8-channel center-shortened dipole coil array [15] (Figure 1.20H) are also shown.

1.6 Receive coil arrays at 7T

Transmit coil arrays are used to produce an increased B_1^+-field homogeneity over larger FOVs compared to single-channel volume coils. However, the achievable SNR is usually limited since each transmit element is sensitive to a large region. Conversely, high SNR levels can be obtained over smaller regions using, for example, surface loop coils. Therefore,

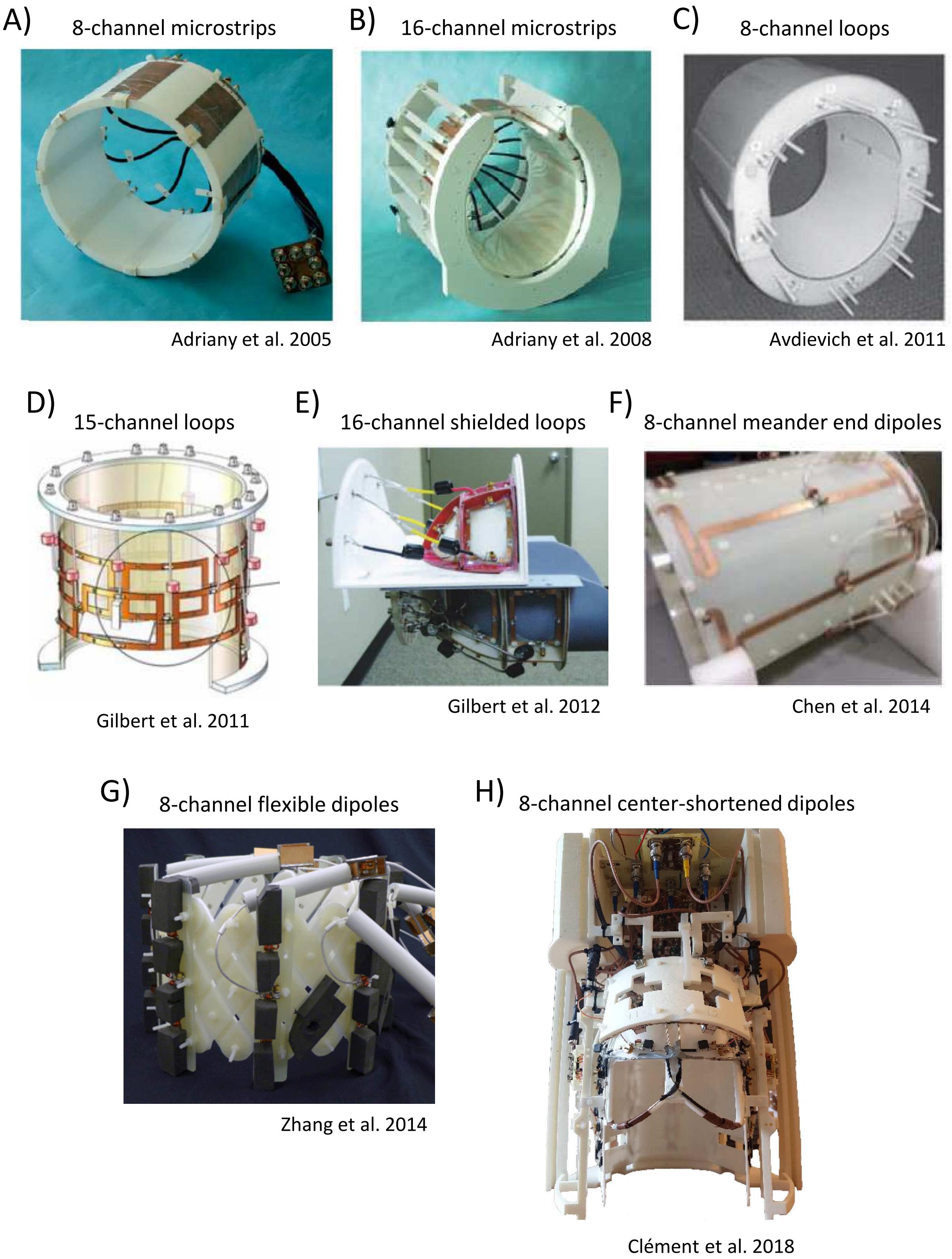

A) 8-channel microstrips
Adriany et al. 2005

B) 16-channel microstrips
Adriany et al. 2008

C) 8-channel loops
Avdievich et al. 2011

D) 15-channel loops
Gilbert et al. 2011

E) 16-channel shielded loops
Gilbert et al. 2012

F) 8-channel meander end dipoles
Chen et al. 2014

G) 8-channel flexible dipoles
Zhang et al. 2014

H) 8-channel center-shortened dipoles
Clément et al. 2018

Figure 1.20: *Pictures of the different coil array designs presented in Table 1.1. A brief description of the design is given and the corresponding journal reference is indicated.*

high SNR could be achieved over large FOV by using a multitude of closely positioned RF coils [41]. Moreover, the acquisition time of an MR image can be reduced by making use of the subsequent multiple signals [62]. In this section, the methods used to build large receive arrays are described, and the quantities used to characterize their efficiency are detailed (noise correlation matrix, g-factor and SNR).

1.6.1 Preamplifier decoupling

When the number of receivers is limited or the geometrical arrangement is simple (like with a single/dual line of receivers), the overlapping method can provide sufficient decoupling (see 1.5.5). However, when designing a dense receive array, the next neighbors cannot be overlapped (Figure 1.21, L_1, L_5 and L_6).

Looking at equation 1.58, the coupling term can be decreased either by acting on the mutual inductance constant M_{12} or by decreasing the current I_2. This second method make use of low-input-impedance preamplifiers to reduce the current flow in the receive elements [41]. It is not applicable to transmit arrays since high current is required to produce the B_1^+ field. The working principle of this so-called *preamplifier decoupling* can be easily understood with the Figure 1.22. The inductor value L_1 can be adjusted to form with C_1 a parallel resonant circuit when the input impedance of the preamplifier R_1 (nodes A-B) is close to zero. Therefore, it in turns introduce a high series impedance in the RF coil (at nodes C-D), which prevents large current flow from taking place. The NMR signal measurement is not altered by this phenomenon. Indeed, the electrical power induced by the spins inside the RF coil could be measured either as a voltage across the nodes C-D (Figure 1.22) or a current (P = VI).

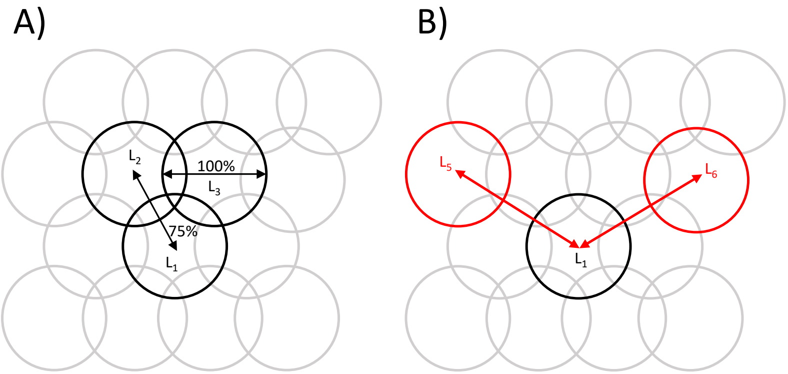

Figure 1.21: *A) Neighbor loops coils L_2 and L_3 are overlapped with the loop coil L_1 B) Next neighbor loop coils L_5 and L_6 can't be overlapped with the loop coil L_1*

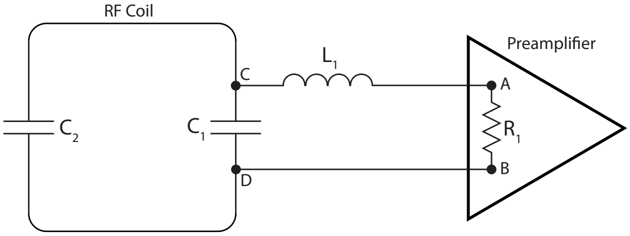

Figure 1.22: *Schematic of a loop coil connected to a low input-impedance preamplifier. The preamplifier decoupling is ensured by the fine adjustment of* C_1 *and* L_1*.*

1.6.2 Noise correlation matrix

In the previous section, two elegant methods to eliminate the mutual inductive coupling were presented. However, to get a more accurate characterization of the receive array the noise coupling between receivers needs to be taken into account. The SNR for multiple receivers, as described by Roemer et al. [41] is given by equation 1.60, where the numerator corresponds to the instantaneous total NMR signal and the denominator characterizes the rms noise voltage [63]. The R_{tot} relates to the total noise resistance (at the output terminals), Δf is the receiver bandwidth while the term 4kT corresponds to the thermal fluctuations. The total noise resistance term depends on the so-called *noise resistance matrix* R_{ik}, which in turn is proportional to the spatial electric field induced in the sample by a sinusoidal current in coil i or k. In this sense, the noise resistance matrix gives the correlated noise between coils. Analogously to the mutual inductance, an electric coupling coefficient can be defined as in equation 1.61.

$$\mathrm{SNR} = \frac{|V_{tot}|}{\sqrt{4kT\Delta f R_{tot}}} \tag{1.60}$$

$$k_{e,ik} \equiv \frac{R_{ik}}{\sqrt{R_{ii}R_{kk}}} \tag{1.61}$$

As described previously, the magnetic coupling can be eliminated for a critical overlap value. However, the electric coupling coefficient cannot be canceled. More concretely, this means that even in the absence of magnetic flux between two coils (where mutual inductance is eliminated) noise can be correlated between them. The noise resistance matrix also called *noise correlation matrix* or *noise covariance matrix* can be calculated from the complex raw data acquired with no RF excitation by using equation 1.62.

$$R_{ij} = \frac{1}{N}\sum_{k=1}^{N} n_i(k)n_j^*(k) \tag{1.62}$$

The N value corresponds to the number of noise samples (matrix size of the image), while n_i(k) is the k^{th} noise sample from the channel i. Since it indicates the correlation between the coils, the noise covariance matrix can be very helpful for qualitatively assessing coil failure [64]. Large variations of one or more of the on-diagonal terms may indicate a failing component on the corresponding RF coil and will produce a decreased SNR. Similarly, large off-diagonal elements may indicate an increased mutual inductance coupling or high sample noise in the region covered by the two RF coils. This could result from an insufficient preamplifier decoupling or a sub-optimal loading of the coils.

1.6.3 SENSE method and g-factor

The main idea behind parallel imaging is to make use of the spatial localization of each receiver to reduce the number of phase-encoding steps required to reconstruct a full-FOV image. Indeed, each coil is sensitive to a different region since the receive array is placed all around the volume-of-interest. Therefore, the signal recorded by each coil varies as a function of its position (Figure 1.23B). The SENSE method [62] relies on this characteristic to perform parallel imaging.

Reducing the sampling density in k-space results in a reduced FOV, and aliasing effects appear (Figure 1.23A). This is because the number of spatial frequencies collected was insufficient for an accurate representation of the sample. Each pixel in the reduced FOV therefore contains the signal contribution from different positions in the full FOV. The main principle of the SENSE reconstruction method is to use the coil sensitivities to separate the signal contributions since, for each single-coil image, the superposed pixels will be weighted according to the coil's position. The coil sensitivity matrix is defined as in equation 1.63, and each coil sensitivity map s_γ is taken at the superimposed $\vec{r}_\rho$ positions to construct it. The matrix size is n_c x n_p where n_c, is the number of coils and n_p is the number of superimposed pixels.

$$S_{\gamma,\rho} = s_\gamma(\vec{r}_\rho) \tag{1.63}$$

The *unfolding matrix* U is therefore computed with equation 1.64, where ψ corresponds to the n_c x n_c noise correlation matrix defined previously.

$$U = \left(S^H \psi^{-1} S\right)^{-1} S^H \psi^{-1} \tag{1.64}$$

The main computational load comes from the matrix inversion which can be performed as long as the number of superimposed pixels do not exceed the number of channels. Once the unfolding matrix is determined, it can be applied to the vector $\vec{a}$ which contains for a given superimposed pixel, the complex image value of all the receive channels (Equation 1.65). The resulting vector $\vec{v}$ lists separated pixel values for the originally superimposed positions (1 x n_p vector).

$$\vec{v} = U\vec{a} \tag{1.65}$$

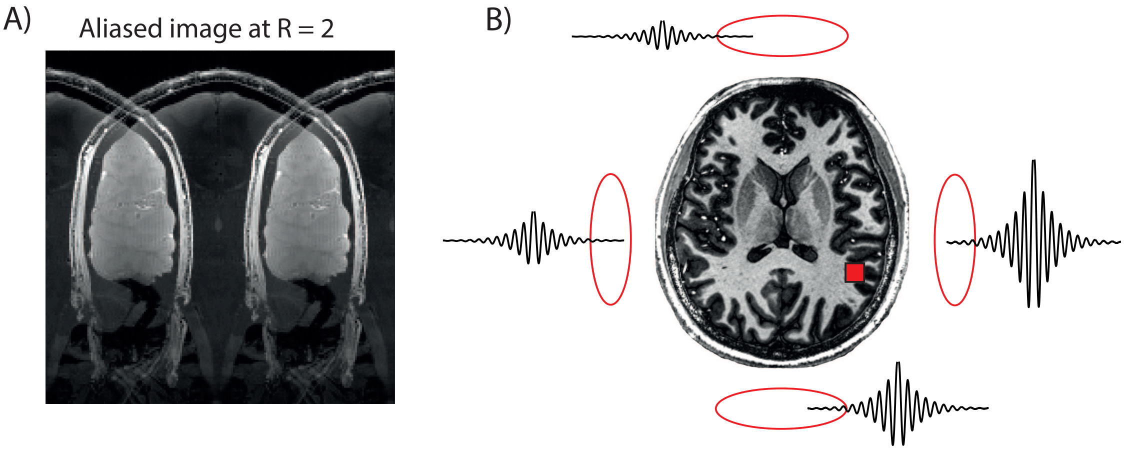

Figure 1.23: *A) Reconstructed raw data without using SENSE approach. Aliasing is visible in left-right direction. B) Visual representation of the working principle for SENSE reconstruction.*

One critical parameter to consider when using parallel imaging techniques is the SNR reduction which results from the reduced number of phase encoding steps. Moreover, the correlations between the channels can impair the final SNR and reconstruction quality. This is why minimizing the coupling between the channels is of utmost importance. If the coil sensitivity maps of two separate receivers are highly coupled, the SENSE reconstruction is impaired. The *geometrical factor* g_ρ was defined for each pixel ρ in the image to evaluate the SNR reduction in SENSE reconstruction (Equation 1.66) [62]. The R term is the *reduction factor* and is defined as the ratio between the total number of k-space lines and the effective number of lines which were acquired.

$$g_\rho = \frac{SNR_\rho^{full}}{SNR_\rho^{reduced}\sqrt{R}} \tag{1.66}$$

Ideally, the g-factor values should remain close to 1 since it would indicate that the SNR reduction is only caused by the reduced sampling of k-space. However, in practice the noise couplings will degrade the SNR and the g-factor will grow with increasing reduction factor.

1.6.4 SNR calculation

The SNR calculation is an essential measure of RF coil quality since it estimates the efficiency of the receivers to detect the MR signal with respect to noise. Image quality depends on SNR, and once it is measured the MR protocols can be optimized to enhance the SNR levels. SNR is usually quantified from the reconstructed images from the MR acquisitions, either by estimating the noise from a noise-only region in the FOV [65, 66] or by subtracting two images acquired consecutively to obtain noise only [67]. However, the presence of artifacts in noise regions, the non-uniformity of noise across the FOV in parallel MR image reconstruction or non-stationary tissues can impair a good estimation of the SNR [68]. The reconstruction of the image in SNR units was proposed to address these challenges by estimating the noise statistics directly from noise-only data, and are therefore included in the reconstruction algorithm [68]. In the next sub-sections, a description of the method is given following the steps presented in Figure 1.24.

Acquiring noise data is the first step of the procedure. It can be performed together with or separately from the sequence used for signal acquisition by setting the RF power to 0 or removing the RF pulses. The raw data is used to compute the noise covariance matrix (Equation 1.62). A noise decorrelation matrix (or pre-whitening) is therefore calculated and will be applied to the data to get a noise standard deviation of 1 (Figure 1.24) [68]. It can be understood as a way to uncorrelate the noise from receive channels.

Acquiring signal data was done throughout this work with a single-slice fully-sampled 2D-GRE sequence (1 x 1 mm^2, slice thickness = 1 mm, TR/TE = 1000/3.37 ms, FA = 48°, 192 x 192 matrix). In Figure 1.24, it is referred to as the raw data and corresponds to the individual signal from each receiver in k-space. The sensitivity maps for SENSE reconstruction (calibration data) are computed as the individual receive coil images divided by the sum-of-squares combination of all channels [62].

Signal processing The noise decorrelation matrix is applied to both the sensitivity maps and the raw data (signal processing step, Figure 1.24). Afterwards, the unmixing (unfolding) coefficients are computed according to equation 1.64, including the noise correlations, which is not strictly required by Kellman's method [68] or SENSE reconstruction [62] but is important for a quality assessment of the receive array. The unmixing matrix is applied to the individual images of the receivers (see 1.6.3 on SENSE method), which are summed to get a combined image. In the last step, the SNR for SENSE reconstruction is computed as defined by equation 1.67, where $\mathbf{U}$ is the unfolding matrix (Equation 1.64), and the term $\left|\mathbf{U}^T\vec{p}\right|$ corresponds to the combined image calculated before.

$$SNR_{SENSE} = \frac{\left|\mathbf{U}^T\vec{p}\right|}{\sqrt{\mathbf{U}^T\mathbf{U}^*}} \tag{1.67}$$

At the end of the reconstruction process, the pixel intensity of the final image is scaled in SNR units.

1.6.4.1 Transmit-only/Receive-only head coil arrays at 7T

While multi-channel receive-only RF coil arrays are widely used in routine clinical practice at 1.5T, 3T or 4T for various body parts (head, torso, wrist, etc.) [69–72], there are only a few designs of independent receivers in combination with a multi-channel transmit coil array

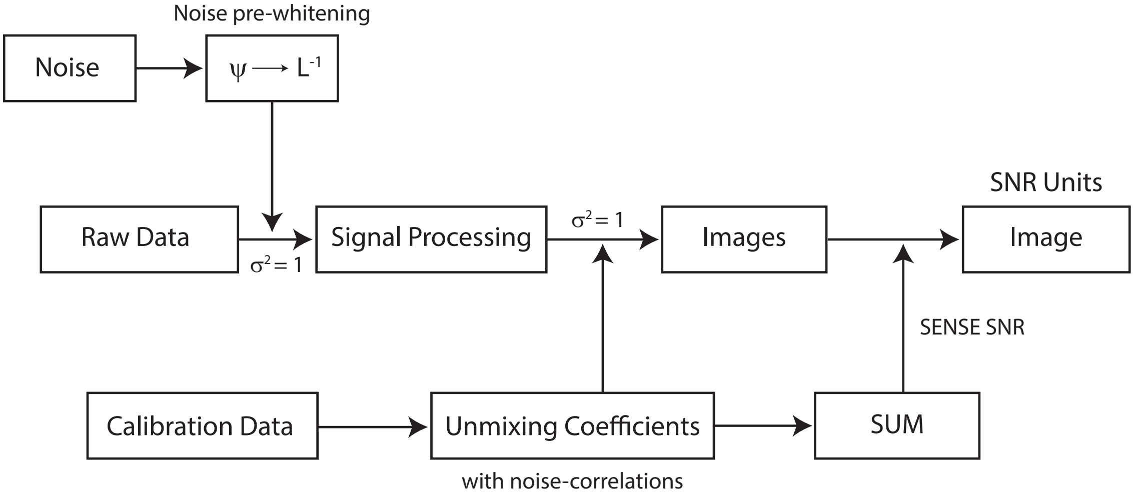
Noise pre-whitening
Noise
ψ ⟶ L⁻¹
SNR Units
Raw Data
Signal Processing
σ² = 1
Images
Image
σ² = 1
SENSE SNR
Calibration Data
Unmixing Coefficients
SUM
with noise-correlations

Figure 1.24: *A) Raw data reconstructed without using the SENSE approach. Aliasing is visible in left-right direction. B) Visual representation of the working principle for SENSE reconstruction.*

Table 1.2: *For the different 7T head transmit-only/receive-only coil arrays shown in the second column, the central SNR is given when it is known.*

Authors	Coil Design	Central SNR
Adriany et al. 2010	16Tx/32Rx transmission lines	-
Gilbert et al. 2015	8Tx/32Rx loops	-
Shajan et al. 2016	16Tx/31Rx loops	-
Zhang et al. 2017	8Tx/29Rx dipoles	56.81
Clément et al.	8Tx dipoles/32Rx loops	63

built for 7T MR scanners [16, 61, 73, 74]. In the next subsection, the designs are described, and a summary is shown in Table 1.2.

To our knowledge, the first setup combining a transmit-only coil array with an independent receive array at 7T was proposed by Adriany et al. [16] in 2010. The transmit array was designed with 16-channel transmission lines placed on a 32 cm circular support. The receive array consisted of 16 additional transmission-lines on a 24 cm circular support aligned with the outer transmit array (Figure 1.25A). However, the receive elements were aligned perpendicular to the outer transmission lines and thus to the main magnetic field. While this orientation is sub-optimal for transmit purposes, they can significantly contribute for improved SNR and parallel imaging performance. Moreover, the level of noise correlations is reduced since the transmit and receive arrays are, by orthogonality, poorly coupled. A net gain in SNR was measured with the addition of the independent 16-channel receivers, while no noticeable differences in the transmit field efficiency was observed. In 2015, the first transmit-only coil array combined with a receive-only array was introduced [74] for 7T head-only MR scanners. The transmit array consisted of eight large rectangular loops (130 x 234 mm^2) arranged on a quasi-elliptical polycarbonate former, while 32-channel receive loop coils with soccer-ball geometry were arranged on a head shape former [69] (Figure 1.25B). Sufficient decoupling was achieved between the receivers, with mean and maximum noise correlation values of 3.4% and 25%, respectively. However, even though homogeneous coverage of the whole-brain was achieved with the MP2RAGE [75] sequence, the coil array was not further investigated. In 2016, a 16-channel dual-row transmit array combined with a 31-element receive array originally designed for 9.4T magnet [76] was proposed for 7T applications [73]. Sixteen loops were arranged on two rows for the transmit array, while 31 loops were positioned on four rows and used as receivers (Figure 1.25C). The geometrical arrangement of the receivers contributed to further enhance the SNR in the upper regions of the head compared to the design presented for 9.4T [76]. While the previous designs described relied either on receive loop coils or transmission-lines, using dipoles as receivers was proposed in 2017 [61]. The main motivation was that dipoles were shown to achieve higher in-depth SNR compared to loop coils [77]. The transmit array was constituted of 8-dipoles [60] circularly arranged around the head. The 29 receive dipoles were mounted on a 3D-printed support and special care was taken to efficiently detune dipoles during the RF transmission. Even without the possibility of overlapping adjacent dipoles, good decoupling coefficients were achieved (lower than -12 dB). However, while higher SNR was measured in the spinal cord compared to a commercial 32Rx coil array (Nova Medical, USA), the central and peripheral SNR was lower.

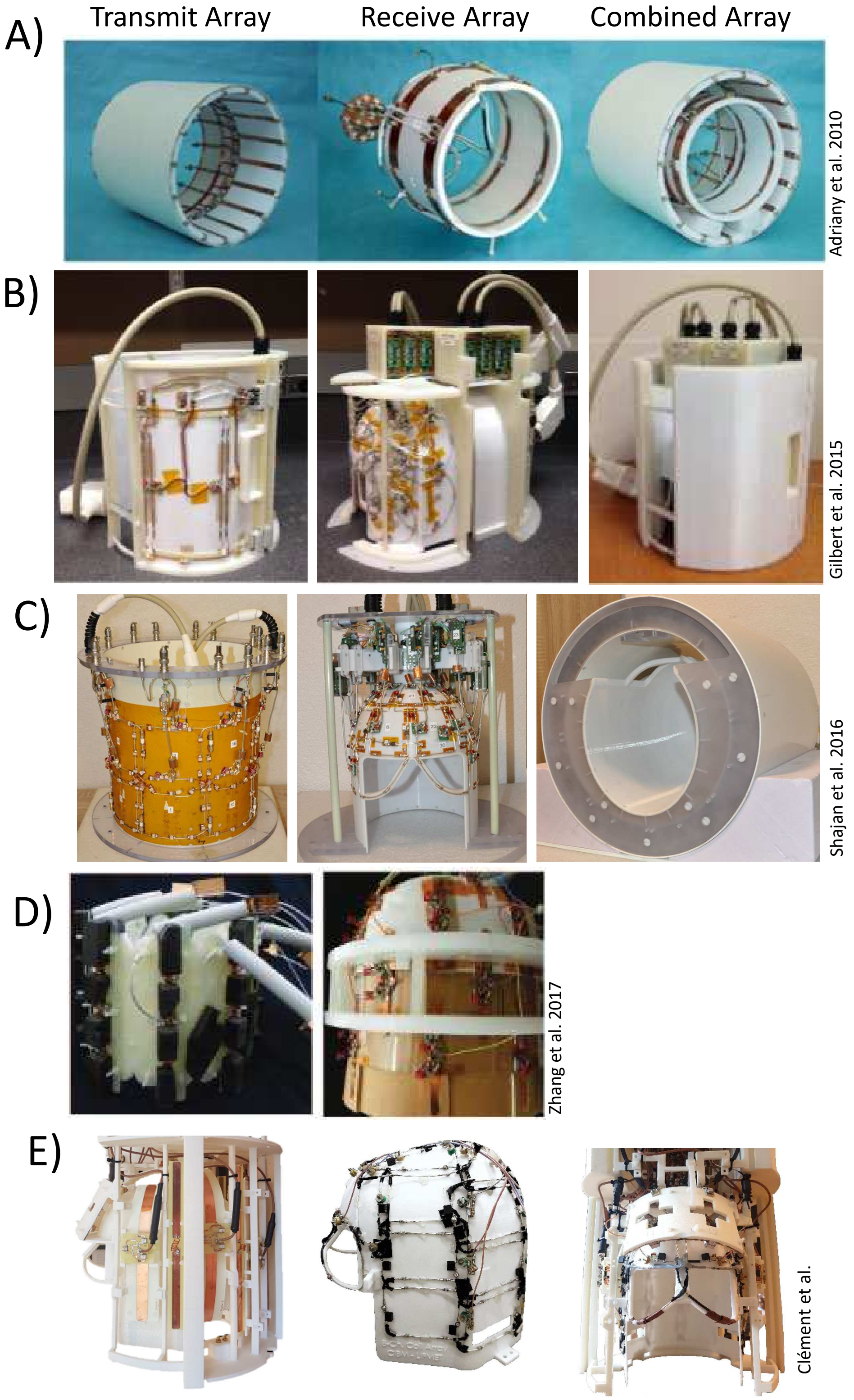
A)
Transmit Array
Receive Array
Combined Array
Adriany et al. 2010
B)
Gilbert et al. 2015
C)
Shajan et al. 2016
D)
Zhang et al. 2017
E)
Clément et al.

Figure 1.25: *Pictures of the different coil array designs presented in Table 1.2. The transmit-array only, the receive-array only and the combined transmit-receive arrays are shown. The corresponding journal reference is indicated.*

2

A whole-brain dipole coil array at 7T

Adapted from:

Jérémie D. Clément, Rolf Gruetter, Özlem Ipek
A human cerebral and cerebellar 8-channel transceive RF dipole coil array at 7T
Magnetic Resonance in Medicine, 2018, `https://doi.org/10.1002/mrm.27476`

Jérémie D. Clément designed and built the 8-channel transceive RF dipole coil array, contributed to experimental design and performing MR experiments, co-writing the paper.

Abstract

Purpose Dipole antennas that provide high transmit field penetration with large coverage, and their use in a parallel transmit setup, may be advantageous in minimizing B_1^+-field inhomogeneities at ultra-high field, i.e 7T. We have developed and evaluated an 8-channel RF dipole coil array for imaging the entire cerebral and cerebellar regions in man.

Methods A coil array was modeled with seven dipoles: six placed covering the occipital and temporal lobes; one covering the parietal lobe; and two loops covering the frontal lobe. Center-shortened and fractionated dipoles were simulated for the array configuration and assessed with respect to B_1^+-field at maximum specific absorption rate averaged over 10 g tissue regions in human brain. The whole-brain center-shortened dipoles with frontal loops coil array was constructed and its transmit properties were assessed with respect to MR images, B_1^+-field, and homogeneity.

Results In simulations, the dipole arrays showed comparable performances to cover the whole-brain. However, for ease of construction, the center-shortened dipole was favored. High spatial resolution anatomical images of the human brain with the coil array demonstrated a full coverage of the cerebral cortex and cerebellum.

Conclusion The 8-channel center-shortened dipoles and frontal loops coil array promises remarkable efficiency in highly challenging regions as the cerebellum, and phase-only RF shimming of whole-brain could greatly benefit ultra-high field magnetic resonance imaging of the human brain at 7T.

2.1 Introduction

At ultra-high field, magnetic resonance (MR) studies benefit from higher signal-to-noise ratio (SNR) [78, 79] and better spectral [80] and spatial resolution [22], compared to lower field MR scanners. However, the shorter wavelength ($\lambda \approx 12$ cm at 7T in the brain) causes noticeable RF inhomogeneity and decreased RF penetration of human tissues [25]. Furthermore, the rise in tissue temperature during RF excitation can be higher, as the requirements for energy of RF pulses generally scale with frequency [81–83]. For these reasons, there are three general challenges when working at ultra-high field: increased RF inhomogeneity, limited RF penetration and high energy deposition in tissues. At lower fields, i.e 1.5T and 3T, limited RF penetration and inhomogeneities are not a big limitation, as the wavelength is longer than the dimensions of the brain. Thus, RF volume coils such as birdcage coil or transverse electromagnetic (TEM) coils are frequently used [18, 23, 84, 85]. However, at 7T and higher field MRI, those coils typically show a central brightening effect in the brain, with low transmit field at the edges of the brain, such as the temporal lobes [25, 86]. Dielectric pads were proposed to address this issue but they only offer a limited and local improvement of the transmit field generated by volume coils [87, 88]. Moreover, the quality (e.g the compound's properties) of dielectric pads could degrade over time and different head shapes or head movements can also impact its performances. Thus the capability to offer a large and efficient coverage of the head with a robust and reliable setup remains unsolved. Parallel transmit systems, where an array of multiple independent RF coils are used for the brain or body MR scans have been proposed to minimize such obstacles at ultra-high field. By modulating the RF phases and amplitudes [89] of each transmit element in the array, constructive transmit field (B_1^+) interferences can be generated over the region-of-interest (ROI), and thus improve signal homogeneity. Several RF coil array designs have been previously reported based on loop coils [44, 76, 90, 91] or micro-strips [53, 92] elements for human brain imaging and demonstrated good B_1^+ efficiencies in the cerebral cortex.

Dipole antennas were proposed as an alternative to loop coils as they were shown to have better RF signal penetration depth and field symmetry at 7T MRI [12, 58]. With a center-shortened dipole antenna (where the shortening inductance were placed at the center) on a ceramic substrate, the strong electric fields were largely kept outside the subject tissues, and high B_1^+ field was achieved in deep body tissues. Thereafter, various others designs such as bow-tie (with the dipole placed on water-filled substrate), snake dipole, distributed inductance or dipole-loop configurations were investigated for body imaging [93–96]. In particular, a fractionated dipole design (where the two legs of the dipole are split and connected through lumped elements) without ceramic substrate demonstrated higher $B^+_{1,\text{in-depth}}/\sqrt{\text{SAR}_{10g,\max}}$ compared to a center-shortened dipole with and without substrate [96–98]. Making use of the properties previously stated, an RF coil array built with dipoles might be able to cover the auditory cortex, the cerebral lobes (frontal, occipital, parietal, temporal) and the cerebellum, either together, or with high B_1^+ field through RF phases optimization. Chen et al. [59] previously reported a dipole coil array for head imaging based on meander ends dipole and observed an extended coverage in the neck compared to a commercially available birdcage coil. However, due to the longitudinal extent of the coil array (dipoles' length = 320 mm), an excessive loading by the shoulders negatively affected the B_1^+ efficiency. By adapting the geometry of the coil array to cover specifically the whole-brain (cerebral cortex and cerebellum) higher B_1^+ efficiency might be achieved. Moreover, even though for body imaging, the fractionated dipole demonstrated better performance compared to the center-shortened dipole, it is still undetermined whether a center-shortened or fractionated dipole coil array design would be more suitable to achieve a B_1^+-efficient whole-brain coverage, as no comparison was yet been made. For body dipole coil arrays the individual properties of dipole designs (center-shortened or fractionated) might be extended to array configurations as the sufficient distance between neighbors allows for enough decoupling. But for a B_1^+-efficient imaging of the brain, a tight geometrical arrangement requires the dipoles to be positioned looking to each other, which will increase the coupling.

For body MRI, the better signal penetration depth of dipoles compared to loop coils has been clearly demonstrated beneficial but for brain MR imaging, reaching deep structures is not a main concern because of the limited size of the head. Nevertheless, the extended longitudinal coverage attained with dipoles might yield higher MR signal in challenging regions such as the cerebellum. However, the inter-element interaction can alter the fine tuning, and matching of the dipoles, and might induce field cancellations. Thus, the placement of the dipoles is a critical step to generate a high B_1^+ field. Therefore, the aim of the present study was to design, develop and evaluate an 8-channel dipole coil array able of providing whole coverage of the human brain with a high B_1^+ field for MR measurements at 7T.

2.2 Methods

2.2.1 Single dipole design

A single center-shortened dipole and a fractionated dipole (170 mm long, 15 mm width, 12 mm gap between legs) were etched from 35 µm copper on a FR4 substrate with a thickness of 0.1 mm. For center-shortened dipole, hand-wound shielded-copper inductors ($\varnothing = 1$ mm, Rowan Cable Products Ltd, England) were placed close to the feeding point while for the fractionated dipole, each leg was split in two pieces with a 5 mm gap in between to place the inductors (Fig. 2.1A). Non-magnetic capacitors (American Technical Ceramics, NY, USA) were used as additional lumped elements to match the dipoles to 50 Ohms at 297.2 MHz (7T). Then, a single center-shortened and fractionated dipole B_1^+ excitation profiles were experimentally measured. Thereafter, a dipole coil array was modeled and simulated for the center-shortened and the fractionated dipole designs.

2.2.2 Coil array design

The center-shortened and fractionated dipoles for the arrays were modeled with lengths from 158.5 mm to 230 mm and 15 mm width, to ensure an efficient coverage of the head and a tight placement. For both dipole designs, the same geometrical arrangement was applied. Six dipoles were placed around the occipital and temporal lobes of the brain, arranged symmetrically (left-right) but non-uniformly centered along the longitudinal axis to account for the human brain geometry (Fig. 2.1B). The dipoles 3 and 4, placed on the back side of the head, were centered closer to the cerebellum to provide higher signal in this region. A seventh dipole was placed around the parietal lobe and aligned in the anterior-posterior direction, perpendicular to the main magnetic field to provide high RF field at the top of the head where it is usually challenging to achieve high B_1^+ field (Fig. 2.1B). The dipoles 1, 2, 5, 6 and 7 were slightly bent to follow the curvature of the head. Compared to placing dipoles at the frontal lobe, loop coils demonstrated higher B_1^+ efficiency and lower mutual coupling by coil overlapping. Thus, two 95 x 85 mm^2 loops were placed over the frontal region of the head and tilted.

2.2.3 Electromagnetic field simulations

Both arrays were simulated with the finite-difference time-domain (FDTD) method on Sim4Life 3.4 (ZMT AG, Switzerland) on a whole body human model, Duke [35] (Fig. 2.1B). All the coil array elements (dipoles and loops) were defined as perfect electric conductors (PEC), gridded at 3 mm-iso, and lumped elements were placed for tuning and matching. Moreover, a topological voxeler was used for the coils to guarantee that their geometry was correctly voxelised. The Duke model was gridded at 2 mm-iso and truncated below the torso to reduce the simulation time without impacting the area of interest (20 Mcells in total). All the coils were driven individually by a Gaussian excitation centered at 297.2 MHz with a 500 MHz bandwidth and computations were carried out on a dedicated GPU (2 x GTX 1080Ti, Nvidia Corp., USA) with an average simulation time of 1 hour per channel for a convergence better than -50 dB (quantifying the variations in the results between two consecutive iterations). An integrated match-tool was used to tune and match the resonant elements in post-processing by adapting the lumped element values which were then introduced into the simulation model. Both arrays were simulated including the inductor losses, modeled with series resistors, as calculated in [99]. Absorbing boundary conditions were applied at the edges of the simulation space to ensure that no reflected wave would interfere with the forward electromagnetic wave.

All the results were interpolated at 1 mm-iso inside a virtual box (200 x 250 x 230 mm^3) surrounding the head of the human model and normalized to 1 W input power. When compared with experimental data, the simulations were corrected for the losses in the line till the coil array (more details are given in the paragraph about transmit field characterization). Individual B_1^+ maps and scattering matrices were exported to Matlab (2017a, the Mathworks, Natick, MA) to be processed. The $B_1^+ / \sqrt{SAR_{10g,max}}$ maps were computed for individual center-shortened and fractionated dipoles in the array. Then, RF phases were optimized for two distinct areas, either whole-brain or cerebellum and the $B_1^+ / \sqrt{SAR_{10g,max}}$ map was calculated for both center-shortened and fractionated dipole arrays. Thereafter, the center-shortened dipole array was built and further investigated as it demonstrated the best balance between RF performances, mechanical strength and ease of construction.

2.2.4 Coil array construction

The center-shortened dipoles for the array were etched from 35 μm copper on a FR4 substrate with a thickness of 0.1 mm while the two loops were built with silver-plated copper wire. All geometrical dimensions, distances and placement were kept the same as in the simulated model. The RF feeding ports were placed at the center of the dipoles and connected to an in-house built transmit-receive switch with low noise preamplifiers (Stark Contrast, Erlangen, Germany) through 50 Ohms coaxial cables with equal phase length ($\varnothing = 3$ mm, Huber-Suhner, Switzerland). A single Tx power input was divided into quadrature and fed the two loops. Common-modes on the coaxial cables were diminished with a balun that is a quarter-wavelength transformer tuned to 297.2 MHz with capacitors. Tuning/matching to 297.2 MHz and S-parameter matrix measurement were performed using a 4-channel vector network analyser (Agilent Technologies 5071C-ENA Series, USA). To accommodate the shape of the human head, a helmet was designed with maximal dimensions in anterior-posterior direction equal to 222 mm, 187 mm from left to right and 231 mm from top to bottom. The whole structure was designed on Solidworks 2016 (Dassault Systems, France) and 3D printed (EOSINT P395, EOS, Germany) in nylon (EOS, PA2200) giving a maximal distance between the helmet and the RF coils of 15 mm (Fig. 2.2B-C).

However, the center-shortened dipole design was more sensitive to high currents and voltages compared to other resonant coils as the inductors required to tune the dipoles were placed in the gap between the dipole legs. At resonance, electric arcs could occasionally occur between the inductors/capacitors and the dipole's legs, especially with power-intensive MR sequences. To avoid these side effects, the feeding line and the matching capacitors were soldered on a separate rigid PCB (0.8 mm thickness) placed 16 mm above the dipole (Fig. 2.2D-E, $C_{s,1}$, $C_{s,2}$ and C_p). Then, the tuning inductors could be connected in between the rigid PCB and the legs (Fig. 2.2D-E, L1 and L2), which eliminated arcing, and provided high resistance to mechanical stress, particularly for adjustments of the inductor value.

The close distance between the dipoles (≈ 75 mm between the center of dipoles) placed around the head resulted in high couplings between neighbors. Thus, a decoupling method based on a magnetic wall approach was applied by placing a decoupling dipole (DecD) at equal distance between two dipoles, with no power input and with its legs short-circuited by an hand-wounded inductor adjusted to maximize the dipoles' isolation [50]. The DecDs (10 mm width, 12 mm gap between legs) were etched from 35 μm copper on a FR4 substrate with a thickness of 0.8 mm and a length equal to the mean length of the two dipoles in between which they were placed. Five DecDs were used between the dipoles 1 to 6 (Fig. 2.2A, in white) and added to the simulation model, to account for their interactions with the dipoles.

2.2.5 MR Experiments

For a single center-shortened and a single fractionated dipole, measurements were performed on a spherical phantom (⌀ ≈ 180 mm, Siemens D165-10606820) using a Magnetom 7T MR scanner with 8 x 1 kW RF amplifier (Step 1, Siemens, Erlangen, Germany). Measurements on the brain were acquired using the whole-brain center-shortened dipoles and frontal loop coil array (Magnetom 7T, Step 2.3).

2.2.5.1 Particle-swarm optimization (see also chapter 4)

In both phantom and human brain measurements, phase-only RF shimming was performed using a particle-swarm optimization (PSO) method [100, 101]. Based on swarm intelligence, this iterative method aimed to minimize a cost function defined either for maximal B_1^+ field (Eq. 2.1) or homogeneity (Eq. 2.2).

$$\text{cost}_{\text{MaximalB1}} = \left(1 - \frac{\sum\sum_{i,j} Ratio(i,j)}{Size_{ROI}}\right) * 100 \tag{2.1}$$

$$\text{cost}_{\text{Homogeneity}} = \alpha . \frac{1}{\langle B_1^+ \rangle_{ROI}} + \beta . \text{std}(B_{1,ROI}^+) \tag{2.2}$$

For maximal B_1^+ field (Eq. 2.1), the Ratio(i,j) was defined as the ratio between the non-shimmed B_1^+ field and the sum-of-magnitudes for each pixel in the ROI, while for homogeneity (Eq. 2.2) the cost function was defined as the weighted sum of the standard deviation and the inverse value of the mean B_1^+ field over the ROI. The weighting coefficients α and β could be adapted to balance B_1^+ efficiency and homogeneity. Using a multi-core processor (Intel Core i7-4790, 3.60 GHz), the convergence of the method was achieved in less than 20 seconds for maximal B_1^+ field and less than 40 seconds with the homogeneity cost function for any ROI considered.

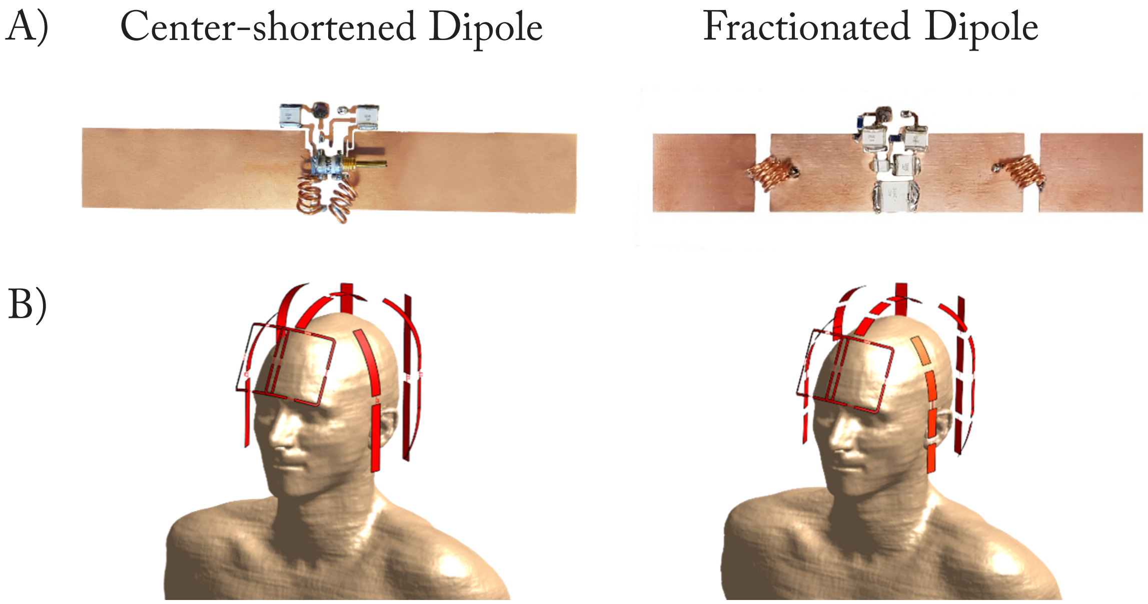

Figure 2.1: *A) Photos of the center-shortened and fractionated dipole designs. The inductors are placed in series and connected to each leg. They are used to tune the dipole at the right frequency by extending its electrical length. Three capacitors (2 in series, 1 in parallel) are used to match the dipole to 50 Ohms. B) Simulation model for the 8-channel center-shortened/fractionated dipole coil arrays with frontal loops.*

2.2.5.2 Transmit Field Characterization

All the B_1^+ maps were acquired with a SA2RAGE sequence for a 500 µs, 90°, 1 kW hard pulse [102]. To optimize the RF field in regions-of-interest (ROI), B_1^+ sensitivities (magnitude and phase) were extracted on Matlab, from a GRE-based sequence, and then processed with the PSO algorithm. The local SAR_{10g} maps were computed from the simulation results for the RF phases applied in measurements to evaluate the $B_1^+/\sqrt{SAR_{10g,max}}$ efficiency for such close-fitted dipole array. In phantom and human brain measurements, the B_1^+ field was normalized to 1 kW input power per channel, while the homogeneity was evaluated with the standard deviation. The B_1^+ field was compared for single center-shortened and single fractionated dipole that were placed at a distance of 15 mm from the phantom. The transmit losses, were measured to 37% (Siemens, Erlangen, Germany) between the RF amplifiers and the coil plug and approximately to 13% from the TR switch connected at the coil plug and the coils.

2.2.5.3 Anatomical images

Healthy male volunteers who had signed a written consent approved by the local ethics committee were imaged with the whole-brain center-shortened dipoles and frontal loops coil array (Fig. 2.2) and with the safety parameters set to the worst-case scenario as evaluated from the Q-matrix [29], for a simulated model with the decoupling dipoles and with-

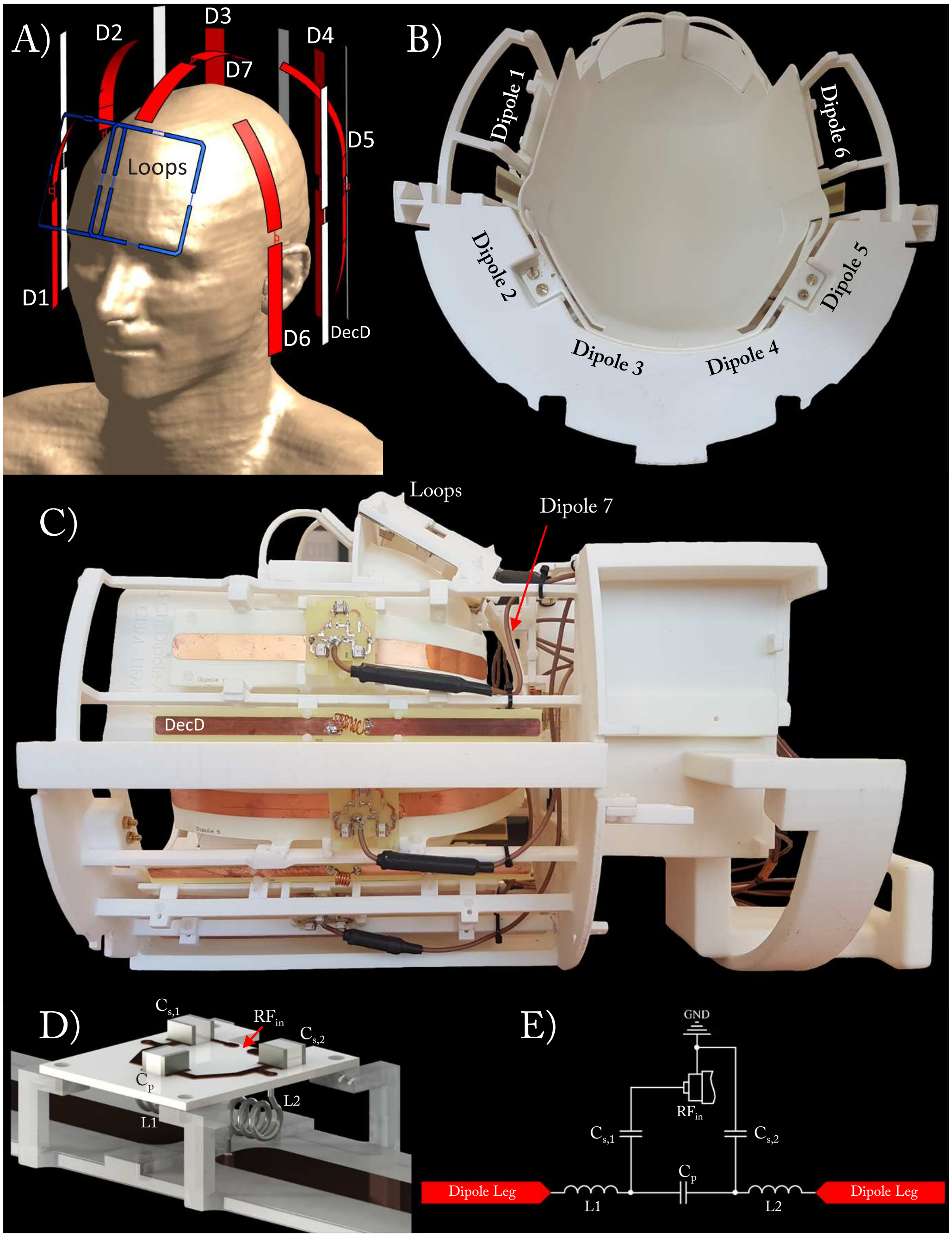
A)
D1
D2
D3
D4
D5
D6
D7
DecD
Loops
B)
Dipole 1
Dipole 2
Dipole 3
Dipole 4
Dipole 5
Dipole 6
C)
Loops
Dipole 7
DecD
D)
$C_{s,1}$
RF_{in}
$C_{s,2}$
C_p
L1
L2
E)
GND
RF_{in}
$C_{s,1}$
$C_{s,2}$
C_p
Dipole Leg
L1
L2
Dipole Leg

Figure 2.2: *A) Simulation model for the whole-brain center-shortened dipoles and frontal loops coil array. B) and C) Photos of the general design of the array. Six center-shortened dipoles were placed around occipital and temporal lobes (D1-D6) and one (D7) was placed around the parietal lobe. Two loop coils (1 and 2) were placed over the frontal lobe of the brain. D) Isometric view of the feeding circuit, including the dipole, the tuning/matching circuit and the support structure for the dipole, and E) corresponding schematics.* $C_{s,1}$ *and* $C_{s,2}$ *are capacitors, L1 and L2 are inductors placed in series with respect to the RF input and were mainly used to tune the dipole to 297.2 MHz.* C_p *is a capacitor connected between the two dipole's legs, in parallel of the RF input port and was mainly used to match the dipole to 50 Ohms.*

out the inductor losses. RF phases of the individual channels were optimized with the PSO method and the B_1^+ field of individual coils and RF shimmed B_1^+ maps were evaluated. To acquire MR images, a 3D turbo-spin echo (3D-TSE, TE/TR = 120/2000 ms, resolution = 0.8 x 0.8 x 0.8 mm^3, FOV = 210 x 210 mm^2, Turbo Factor = 60, GRAPPA = 2, TA = 10 min 28 s), MP2RAGE [75] and multi-slice GRE (TE/TR = 16/1000 ms, resolution = 0.3 x 0.3 x 3 mm^3, FA = 60°, slices = 8, FOV = 210 x 210 mm^2, GRAPPA = 2, TA = 5 min 34 s) sequences were used.

2.3 Results

Individual B_1^+ excitation patterns for center-shortened and fractionated (where the two legs were splitted and connected with inductors) dipoles in a phantom showed that while the center-shortened dipole yielded slightly higher B_1^+ field in deeper regions, the fractionated dipole provided larger longitudinal field coverage (Fig. 2.3).

No significant differences were observed in $B_1^+/\sqrt{SAR_{10g,max}}$ maps, shown for individual center-shortened and fractionated dipole elements in the array (Fig. 2.4A). Nevertheless, the individual fractionated dipoles in array demonstrated up to a 20% decrease in local $SAR_{10g,max}$ value compared to the center-shortened dipoles.

Over the mid-brain (transverse slice), the center-shortened dipole array showed a slightly better $B^+_{1,slice\text{-}mean}/\sqrt{SAR_{10g,max}}$ value compared to the fractionated dipole array (0.54 vs 0.49 $\mu T\sqrt{kg}/\sqrt{W}$) while both dipole arrays had similar results over the whole head (less than 5% difference, Fig. 2.4B). Specifically, with the center-shortened dipole array, higher $B^+_{1,in\text{-}depth}$-field and lower local $SAR_{10g,max}$ were observed. Over the mid-cerebellum (coronal slice), the fractionated dipole coil array showed a noticeably larger longitudinal coverage at similar $B^+_{1,cerebellum\text{-}mean}/\sqrt{SAR_{10g,max}}$ values (0.57 $\mu T\sqrt{kg}/\sqrt{W}$ for center-shortened and 0.60 $\mu T\sqrt{kg}/\sqrt{W}$ for fractionated dipole array). However, better field penetration in depth was obtained with the center-shortened dipole array, particularly visible on sagittal view (Fig. 2.4B). Nevertheless, as the differences between the two dipole arrays were marginal, only the 8-channel center-shortened dipole coil array was further investigated.

Measured S-matrix for the whole-brain center-shortened dipoles with frontal loops coil array demonstrated coupling values between neighbors and next neighbors below -15 dB for all the dipoles, which demonstrated the efficient isolation provided by the decoupling dipoles (Fig. 2.5). Individually measured and simulated B_1^+ maps (Fig. 2.6) were similar, and indicated a uniform transmit field distribution for the dipoles except for the dipole 1 which was visibly coupled to the closest loop. We note that the B_1^+-field for dipole 7 was quite efficient although it was placed perpendicular to the B_0 orientation.

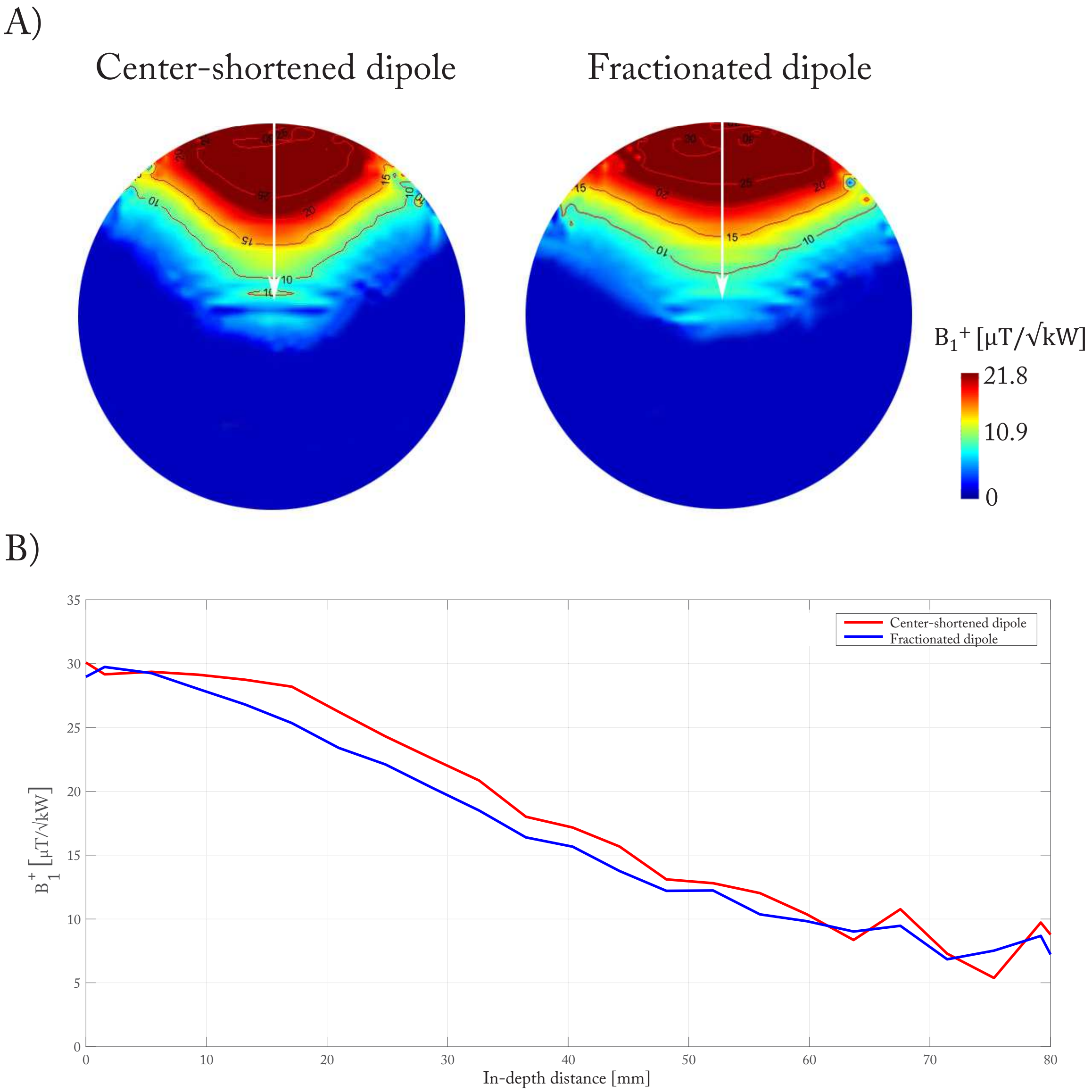

Figure 2.3: *A) Experimentally measured* B_1^+ *maps, normalized to 1 kW input power, along the dipole, for center-shortened and fractionated dipoles. Isolines are represented in red with their corresponding value inserted. B) In-depth* B_1^+ *profiles for center-shortened and fractionated dipoles, taken along the white arrow visible in A).*

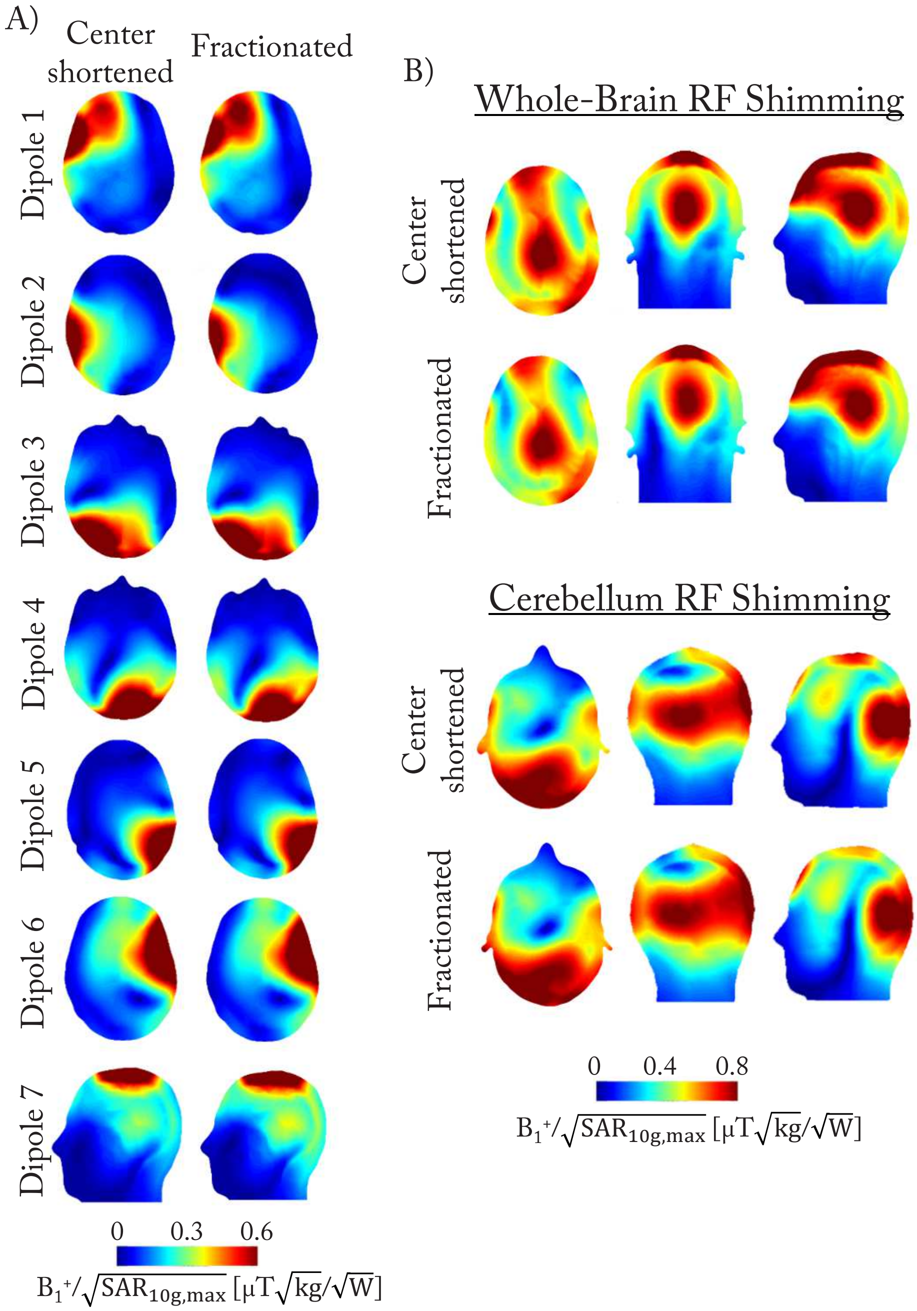
A)
Center shortened
Fractionated
Dipole 1
Dipole 2
Dipole 3
Dipole 4
Dipole 5
Dipole 6
Dipole 7
0
0.3
0.6
B1+/√SAR10g,max [μT√kg/√W]
B)
Whole-Brain RF Shimming
Center shortened
Fractionated
Cerebellum RF Shimming
Center shortened
Fractionated
0
0.4
0.8
B1+/√SAR10g,max [μT√kg/√W]

Figure 2.4: *For the whole-brain center-shortened/fractionated dipole with frontal loops coil array, including the inductor losses: A) simulated individual* $B_1^+ / \sqrt{SAR_{10g,max}}$ *maps B) simulated* $B_1^+ / \sqrt{SAR_{10g,max}}$ *maps for RF phases optimized over whole-brain (upper maps) and cerebellum (bottom maps for maximal* B_1^+ *optimization)*

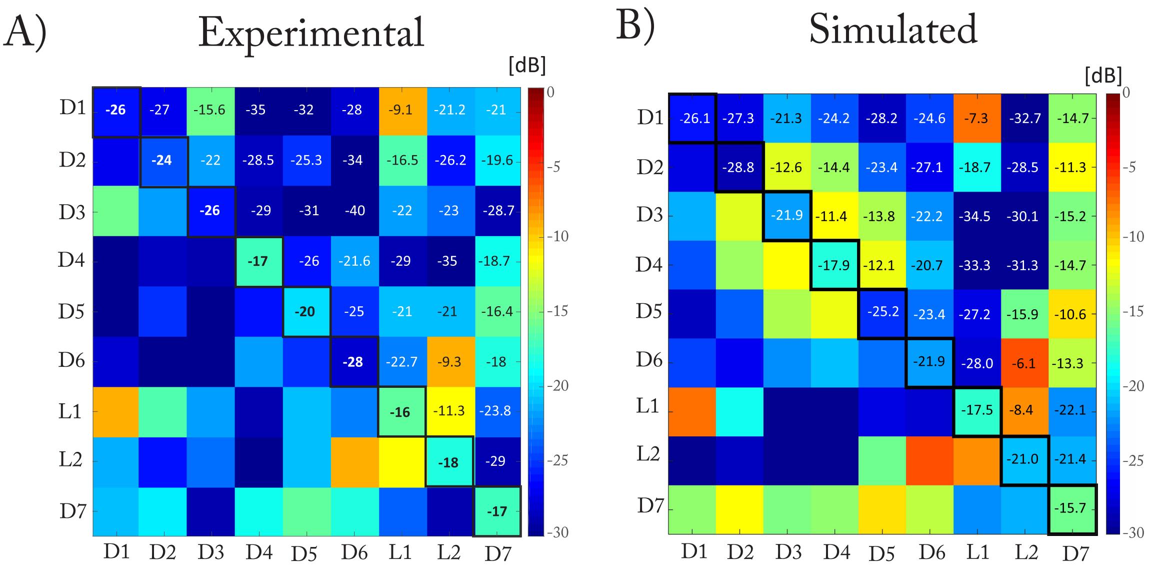

A) Experimental

	D1	D2	D3	D4	D5	D6	L1	L2	D7
D1	**-26**	-27	-15.6	-35	-32	-28	-9.1	-21.2	-21
D2		**-24**	-22	-28.5	-25.3	-34	-16.5	-26.2	-19.6
D3			**-26**	-29	-31	-40	-22	-23	-28.7
D4				**-17**	-26	-21.6	-29	-35	-18.7
D5					**-20**	-25	-21	-21	-16.4
D6						**-28**	-22.7	-9.3	-18
L1							**-16**	-11.3	-23.8
L2								**-18**	-29
D7									**-17**

B) Simulated

	D1	D2	D3	D4	D5	D6	L1	L2	D7
D1	-26.1	-27.3	-21.3	-24.2	-28.2	-24.6	-7.3	-32.7	-14.7
D2		-28.8	-12.6	-14.4	-23.4	-27.1	-18.7	-28.5	-11.3
D3			-21.9	-11.4	-13.8	-22.2	-34.5	-30.1	-15.2
D4				-17.9	-12.1	-20.7	-33.3	-31.3	-14.7
D5					-25.2	-23.4	-27.2	-15.9	-10.6
D6						-21.9	-28.0	-6.1	-13.3
L1							-17.5	-8.4	-22.1
L2								-21.0	-21.4
D7									-15.7

[dB]
0
-5
-10
-15
-20
-25
-30

Figure 2.5: *A) Experimental and B) simulated S-matrices for the whole-brain center-shortened dipoles and frontal loops coil array.*

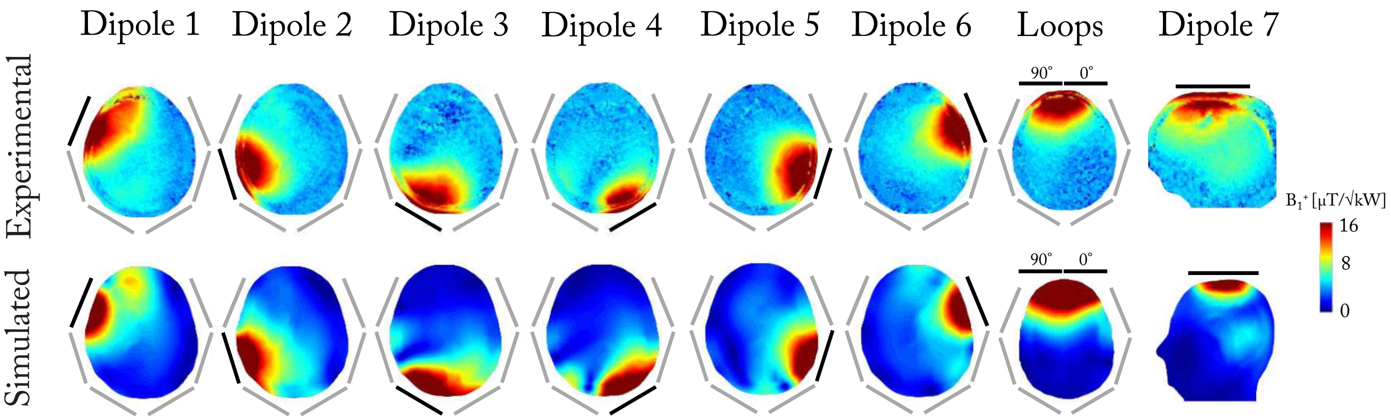

Dipole 1
Dipole 2
Dipole 3
Dipole 4
Dipole 5
Dipole 6
Loops
Dipole 7
Experimental
Simulated
90°
0°
90°
0°
B1+ [μT/√kW]
16
8
0

Figure 2.6: *Experimentally measured (upper row) and simulated (bottom row) individual B_1^+ maps, normalized to 1 kW input power at the coil plug. The simulated maps were scaled for 50% losses. The transverse slice was taken in the midbrain region for dipoles 1 to 6 while the maximum slice was chosen for the loops and the middle sagittal slice for the dipole 7. In each map, the active coil is represented as a black line, for the whole-brain center-shortened dipoles and frontal loops coil array.*

To determine if the B_1^+ field coverage can be improved, B_1^+ RF fields were phase-shimmed in mid-brain (transverse slice) and the corresponding simulated $SAR_{10g,max}$, normalized to 1W input power was 0.69 W/kg (Fig. 2.8A). A mean B_1^+ value of 28 ± 2.3 $\mu T/\sqrt{kW}$ was measured over the shimmed ROI (Fig. 2.7A, white solid line) while over a 3D volume encompassing the whole cerebral cortex (Fig. 2.7A, white dashed rectangle), a mean B_1^+ value of 23.2 ± 3.7 $\mu T/\sqrt{kW}$ was achieved. Nevertheless, the high-resolution 3D-TSE images demonstrated a whole-brain coverage with relatively good homogeneity across the slices in transverse and sagittal orientations (Fig. 2.7B) while MP2RAGE images showed high homogeneity across multiples slices. High-resolution GRE images were acquired with the RF phases optimized in sagittal (Fig. 2.9A) and transverse planes (Fig. 2.9B) and demonstrated an homogeneous coverage of the whole-brain, including the cerebellum.

To evaluate the capability for the coil array to efficiently cover the deeper-lying brain regions, RF phase shimming was applied in mid-cerebellum coronal slice using the two different cost functions, maximal B_1^+ field and homogeneity. As the ROI for phase optimization covered specifically the lower part of the brain, low transmit field was obtained in the upper regions. A mean B_1^+ value of 21 ± 3.1 $\mu T/\sqrt{kW}$ was measured over a 3D volume encompassing the whole cerebellum (Fig. 2.10A) for the maximal B_1^+ field optimization ($SAR_{10g,max}$ = 1.28 W/kg, Fig. 2.8B) and a mean B_1^+ value of 20.1 ± 2 $\mu T/\sqrt{kW}$ was measured over the same volume for the homogeneous optimization. The high-resolution MP2RAGE (0.6 mm iso) images demonstrated a complete and relatively homogeneous coverage of the cerebellum (Fig. 2.10B). On the edges of the cerebellum, the high-resolution 3D TSE (0.8 mm iso) image in coronal plane demonstrated the improvements achieved with the homogeneous goal (Fig. 2.10B, red arrow) while B_1^+ field was not significantly decreased, and signal quality in the others directions (sagittal and transverse) was not visibly altered.

2.4 Discussion

In this study, a robust and reliable array configuration for whole-brain imaging was shown for an 8-channel center-shortened dipoles with a quadrature frontal loops coil array by B_1^+ maps and anatomical images with phase-only RF shimming. This conformal array design exploited the placement of center-shortened dipoles on the temporal, occipital and parietal lobes of the brain and two loop coils on the frontal lobe.

The geometrically adjusted conformal dipole coil array provided a homogeneous coverage of the cerebellum with less than 10% signal variation with RF phase-only shimming. Similar signal homogeneity was achieved in the cerebellum with an 8-channel microstrip Tx/15-channel Rx array covering the cerebellum [103]. However, while the longitudinal extent of this microstrip along the head was 310 mm long, our dipole array was designed in a

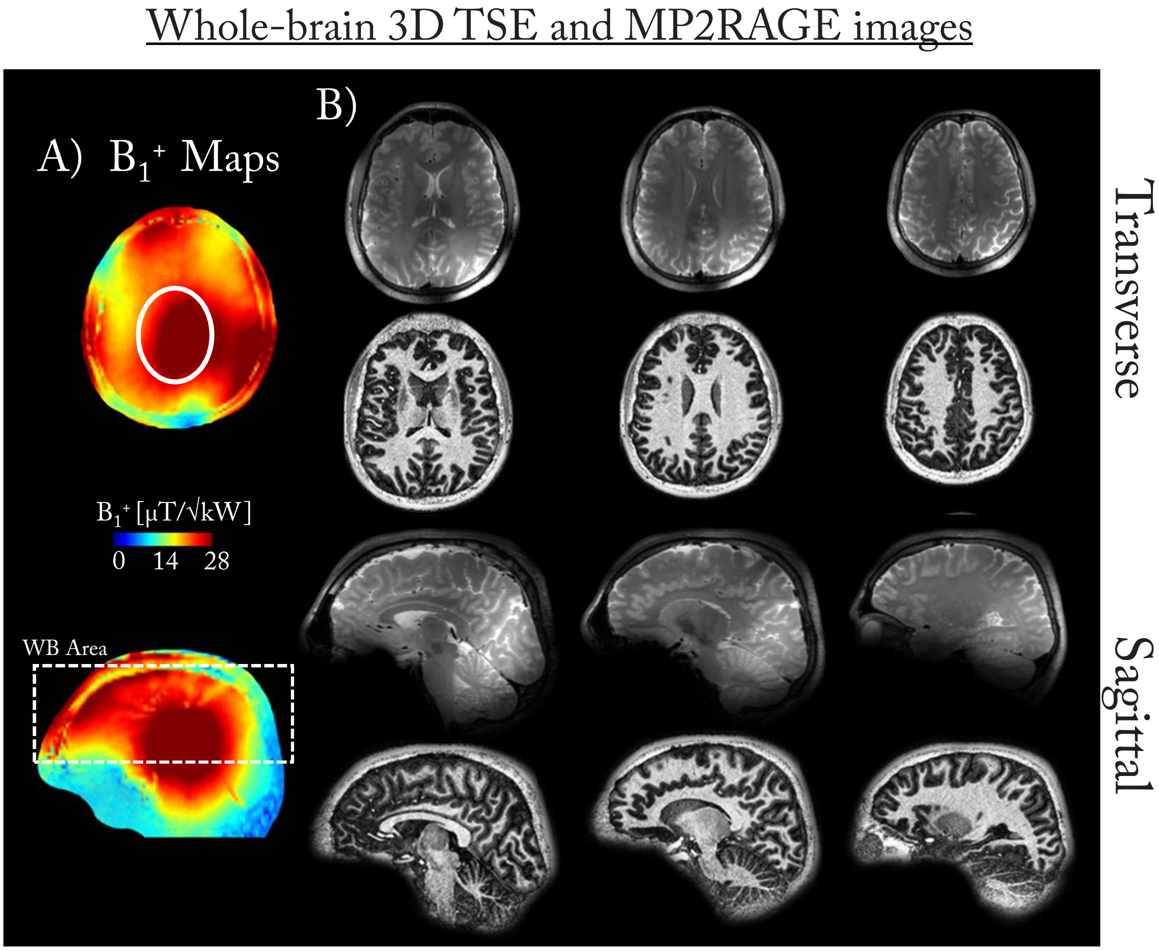
Whole-brain 3D TSE and MP2RAGE images
A) B1+ Maps
B)
B1+ [µT/√kW]
0 14 28
WB Area
Transverse
Sagittal

Figure 2.7: *A) RF phase-shimmed* B_1^+ *maps shown in transverse and sagittal plane, normalized to 1 kW input power per channel. Phase-only RF shimming was applied in the elliptical ROI (white solid lines) visible on transverse plane. A 3D region encompassing the whole cerebral cortex (white dashed rectangle in sagittal view) was selected to evaluate the* B_1^+ *efficiency across multiple slices B) High-resolution 3D-TSE (first row, 0.8 x 0.8 x 0.8* mm^3*) and MP2RAGE (second row, 0.6 x 0.6 x 0.6* mm^3*) images displayed in transverse and sagittal planes for different slices with the RF phases applied in A). No post-processing correction was applied.*

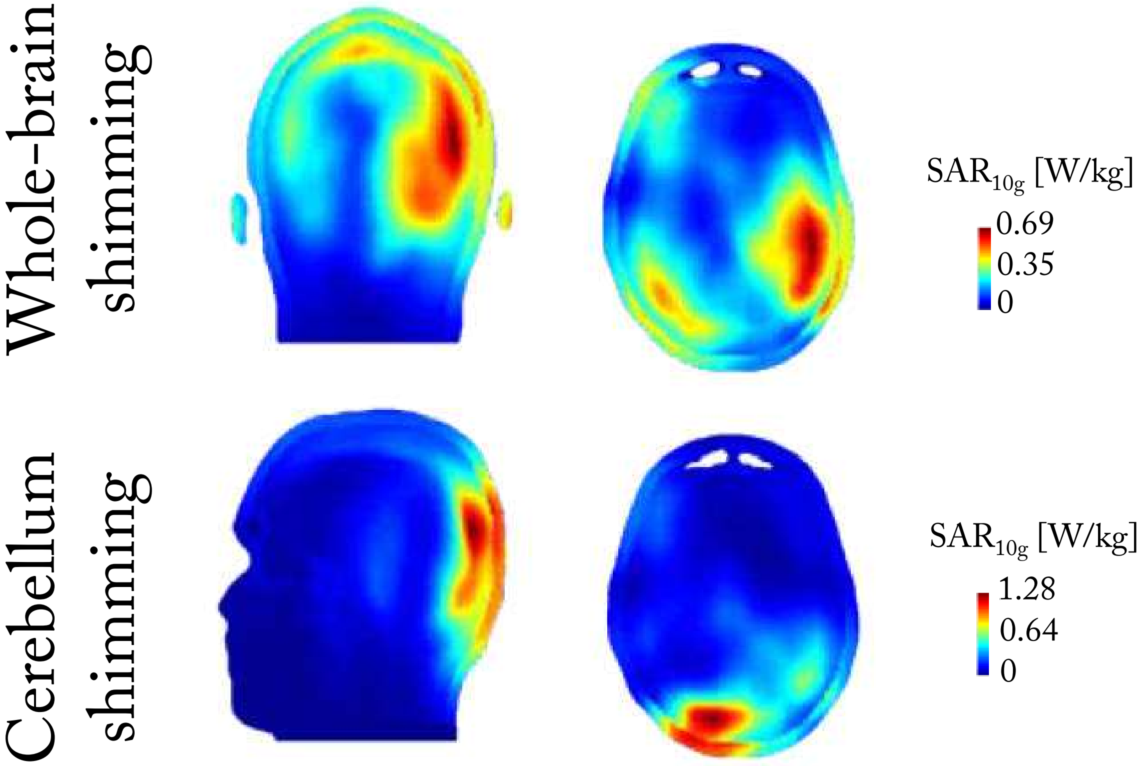
Whole-brain shimming
Cerebellum shimming
SAR$_{10g}$ [W/kg]
0.69
0.35
0
SAR$_{10g}$ [W/kg]
1.28
0.64
0

Figure 2.8: *Local* SAR_{10g} *maps computed for the RF phases used in MR measurements and optimized for A) whole-brain and B) maximal* B_1^+ *in cerebellum. The maximum's slice was chosen and scaled to the corresponding* $SAR_{10g,max}$ *value. The simulation model did not include the inductor losses.*

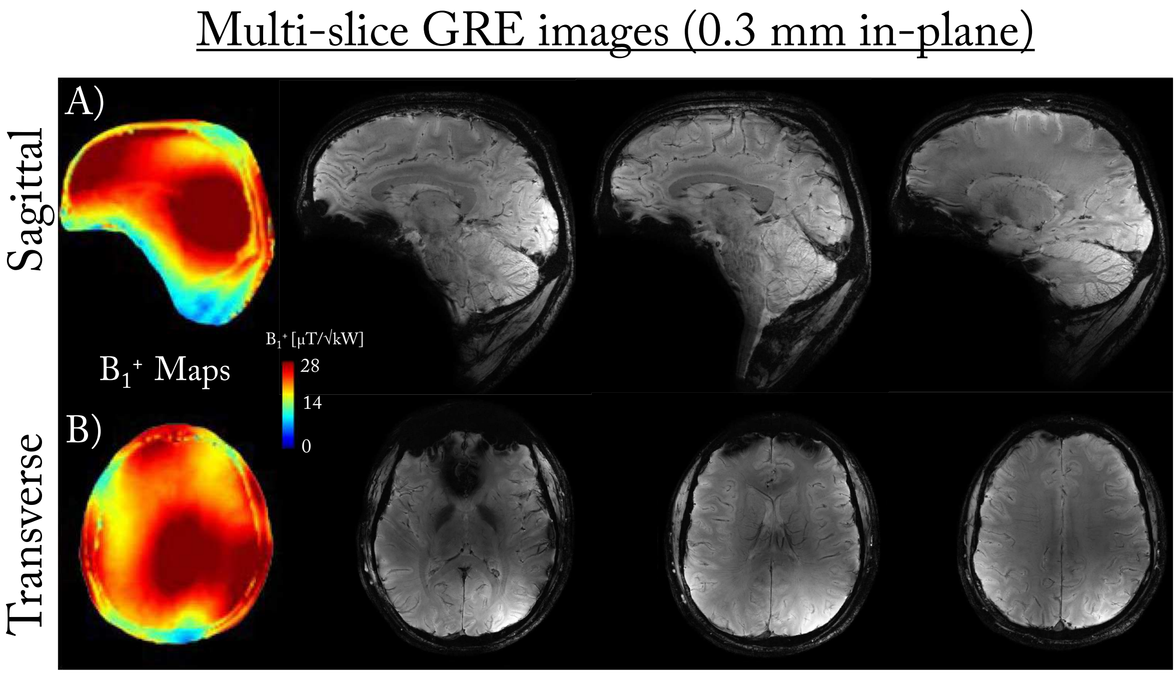

Figure 2.9: *RF phase-shimmed B_1^+ maps, normalized to 1 kW input power per channel, and high-resolution GRE images (0.3 x 0.3 mm^2 in plane) for RF phases optimized in A) sagittal and B) transverse planes. No post-processing correction was applied.*

way that dipole 3 and 4 were placed close to the cerebellum with a length of 220 mm. This might result in lower power input demand and consequently lower $SAR_{10g,max}$ values in the favor of the dipole array to achieve similar homogeneity. Notably, a 20% voltage input difference was measured in the cerebral and cerebellar regions to get a 90° flip angle with the dipole coil array. MR spectroscopy in cerebellum could greatly benefit from this result, as the power demand is usually higher compared to other MR applications. In comparison with the dipole coil array, a commercial single channel transmit/32-channel receive head coil (Nova Medical, USA) excited homogeneously the cerebral cortex with lower SAR restrictions. However, in the cerebellum region, the Nova coil demonstrated a clear lack of signal (Figure 2.11).

The dipole coil array demonstrated the capability to cover simultaneously the cerebral and cerebellar regions in MR images. Therefore, both areas could be investigated in a single MR session without mechanical adjustments of the coil array. The transmit field efficiency reached by the dipole coil array competes with previously reported coil arrays at 7T [53–55, 57] (within a 20% range) at the center of the brain. However, most of the 8-channel single-row coil arrays could not provide together whole-brain coverage and sufficient transmit field [44, 55], especially in the region of the cerebellum. Recently, a close fitting single-row coil array built with loop coils, was shown at 9.4T [104]. At similar B_1^+ efficiency at

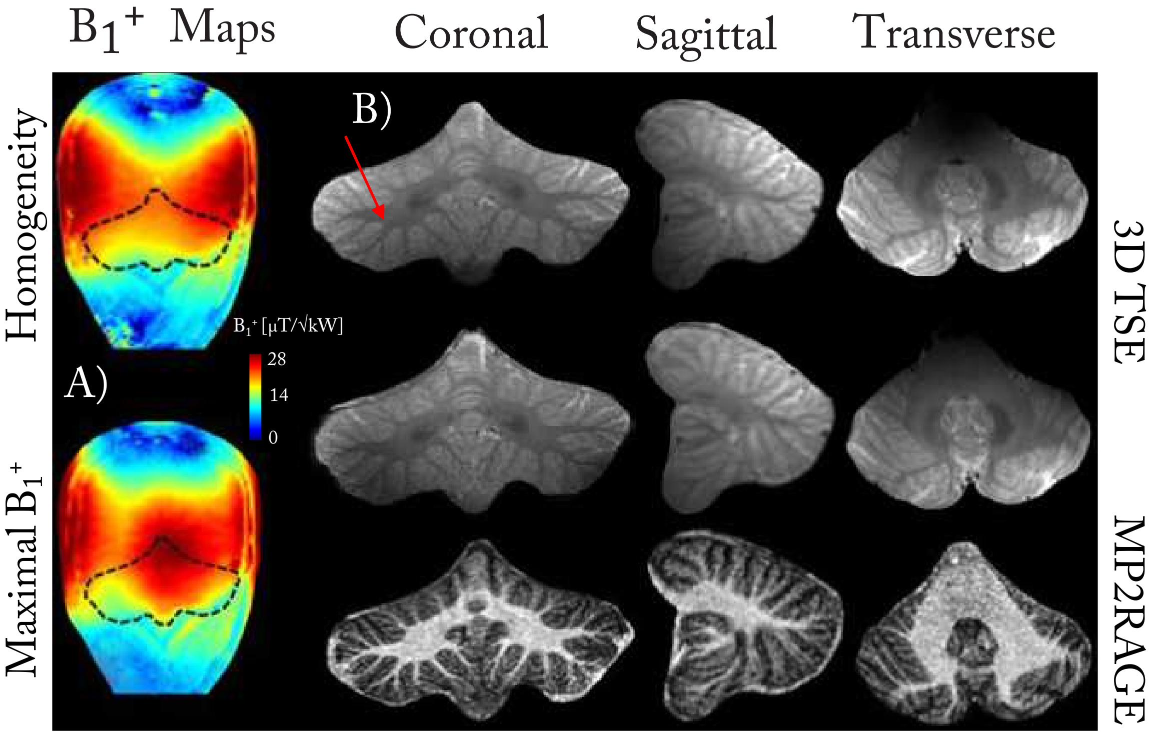
B_1^+ Maps
Coronal
Sagittal
Transverse
Homogeneity
Maximal B_1^+
A)
B)
B_1^+ [μT/√kW]
28
14
0
3D TSE
MP2RAGE

Figure 2.10: *A) Experimentally measured RF phase-shimmed* B_1^+ *maps, normalized to 1 kW input power per channel for the homogeneous and maximal* B_1^+ *cost functions. The cerebellum position is indicated for information (dashed black line) B) High-resolution 3D TSE images (0.8 x 0.8 x 0.8* mm^3*) and MP2RAGE (0.6 x 0.6 x 0.6* mm^3*) images displayed in coronal, sagittal and transverse orientations for the RF phases applied in A). The red arrow indicates the local improvement in signal homogeneity achieved with the homogeneous cost function. No post-processing correction was applied.*

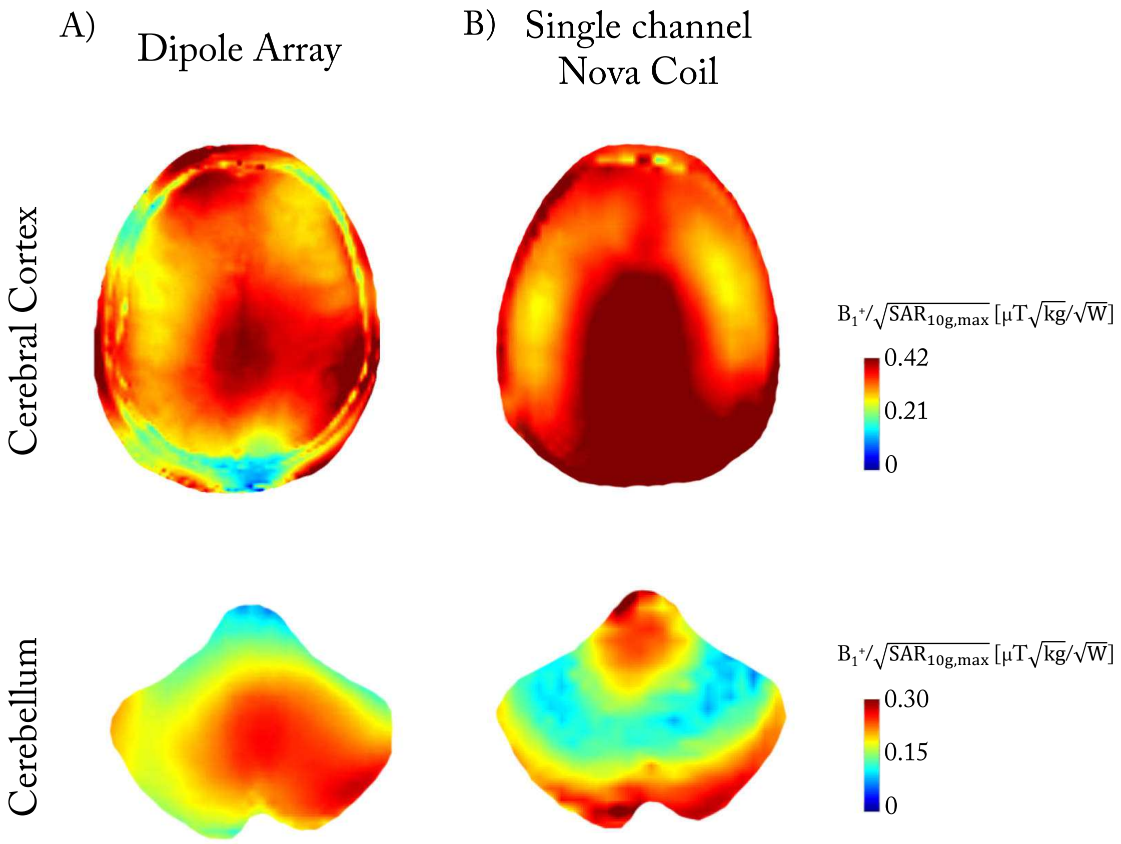
A)
Dipole Array
B)
Single channel
Nova Coil
Cerebral Cortex
Cerebellum
B1+/√SAR10g,max [μT√kg/√W]
0.42
0.21
0
B1+/√SAR10g,max [μT√kg/√W]
0.30
0.15
0

Figure 2.11: *A) Experimentally measured* B_1^+ / $\sqrt{SAR_{10g,max}}$ *maps in midbrain slice (transverse, upper row) and mid-cerebellum slice (transverse, bottom row) for: A) the dipole coil array with RF phases optimized over whole-brain and for maximal* B_1^+*-field in the cerebellum. B) a single channel birdcage coil (Nova Medical, USA).*

the cerebral cortex, the dipole coil array demonstrated a slightly higher $SAR_{10g,max}$ which lead to 17% lower $B_{1,mean}^{+}/\sqrt{SAR_{10g,max}}$ value. However, while the $SAR_{10g,max}$ value was observed in the brain for the dipole array, it is difficult to avoid the $SAR_{10g,max}$ value close to the eyes for the loop array due to the conformal placement of the loops around the head. Moreover, a clear lack of signal could be observed in the cerebellum with this loop coil array. Therefore, 2 x 8 channels, distributed on two rows might lead to increased B_1^+ efficiency beyond the cerebral cortex [44, 76]. In this study, we showed that the whole-brain coverage was achieved by the single row center-shortened dipoles and frontal loops coil array. However, even though good homogeneity could be achieved over relatively small regions, an asymmetric transmit field distribution was observed over larger areas such as whole cerebral cortex (Fig. 2.7A). While phase-only RF shimming might be limited to optimize the homogeneity over large regions, other techniques such as strongly modulating pulses [105] or k_T-points could be used [106, 107].

Using decoupling dipoles is an useful method to decouple the close-fitting dipoles around the human head. A simple design of dipoles, tuned to the Larmor frequency with an inductor only enables decoupling of the dipoles in the array mostly lower than -20 dB in comparison to the decoupling value of -10 dB if no decoupling dipoles are present. Moreover, no decreased transmit field efficiency was observed in RF shimmed B_1^+ maps acquired with and without the DecDs. However, in the simulation model including the DecDs, the dipoles 2, 3 and 4 exhibited lower decoupling values compared to the measurements, which might be due to the absence of components (RF cables and baluns) and material losses in the simulated model. It also appeared in both the simulations and measured transmit field maps that despite a symmetrical placement of the dipoles, the dipole 1 is more affected by its closest loop (loop 1) than dipole 6 by loop 2. This behavior might be induced by a different field polarization from the dipoles placed either on left or right side of the head, but this needs to be further investigated.

As a fractionated dipole shows higher $B_1^+/\sqrt{SAR_{10g,max}}$ level compared to a center-shortened dipole at the depth of 5 cm and further [97], it might be preferable to build coil arrays using fractionated dipoles. However, it appears that for close-fitted brain coil arrays this statement might not apply. The head size being considerably smaller compared to body regions, it requires a much tighter placement of the coil array elements. With our coil array design, even though the single fractionated dipoles in the array yielded lower SAR_{10g} levels compared to the center-shortened dipole in the array, the center-shortened dipole array offered comparable performances and could even perform slightly better in terms of $B_1^+/\sqrt{SAR_{10g,max}}$ ratio depending on the ROI chosen for RF phases optimization. Moreover, individual $B_1^+/\sqrt{SAR_{10g,max}}$ maps did not show significant differences between the center-shortened and fractionated dipoles (Fig. 2.4A).

It might be beneficial to combine the 8-channel whole-brain center-shortened dipoles and frontal loops coil array with a multi receivers loop array to improve SNR and acquisition speed [108, 109]. With the 8-channel dipole array, it might be possible to place e.g 32 independent receive loops between the dipoles and the head without increasing the dipoles' distance to the head or modifying their position. Then, this coil array could be used to perform studies, where timing of the acquisition and SNR are critical [110]. Another potential field of application for this coil array could be in arterial spin labelling (ASL). Introduced in 1992 [111], it aimed to measure the cerebral blood flow during brain activity. However, this method requires a inversion pulse to be applied on the neck region to "label" the inflowing water proton spins in the arterial blood. Thus, high B_1^+ efficiency is required in both brain and neck regions. With the coil array presented here, the idea is to simply replace the dipole 7 (placed on top of the head) by a single loop coil positioned over the neck and uniquely dedicated to apply the inversion pulse required by the ASL method.

2.5 Conclusion

A *robust* and *structurally optimized* seven center-shortened dipoles with frontal loop coils array enabled whole-brain imaging, including cerebellum, with high transmit efficiency and RF homogeneity achieved with only RF phase shimming. The high B_1^+ efficiency achieved in cerebellum, combined with moderate SAR levels, would greatly benefit MR spectroscopy studies in this challenging region and the appreciable phase-only RF shimming qualities could contribute to enhance the robustness of fMRI data, particularly compared to single channel systems when the transmit field is too low. We conclude that the whole-brain center-shortened dipoles and frontal loop coil array represents a valuable contribution to MR applications at 7 Tesla.

3

A combined 32-channel loop coil receive array with a 8-channel transmit dipole array

Adapted from:

Jérémie D. Clément, Rolf Gruetter, Özlem Ipek
A combined 32-channel receive-loops/8-channel transmit-dipoles coil array for whole-brain MR imaging at 7T
Early View - Magnetic Resonance in Medicine, https://doi.org/10.1002/mrm.27808

Jérémie D. Clément designed and built the 8Tx/32Rx RF coil array, contributed to experimental design and performing MR experiments, co-writing the paper.

Abstract

Purpose Multi-channel receive arrays provide high SNR and parallel-imaging capabilities, while transmit-only dipole arrays have been shown to achieve a large coverage of the whole-brain including the cerebellum. The aim of this study was to develop and characterize the performances of a 32-channel receive-only loop array combined with an 8-channel dipole coil array at 7T for the first time.

Methods The 8Tx-dipoles/32Rx-loops coil array was characterized by the SNR, g-factors, noise correlation matrix, accelerated image quality and B_1^+ maps, and compared with a commercial 1Tx-birdcage/32Rx-loops array. Simulated and measured B_1^+ maps were shown for the 8Tx-dipoles/32Rx-loops coil array and compared with the 8Tx/Rx dipole array.

Results The in-house built 32-channel receive coil demonstrated a large longitudinal coverage of the brain, particularly the upper-neck area. G-factors and accelerated MR acquisitions demonstrated robust performances up to R = 4 in 2D, and R = 8 (4x2) in 3D. A 83% increase of SNR was measured over the cerebellum with the in-house built 8Tx/32Rx coil array compared to the commercial 1Tx/32Rx, while similar performances were obtained in the cerebral cortex.

Conclusion The combined 32-channel receive/8-channel transmit coil array demonstrated high transmit-receive performances compared to the commercial receive array at 7T, notably in the cerebellum. We conclude that in combination with parallel transmit capabilities, this coil is particularly suitable for whole-brain MR studies at 7T.

3.1 Introduction

Parallel imaging was originally proposed as a method to combine the high signal-to-noise ratio (SNR) achieved by small surface coils with the large field-of-view (FOV) offered by volume coils [41]. Indeed, in clinical routine (at 1.5T and 3T), the large body volume coils used for the transmit radio-frequency (RF) signal generally lack receive-sensitivity. The simultaneous acquisition of spatial harmonics (SMASH) [112] method made use of the subsequent multiple-receiver signals to enable accelerated image encoding without compromising the SNR. It was followed by the sensitivity encoding (SENSE)[62], and later the generalized auto-calibrating partially parallel acquisitions (GRAPPA)[113] methods, making parallel imaging an important tool for MR applications [114]. However, the accelerated-reconstruction quality is closely related e.g in SENSE to a clear discrimination between the individual profiles of the receive array elements. Therefore, an efficient spatial decoupling is advantageous between the individual receive elements. Two main methods, coil overlapping and preamplifier decoupling are therefore used when building receive arrays. To characterize the noise amplification associated with increasing acceleration rates, g-factor and noise correlation matrix have been defined [62]. Most of the receive arrays consist of 32 channels [69–72], but 64-channel [115, 116] or even 96-channel [117] arrays have been reported at 3T, and have shown an increase in peripheral SNR and increased acceleration capabilities.

While receive arrays are widely used at 1.5T and 3T, there are distinct advantages in applying parallel imaging at ultra-high fields ($\geqslant$ 7T), as the SNR increases with the field strength and the number of coils elements [41, 78, 79]. Therefore, better spectral [80] and spatial resolutions [22] are achieved. However, there are no available full-body coils at ultra-high field since RF homogeneity is compromised by the shorter wavelength [25]. Receive arrays are therefore built within local transmit coils, typically birdcage or transverse electromagnetic (TEM) coils [18, 23, 84, 85] which must be deactivated to avoid interactions between the two coils [118, 119]. However, they demonstrate at ultra-high field a central brightening effect and low transmit field (B_1^+) is commonly observed in the temporal lobes of the brain [25, 86].

Arrays of multiple independent RF coils have been proposed to improve the B_1^+-field through parallel transmit methods [120]. By optimizing the RF phases and amplitudes [89] of in the individual transmit RF coils in the array, constructive B_1^+-field interferences can be generated over the region-of-interest (ROI) and thus improve the homogeneity of the transmit field. For body imaging, dipole antennas demonstrated an advantageous RF signal penetration depth compared to loop coils [12, 58, 121] and were therefore used in transmit array configurations [93, 94, 96, 122]. For brain imaging, the extended longitudinal FOV attained with dipoles enables a complete coverage of the brain, including the cerebellum [15, 59]. However, only 8 to 16 transmit channels are usually available, depending on the RF hardware in the scanner. The SNR levels and parallel imaging capabilities being restrained by this limitation, high-density receive-only arrays are used to significantly enhance SNR and parallel imaging.

To maximize the signal, receive arrays are usually placed as close as possible to the head while the transmit arrays surrounding them have a large diameter [16, 76], because of structural constraints. The constrained space of head-gradient 7T MR systems make the construction of combined (transmit/receive arrays separately) designs highly challenging. Nevertheless, the fine adjustment of the geometry can limit strong interactions between the closely-placed arrays [74]. A recent approach to increase the number of receivers while maintaining a tight configuration consisted in combining a loop coil array with so-called "vertical loops", resulting in a 16-channel transmit/receive with 16 additional receive-only loop coils [123]. However, while higher SNR was measured at center of the brain, the peripheral SNR was lower compared to a 32-channel receive arrray without vertical loops [76, 124]. Using dipoles, the intrinsic low coupling with loop coils could be exploited as in dipole-loop configuration [96] or in combination with receive-only loop coils, as it was shown for cardiac and spine MRI [108, 125]. Nevertheless, while these configurations demonstrated advantageous in-depth receive performances, they were not applied to human brain imaging.
It is advantageous to combine a tight-fitted transmit-only dipole head coil array with a high-density receive-only loop coil array in terms of individual performances of the dipole coil array to cover the whole-brain and of the receive array to improve SNR and acceleration capabilities. However, it is challenging to bring 41-channel independent dipole transmit and receive loop head RF coil array in tight fitting. Moreover, it is still undetermined how the high-density receive-only array would alter the transmit performances of the dipoles. The aim of the present study was, therefore, to design, built and evaluate a 32-channel receive-only loop coil array combined with a tight-fitted dipole head coil array at 7T.

3.2 Methods

3.2.1 Receive Array

The receive coils were arranged on a 3D-printed (EOSINT P395, EOS, Germany) nylon-helmet (EOS, PA2200) designed to accommodate most of the human heads [126]. The maximal dimension in anterior-posterior direction was equal to 222 mm, of 187 mm from left to right and 231 mm in head-foot direction. The 32 receive loop coils were built with silver-platted copper wire, and arranged symmetrically in the left-right direction. To achieve decoupling, neighboring loops were overlapped by approximately 10 mm. Most of the loops were rectangular with their dimensions adjusted according to their position regarding to the transmit array, as each symmetric pairs of dipoles (1 and 6, 2 and 5, 3 and 4) had different lengths, and longitudinal alignment along z-direction. The larger loop coil measured 88 x 60 mm, and the smaller one 68 x 30 mm. Three to four loops were positioned under each dipole with their center aligned with the center-line of the dipoles. To complete the helmet's covering, a few non-rectangular loops were built and placed in-between the others receivers. Particularly, two loops were mounted over the subject's eyes without compromising the visual field.

Non-magnetic fixed-value capacitors (American Technical Ceramics, NY, USA) and two variable capacitors (Philips Components, Netherlands) were used for tuning/matching of the loops. Each loop was divided symmetrically, and the lumped elements were placed such as none of them would fall under the dipoles' legs. One of the variable capacitors was mounted in parallel of the circuit for impedance matching (Figure 3.1C, C_M), and was part of the active detuning circuit, including also a PIN diode (MA4P7470F-1072T; M/A-COM, USA) in series with a hand-wounded inductor (Figure 3.1C, L_1). Together, the capacitor C_M and inductor L_1 formed a parallel resonant circuit tuned at the Larmor frequency when the PIN diode is forward biased via the coaxial cable. This DC-enabled trap prevented current from running on the receive loops during transmit. Nevertheless, a protection fuse (400 Series, $R \approx 0.1950\ \Omega$, Littelfuse, USA) was incorporated in series with each loop coil, in case of failure of the active detuning circuit.

The receive coaxial cables (diameter = 1.3 mm, ODU Inc., USA) were routed such as no cable should pass below the dipoles to avoid interactions (Figure 3.1B). Twelve non-shielded cable traps (1 for 3 cables, and 2 individuals) were added on the path from the loops to the preamplifier board, but placed outside the FOV of the transmit array. Low input-impedance preamplifiers (WMM7RP, WanTcom Inc., USA) were used, and preamplifier decoupling was adjusted by making the length of the coaxial cable to be near a half-wavelength ($\approx$ 34 cm). The low impedance is therefore preserved across the diode D_1 (Figure 3.1C), which completes the resonant LC circuit (Figure 3.1C, L_1 and C_M). The subsequent high series impedance introduced, decreases the currents running on the loops, and therefore reduces the loop coils inductive coupling. All the preamplifiers were placed horizontally on x-z plane and their output was connected to the plugs that fit into the scanner's bed sockets. No additional cable trap was required since the cables from the plugs were positioned largely outside the FOV of the transmit array.

The 32 loop coils ($Q_{unl}/Q_{load} \approx 5.5$ for an isolated receive loop) were tuned and matched on bench using a 4-channel vector network analyser (Agilent Technologies 5071C-ENA Series, USA) with a head-and-neck phantom loading the coil array, and mimicking the tissues properties of the brain (total volume = 3.850L of water, 3% of Agar as gelling agent, 9.35 μL/50 mL of Gadolinium and 9 g/L of salt). While the reflection coefficient (S_{11}) of one loop was adjusted, all the other loops were detuned and their respective preamplifier was connected, and powered. To fine-tune the overlap, the coupling values S_{12} were measured for each loop with respect to the neighbor loops, which were connected to the same plug, by replacing the corresponding preamplifiers with a dummy board. The additional isolation provided by preamplifier decoupling was therefore not included. The transmit coil was

in-place but detuned via the PIN diodes during all these measurements. To estimate the coupling between the two arrays, the S_{12} value was measured between each dipole and the actively-detuned receive loop placed beneath the feeding point of the dipole since it is the most sensitive position in terms of electrical coupling.
A double-pickup probe placed over the receive loops in the array was used to test the active detuning circuit. The S_{12} response curve was measured in the tuned/detuned states to assess the presence of the typical "dip" at Larmor frequency. Similarly, the preamplifier decoupling was tested by comparing the S_{12} response curve with and without the preamplifier in-place.

3.2.2 Transmit Array

The in-house built transmit coil consisted of seven center-shortened dipoles and two frontal loops in quadrature [15]. Dipoles were etched from 35 μm copper (15 mm width) on a FR4 substrate with a thickness of 0.1 mm, and lengths ranging from 158.5 mm to 230 mm. They were geometrically arranged such as the maximal distance between the dipoles and the head was around 17 mm. However, the passive decoupling dipoles were removed from the original design since they could not be detuned and therefore interfered with the receive array adjustments. For the transmit dipoles, PIN diodes were added in series of the tuning/matching circuit to actively detune them during the signal's reception, with the DC current coming through the RF cables (Figure 3.1D). The two transmit loops (95 x 85 mm^2) were placed over the frontal region. A PIN-diode was added in series with an hand-wounded inductor, and connected in parallel of a capacitor in the loop to enable active detuning during receive mode. To decrease the common-modes on coaxial cables, baluns that are quarter-wavelength transformers were added and tuned with capacitors to 297.2 MHz. Tuning/matching to 297.2 MHz and S-parameter matrix measurement were performed using the vector network analyzer.

3.2.3 Electromagnetic field simulations

An accurate model of the in-house built 8Tx/32Rx RF coil array was simulated with the the finite-difference time-domain (FDTD) method on Sim4Life 4.2 (ZMT AG, Switzerland) on a whole body human model, Duke [35].
All transmit coil array's elements (dipoles and loops) were defined as perfect electric conductors (PEC), gridded at 3 mm-iso, and with lumped elements according to the realistic coil design. The Duke model was gridded at 2 mm-iso, and truncated below the torso to decrease the total grid size (80 Mcells). All the transmit coils were driven individually by a Gaussian excitation centered at 297.2 MHz with a 500 MHz bandwidth and computations were carried out on a dedicated GPU (1 x GTX 1080Ti, Nvidia Corp., USA) with an average simulation time of 16 hour per channel for 150 periods of excitation to ensure convergence of the simulation. Transmit coils were tuned and matched to 297.2 MHz at 50 Ohms better

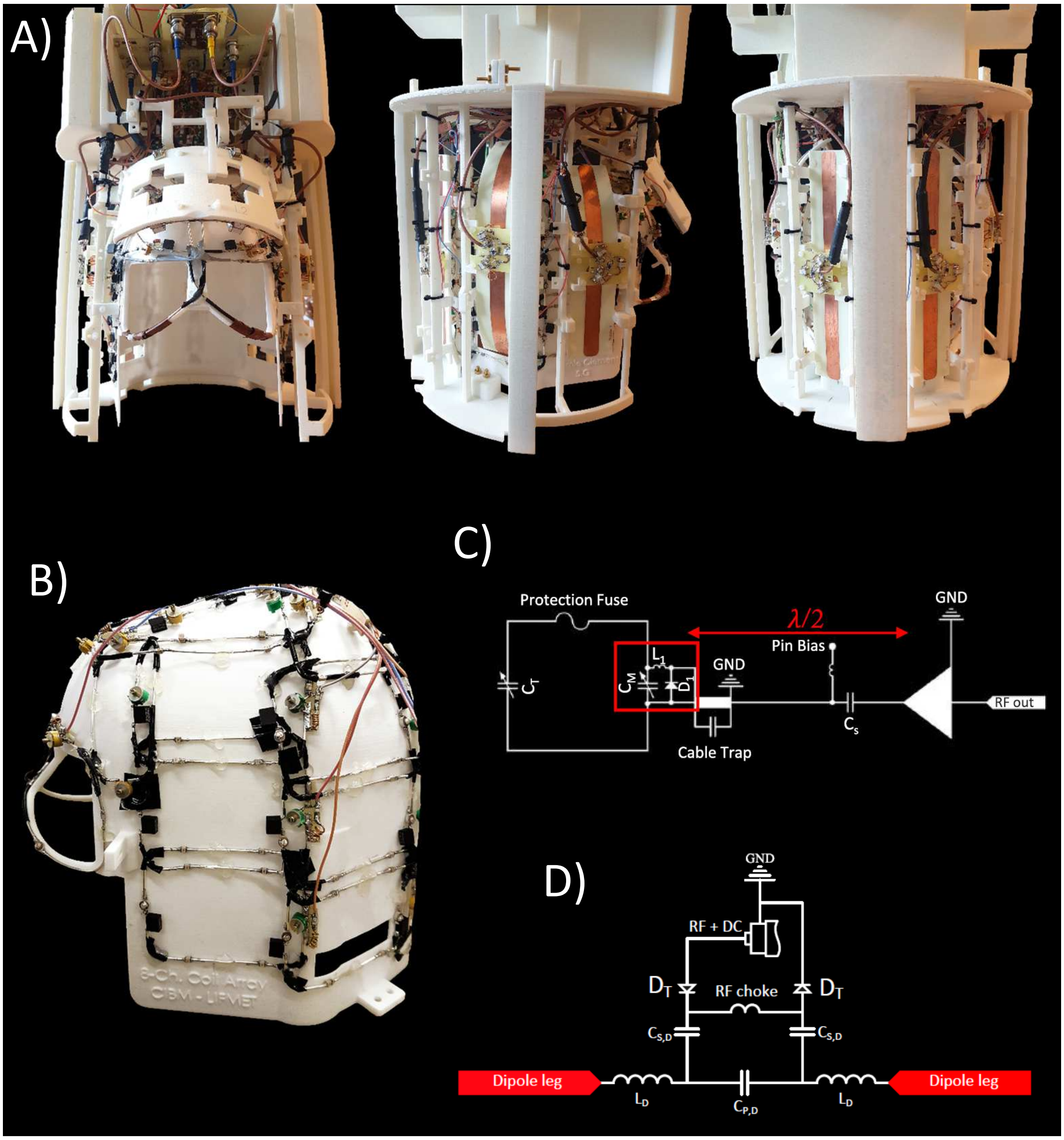
A)
B)
C)
Protection Fuse
$\lambda/2$
GND
Pin Bias
C_T
C_M
L_1
D_1
GND
C_s
RF out
Cable Trap
D)
GND
RF + DC
D_T
RF choke
D_T
$C_{S,D}$
$C_{S,D}$
Dipole leg
L_D
$C_{P,D}$
L_D
Dipole leg

Figure 3.1: *A) Photos of the design showing the transmit and the receive arrays B) Photo of the receive array only C) Schematics of a single receive loop circuit. The active detuning circuit is surrounded in red and consists of the PIN diode* D_1*, the capacitor* C_M*, and the inductor* L_1*. D) Schematics of the transmit dipoles showing the active detuning circuit which consisted in the PIN diodes* D_T *with the RF choke.*

than -15 dB.

The receive loop coils were modeled as wires, and defined as perfect electric conductors (PEC). To ensure an accurate placement of the loops, the 3D model of the helmet was imported into Sim4Life. Each loop was segmented according to the built model and capacitors (6 pF) and fuses ($R \approx 0.2\Omega$) were added. The open-circuit condition was satisfied for the active detuning during the transmit. The PIN diodes, receive coaxial cables, and cable traps were not included in the simulation. The total receive array was gridded at 1.2 mm-iso, and the voxelization was carefully verified such as the loops overlapped without touching each others as in the realistic RF coil array.

The B_1^+ maps were normalized to 1 kW delivered power per channel, and included the transmit losses measured at 37% from the RF amplifiers to the coil plug (Siemens, Erlangen, Germany) and ≈ 13% from the coil plug to the RF coils. SAR_{10g} maps and 10-gram tissue-averaged Q-matrices [29] were evaluated, and the worst-case local SAR value was used for the MR experiments to ensure the subject's safety.

3.2.4 MR Experiments

All the measurements were performed on a 7T Magnetom MR scanner equipped with 8 x 1 kW RF amplifier (Step 2.3, Siemens, Erlangen, Germany) and 32 receive channels on healthy volunteers (2 women and 2 men, mean age = 26 years old) who had signed a written consent approved by the local ethics committee. Phase-only RF shimming was performed using a particle-swarm optimization (PSO) method [100, 101] (see also chapter 4).

Two-dimensional (2D) sagittal (head-foot phase encoding) and transverse (anterior-posterior phase encoding) fully sampled GRE images (1 x 1 mm^2, slice thickness = 1 mm, TR/TE = 1000/3.37 ms, FA = 48°, 192 x 192 matrix) were acquired with the RF phases optimized according to the slice orientation and areas-of-interest. Receive noise correlation matrix was computed from a noise-only scan (no RF excitation). Receive coil sensitivities were estimated from the raw data by dividing the reconstructed signal from each loop with the sum-of-squares of all the receivers. The image was reconstructed in SNR units for no-acceleration [68], including the noise covariance information but without B_1^+-correction. The raw data was under-sampled in post-processing by setting to 0 the lines in k-space, according to the acceleration rate needed, and reconstructed with the SENSE method [62]. The g-factor maps were calculated for the whole FOV, and for acceleration factors of 2, 3, 4, and 5 in left-right (LR) direction for the transverse slice and anterior-posterior (AP) in sagittal, to assess the noise amplification during SENSE reconstruction. Three-dimensional (3D) GRE images (1 x 1 x 1 mm^3, TR/TE = 8/2.34 ms, FA = 10°, 256 x 256 matrix, AP phase encoding) were acquired to evaluate the acceleration performances in two directions. All these results were compared to a commercial single Tx birdcage coil with 32-channel receivers (Nova Medical, USA).

All the B_1^+ maps were acquired with a SA2RAGE sequence for a 500 µs, 90° hard pulse, and normalized to 1 kW peak-power (at the coil plug) per channel [102]. The transmit field maps acquired with the in-house built 8Tx/32Rx coil array were compared to the commercial 1Tx/32Rx coil and to the in-house built 8Tx/8Rx dipole coil array with decoupling dipoles. B_1^+ sensitivities (magnitude and phase) were derived on Matlab from a GRE-based sequence.

Anatomical images RF phases of the individual channels were optimized with the PSO method in central sagittal slice and the RF shimmed B_1^+ maps were measured to evaluate the influence of the receivers. MR images were acquired with the 3D turbo-spin echo (3D-TSE, TE/TR = 120/2000 ms, resolution = 0.8 x 0.8 x 0.8 mm^3, FOV = 210 x 210 mm^2, Turbo Factor = 60, GRAPPA = 2, TA = 10 min 25 s), MP2RAGE (resolution = 0.6 x 0.6 x 0.6 mm^3, FOV = 192 x 192 mm^2, GRAPPA = 3, TA = 10 min 04 s) [75], and multi-slice GRE (TE/TR = 16/1000 ms, resolution = 0.3 x 0.3 x 3 mm^3, FA = 60°, slices = 8, FOV = 210 x 210 mm^2, GRAPPA = 4, TA = 2 min 58 s) sequences.

3.3 Results

The in-house built 32-channel receive array achieved -30 dB isolation between the tuned and actively-detuned states, and -25 dB difference with and without the preamplifiers connected. With the preamplifiers replaced by a dummy board, a maximal coupling value of -10 dB was measured between the in-house built receive loops whose overlap could not be optimized, because of geometrical constraints. With the preamplifiers in-place, sufficient decoupling was achieved between the 32 loops, with a mean and a maximum noise correlation of 6% and 33%, respectively (Figure 3.2A). In comparison, the commercial 1Tx/32Rx coil demonstrated a maximum noise correlation of 47%, and a similar mean value (Figure 2.2B).

When the decoupling dipoles were removed, the dipoles demonstrated an elevated maximum coupling of -9.8 dB compared to the in-house built 8Tx/Rx RF coil array [15], while all the reflections coefficient were below -15 dB (Figure 3.3A). High isolation (better than -35 dB) was measured between the transmit dipoles and the actively-detuned receive loops located beneath the feeding point. For the frontal transmit loops, a -25 dB isolation was measured with the in-house built receivers. No substantial loss in transmit field efficiency (approximately 7%) was measured over a central axial slice with the in-house built 8Tx/32Rx coil array when the decoupling dipoles were removed and the receivers in-place (Figure 3.3B). Moreover, while the overall transmit field distribution patterns were comparable, a slight enhancement of the transmit efficiency was measured in the lower brain and the cerebellum areas (Figure 3.3B). With the commercial 1Tx/32Rx coil array (single-Tx birdcage coil), lower power was required to get a 90° flip angle at center of the brain compared to the in-house

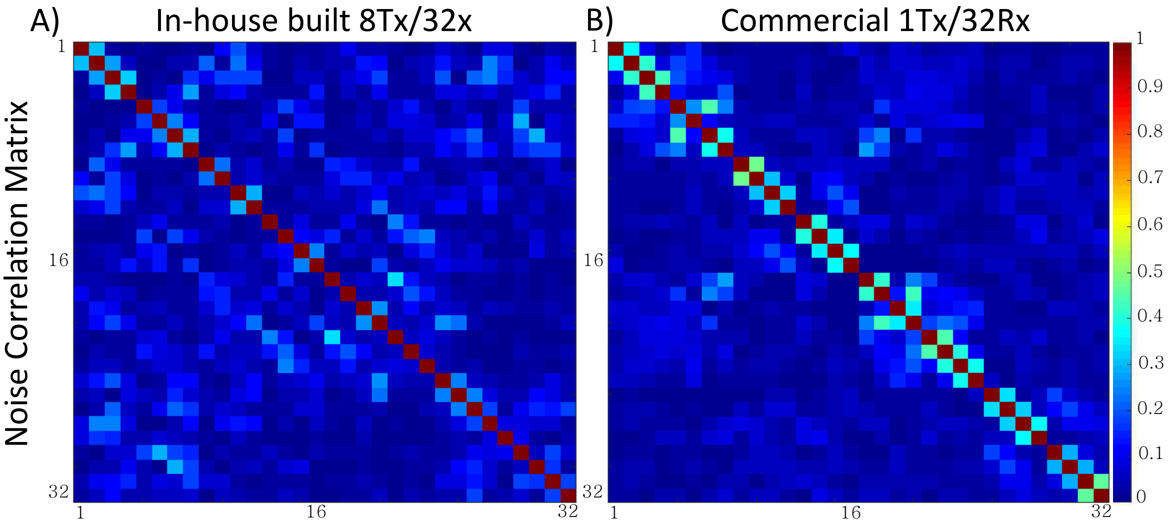

Figure 3.2: *Noise correlation matrices calculated for A) the in-house built 8Tx/32Rx coil array (mean = 6%, max = 33%) and B) the commercial 1Tx/32Rx coil (mean = 6%, max = 47%). The diagonal terms were normalized to 1.*

built 8Tx/32Rx dipole coil array. However, better B_1^+-field homogeneity was achieved with the in-house built 8Tx/32Rx dipole coil array (Figure 3.4).

The transmit field map acquired on the human brain for the RF phases optimized over the cerebellum demonstrated similar pattern compared to the simulated result (Figure 3.5A-B). Even though the reflection coefficients were higher (maximum value of -4 dB), the coupling matrix for the simulated 8Tx/32Rx coil array was comparable to the fabricated RF coil array. The corresponding simulated $SAR_{10g,max}$, normalized to 1W input power was 0.81 W/kg and localized at the back of the head (Figure 3.5C).

The 3D-acquisitions with 8-times (4 x 2) acceleration were without significant alteration of the signal for both the in-house built 8Tx/32Rx coil array and the commercial 1Tx/32Rx coil (Figure 3.6A). Nevertheless, the cerebellum appeared more blurred in sagittal slices with the commercial 1Tx/32Rx coil since the transmit field was low in this area. In transverse slices, the two receive arrays demonstrated similar results with lower signal intensity at the center of the brain (Figure 3.6B). Both coils produced similar mean g-factor values for an acceleration up to R = 4, while the maximal g-factor value was in most cases lower for the commercial 1Tx/32Rx coil (Figure 3.7). At R = 5, the mean g-factor for both coils were increased to approximately 1.65 in sagittal, and 1.55 in transverse slices. Multi-slice high-resolution (0.3 mm^2 in-plane) GRE images were acquired at R = 4, and demonstrated an unaltered signal in cerebral cortex and cerebellum for the in-house built 8Tx/32Rx dipole coil array (Figure 3.8). However, acceleration-related artifacts were observed in the brain stem, where the g-factor values were maximal. The highest SNR values were achieved at the periphery of the brain (Figure 3.7), as expected when using surface loop coils. Mean

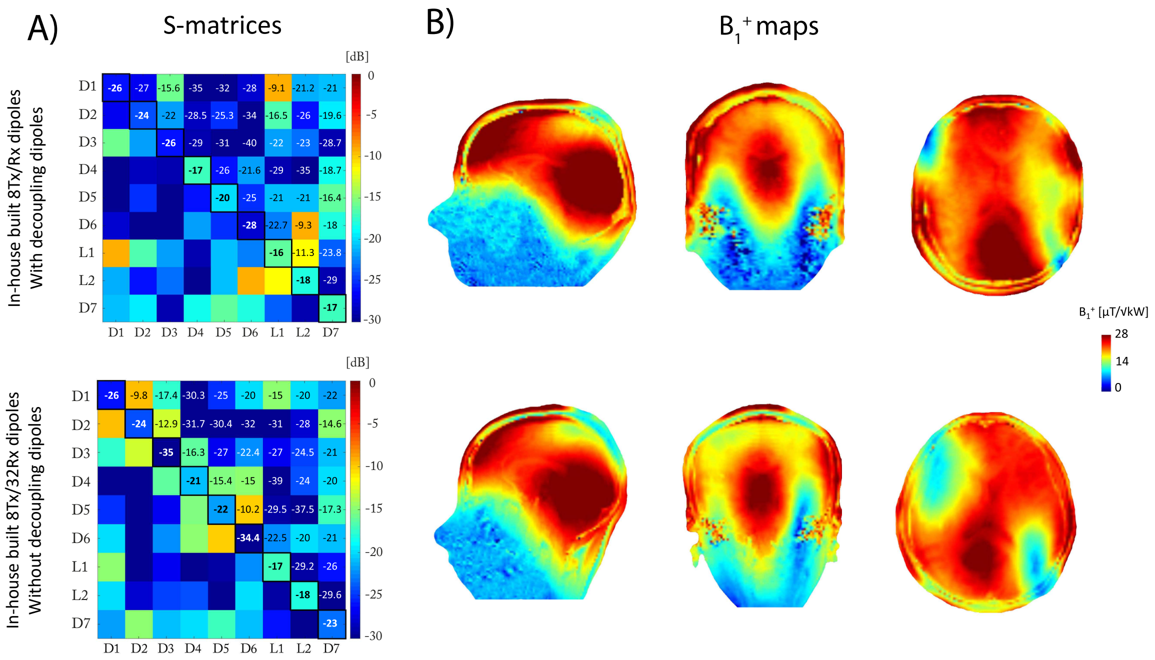

	D1	D2	D3	D4	D5	D6	L1	L2	D7
D1	**-26**	-27	-15.6	-35	-32	-28	-9.1	-21.2	-21
D2		**-24**	-22	-28.5	-25.3	-34	-16.5	-26	-19.6
D3			**-26**	-29	-31	-40	-22	-23	-28.7
D4				**-17**	-26	-21.6	-29	-35	-18.7
D5					**-20**	-25	-21	-21	-16.4
D6						**-28**	-22.7	-9.3	-18
L1							**-16**	-11.3	-23.8
L2								**-18**	-29
D7									**-17**

	D1	D2	D3	D4	D5	D6	L1	L2	D7
D1	**-26**	-9.8	-17.4	-30.3	-25	-20	-15	-20	-22
D2		**-24**	-12.9	-31.7	-30.4	-32	-31	-28	-14.6
D3			**-35**	-16.3	-27	-22.4	-27	-24.5	-21
D4				**-21**	-15.4	-15	-39	-24	-20
D5					**-22**	-10.2	-29.5	-37.5	-17.3
D6						**-34.4**	-22.5	-20	-21
L1							**-17**	-29.2	-26
L2								**-18**	-29.6
D7									**-23**

Figure 3.3: *For the in-house built 8Tx/Rx coil array with decoupling dipoles (upper row) and the in-house built 8Tx/32Rx coil array without the decoupling dipoles (bottom row): A) Scattering matrices measured on the phantom. B) Experimentally measured RF shimmed* B_1^+ *maps on the human brain, for RF phases optimized in sagittal slice, and normalized to 1 kW input peak-power per channel (at coil plug). Two different subjects are shown.*

SNR values of 115 and 104 were measured over the brain in transverse and sagittal slices with the in-house built 8Tx/32Rx coil array. In comparison, the commercial 1Tx/32Rx coil demonstrated similar values (111 in transverse and 90 in sagittal) (Figure 3.7). Over the mid-cerebellum (Figure 3.9), a mean SNR of 121 was measured with the in-house built 8Tx/32Rx coil array, which represents a 83% increase compared to the commercial 1Tx/32Rx (mean SNR of 66).

A high signal homogeneity was observed over the cerebellum in the high-resolution 3D-TSE (0.8 mm^3, Figure 3.10A) and MP2RAGE images (0.6 mm^3, Figure 3.10B). Over the whole-brain, the high-resolution (0.6 mm^3) MP2RAGE images demonstrated the large coverage achieved with the in-house built 8Tx/32Rx (Figure 3.11).

3.4 Discussion

The present study shows for the first time that significant performance improvements were obtained in low-brain SNR and coverage for the combination of a 32-channel receive array with a tight-fitted dipole transmit coil array. The design exploited the placement of 32 receive loop coils on a helmet designed to minimize the distance with the head.

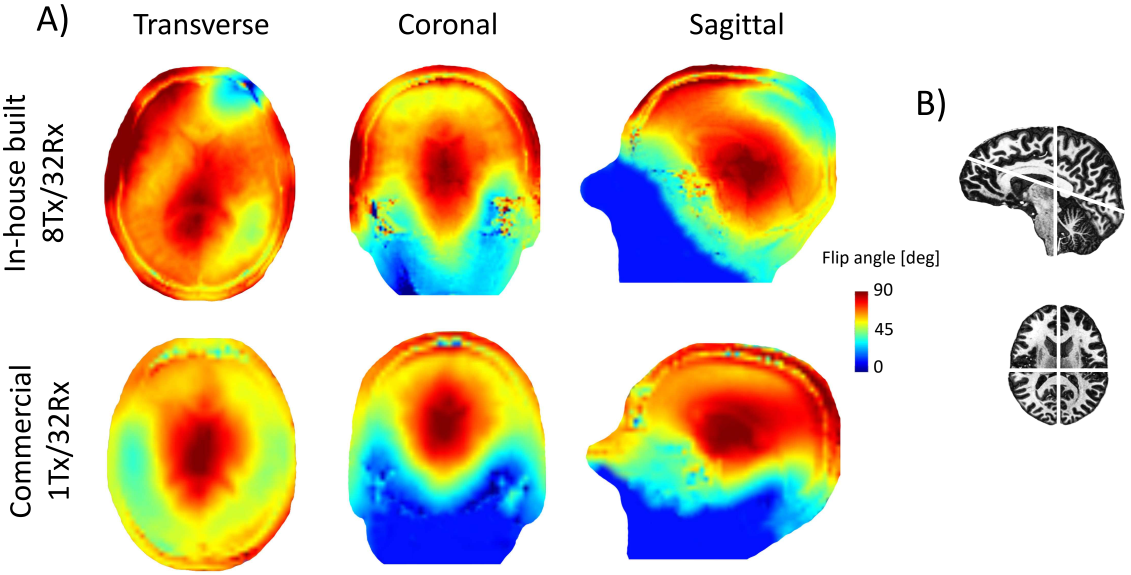

Figure 3.4: *A) Experimentally measured* B_1^+ *maps shown in the three orientations, and normalized to a 90° flip angle at the center of the brain for the in-house built 8Tx/32Rx coil array (upper row) and the commercial 1Tx/32Rx coil (bottom row). The total input voltages were 249V for the in-house built 8Tx/32Rx coil array and 187V for the commercial 1Tx/32Rx coil. For the in-house built 8Tx/32Rx coil array, the RF phases were optimized in transverse slice to cover the whole-brain. The same subject is shown for both coils. Nevertheless, the different fitting of the commercial 1Tx/32Rx coil on the head is responsible for the apparent differences on head's shape in sagittal slice. All measurements were performed within the SAR limits. B) Structural MP2RAGE image (0.6 mm-iso) masked to the brain tissues, and indicating the slices' positions shown in A) (white solid lines). The axial slice was oblique and oriented from the frontal to the occipital lobes.*

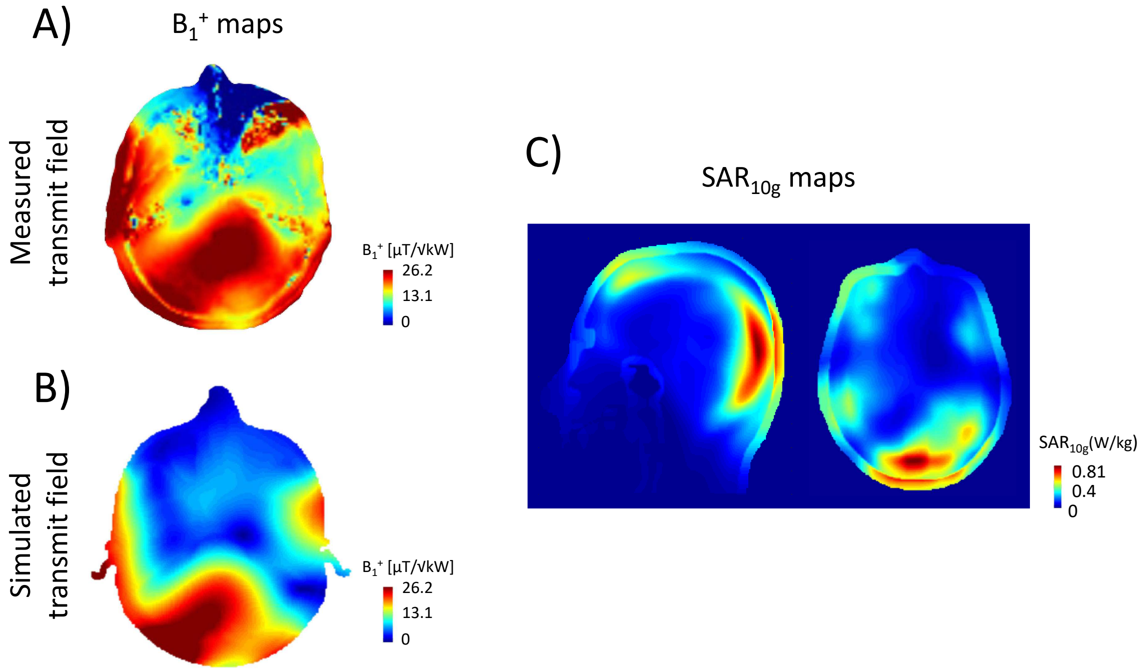
A)
B1+ maps
Measured transmit field
B1+ [µT/√kW]
26.2
13.1
0
B)
Simulated transmit field
B1+ [µT/√kW]
26.2
13.1
0
C)
SAR10g maps
SAR10g(W/kg)
0.81
0.4
0

Figure 3.5: *For the in-house built 8Tx/32Rx dipole coil array - A) Experimentally measured RF phase-shimmed* B_1^+ *map for a mid-transverse slice in the cerebellum, and normalized to 1 kW delivered peak-power per channel at the coil plug. B) Corresponding simulated* B_1^+ *map, normalized to 1 kW delivered (including RF losses) peak-power per channel. C)* SAR_{10g} *maps computed for the RF phases used in B), and normalized to 1W input power. The sagittal and transverse slices are shown at the position of the maximal* SAR_{10g} *value, and scaled to this value.*

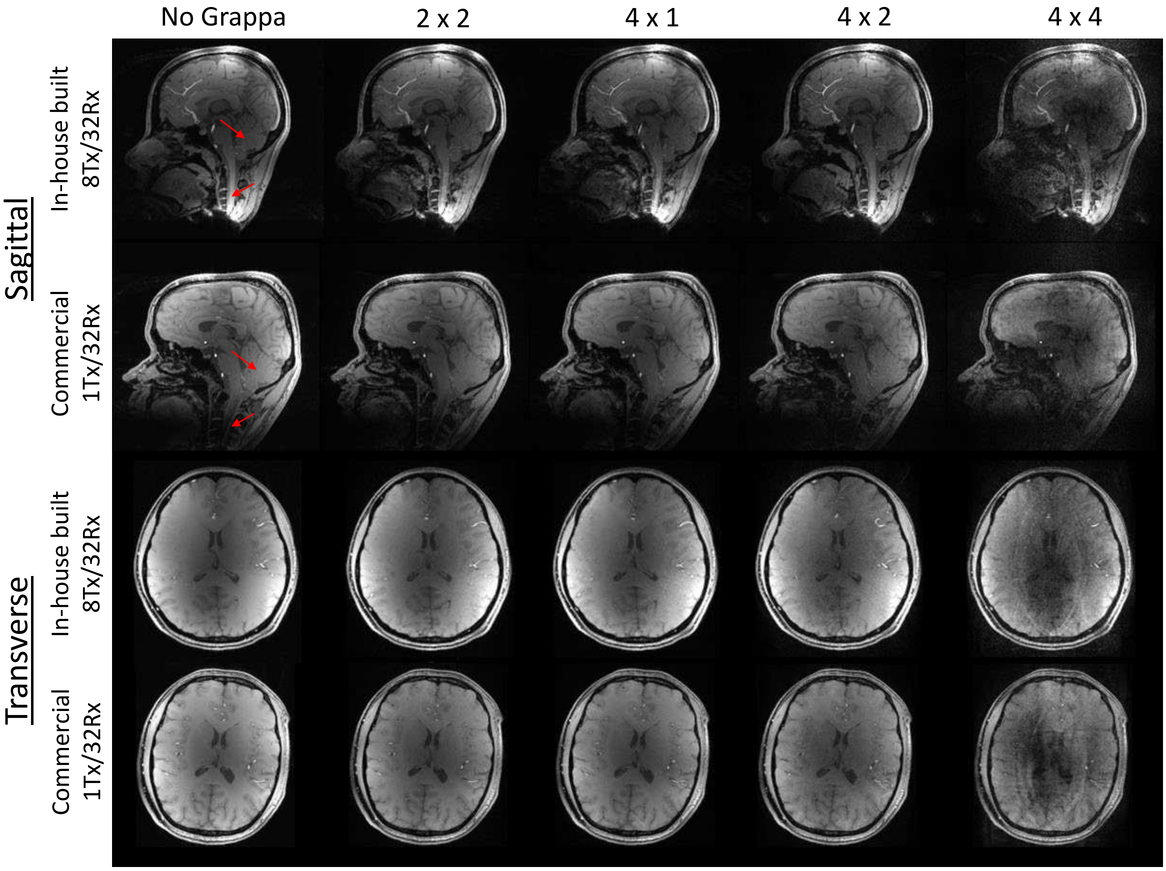
No Grappa
2 x 2
4 x 1
4 x 2
4 x 4
Sagittal
In-house built 8Tx/32Rx
Commercial 1Tx/32Rx
Transverse
In-house built 8Tx/32Rx
Commercial 1Tx/32Rx

Figure 3.6: *3D-GRE images, shown in A) sagittal and B) transverse slices, and acquired at different acceleration factors for the in-house built 8Tx/32Rx coil array and the commercial 1Tx/32Rx coil. The same parameters were used, but two volunteers are shown. The red arrows point to the areas where the signal quality was improved for the in-house built 8Tx/32Rx coil compared to the commercial 1Tx/32Rx coil. The scales were adjusted to display comparable intensities.*

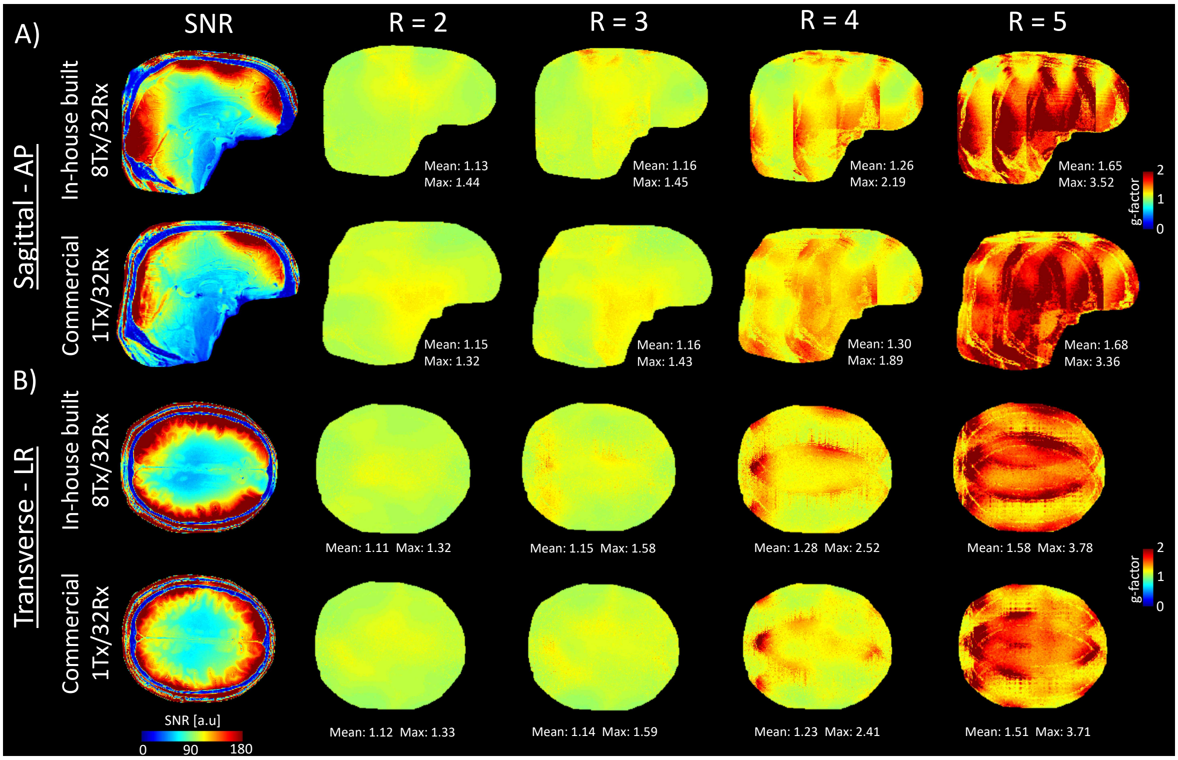
A)
SNR
R = 2
R = 3
R = 4
R = 5
Sagittal - AP
In-house built 8Tx/32Rx
Mean: 1.13 Max: 1.44
Mean: 1.16 Max: 1.45
Mean: 1.26 Max: 2.19
Mean: 1.65 Max: 3.52
g-factor
2
1
0
Commercial 1Tx/32Rx
Mean: 1.15 Max: 1.32
Mean: 1.16 Max: 1.43
Mean: 1.30 Max: 1.89
Mean: 1.68 Max: 3.36
B)
Transverse - LR
In-house built 8Tx/32Rx
Mean: 1.11 Max: 1.32
Mean: 1.15 Max: 1.58
Mean: 1.28 Max: 2.52
Mean: 1.58 Max: 3.78
g-factor
2
1
0
Commercial 1Tx/32Rx
SNR [a.u]
0
90
180
Mean: 1.12 Max: 1.33
Mean: 1.14 Max: 1.59
Mean: 1.23 Max: 2.41
Mean: 1.51 Max: 3.71

Figure 3.7: *SNR and g-factor maps, for the in-house built 8Tx/32Rx coil array and the commercial 1Tx/32Rx coil in A) sagittal (different volunteers with comparable head shape and size) and B) transverse slices. The g-factor maps were computed at R = 2, 3, 4 and 5 in anterior-posterior direction for the sagittal slice and in left-right direction for the transverse slice. The RF phases were optimized for A) in the sagittal slice and B) in the transverse slice.*

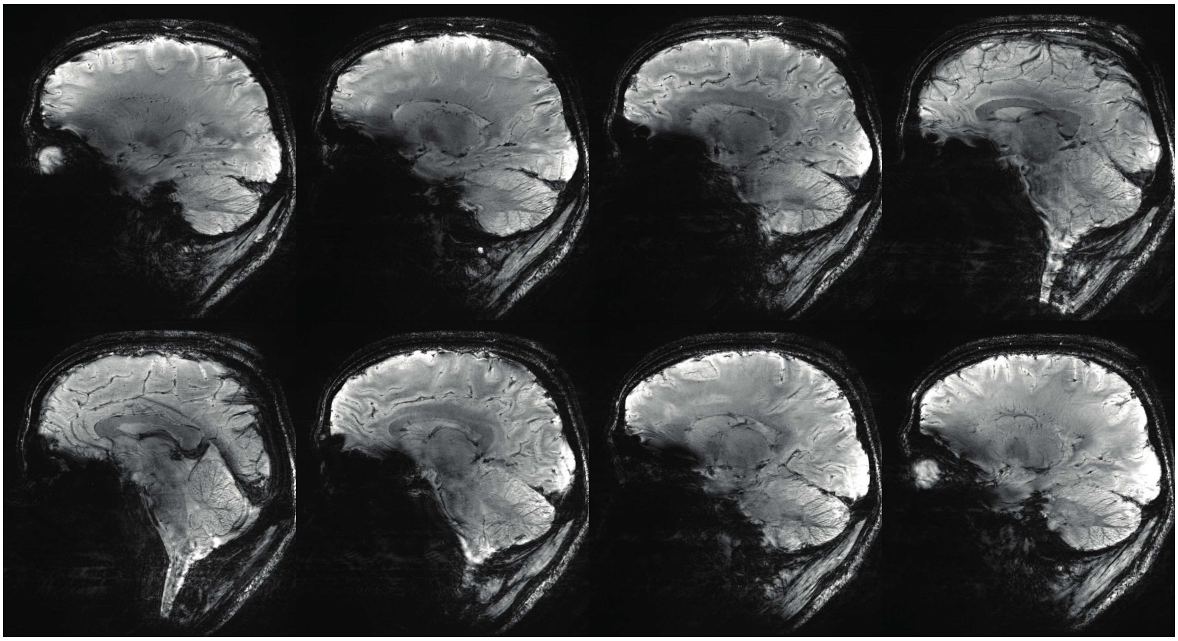

Figure 3.8: *High-resolution (0.3 x 0.3 mm^2) multi-slice GRE images acquired at R = 4, shown for the in-house built 8Tx/32Rx coil array. No post-processing correction was applied.*

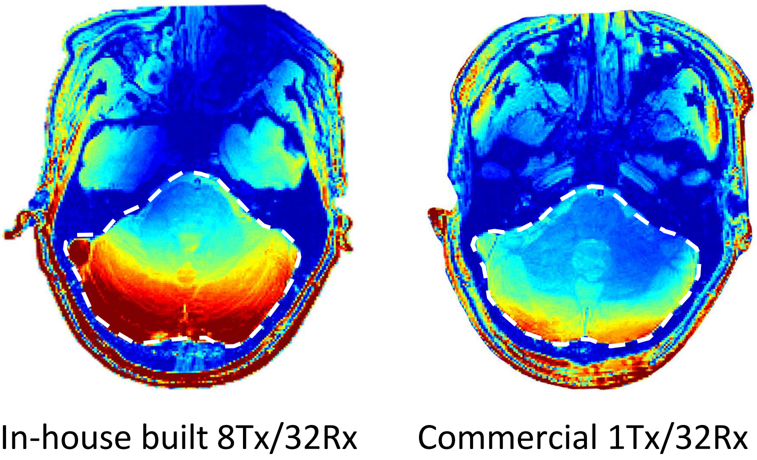

Figure 3.9: *Measured SNR maps for the in-house built 8Tx/32Rx coil array and the commercial 1Tx/32Rx coil in mid-cerebellum slice. The mean SNR value was calculated over the white-dashed area, for RF phases optimized in the cerebellum.*

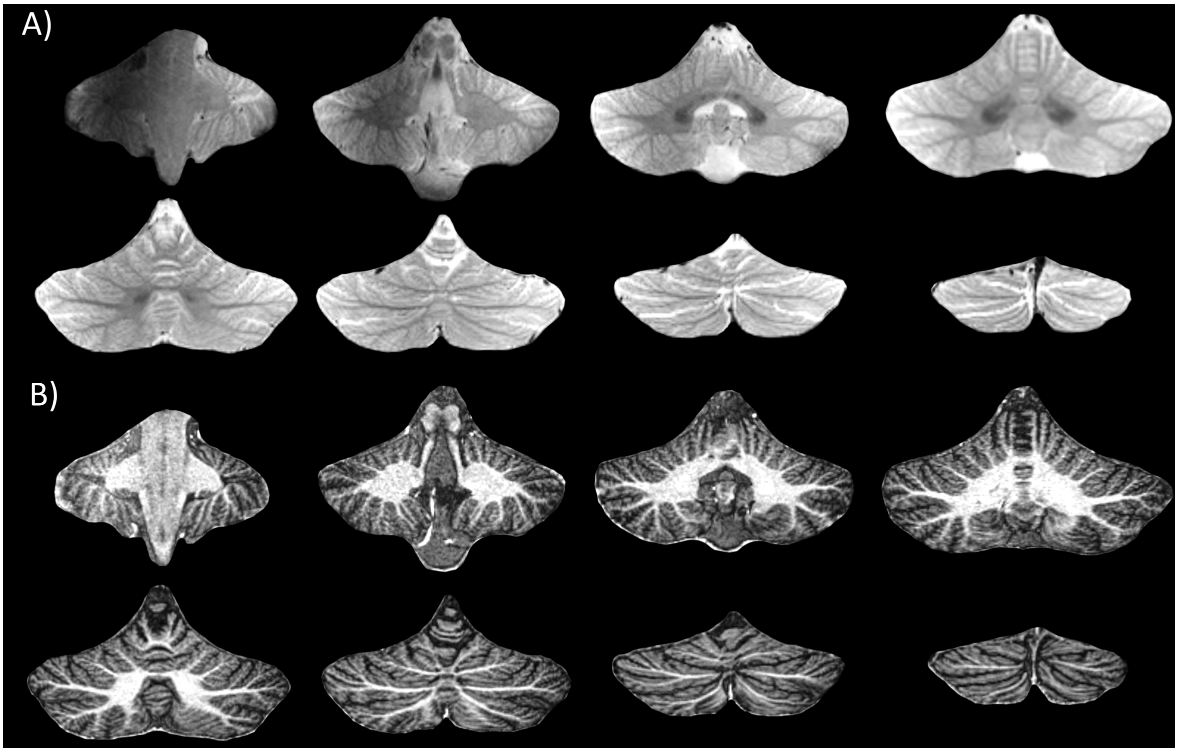

Figure 3.10: *For the in-house built 8Tx/32Rx coil array - A) High-resolution 3D TSE images (0.8 x 0.8 x 0.8 mm^3) and MP2RAGE (0.6 x 0.6 x 0.6 mm^3) images of the cerebellum displayed for 8 coronal slices, and for the RF phases applied in Figure 2.8A. No post-processing correction was applied.*

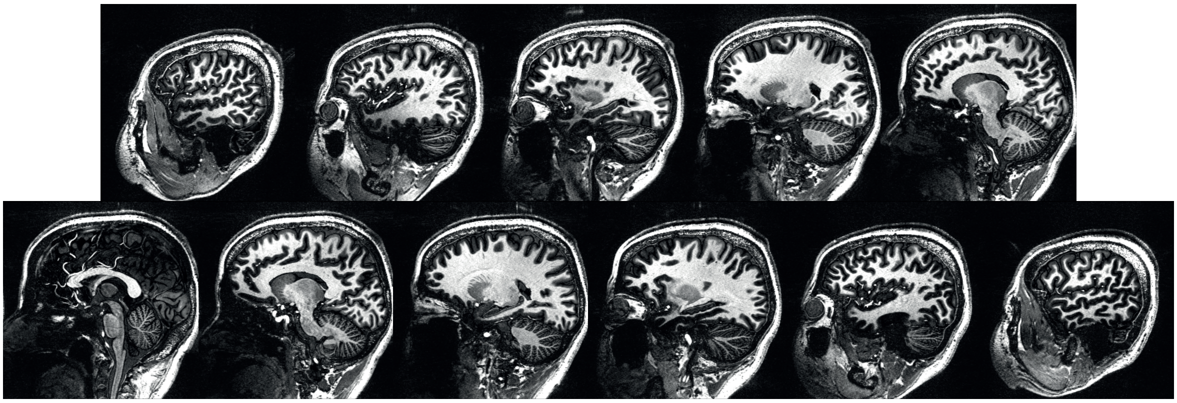

Figure 3.11: *High-resolution (0.6 x 0.6 x 0.6 mm^3) MP2RAGE images acquired with the in-house built 8Tx/32Rx coil array, and shown for sagittal slices taken each 9.6 mm, and covering the whole-brain. No post-processing correction was applied.*

The placement of 32-channel independent receivers contributed to enhance the signal in low-brain and cerebellar regions. Indeed, while the position of the dipoles was optimized to maximize both the transmit field and coverage of the brain, the multi-receivers could be centered over more local areas. The brain stem was e.g homogeneously covered with high SNR in the MP2RAGE results (Figure 3.11). For optimized RF phases in the mid-cerebellum slice, the SNR gain was clearly demonstrated compared to the commercial 1Tx/32Rx coil (Figure 3.9), which could improve e.g MR of the cerebellum. The 3D-GRE images demonstrated a well detailed cerebellum with the in-house built 8Tx/32Rx coil array while the tissue's contrast was altered for the commercial 1Tx/32Rx coil due to the lack of transmit field (Figure 3.6).

The low noise correlation coefficients achieved with the in-house built 32-channel receive array demonstrated an efficient decoupling of the loops. However, these values include the additional isolation provided by preamplifier decoupling, and not only the overlap efficiency. The commercial 1Tx/32Rx coil demonstrated in comparison increased noise coefficients between neighbors with a maximal coupling 48% stronger than the in-house built 8Tx/32Rx coil array. Both coils produced nevertheless a similar mean noise correlation value, lower than 32-channel receive arrays previously reported at 7T [127–129]. Signal quality was essentially preserved in accelerated 3D-GRE acquisitions up to R = 8 (4 x 2 in AP direction). A slight increase in SNR was observed at the top of the head and in the occipital lobe with the in-house built 8Tx/32Rx coil compared to the commercial 1Tx/32Rx coil, while comparable SNR value was measured at the middle of the brain. In future developments, the transmit dipoles could be included as combined or multiple receivers since their current distribution pattern was shown to be advantageous for in-depth SNR performances at ultra-high fields [77].
The g-factors appeared to be relatively insensitive to the direction of acceleration, as the

mean values were comparable in transverse and sagittal slices. However, in sagittal slice the g-factor achieved with the in-house built 8Tx/32Rx was impaired by a sub-optimal overlap efficiency due to the geometrical constraints of the design. Consequently, higher peak values were measured compared to the commercial 1Tx/32Rx coil at all acceleration rates.

The transmit field distribution was not significantly modified and the B_1^+ efficiency was only slightly decreased (by approximately 7%) compared to the in-house built 8Tx/Rx dipole coil array with decoupling dipoles. Moreover, the modified coupling values between the dipoles when the decoupling method was removed may have contributed to the enhancements observed in the cerebellum. The adequate placement of the receivers and the efficient decoupling between the two arrays could be assessed since no shielding effect or transmit field cancellations were observed. It is therefore of utmost importance to carefully align the receive loops with the dipoles such as the active-detuning circuit is distant from the dipole's feeding point when designing equivalent coil arrays. Similarly, no lumped element should be positioned under the dipoles. While the multi-receivers can locally improve the signal quality in low-field areas, larger inhomogeneities may be visible. Phase-only RF shimming being limited to optimize the homogeneity over large regions, other techniques such as the recently-proposed universal pulses, kt-points or spiral non-selective RF pulses could be used [106, 107, 130, 131]. The field of applications of the in-house built 8Tx/32Rx coil array could therefore be extended to others MR experiments such as functional MRI.

No significant differences were observed in terms of transmit field intensity and distribution with the simulated 8Tx/32Rx dipole coil array compared to the simulation model not including the receivers. This is consistent with the experimental results. The SAR_{10g} levels calculated e.g for optimized RF phases in the cerebellum were moderate given the high intensity and homogeneity of the transmit field which was achieved.

3.5 Conclusion

The combined 8-channel dipole coil array with a 32-channel receive-only loop coil array was investigated and demonstrated high transmit/receive properties over the whole-brain. Moreover, the coil dimensions were compatible with head-only MR systems. Parallel imaging and SNR performances were compared to a commercial 1Tx/32Rx coil. While both coils produced comparable SNR at the periphery of the cerebral cortex, the in-house built 8Tx/32Rx coil array demonstrated superior results in the low-brain and cerebellum regions. We conclude that these properties combined to the parallel transmit capabilities make this coil particularly suitable for whole-brain MR studies at 7T.

4

Particle-swarm algorithm for RF phases optimization at 7T

Dumb parts, properly connected into a swarm, yield smart results.
Kevin Kelly

Adapted from:

Jérémie D. Clément, Rolf Gruetter, Özlem Ipek
Comparison of passive RF Phase Shimming Methods on the Human Brain at 7T Using Particle-Swarm Optimization
Proceedings of the 33^{rd} Annual Meeting of ESMRMB, Austria, 2015 (503)

Jérémie D. Clément implemented the existing particle-swarm algorithm for RF phase shimming, contributed to experimental design and performing MR experiments, co-writing the abstract.

Abstract

Purpose At ultra-high field ($\geqslant$ 7T), transmit field inhomogeneities represent a challenge for an efficient coverage of the brain. Multi-channel transmit coil arrays have been shown to address these challenges, when combined with RF phase optimization of the individual channels. The aim of this study was to implement and evaluate the performances of the particle-swarm algorithm in optimizing the RF phases for a multi-channel dipole coil array at 7T.

Methods The particle-swarm algorithm was defined for a cost-function optimizing both the transmit field intensity and homogeneity over large regions of the human brain. The ability to optimize the RF phases over the whole-brain and the robustness of the algorithm across multiple subjects were evaluated. A comparison with the mean method, which relies on a mathematical approach instead of algorithmic, was done.

Results The RF shimmed B_1^+ maps measured for RF phases optimized with the particle-swarm algorithm demonstrated a complete coverage of the brain. Moreover, the RF phases could be determined once for all on a reference subject, and therefore applied to other subjects without loss of transmit field efficiency. Whole-brain coverage could not be achieved with the mean method. Nevertheless, over small areas, the particle-swarm algorithm and the mean method demonstrated similar results.

Conclusion Over large areas such as whole-brain, the particle-swarm algorithm outperformed the mean method. Moreover, the optimized RF phases could be applied indiscriminately of the subjects placed inside the coil array. With a convergence time shorter than 20s, this approach is well suited for real-time calculation during an MR session. We conclude that particle-swarm optimization is a valuable approach for a transmit-efficient RF phase shimming over the whole-brain at 7T.

4.1 Introduction

At ultra-high field, the destructive interferences induce B_1^+-field inhomogeneities and constitute a challenge for MR imaging. One approach to address these challenges is to manipulate the initial RF phases to favor constructive interferences, which lead to significant enhancements of the B_1^+-field [89]. An other way to proceed is using RF spokes [132], which basically consist in using slice-selective RF pulses (with specific gradient shapes) to achieve an homogeneous excitation in 2D. For both methods, the optimization procedure can be performed using either algebraic operations [55, 89] or with numerical algorithms [133]. RF phases could be e.g optimized for both the transmit field efficiency and RF power deposition using an eigenvalue method [134].

However, while the algebraic approach is usually fast and produces always the best solution, the complexity of the operations is increased when the optimization includes nonlinear problems with multiple constraints. Therefore, it may be more appropriate to use numerical algorithms. The global aim remains to optimize the RF weights for the individual transmit elements. However, some additional parameters can be incorporated. For example, Beqiri et al. [135] included RF pulse duration in the optimization procedure, using a derivative-free method whose benefit is to optimize non-smooth cost functions. In 2008, Setsompop et al. [133] used the golden-section algorithm in which an optimal solution is found by successively narrowing the range of values in which the extremum is known to exist. The gradient waveform was optimized to produce a spatially uniform flip angle distribution using a multi-channel coil array at 7T. The interior-point algorithm was proposed by Santini et al. [136], with the benefit of fast convergence but with the risk of finding local optimum solution. In 2011, Tang et al. used a combined gradient-based and genetic algorithms to add RF power absorption optimization to the goodness assessment of the RF weights. Gradient-based algorithms compute the gradient of the cost function at each iteration to determine the next search direction. They generally result in a rapid convergence with a clear criterion. Indeed, when the gradient magnitude is significantly reduced, at least a local optimum is certainly reached [137]. The risk to find a local rather than a global optimum is more pronounced when the problem is only slightly constrained, which is the case for RF phases optimization (the system can not be constrained to exclude hypothetical "bad" combinations). The genetic algorithm, first described in 1975 [138] aimed to reflect the process of natural selection where the fittest individuals are selected for reproduction in order to produce offspring of the next generation. Contrary to the gradient-based method, the genetic algorithm is derivative-free and does not make use directly of the cost function. Instead, it gets the cost function's evaluation for a given population spread over the solution space, and proceeds to the natural selection, including mutations, in order to get an efficient solution. The main advantage of such method is that a global optimum is in principle always found. However, the convergence can be slower, especially near to the optimum [137].

An other nature-inspired algorithm, the particle-swarm optimization algorithm was originally described in 1995 by Kennedy and Eberhart [100]. Based on swarm intelligence, it relies on the capability for a socially-linked group of individuals to find the global optimum result to a given problem by exploring a multidimensional space of possible solutions. It was e.g used to adjust the weights to train a feedforward multilayer perceptron neural network (NN) [100]. Compared to a gradient-based method, better performances were obtained with the particle-swarm optimizer. Applied to the electrical engineering field, the method was used to optimize the far-field pattern of a corrugated horn antenna [139, 140] by finely tuning five uncorrelated design parameters (profile, number of corrugation per wavelength etc.). An extensive analysis of all the publications using a PSO optimization was performed by Poli et al. in 2007 [141, 142]. More than 650 published articles were found, making explicitly use of the PSO algorithm for very different applications (26 areas in total) such as the antennas designs, communication networks, engine and motors, financial, neural networks, robotics, or signal processing. This demonstrate the high adaptability of the PSO algorithm to distinct domains.

In MRI, the particle-swarm algorithm was not widely used. To our knowledge, three different applications were reported in the last 10 years. The method was e.g proposed to detect human brain tumors by using a clustering algorithm based on particle-swarm optimization [143]. Each MR samples was assigned to a cluster, and the algorithm evaluated how close the sample was to the others in the cluster to adequately distribute the samples. Thereafter, the particle-swarm optimization was proposed to get the smoothest phase unwrapping by minimizing the total length of branch-cuts [144]. Those branch-cuts connect together the so-called residues, which can be understood as local inconsistencies (starting and end of 2π discontinuities). In 2014, a variant of the particle-swarm algorithm (PSO) named PSO-2S was proposed for brain MRI segmentation [145]. Briefly, the PSO algorithm optimized the parameters (amplitude, mean and variance) of N (known value) gaussian functions in order to best approximate the histogram h(j) of the MR image (i.e the observed probability of gray level j). Therefore, thresholds could be computed to accurately segment the MR images.

Most of the algorithms presented here (golden-section, interior-point etc.) rely on mathematical formulas to guide the optimization towards a maximum. In this sense, it could be compared to a single individual moved by an extraordinary evolved intelligence (to perform complex mathematical operations). In contrary, the particle-swarm optimization belongs to a different kind of methods called *swarm intelligence* in which each individual (or agent) is not very clever by itself (like bees, ants etc.). The agent obeys to very simple instructions and it would take him an infinite time to find a solution if left alone. The social link is what makes the strength of the method. The communication between the individuals (Equation 4.2 is further described later) and the individual/collective memory allows to find solutions for advanced problems. The genetic algoritm (GA) is probably one of the closest to PSO in terms of working principle, even though they belong to distinct categories (swarm intelligence for PSO and evolutionary algorithm for GA). Indeed in both cases a large set of agents is defined, and each individual evolves independently and with the others. However, in GA the strong struggle for high cost-function values drives the new solutions while in PSO novelty is driven by social interactions. These two algorithm were previously compared [146], and while both algorithms could obtain high quality solutions the computational effort required by PSO was largely lower than for GA to solve unconstrained nonlinear problem with continuous design variables. The RF phases optimization clearly corresponds to this kind of problems. However, there was to our knowledge no attempt to characterize the PSO algorithm for RF phases optimization, and further. The purpose of this study was therefore to implement the particle-swarm algorithm into a user-friendly interface, and to compare its performances with the mean-method for whole-brain RF phase shimming, using a multichannel coil array at 7T [101].

4.2 Methods

4.2.1 Particle-swarm algorithm theory

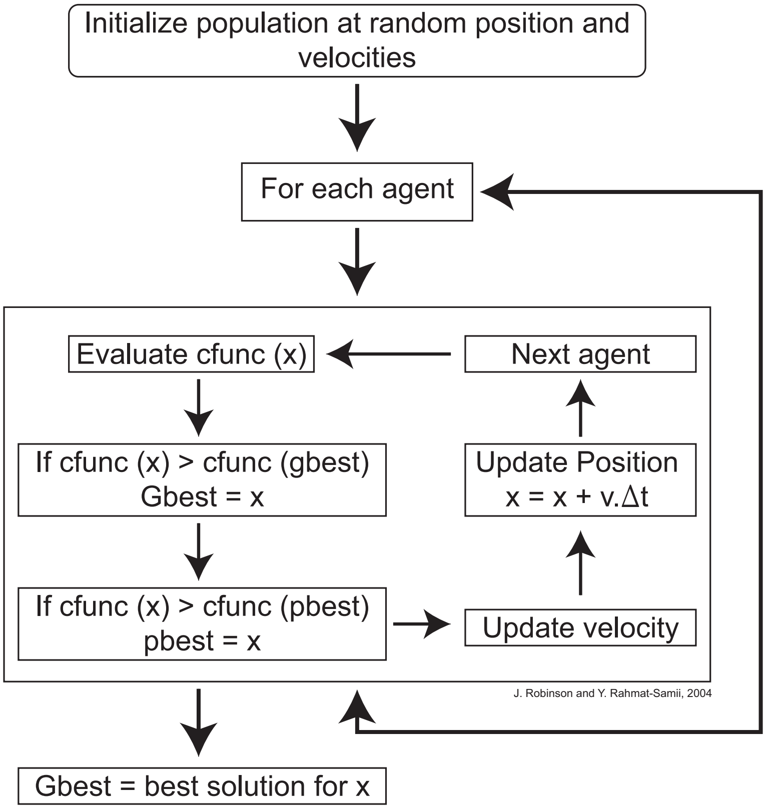
Initialize population at random position and velocities
For each agent
Evaluate cfunc (x)
Next agent
If cfunc (x) > cfunc (gbest)
Gbest = x
Update Position
x = x + v.Δt
If cfunc (x) > cfunc (pbest)
pbest = x
Update velocity
J. Robinson and Y. Rahmat-Samii, 2004
Gbest = best solution for x

Figure 4.1: *Schematic of the PSO algorithm process*

The working principle of the algorithm is given by Figure 4.1. The agent represents the individual unit of the swarm, and at the first step all the agents are given an initial random position and velocity within the space of solutions. The *cfunc* function (cost function) evaluates for each agent of the swarm the goodness of their position according to the user-defined objective, and the best position among all the agents is called *gbest*. Similarly, the *pbest* stands for the individual best position of each agent in the swarm. At each iteration, the position of the agents are updated according to the equation 4.1. The *pbest* and *gbest* results are revised when improvements of the *cfunc* value are found.

$$x = x + v.\Delta t \tag{4.1}$$

In equation 4.1, the updated velocity v represents the core of the algorithm since it determines how fast the optimization is performed. At each iteration, the updated velocity is defined as in equation 4.2.

$$v_{n+1} = w * v_n + c_1 * rand_1() * (p_{best} - x_n) + c_2 * rand_2() * (g_{best} - x_n) \tag{4.2}$$

The term w is called **inertial weight**, and determines to what extent the agent remains along its original course. The c_1 and c_2 parameters, also called **self-adjustment** and **social-adjustment** factors determine how much the agent is influenced by the memory of its best position and by the swarm, respectively. The *rand*$_1$*()* and *rand*$_2$*()* functions return independent values between 0 and 1, and are used to stochastically vary the relative pull of *gbest* and *pbest*. Therefore, to achieve a fast optimization the c_2 parameter has to be increased compared to w and c_1. However, a high value will impair the capability for the swarm to cover a large area of solutions. At the end of a pre-defined number of iterations, or when the global best solution does not vary, the algorithm stops and the *gbest* value corresponds to the solution of the problem.

4.2.2 The Matlab GUI interface for B_1^+ optimization

A user-friendly interface was developed to optimize the RF fields on the parallel transmit system. In this subsection, the different panels of the interface are described (Figure 4.2).

Choose DataSet Transmit magnitude and phase sensitivities of the individual channels are estimated from a 2D-GRE sequence (FA=25deg, TR/TE = 100/10 ms, 2.3 x 2.3 mm^2, slice thickness = 5 mm, matrix = 128 x 128, TA = 1 min 42s) configured to acquire 8 times the slice-of-interest with only one active transmit channel at each time. The resulting raw data size is therefore 128 x 128 x 8 x 8, where the two last numbers stand respectively for the number of transmitters (N) and number of receivers (M). The GRE signal can be described with equation 4.3, where A is proportional to the proton density ρ, $\sin\alpha$ is related to the B_1^+-field

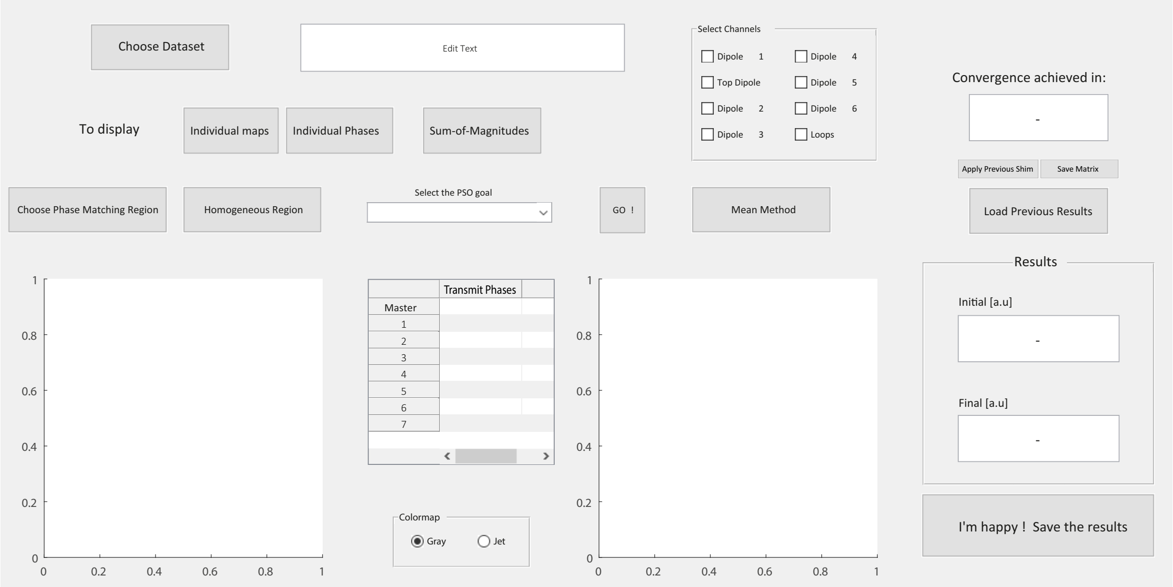
Choose Dataset
Edit Text
Select Channels
☐ Dipole 1
☐ Top Dipole
☐ Dipole 2
☐ Dipole 3
☐ Dipole 4
☐ Dipole 5
☐ Dipole 6
☐ Loops
Convergence achieved in:
-
To display
Individual maps
Individual Phases
Sum-of-Magnitudes
Apply Previous Shim
Save Matrix
Choose Phase Matching Region
Homogeneous Region
Select the PSO goal
GO !
Mean Method
Load Previous Results
Results
Initial [a.u]
-
Final [a.u]
-
Transmit Phases
Master
1
2
3
4
5
6
7
Colormap
● Gray
○ Jet
I'm happy ! Save the results
0
0.2
0.4
0.6
0.8
1

Figure 4.2: *GUI interface developed in Matlab for RF phases optimization*

through the flip angle α (Equation 1.20), and the fractional term corresponds to the evolution of the magnetization which is proportional to the B_1^--field. Therefore, in the low-flip angle approximation ($\leqslant$ 30 degrees), $\sin\alpha \approx \alpha$) and the signal equation can be very simply approximated with equation 4.4. The raw data matrix contains for each voxel/pixel in the image, the combined signal of the three quantities ρ, B_1^+ and B_1^-.

$$S = A\frac{\sin\alpha\left(1 - e^{-TR/T_1}\right)}{\left(1 - (\cos\alpha)e^{-TR/T_1}\right)}e^{-TE/T_2^*} \tag{4.3}$$

$$S(\vec{r}) \approx B_1^+(\vec{r})B_1^-(\vec{r})\rho(\vec{r}) \tag{4.4}$$

As shown in [147], the equation 4.4 can be re-written (Equation 4.5).

$$\mathbf{S} = \rho\mathbf{b}^+\mathbf{b}^{-\mathbf{T}} \tag{4.5}$$

where $\mathbf{b}^+ \equiv \left[B_1^+, B_2^+, ..., B_N^+\right]$ (1 x N matrix) and $\mathbf{b}^- \equiv \left[B_1^-, B_2^-, ..., B_M^+\right]$ (1 x M matrix). The transpose comes from the matrix notation in order to get for each voxel an N x M matrix. To separate the B_1^+ and B_1^- contributions to the signal **S**, a singular-value-decomposition (SVD) is applied to each pixel in the image. Indeed, the SVD can be seen as a generalization to any m x n of the eigen-decomposition, which is a way to represent a matrix in terms of its eigenvalues and eigenvectors. The factorization of a real or complex matrix **S** (m x n) with SVD is described by Equation 4.6.

$$\mathbf{S} = \mathbf{U}\boldsymbol{\Sigma}\mathbf{V}^{*} \tag{4.6}$$

where **U** is an m x m unitary matrix, **Σ** is a diagonal m x n matrix containing the so-called *singular values* of **S**, and **V** is an n x n unitary matrix. Applied to the signal equation, there is in the ideal case (matrix **S** only slightly altered by noise) only one singular value σ_1 and the equation 4.6 can be simplified into the equation 4.7.

$$\mathbf{S} = \mathbf{t}\sigma_1\mathbf{w}^{*} \tag{4.7}$$

where **t** and **w** are respectively the left and right singular vectors associated to the singular value σ_1, and represent the transmit and receive sensitivities for each pixel in the image. From equations 4.5 and 4.7, it follows that:

$$\rho\mathbf{b}^{+}\mathbf{b}^{-^{\mathrm{T}}} = \sigma_1\mathbf{t}\mathbf{w}^{*} \tag{4.8}$$

Since t and **w** are by definition unit length vectors, they represent a normalized version of the $\mathbf{b}^{+}$ and $\mathbf{b}^{-}$ RF fields. To determine with higher accuracy the true B_1^+ and B_1^- fields, a further step is required as described in [147]. Nevertheless, the transmit sensitivities were sufficient to optimize the RF fields in the present work. The transmit sensitivity field for the zero-phase mode (no phase-shifts applied to the individual channels) is therefore computed as the complex sum of the individual maps and displayed in the left window (Figure 4.2). Similarly, the sum-of-magnitudes map is calculated, and corresponds to the best achievable transmit field. The user can also display the individual B_1^+ sensitivities to assess the accuracy of the computation.

Choose Phase Matching Region / Homogeneous Region At this step, the user can define the regions to optimize. The phase matching region corresponds to the area where the algorithm will try to achieve a homogeneous phase distribution across all the channels. The transmit field will therefore be maximized over the selected region. The homogeneous region should be selected such as it includes the phase matching region. The algorithm will aim to homogenize the field distribution in the extended area with respect to the phase matching region.

Select the PSO goal There are two different goals available and called respectively, **Maximal B1** and **Maximal and Homogeneous B1**. The solution space for the algorithm has seven dimensions, each of those corresponding to the phases given to the individual complex transmit field maps. One coil channel is excluded and is defined as a reference, since only relative phases can be calculated. The reference channel corresponds to the transmit element with the maximal mean intensity over the area-of-interest.

The cost function for the maximal B_1^+ optimization is defined in equation 4.9.

$$\text{cost}_{\text{MaximalB1}} = \alpha * \left(1 - \frac{\sum\sum_{i,j} \text{Ratio(i,j)}}{\text{Size}_{\text{ROI}}}\right) * 100 \tag{4.9}$$

The Ratio(i,j) was defined as the ratio between the non-shimmed B_1^+ field over the phase matching region and the sum-of-magnitudes for each pixel in the area. Since the sum-of-magnitudes represents the maximal achievable field, the sum of the ratios is bounded to the size of the ROI. Therefore, by minimizing the equation 4.9, the field is maximized over the area-of-interest. However, this may result in large transmit field inhomogeneities outside the shimmed area. A second equation (Equation 4.10) was therefore implemented, making use of the two different drawn regions.

$$\text{cost}_{\text{DoubleRegion}} = \alpha * \left(1 - \frac{\sum\sum_{i,j} \text{Ratio(i,j)}}{\text{Size}_{\text{ROI}}}\right) * 100 + \beta * \frac{\text{std}(B_{1,\text{totHomo}})}{\min(B_{1,\text{totHomo}})} \tag{4.10}$$

The first term of the equation is same as in equation 4.9, and optimizes the phase match region. The second term is calculated over the homogeneous region, and aims to minimize the standard deviation of the transmit field over the total area (encompassing the phase match region) without impairing the B_1^+ efficiency. The coefficients α and β can be adjusted in the code to balance the two terms of the equation. In our case, the values $\alpha = 1.7$ and $\beta = 2.3$ provided the best results in all the conditions. The equation 4.10 will be further referred as the double-region cost function.

An other approach was proposed by Schmitter et al. [148] to optimize the RF phases over the whole-brain. A single large or small region is selected, and a 2D gaussian function is defined over the area. The method was implemented with the adjustable parameters given in table 4.1 defining the gaussian function.

The standard deviations along x and y directions were determined empirically according to the results obtained when the denominator value α was varied. For a whole-brain shimming on transverse slice, the coefficient α must be $\geqslant 2.7$ to avoid signal voids at the center of the slice. However, over smaller areas or other orientations α can be decreased to unity without compromising the optimized field distribution. The cost function was defined by equation 4.11.

$$\text{cost}_{\text{Gaussian}} = \text{rms}(\mathbf{Ratio} - \mathbf{GaussianExcitation}) \tag{4.11}$$

where **Ratio** and **GaussianExcitation** represent respectively the vectors containing the values for the ratio as defined previously and the gaussian defined by the parameters given in table 4.1. The algorithm will maximize the field at the center of the ROI (where the gaussian function is close to 1) while avoiding the presence of signal voids. The equation 4.11 will be further referred as the gaussian cost function.

Table 4.1: *Available parameters for the 2D-gaussian surface defined over the shimming ROI*

Parameter	Definition	Default Value
x	x-size of the ROI	x
y	y-size of the ROI	y
σ_x	Standard deviation along x-direction	x/α
σ_y	Standard deviation along y-direction	y/α
θ	Rotation angle for the distribution (in degrees)	0
offset	Minimum value in the output	0
factor	Relate to maximum value of output (>0)	1
center	Center position of the gaussian	[0, 0]

Mean method The particle-swarm optimization method was compared to the so-called mean method. In this approach, the shimmed RF phases are determined as the mean value of the phase over the phase matching region. Assuming the phase differences over the ROI are smooth, this results in having an homogeneous phase for each channel, and therefore a maximized B_1^+ field.

Miscellaneous functions The function "Apply Previous Shim" allows the user to apply the RF phases calculated previously on a different data set, independently of the slice orientation or subject. Other tools are available, such as the possibility to select the channels for optimization, or to save the results in a file directly readable by the MR scanner. The "results" windows give the mean value achieved over the phase match region with the corresponding standard deviation to estimate the efficiency of the shimming.

The optimization time was highly dependent on the ROI-size and the selected cost function. Since the in-vivo data was quite small (matrix size 128x128), the area to shim only covered a few pixels. Moreover, the algorithm was implemented such as the processed data was bounded to the area-of-interest. The convergence of the algorithm was therefore achieved in approximately 15s when using the equation 4.9, and 25s with the equation 4.10. The time difference between the two optimization goals can be attributed to the increased area-of-interest used in equation 4.10, and to the larger iteration steps needed to get a convergence. Using the gaussian cost function, similar convergence times were reached compared to the double region cost function. With the mean method, the shimmed RF phases being determined without an algorithmic approach, the result is immediate.

4.2.3 Characterization of the algorithm performances

To assess the performances of the algorithm, the simulated models for the 8Tx/Rx center-shortened dipole coil array and the 8Tx/Rx fractionated dipole coil array were used (chapter 2). Individual complex B_1^+ maps were exported to Matlab (2018a, the Mathworks, Natick, MA) and processed with the particle-swarm algorithm. Different areas were selected for optimization and the results were compared with the mean method in terms of transmit field efficiency. As an indication, the same regions were measured for the circularly polarized (CP) mode. All the results were interpolated at 1 mm-iso inside a virtual box (200 x 250 x 230 mm^3) surrounding the head of a human model and normalized to 1 kW input power per channel.

MR measurements were performed on a Magnetom 7T MR scanner (Step 2.3, Siemens, Erlangen, Germany) equipped with 8 x 1 kW RF amplifiers and 32-channel independent receive lines. All the B_1^+ maps were acquired with a SA2RAGE sequence for a 500 µs, 90°, 1 kW hard pulse [102].

The particle-swarm optimization algorithm was extensively used for human head acquisitions using the in-house built 8Tx/32Rx coil array presented in the previous chapter. The double region cost function (Equation 4.10) was used to assess the PSO efficiency over the whole-brain when experimental data acquired on the human brain is used, and the resulting RF shimmed transmit sensitivity maps were compared to the mean method approach. To estimate if the RF phases optimized for a given human brain could be applied to different people, first the transmit sensitivities were calculated for 4 volunteers (1 women, 3 men) having different head size and shape. The optimal RF phases were therefore calculated in sagittal slice for one of the heads (reference volunteer) with the gaussian cost function, and the calculated phases were applied to the other heads in both mid-sagittal and mid-brain transverse slices. The results were assessed in measured B_1^+ for two of the volunteers. Transmit field maps were experimentally measured on human brain for RF phases optimized with the double region and the gaussian cost functions over the whole-brain, and the cerebellum. Thereafter, the optimal RF phases were calculated with the gaussian cost function for five different regions, and the computed transmit sensitivity maps were compared to the experimentally measured B_1^+ maps. The $SAR_{10g,max}$ values were calculated in simulation for the RF phases used in measurements. The same areas were optimized for the simulated model of the 8Tx/Rx center-shortened dipole coil array, and the B_1^+ maps were computed. Similarly, the $SAR_{10g,max}$ values were calculated for the RF phases used in simulation.

4.3 Results

When RF phases optimization was performed over small areas, the PSO algorithm and the mean method resulted in comparable B_1^+-field distributions and mean values. This could be particularly observed in the cerebellum, and the temporal and frontal lobes (Figure 4.3A).

However, when RF phases were optimized over the larger area (Figure 4.3A - Large Central Shim), the mean-method optimal RF phases could not produce an efficient transmit field distribution. Specifically, a B_1^+-field void was observed inside the brain. Nevertheless, with both the PSO algorithm and the mean method, the gain compared to the CP mode was clearly demonstrated (Figure 4.3B). No significant difference were observed between the 8Tx/Rx fractionated dipole coil array and the 8Tx/Rx center-shortened dipole coil array, as it was shown also in chapter 2.

The limits of the mean method to optimize the RF phases over large areas were demonstrated for measured human brain data in Figure 4.4. On the human brain, the PSO algorithm produced a highly-efficient coverage of the whole-brain when the double-region cost function was used, while strong field inhomogeneities and cancellations were observed with the mean method approach, notably in the transverse slices. The next results are therefore exclusively acquired with RF phases optimized by the PSO algorithm.

The shimmed RF phases calculated in sagittal plane for the reference volunteer were applied to three different people, and the resulting transmit sensitivity maps are shown in Figure 4.5A for sagittal and transverse slices. With a maximum decrease of 6% in sagittal slice, the mean transmit sensitivity was shown to be well preserved for all the volunteers (Figure 4.5B). In transverse slice, the reference volunteer and the volunteer 1 presented comparable field distribution, close to a quadrature mode. On volunteer 2 the transmit sensitivity voids in transverse slice were reduced, while on volunteer 3 they were more pronounced. Nevertheless, no decrease in the mean transmit sensitivity was measured (Figure 4.5B).

As shown with the transmit sensitivity maps (Figure 4.5), no differences were observed in the measured B_1^+ field distributions acquired with the same RF phases on two different heads for whole-brain RF shimming (Figure 4.6A). The averaged B_1^+-field values over the brain tissues differed by less than 3% when the RF phases calculated for the reference volunteer were applied to the volunteer 1. Similarly, for the temporal RF shimming the two heads presented comparable transmit field distribution patterns.

For RF phases optimized over the whole-brain transverse slice, both the double-region and gaussian cost functions demonstrated comparable performances in measured B_1^+ maps (Figure 4.7A), with a good homogeneity shown in the three main orientations. Nevertheless, a noticeable transmit field drop could be observed at the top right of the transverse slice in both cases. In cerebellum, a better coverage and transmit field efficiency was achieved using the double-region cost function.

The measured B_1^+ maps for the five different regions were well predicted by the computed transmit sensitivity maps (Figure 4.8A). Similarly, the simulated B_1^+ maps were mostly similar to the acquired maps (Figure 4.8C). However, the measured whole-brain transmit field distribution pattern could not be retrieved in simulations. Moreover, different combination of RF phases were used in measurements and in simulations to achieve the same RF field distribution (Table 4.2). Consequently, the $SAR_{10g,max}$ values differed significantly between the measured and simulated RF phases. The corresponding SAR_{10g} maps calculated for the

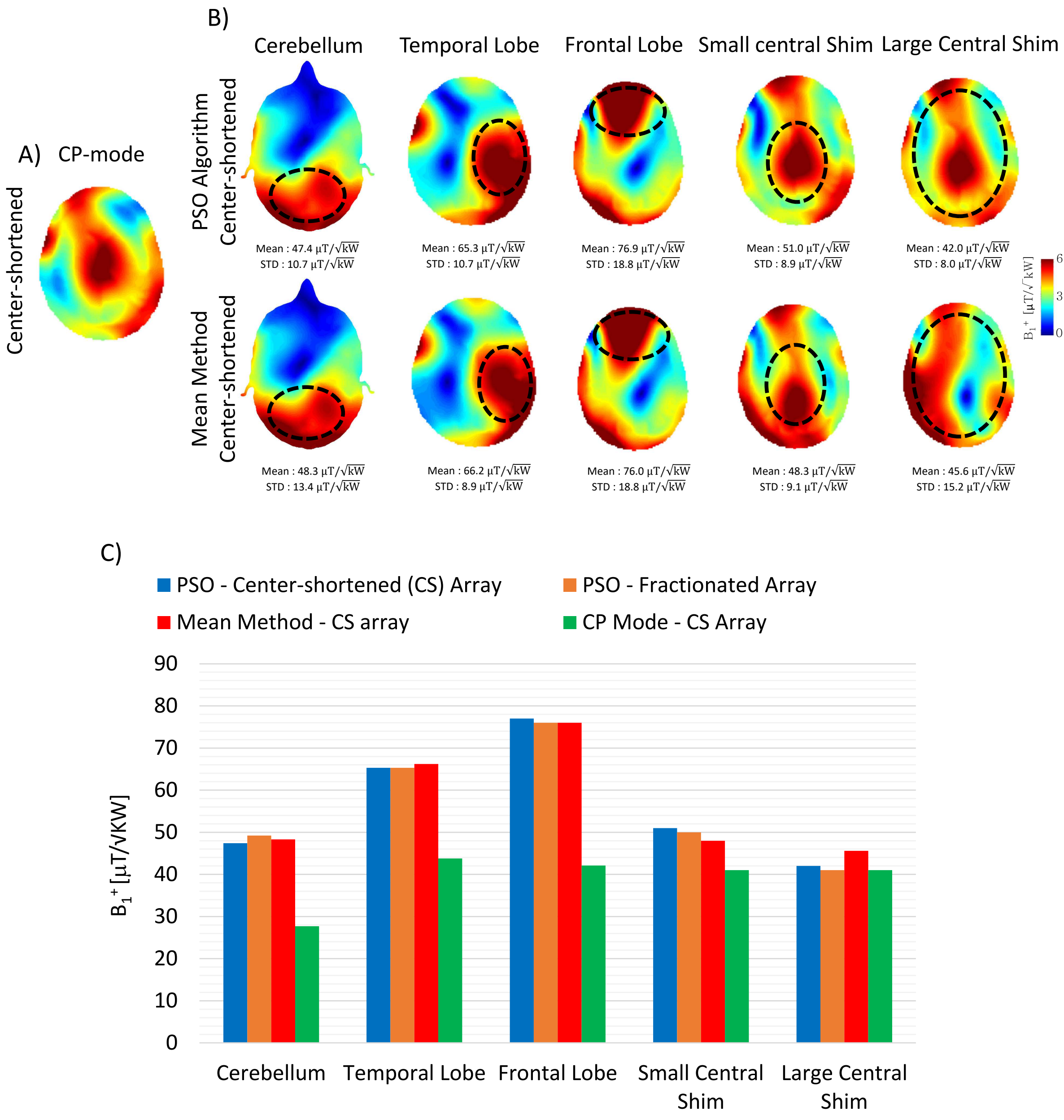

Figure 4.3: *A) CP mode for the 8 Tx/Rx center-shortened dipole coil array B) Simulated RF shimmed* B_1^+ *maps for the 8Tx/Rx center-shortened dipole coil array. The RF phases were optimized over different areas in the human brain (black dashed ellipses) with the PSO algorithm and the mean method. The maps were normalized to 1 kW per channel. C) Mean* B_1^+ *values calculated over the shimmed area for the 8Tx/Rx center-shortened and the 8Tx/Rx fractionated coil arrays. The results obtained with both arrays by using the PSO algorithm are compared to the mean method and to the circularly (CP) polarized mode.*

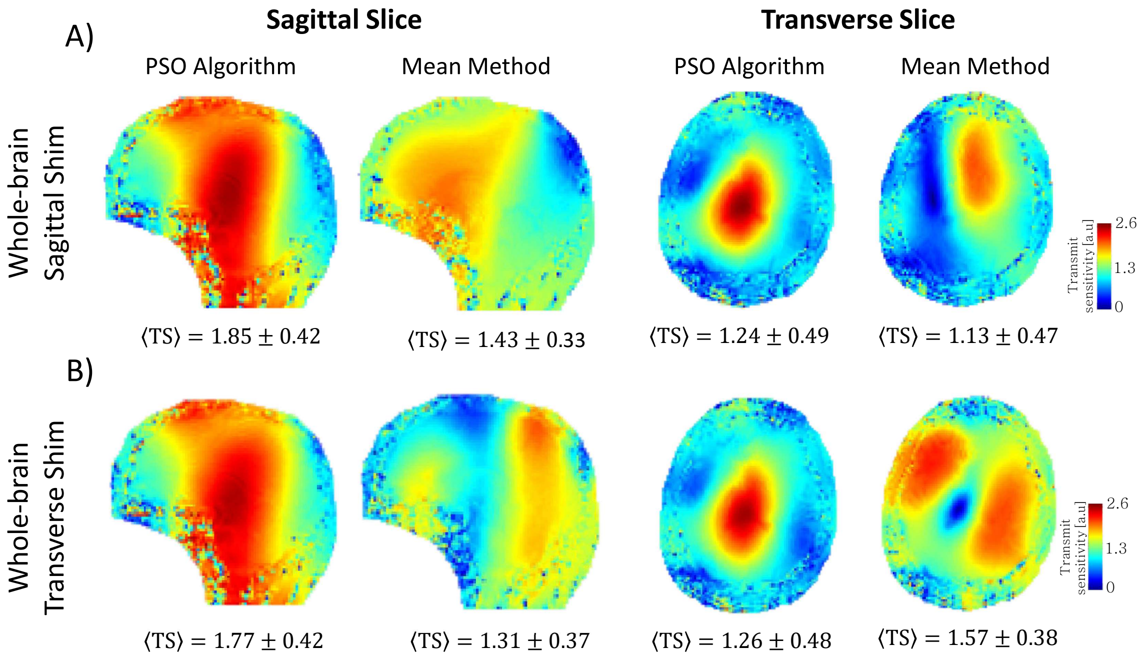
A)
Sagittal Slice
Transverse Slice
PSO Algorithm
Mean Method
PSO Algorithm
Mean Method
Whole-brain Sagittal Shim
⟨TS⟩ = 1.85 ± 0.42
⟨TS⟩ = 1.43 ± 0.33
⟨TS⟩ = 1.24 ± 0.49
⟨TS⟩ = 1.13 ± 0.47
Transmit sensitivity [a.u]
2.6
1.3
0
B)
Whole-brain Transverse Shim
⟨TS⟩ = 1.77 ± 0.42
⟨TS⟩ = 1.31 ± 0.37
⟨TS⟩ = 1.26 ± 0.48
⟨TS⟩ = 1.57 ± 0.38
Transmit sensitivity [a.u]
2.6
1.3
0

Figure 4.4: *For the 8Tx/32Rx center-shortened dipole coil array, computed transmit sensitivities (from measured human brain data) shown in sagittal and transverse slices for A) RF phases optimized in sagittal slice and B) RF phases optimized in transverse slice. The results for the two methods (PSO and mean method) are shown, and the mean transmit sensitivity (TS) value calculated over the brain tissues is given below the images.*

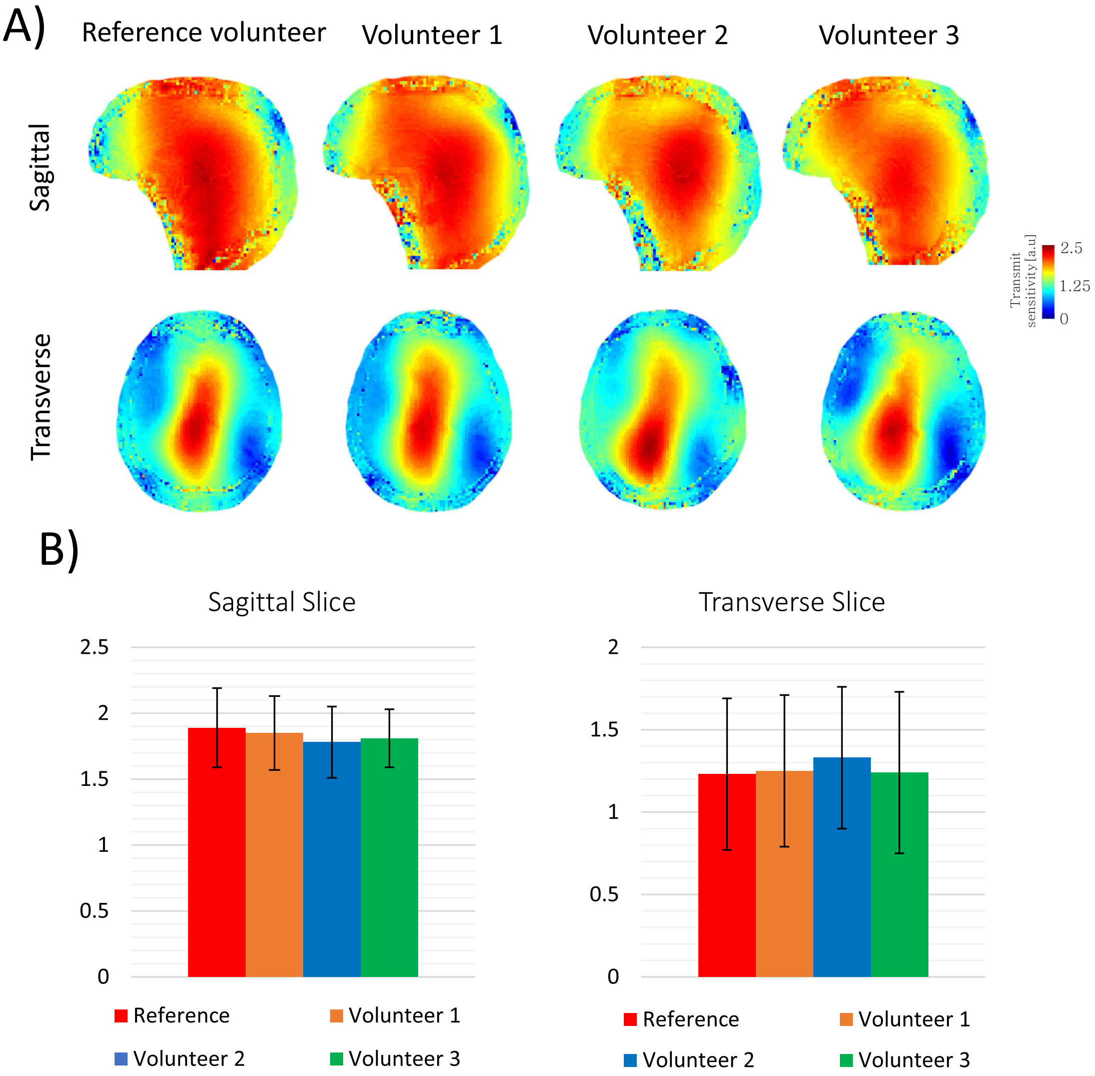

Figure 4.5: *A) Transmit sensitivity maps computed for the 8Tx/32Rx center-shortened dipole coil array, and RF phases optimized over the whole-brain sagittal slice on the reference volunteer ([242, 104, 210, 21, 0, 77, 21, 108] degrees). The sagittal and transverse slices are shown. B) Mean value of the transmit sensitivity calculated over the brain tissues in sagittal and transverse slices. The error bars correspond to the standard deviation.*

simulated optimal RF phases demonstrated very localized regions of high SAR_{10g} values (Figure 4.9).

4.4 Discussion

In this study, a different approach for RF phases optimization was investigated. Based on the particle-swarm algorithm, the shimming process was integrated into a user-friendly interface to facilitate the use of parallel-transmit systems. The performances of the algorithm were evaluated in terms of the transmit efficiency over the areas-of-interest, the accuracy of

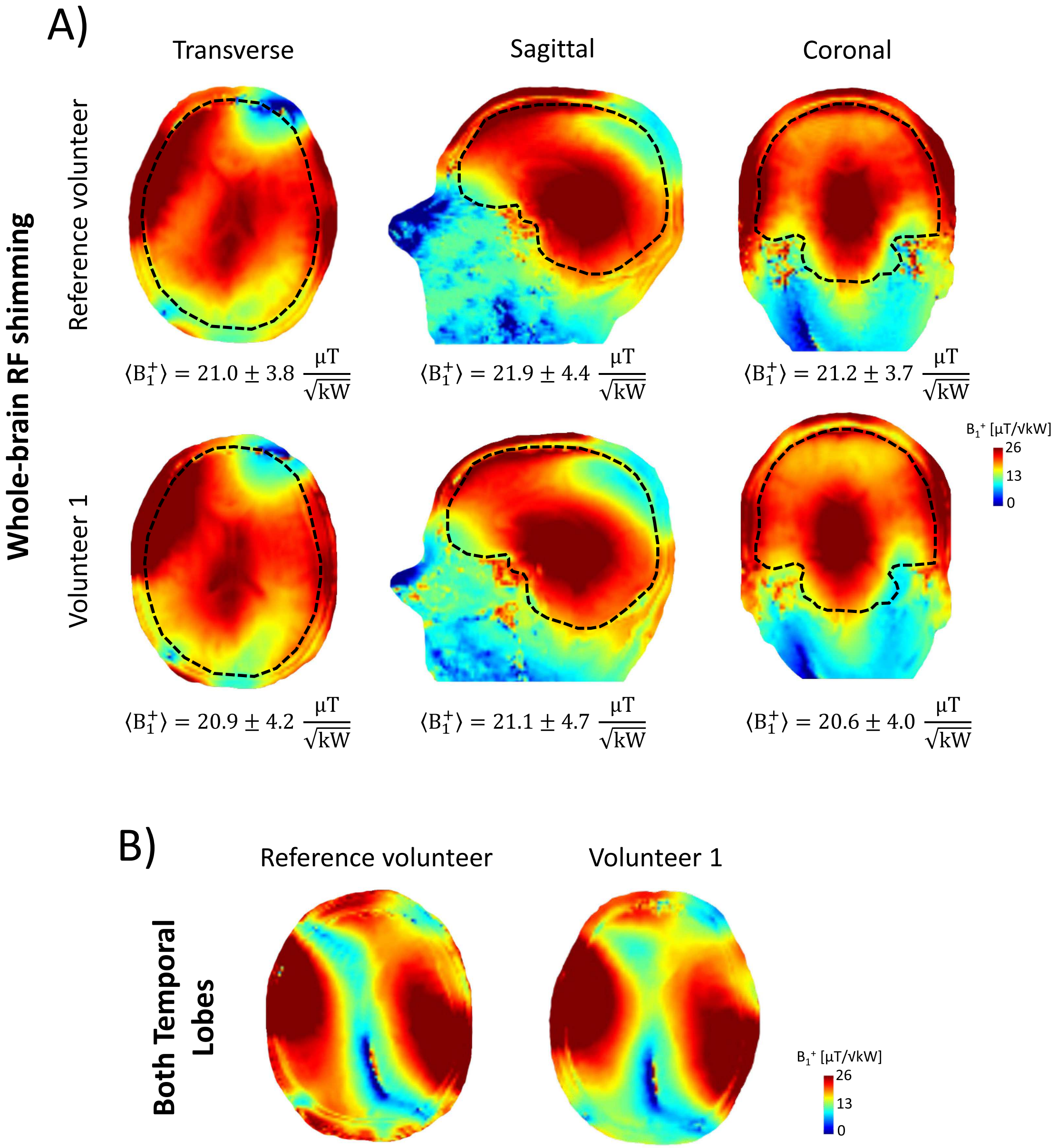
A)
Transverse
Sagittal
Coronal
Whole-brain RF shimming
Reference volunteer
$\langle B_1^+ \rangle = 21.0 \pm 3.8 \frac{\mu T}{\sqrt{kW}}$
$\langle B_1^+ \rangle = 21.9 \pm 4.4 \frac{\mu T}{\sqrt{kW}}$
$\langle B_1^+ \rangle = 21.2 \pm 3.7 \frac{\mu T}{\sqrt{kW}}$
Volunteer 1
$\langle B_1^+ \rangle = 20.9 \pm 4.2 \frac{\mu T}{\sqrt{kW}}$
$\langle B_1^+ \rangle = 21.1 \pm 4.7 \frac{\mu T}{\sqrt{kW}}$
$\langle B_1^+ \rangle = 20.6 \pm 4.0 \frac{\mu T}{\sqrt{kW}}$
B_1^+ [μT/√kW]
26
13
0
B)
Reference volunteer
Volunteer 1
Both Temporal Lobes
B_1^+ [μT/√kW]
26
13
0

Figure 4.6: *Measured B_1^+ maps acquired with the 8Tx/32Rx center-shortened dipole coil array, and RF phases optimized on the original volunteer for A) a whole-brain transverse slice ([285, 124, 217, 337, 0, 110, 13, 106] degrees) and B) both temporal lobes ([161, 268, 0, 117, 0, 65, 0, 117] degrees). In A) the mean transmit field values are given with the corresponding standard deviation.*

the predicted transmit-field maps, and the robustness of the results under different conditions.

With the RF phase shimming applied to small areas such as the cerebellum, temporal and frontal lobes or the central area of the brain, the PSO algorithm and the mean method demonstrated comparable performances. The phase variations over local areas being quite

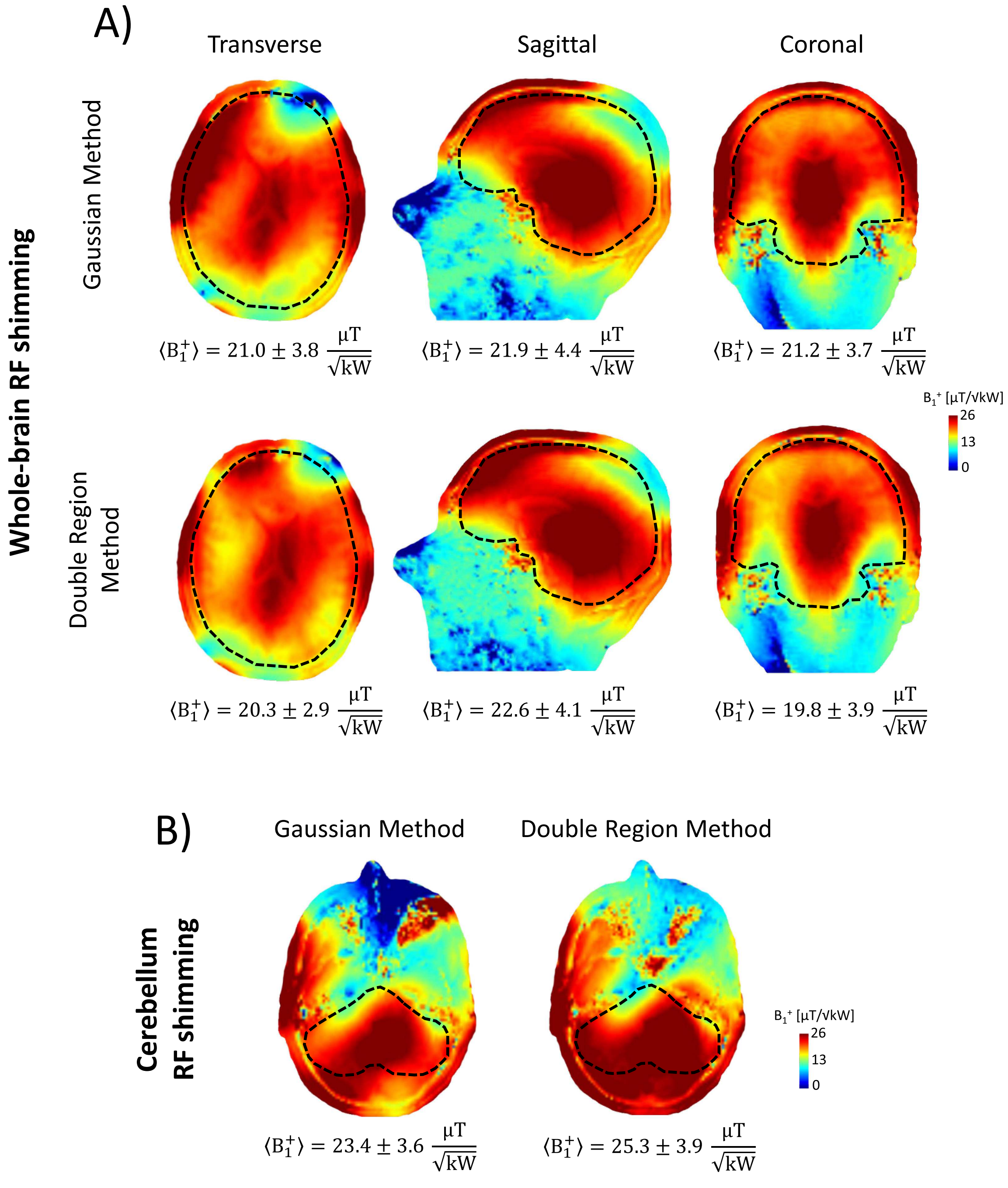
A)
Transverse
Sagittal
Coronal
Whole-brain RF shimming
Gaussian Method
Double Region Method
$\langle B_1^+ \rangle = 21.0 \pm 3.8 \frac{\mu T}{\sqrt{kW}}$
$\langle B_1^+ \rangle = 21.9 \pm 4.4 \frac{\mu T}{\sqrt{kW}}$
$\langle B_1^+ \rangle = 21.2 \pm 3.7 \frac{\mu T}{\sqrt{kW}}$
B_1^+ [μT/√kW]
26
13
0
$\langle B_1^+ \rangle = 20.3 \pm 2.9 \frac{\mu T}{\sqrt{kW}}$
$\langle B_1^+ \rangle = 22.6 \pm 4.1 \frac{\mu T}{\sqrt{kW}}$
$\langle B_1^+ \rangle = 19.8 \pm 3.9 \frac{\mu T}{\sqrt{kW}}$
B)
Gaussian Method
Double Region Method
Cerebellum RF shimming
B_1^+ [μT/√kW]
26
13
0
$\langle B_1^+ \rangle = 23.4 \pm 3.6 \frac{\mu T}{\sqrt{kW}}$
$\langle B_1^+ \rangle = 25.3 \pm 3.9 \frac{\mu T}{\sqrt{kW}}$

Figure 4.7: *Measured B_1^+ maps acquired with the 8Tx/32Rx center-shortened dipole coil array, and RF phases optimized using either the gaussian or the double region cost functions () for A) whole-brain transverse slice ([285, 124, 217, 337, 0, 110, 13, 106] degrees with the gaussian method and [253, 123, 189, 0, 0, 100, 20, 115] degrees with the double-region method), B) cerebellum area ([14, 198, 0, 97, 196, 259, 73, 153] degrees with the gaussian method and [40, 255, 0, 171, 235, 356, 101, 199] degrees with the double-region method).*

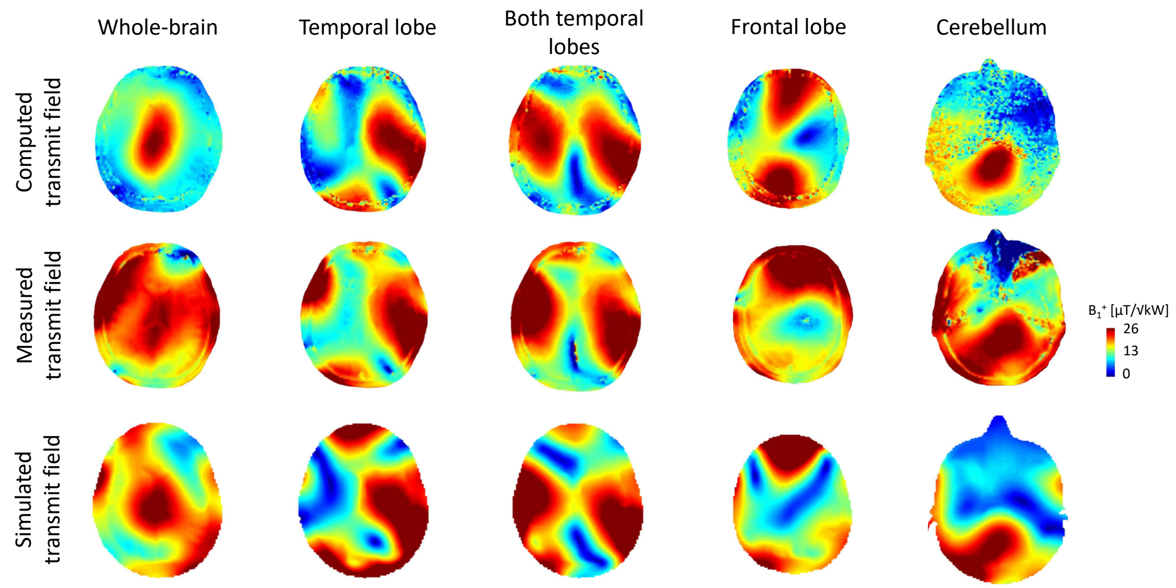

Figure 4.8: *For the 8Tx/32Rx center-shortened dipole coil array: calculated, experimental and simulated transmit field maps with the RF phases optimized over five different regions in the human brain.*

Table 4.2: *RF phases and $SAR_{10g,max}$ corresponding to the measured and simulated transmit field maps shown in Figure 4.8.*

Whole-brain

	Optimized RF phases	Simulated $SAR_{10g,max}$
Measured	**[285, 124, 217, 337, 0, 110, 13, 106]**	1.23 W/kg
Simulated	**[226, 146, 130, 87, 0, 0, 0, 321]**	0.83 W/kg

Temporal Lobe

	Optimized RF phases	Simulated $SAR_{10g,max}$
Measured	**[130, 343, 288, 116, 0, 50, 351, 68]**	1.21 W/kg
Simulated	**[0, 294, 0, 222, 0, 0, 38, 332]**	0.98 W/kg

Both Temporal Lobes

	Optimized RF phases	Simulated $SAR_{10g,max}$
Measured	**[161, 268, 0, 117, 0, 65, 0, 117]**	1.05 W/kg
Simulated	**[0, 15, 223, 221, 0, 0, 357, 284]**	1.25 W/kg

Frontal Lobe

	Optimized RF phases	Simulated $SAR_{10g,max}$
Measured	**[158, 66, 269, 0, 62, 299, 0, 77]**	1.01 W/kg
Simulated	**[29, 302, 89, 57, 287, 263, 0, 24]**	0.94 W/kg

Cerebellum

	Optimized RF phases	Simulated $SAR_{10g,max}$
Measured	**[14, 153, 198, 0, 97, 196, 259, 73]**	1.13 W/kg
Simulated	**[274, 131, 0, 303, 256, 0, 0, 308]**	0.94 W/kg

small, taking the mean phase for each channel smooths the overall phase distribution and produces an efficient transmit field. However, this simple approach is impaired when larger areas are chosen for optimization. A transmit-field dark node and inhomogeneities were observed in the computed maps when the mean method was used. Since with the PSO algorithm the field of solutions (individual RF phase shifts) is widely explored, better results could be demonstrated when using the double-region cost function (Equation 4.10).

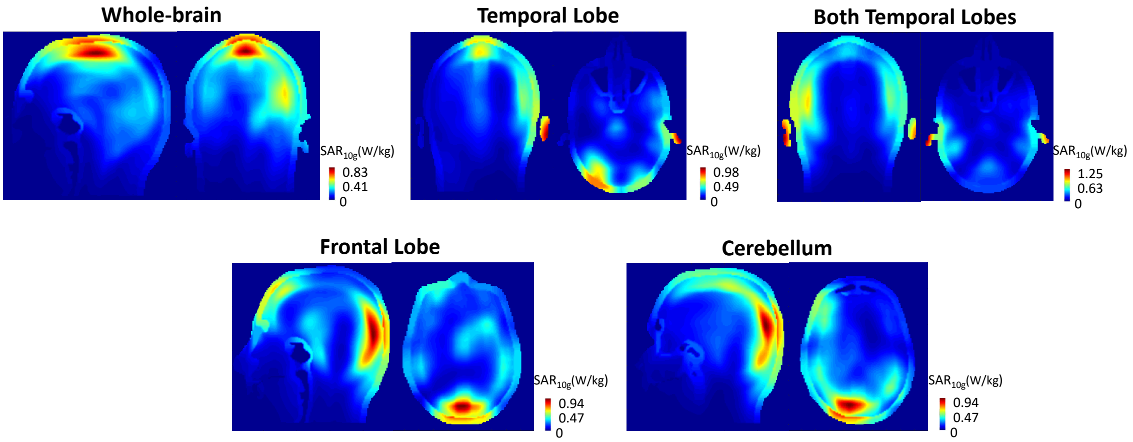

Figure 4.9: *SAR_{10g} maps, normalized to 1W input peak-power, for the optimized RF phases shown in Figure 4.2. The maps are scaled to the maximum SAR_{10g} value. The slices are shown at the position of the maximum value.*

However, when equation 4.9 was used to optimize the RF phases over the large areas the shimmed transmit-field maps were comparable to the mean method approach. To achieve whole-brain coverage with good efficiency, it is therefore essential to consider both the maximal achievable field and the dispersion of the values around the resulting mean value, as with the double-region cost function. The so-called gaussian-method as proposed in 2012 by Schmitter et al. [148] define a gaussian shape pattern of the transmit field efficiency over the large region (meaning whole-slice). By minimizing the root-mean square difference between the shimmed transmit field and the Gaussian pattern, the dark node at center of the brain could be avoided and similar efficiencies compared to the double-region method were shown. However, this approach strictly depends on the user-defined gaussian parameters (Table 4.1). When the same gaussian coefficient ($\alpha = 2.7$ in Table 4.1) was used for the whole-brain transverse and the cerebellum areas, the gaussian cost function produced a sub-optimal transmit field coverage of the cerebellum compared to the double-region method. Since over small areas the sum-of-magnitude distribution is more likely to be achieved, the gaussian coefficient α could be relaxed to lower values in order to get an improved transmit field efficiency.

The accuracy of the predicted and measured RF shimmed B_1^+ maps was assessed mainly in terms of the field distribution. The positions of maximal and lowest field were well represented in the computed transmit sensitivity maps. Nevertheless, the exact intensities could not be precisely predicted. Indeed, the SVD computation gives a spatially scaled version of the true B_1^+ field. To get the true transmit-field distribution, the scaling patterns have to be determined [147]. However, the purpose of this study was to develop a robust tool for RF phases optimization, and providing a good estimation of the expected transmit-field map. The PSO algorithm was able to efficiently optimize the RF phases for different coil setups and loading conditions. Particularly, the parameters α and β in equation 4.10 could be defined once for all.

The computed shimmed transmit sensitivity maps were compared on different brains for a single set of optimized RF phases. The transmit-field distribution was not significantly impaired. Similarly, the measured B_1^+ maps for a single set of RF phases and two different volunteers were almost identical (Figure 4.6A). However, significant differences in head shapes or size could mitigate these observations. For smaller regions such as presented in Figure 4.6B, the variations between different heads are minimal. A database with a collection of phase settings could therefore be prepared for local areas as the cerebellum, the temporal or the occipital lobes.

The problem of RF phases optimization could also have been formulated as a least-square optimization aiming for the sum-of-magnitudes result. However, a mathematical approach would require the solution to be described uniformly. With the PSO algorithm, uniformity of the solution is not a limiting aspect, meaning that the optimization process could include criteria not directly linked to the others. For example, pulse shape parameters and amplitude could be integrated into the single multi-dimensional solution space, and processed the same way as with only RF phases. Furthermore, by deriving the Q-matrices from the simulated model and evaluating the local $SAR_{10g,max}$ with the virtual observation points method [40], RF safety criteria could be included in the cost function.

Adding the $SAR_{10g,max}$ calculation within the optimization process requires however a perfect matching between the simulated and measured transmit fields and optimized RF phases. Large mismatches would expose the patients to safety issues in case the calculated $SAR_{10g,max}$ provides the RF power limits in the scanner. In this study, only the worst-case scenario RF limits could be used. Indeed, while similar transmit field distributions could be observed in measurements and simulations, the optimal RF phases were significantly different. The $SAR_{10g,max}$ were therefore distinct, and could not be used to provide shimmed-specific RF power limits. Moreover, larger differences in transmit field distribution were observed when the RF phases were optimized over the whole-brain. Even though the presence of the receivers did not significantly modified the RF shimming capabilities or B_1^+ field distribution over small areas, the simulated model of the 8Tx/8Rx dipole coil array is non-optimal to accurately predict the transmit field when large areas are shimmed with the 8Tx/32Rx coil array.

Calculation time is an other important criteria when an algorithmic approach is used. In the case of phase-only optimization, the convergence could be achieved most of the time in less than 30s even when whole-brain areas were chosen. The computation time will increase when more parameters are added since the solution space is much larger, and involves uncorrelated quantities. However, the total time for the RF shimming procedure (including the MR sequence) is still expected to take less than 5 min.

4.5 Conclusion

The particle-swarm optimization algorithm was proposed in this study to optimize the RF phases for parallel transmit MR. The performances were compared to the mean-method. Over small areas both methods produced comparable transmit-field efficiencies, and the same optimized RF phases may be applied indiscriminately of the persons placed inside the coil. Over larger areas such as whole-brain, the PSO algorithm outperformed the mean method. However, it is recommended to perform the phase shimming each time a new person is scanned since for large area the differences between heads may lead to a sub-efficient result. We conclude that particle-swarm optimization is a valuable approach for a transmit-efficient RF phase shimming over the whole-brain at 7T.

5

Dedicated surface coils for the temporal and the frontal lobes of the human brain

---

Adapted from:

Jérémie D. Clément, Lijing Xin, Rolf Gruetter, Özlem Ipek
Dedicated surface coils for MR studies in the temporal and the frontal lobes of the human brain at 7T
Proceedings of the 24^{th} Annual Meeting of ISMRM, Singapore, 2016 (3513)

Adapted from:

Jérémie D. Clément, Maxime Aboukrat, Rolf Gruetter, Özlem Ipek
Unilateral/Bilateral RF excitation of temporal lobes using a DC-controlled transmit/receive switch and two surface coils
Proceedings of the 34^{th} Annual Meeting of ESMRMB, Barcelona, 2017 (272)

Jérémie D. Clément designed and built the dedicated RF coils and the TR switch, contributed to experimental design and performing MR experiments, co-writing the abstracts.

Abstract

Purpose Birdcage coils demonstrate high transmit field at the center of the brain and lower transmit field close to the cortex at 7T. Adding a dielectric pad inside the coil leads to a substantial increase of the transmit field under the pad. Surface coils can offer high transmit field in their vicinity. The purpose of the study was first to design highly efficient surface coils for the peripheral temporal and frontal lobes of the human brain regions and compare them with the volume coil with dielectric pads in terms of transmit field efficiency and single-voxel spectroscopy performance. Moreover, to avoid lipid contamination in MR spectra acquired on one of the temporal lobes, a switching circuit between unilateral/bilateral transmit modes is required. Therefore, the second aim of this study was to design a transmit/receive (TR)-switch including DC-controlled paths for unilateral/bilateral transmission.

Methods Ear-to-Ear loops (ETE-loops) and Frontal-Region-Operating loops (FRO-loops) were built. A dedicated TR-switch was designed to enable one-side or both-side transmit modes with the ETE-loops. For comparison, a commercial birdcage coil (Nova Medical, Inc. MA) and a dielectric pad placed on the temporal and frontal regions of the brain were used. Electromagnetic field simulations were performed. The transmit field efficiencies were measured and compared.

Results Both the ETE-loops and FRO-loops demonstrated a higher transmit field efficiency compared to the birdcage coil with dielectric pads. In the frontal lobe, comparable results were achieved with MR spectroscopy. In the temporal lobes, no acquisition could be done with the birdcage coil including the dielectric pads because of the power limitations. The proper working of the dedicated TR-switch was demonstrated.

Conclusion In this study, the efficiency of dedicated surface RF loop coils for the temporal and frontal lobes of the human brain was demonstrated in comparison with a birdcage coil including dielectric pads at 7T. The lack of transmit field efficiency in the temporal lobes when using the birdcage coil with dielectric pad impeded the acquisition of MR spectra. The TR switch has allowed to drive the ETE-loops in three different modes. We conclude that the construction of dedicated surface loop coils is a valuable alternative to the birdcage coil with dielectric pads for 7T MR applications in the human brain.

5.1 Introduction

At ultra-high field, the shorter wavelength ($\lambda \approx$ 12 cm at 7T in the brain) causes noticeable RF inhomogeneity and decreased RF penetration of human tissues. Notably, the birdcage volume coils [23] which were originally developed at lower magnetic fields, show a central brightening effect, with low transmit field at the edges of the brain, such as the temporal lobes [25, 86]. The lack of transmit field lowers the efficiency of MR spectroscopy measurements in these areas. Dielectric pads were proposed to address this issue [87, 88]. When placed inside the birdcage coil they could produce an increased transmit field in the regions with low field.

To understand the working principle of these dielectric pads, first it is important to understand what is a dielectric, how it is characterized [149]. The relative permittivity ϵ_r is defined as the ratio between the complex-value permittivity of a material $\epsilon(\omega)$ and the vacuum permittivity ϵ_0. It characterizes the ability for a material to store energy when place inside an electric field. This effect was briefly introduced in chapter 1 section 1.3.3.4, where it was referred as the polarization of a medium. The relationship between electric field and polarization is given by equation 5.1 where ϵ_0 is the permittivity of vacuum and χ_e is the electric susceptibility defined as $\chi_e = \epsilon_r - 1$.

$$\vec{P} = \epsilon_0 \chi_e \vec{E} \tag{5.1}$$

$$\vec{D} = \epsilon_0 \vec{E} + \vec{P} = \epsilon_0 (1 + \chi_e) \vec{E} = \epsilon_0 \epsilon_r \vec{E} \tag{5.2}$$

The total electric displacement field is then given by equation 5.2. The higher is ϵ_r the stronger is the polarization of a medium. Considering the Ampere's circuital law as defined by Maxwell equations (Equation 5.3) it is seen that the magnetic field intensity and distribution inside a body are both dependent on the conduction currents (the $\vec{J_c}$ term) and on the derivative of the displacement field. Equation 5.3 can be rewritten as Equation 5.4 since in MR the electric field is time-varying. The second term of the equation 5.4 corresponds to a displacement current while i = $\sqrt{-1}$ accounts for the 90°phase difference between the conductive and displacement currents [150, 151].

$$\nabla \times \vec{H} = \vec{J_c} + \frac{\partial \vec{D}}{\partial t} \tag{5.3}$$

$$\nabla \times \vec{H} = \sigma \vec{E} + i \epsilon_0 \epsilon_r \omega \vec{E} \tag{5.4}$$

While conduction currents dissipate the RF power through heating of tissues, the displacement currents are assimilated to secondary sources which favor the propagation of RF fields [48]. High-permittivity dielectric materials are more likely to generate large displacement currents (Equations 5.2 and 5.4), and therefore when they are placed close to the

human tissues in presence of an external RF field (e.g from a birdcage coil) they could locally improve the transmit field (B_1^+) distribution pattern [88, 149, 150, 152, 153]. Barium titanate ($BaTiO_3$) and calcium titanate ($CaTiO_3$) belong to the family of perovskites which present high permittivity properties ($\epsilon_r > 100$) because of their chemical structure [149]. Both are widely used to prepare the dielectric pads in MRI [87, 150, 153, 154]. The compounds are generally in suspension inside a plastic bag filled with deuterated water. The appropriate weight ratio between the two allows to get the desired permittivity [149].
However, the quality (e.g the compound's properties) of dielectric pads could degrade over time and different head shapes or head movements can also impact its performances. To overcome these limitations, surface coils could be used since they offer high transmit field in their vicinity. They were e.g proposed for breast MRI with a specific switch setup that allow for bilateral and unilateral excitation of the breast [155], or for cervical cord and knee [156]. However there was to our knowledge no attempt to characterize dedicated surface coils for MR spectroscopy in the temporal and frontal lobes of the human brain at 7T, in comparison to a standard volume birdcage coil with dielectric pads. Therefore, the aim of this study was to design the dedicated highly-efficient surface coils for peripheral temporal and frontal lobes of the human brain regions at 7T and to compare their performances to a commercial birdcage coil with dielectric pads.

5.2 Methods

5.2.1 Coil design and construction

Two surface loop coils, namely the Ear-to-Ear loops (ETE-loops), were designed to cover the two temporal lobes of the human brain (110 x 90 mm^2 each loop) (Figure 5.1B). Similarly, two loops were designed for the frontal lobe (frontal-region-operating/FRO loops) with different dimensions than the ETE-loops (80 x 60 mm^2 each loop)(Figure 5.2) [157]. Both the ETE and FRO loops were built with copper wire tube (diameter = 3.5 mm). Each loop was divided symmetrically. Non-magnetic fixed-value capacitors (American Technical Ceramics, NY, USA) and two variable capacitors were used for tuning/matching of the loops. The FRO loops were connected through 50 Ohms coaxial cables with equal phase length ($\varnothing = 3$ mm, Huber-Suhner, Switzerland) to a quadrature transmit-receive switch with low noise preamplifiers (Stark Contrast, Erlangen, Germany). Common-modes on the coaxial cables were diminished with a balun that is a quarter-wavelength transformer tuned to 297.2 MHz with capacitors. Tuning/matching to 297.2 MHz (better than -20 dB) and S-parameter matrix measurement were performed using a 4-channel vector network analyser (Agilent Technologies 5071C-ENA Series, USA). The decoupling between the FRO loops was better than -15dB.

For the ETE loops, a dedicated in-house built TR switch was designed and built (see paragraph 5.2.2) to drive the loops as one-side only or two sides depending on the interest [158].

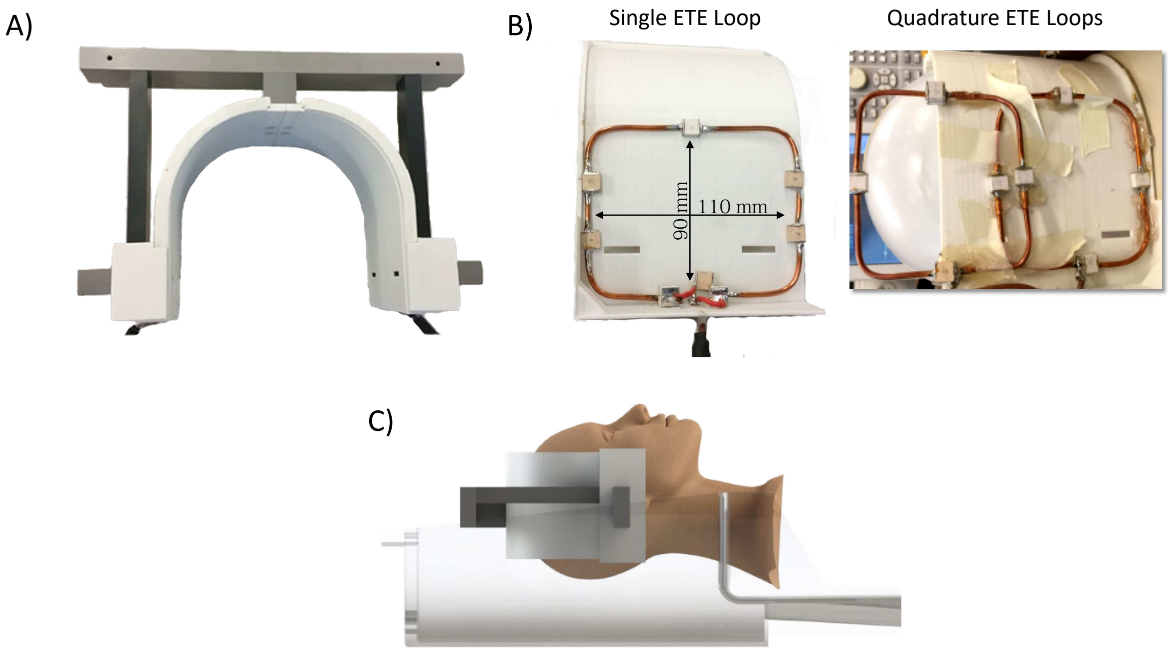
A)
B)
Single ETE Loop
Quadrature ETE Loops
90 mm
110 mm
C)

Figure 5.1: *Photos of A) the whole-design of the ETE loops; B) one side of the ETE loops with the loop dimensions indicated (left) and the quadrature ETE loops (right). C) Position of the ETE loops over the temporal lobes.*

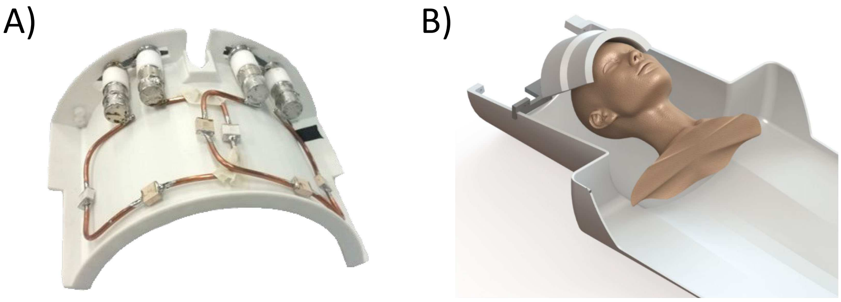

Figure 5.2: *A) Photo of the FRO loops with the support structure and B) Position of the FRO loops over the frontal lobe.*

Support structures for the ETE and FRO loops were drawn on Solidworks (Dassault Systems, France) and 3D printed (CubePro Duo, 3D Systems, MA, USA) in ABS (Acrylonitrile Butadiene Styrene). The two loops were tuned and match better than -15 dB, and well decoupled since they are placed on each side of the brain. Thereafter, the design was improved to include two loop coils (95 x 85 mm^2) on each side of the head which were overlapped by 16 mm for decoupling purposes. Each side was driven through the dedicated TR switch and an additional quadrature hybrid coupler. The design will be further referred as the **quadrature ETE loops** (Figure 5.1B).

A commercial single Tx birdcage (Nova Medical, USA) with a dielectric pad (100 x 100 x 5 mm^3, ϵ_r = 160, BaTi in deuterated water) placed either on temporal or frontal lobe was used as comparison.

5.2.2 TR switch design for the ETE Loops

The TR switch circuit for the ETE loops was designed in Altium (2015, San Diego, CA), and etched from 35 µm copper on a FR4 substrate (thickness = 1.3 mm) (Figure 5.3). Non-magnetic capacitors (American Technical Ceramics, NY, USA) and hand-wounded inductors were used to tune and match the circuit at 50 Ohms. In Figures 5.4 and 5.5, the schematics for the distinct transmit modes are shown. In both cases, the RF signal enters at the J2-port (Figure 5.4-5.5), and to switch between the transmit modes the PIN diodes' polarization is remotely controlled. During transmit, the PIN diodes D2-D5 are forward biased with a 100 mA DC current. In the so-called **unilateral mode**, either the PIN diode D13 or D17 are forward biased and the RF signal is transmitted to only one of the loops connected to the J1 and J3 ports (Figure 5.4). To transmit with both coils, the PIN diodes D14-D16 are forward biased while the diodes D3 and D17 are reverse biased with a -30V DC voltage (Figure 5.5). The RF signal therefore goes through a wilkinson divider to the two loop coils with zero-phase difference. This mode will be further referred as the **bilateral** mode. The attenuation coefficient for each mode were measured with the 4-channel vector network analyser.

The two quadrature loop coils placed on each side were fed through distinct quadrature hybrid couplers connected to the terminals J_1 and J_3 (Figure 5.5). To distinguish the different configurations, in the next paragraphs the **unilateral quadrature left/right modes** corresponds to the quadrature left/right coils fed with the unilateral left/right modes. Similarly, the **bilateral quadrature left/right modes** refers to the same situation but with the left/right coils fed using the bilateral transmit mode.

5.2.3 Electromagnetic field simulations

The ETE loops, the FRO loops, and the commercial birdcage coil were simulated with the finite-difference time-domain (FDTD) method on Sim4Life 2.0 (ZMT AG, Switzerland) on the whole body human model, Duke [35]. The commercial coil was modeled as a 16-legs band-pass birdcage coil using a dedicated tool in Sim4Life. The inner diameter was about

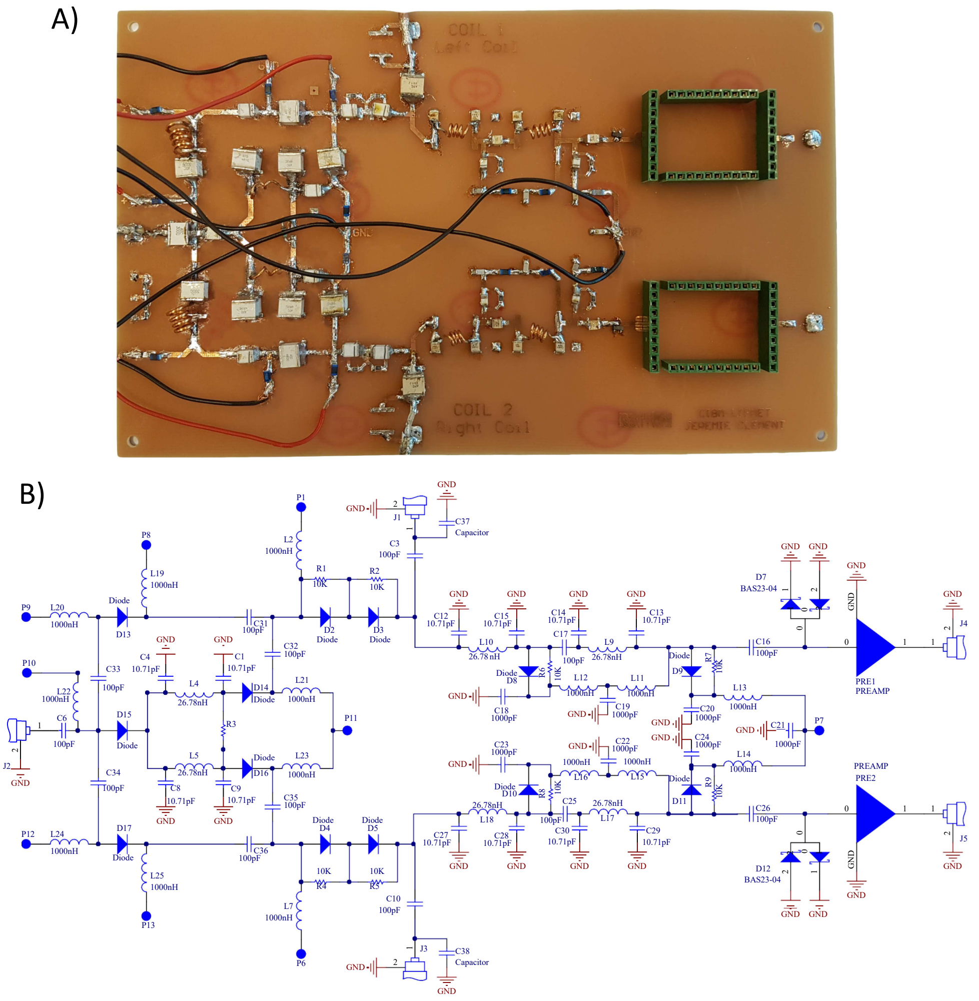
A)
COIL 1
Left Coil
COIL 2
Right Coil
GND
B)
P1
P6
P7
P8
P9
P10
P11
P12
P13
J1
J2
J3
J4
J5
GND
L2 1000nH
L19 1000nH
L20 1000nH
L22 1000nH
L24 1000nH
L25 1000nH
L7 1000nH
R1 10K
R2 10K
R4 10K
R5 10K
C3 100pF
C10 100pF
C37 Capacitor
C38 Capacitor
D2 Diode
D3 Diode
D4 Diode
D5 Diode
D13 Diode
D15 Diode
D17 Diode
D14 Diode
D16 Diode
C31 100pF
C32 100pF
C33 100pF
C34 100pF
C35 100pF
C36 100pF
C6 100pF
C4 10.71pF
C1 10.71pF
C8 10.71pF
C9 10.71pF
L4 26.78nH
L5 26.78nH
L21 1000nH
L23 1000nH
R3
C12 10.71pF
C15 10.71pF
C14 10.71pF
C13 10.71pF
C17 100pF
L10 26.78 nH
L9 26.78nH
D8 Diode
R6 10K
L12 1000nH
L11 1000nH
C18 1000pF
C19 1000pF
D9 Diode
R7 10K
C16 100pF
L13 1000nH
C20 1000pF
C24 1000pF
C21 1000pF
C23 1000pF
C22 1000pF
L16 1000nH
L15 1000nH
D10 Diode
R8 10K
D11 Diode
R9 10K
L14 1000nH
C25 100pF
L18 26.78nH
L17 26.78nH
C27 10.71pF
C28 10.71pF
C30 10.71pF
C29 10.71pF
C26 100pF
D7 BAS23-04
D12 BAS23-04
PRE1 PREAMP
PREAMP PRE2

Figure 5.3: *A) Photo of the complete TR switch for unilateral/bilateral RF excitation and B) corresponding schematics circuit.*

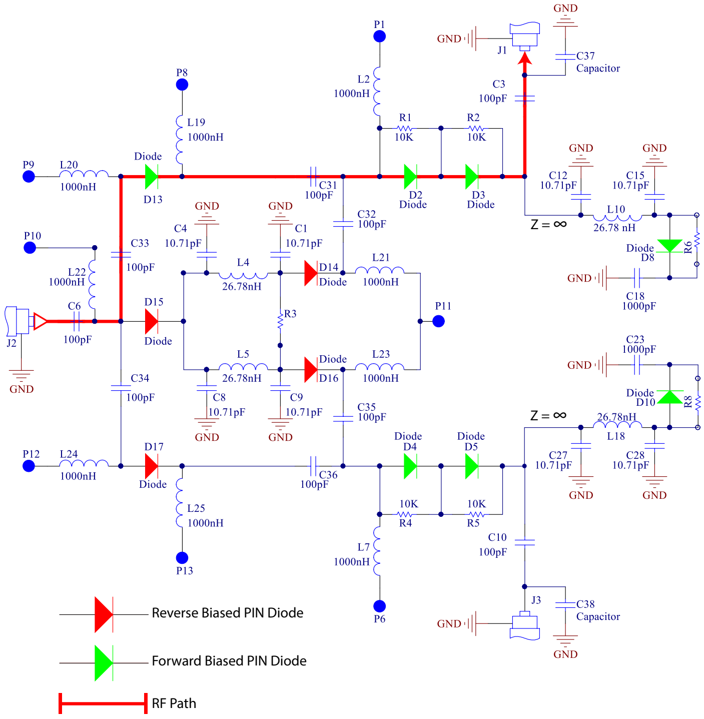
P1
GND
J1
C37
Capacitor
C3
100pF
L2
1000nH
R1
10K
R2
10K
P8
L19
1000nH
P9
L20
1000nH
Diode
D13
C31
100pF
D2
Diode
D3
Diode
GND
C12
10.71pF
GND
C15
10.71pF
L10
26.78 nH
Z = ∞
Diode
D8
R6
GND
C18
1000pF
P10
L22
1000nH
C33
100pF
GND
C4
10.71pF
GND
C1
10.71pF
C32
100pF
L4
26.78nH
D14
Diode
L21
1000nH
C6
100pF
D15
Diode
J2
GND
R3
P11
C23
1000pF
GND
Diode
D10
R8
L5
26.78nH
Diode
D16
L23
1000nH
C34
100pF
C8
10.71pF
C9
10.71pF
GND
GND
C35
100pF
Z = ∞
26.78nH
L18
Diode
D4
Diode
D5
P12
L24
1000nH
D17
Diode
C36
100pF
C27
10.71pF
C28
10.71pF
GND
GND
L25
1000nH
10K
R4
10K
R5
C10
100pF
L7
1000nH
P13
P6
J3
C38
Capacitor
GND
GND
Reverse Biased PIN Diode
Forward Biased PIN Diode
RF Path

Figure 5.4: *Schematics of the circuit showing the unilateral mode.*

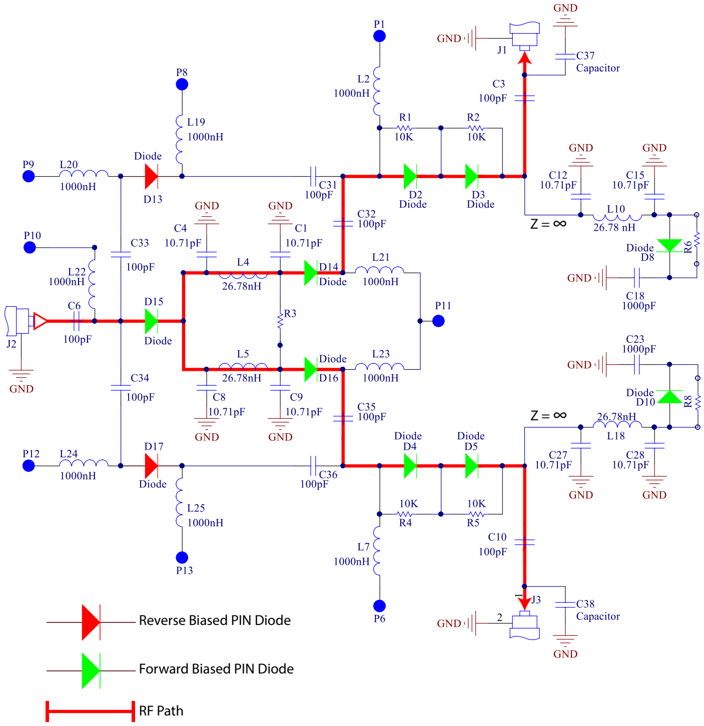
P1
GND
J1
C37
Capacitor
C3
100pF
L2
1000nH
R1
10K
R2
10K
P8
L19
1000nH
P9
L20
1000nH
Diode
D13
C31
100pF
D2
Diode
D3
Diode
GND
C12
10.71pF
GND
C15
10.71pF
L10
26.78 nH
Z = ∞
Diode
D8
R6
GND
C18
1000pF
P10
L22
1000nH
C33
100pF
GND
C4
10.71pF
GND
C1
10.71pF
C32
100pF
L4
26.78nH
D14
Diode
L21
1000nH
C6
100pF
D15
Diode
J2
GND
R3
P11
C23
1000pF
GND
Diode
D10
R8
L5
26.78nH
Diode
D16
L23
1000nH
C34
100pF
C8
10.71pF
C9
10.71pF
GND
GND
C35
100pF
Z = ∞
26.78nH
L18
Diode
D4
Diode
D5
P12
L24
1000nH
D17
Diode
C36
100pF
C27
10.71pF
C28
10.71pF
GND
GND
L25
1000nH
10K
R4
10K
R5
C10
100pF
L7
1000nH
P13
P6
J3
2
C38
Capacitor
GND
GND
Reverse Biased PIN Diode
Forward Biased PIN Diode
RF Path

Figure 5.5: *Schematics of the circuit showing the bilateral mode.*

270 mm and the total length 175 mm. The MR scanner bore was included (diameter = 400 mm, length = 280 mm), and defined as a perfect electric conductor (PEC). The dielectric pad (100 x 100 x 5 mm^3, $\epsilon_r = 160$), was added and placed either on the frontal lobe or the temporal lobe of the head model (Figure 5.6B). The coil was driven in quadrature by a Gaussian excitation centered at 297.2 MHz through two feeding ports (Figure 5.6A-i). The lumped elements values were initialized with the integrated birdcage builder tool, and adjusted to achieve a circularly-polarized (CP) mode.
The ETE and FRO loops were modeled as PEC elements, and their dimensions were defined as for the built loops (Figure 5.7). The positioning around Duke's head was precisely adjusted using the Solidworks model for the coil supports. Lumped elements were added to tune and match the RF coils. All the coils were driven individually by a harmonic excitation centered at 297.2 MHz and computations were carried out on a dedicated GPU (Nvidia Corp., USA) with an average simulation time of 20 minutes per channel. The lumped element values were adjusted by successive iterations according to the results of the simulations. After a few steps, the RF coils were tuned and matched better than -15 dB. In all the simulations, absorbing boundary conditions were applied at the edges of the simulation space to ensure that no reflected wave would interfere with the forward electromagnetic wave.

All the results were interpolated at 1 mm-iso inside a virtual box (200 x 250 x 230 mm^3) surrounding the head of the human model and normalized to 1 kW input power. The simulated B_1^+ maps were computed and compared to the measured maps for the birdcage coil, the ETE loops, and the FRO loops. With the dielectric pad in-place, the simulated transmit field maps for the birdcage coil were computed and the $SAR_{10g,max}$ value normalized to 1W input power was calculated to evaluate the influence of the pad on the RF safety limits.

5.2.4 MR Experiments

MR measurements were performed on a spherical phantom (diameter $\approx$ 180 mm, Siemens D165-10606820) and on human brain using a Magnetom 7T head-only MR scanner equipped with 8 x 1 kW RF amplifiers (Step 1, Siemens, Erlangen, Germany). For the ETE and FRO loops, the $SAR_{10g,max}$ values were calculated in simulations and used to determine the RF power limits. All the B_1^+ maps were acquired with a SA2RAGE sequence [102], and normalized to 1 kW total input peak-power. The transmit field efficiency was calculated for a voxel located in the temporal and frontal lobes, using respectively the ETE and the FRO loops. Spectroscopy measurements were performed with a semi-adiabatic spin-echo full intensity acquired localized (SPECIAL) sequence (VOI = 20 x 20 x 20 mm^3, TR/TE = 6500/16 ms, NA = 64). To position the MRS voxel, anatomical images were acquired with the MP2RAGE sequence [75].

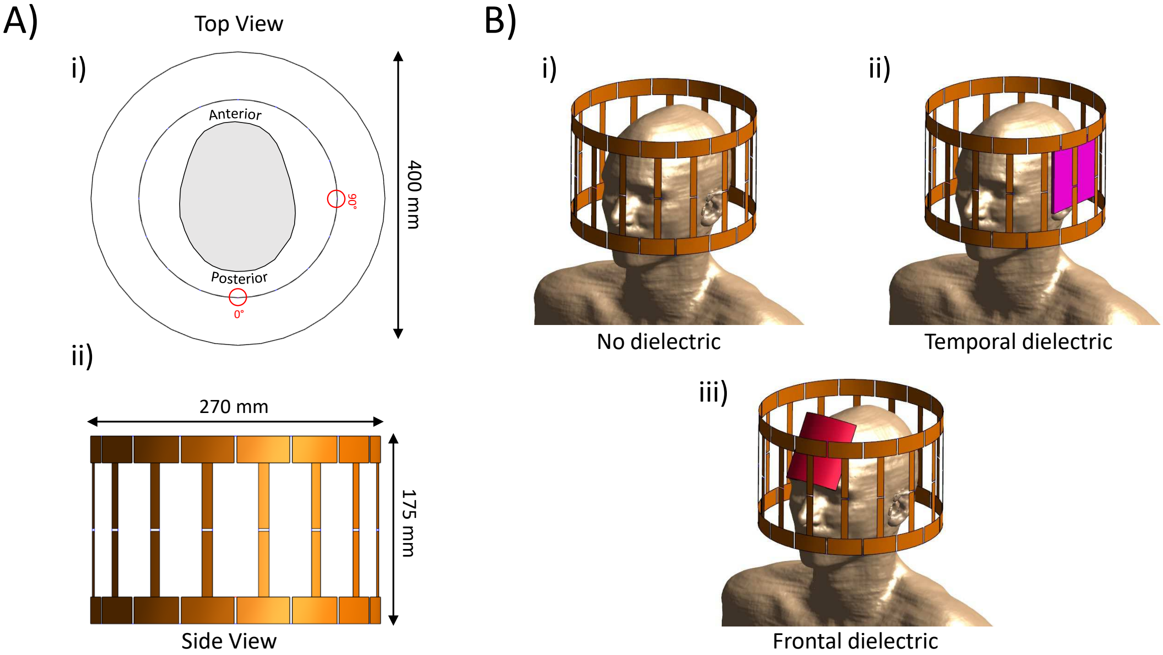
A)
Top View
i)
Anterior
Posterior
90°
0°
400 mm
ii)
270 mm
175 mm
Side View
B)
i)
ii)
No dielectric
Temporal dielectric
iii)
Frontal dielectric

Figure 5.6: *A) For the birdcage coil: i) Top view of the coil indicating the position of the quadrature feeding ports, and the shield dimension. ii) Side view of the coil with the dimensions indicated. B) Simulated model of the birdcage coil for i) no dielectric pad, ii) the dielectric pad placed over the temporal lobe, iii) the dielectric pad placed over the frontal lobe.*

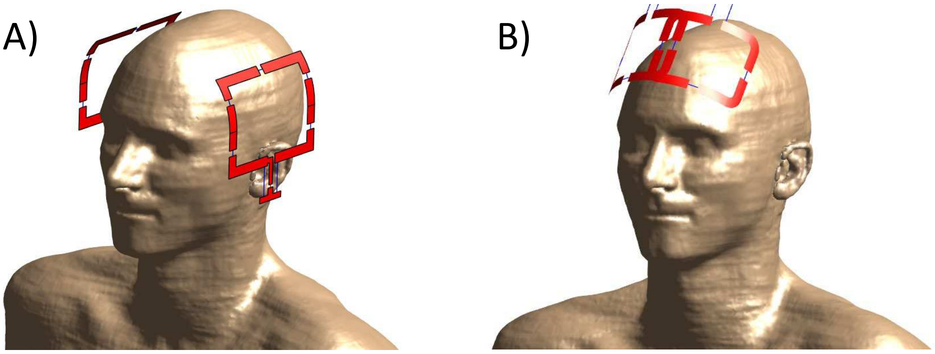

Figure 5.7: *Simulation model for A) the ETE loops and B) the FRO loops*

5.3 Results

The scattering curves and attenuation coefficients measured for the ETE loops TR switch are given in Figure 5.8. In unilateral left/right modes, a -2.1 dB attenuation was measured on the RF path from the input port to the coils (≈ 40% RF power loss), while the reflected power was negligible (less than 1%). No significant RF losses (⩽ 7%) were measured with the addition of the quadrature hybrid couplers in unilateral quadrature left/right modes (Figure 5.9A-B). In bilateral mode, the Wilkinson divider was well balanced (Figure 5.8C), and a -5.8 dB attenuation was measured on the corresponding RF paths. This represents a large RF power loss (almost 50% on each branch). In bilateral quadrature left/right modes, although only low losses were added by the quadrature hybrid couplers only 10% of the original power is really transferred to each of the coils. Nevertheless, when one transmit mode was active, the others RF paths were isolated better than -15 dB (Figure 5.8D). The receive path from the loop coils to the low-noise preamplifiers presented relatively low RF losses (less than 25%).

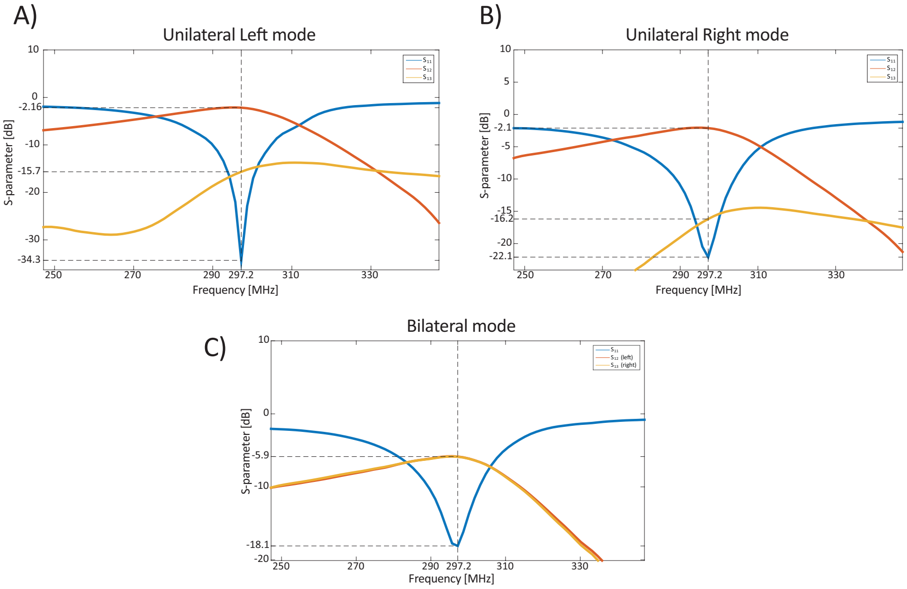

D)

Attenuation Coefficients

	ULM	URM	BM	Receive Path
Unilateral Left mode (ULM)	**-2.16 dB**	-15.7 dB	-16.2 dB	-1.19 dB
Unilateral Right mode (URM)	-16.2 dB	**-2.12 dB**	-15.7 dB	-1.02 dB
Bilateral mode (BM)	-16.2 dB	-15.7 dB	**-5.85/-5.88 dB**	-1.19/-1.02 dB

Figure 5.8: *Scattering curves for A) unilateral left mode, B) unilateral right mode, and C) bilateral mode. D) Attenuation coefficients corresponding to the three transmit modes.*

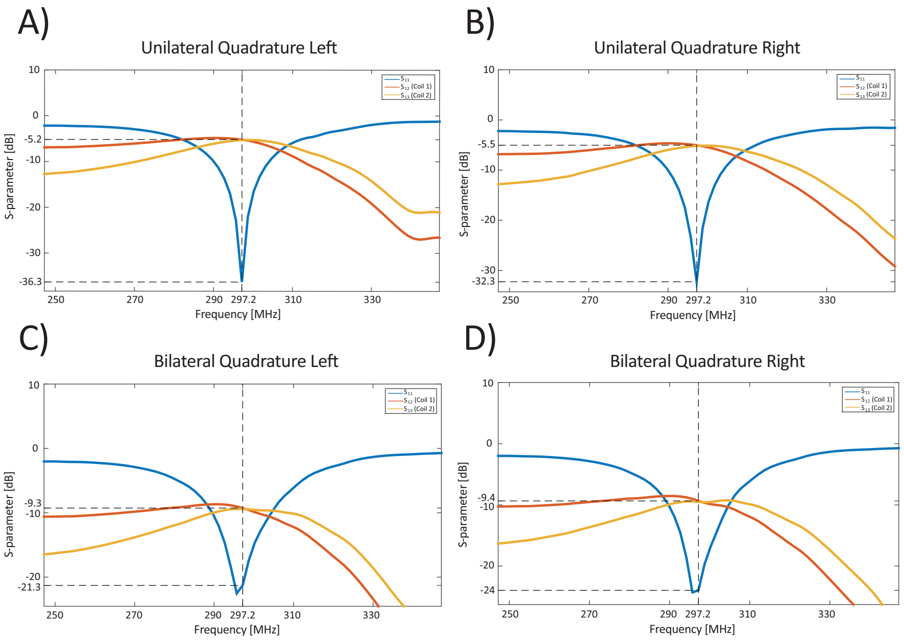

E)

Unilateral Left Mode to Left Coils	**-5.2 dB**
Unilateral Right Mode to Right Coils	**-5.5 dB**
Bilateral Mode to Left/Right Coils	**-9.3 dB / -9.4 dB**

Figure 5.9: *Scattering curves for A) and B) unilateral quadrature left/right modes. C) and D)Bilateral quadrature left/right modes. E) Attenuation coefficients corresponding to the three transmit modes.*

Measured and simulated B_1^+ maps demonstrated a good correlation for the ETE and FRO loops, and the commercial birdcage coil (Figure 5.10). High transmit field efficiency was achieved in the frontal lobe, using the quadrature mode of the FRO loops. On temporal side, the ETE loop produced a stronger transmit field compared to the commercial birdcage coil. A net increase of the transmit field intensity and uniformity was observed when using the quadrature ETE loops in unilateral modes (Figure 5.11A-B). However, the transmit field efficiency was impaired in bilateral quadrature mode by the large RF attenuation along the transmit path (Figure 5.11C).

An increase of the transmit field efficiency was observed in temporal and frontal lobes when the dielectric pad was added inside the commercial birdcage coil. Nevertheless, at the voxel-of-interest in temporal lobe the ETE loop achieved a mean B_1^+ value of 18.9 $\mu T/\sqrt{kW}$ while the commercial birdcage coil achieved 9.03 $\mu T/\sqrt{kW}$. In the frontal lobe, the FRO loops achieved a B_1^+ value of 29.5 $\mu T/\sqrt{kW}$, and the commercial coil 10.5 $\mu T/\sqrt{kW}$.

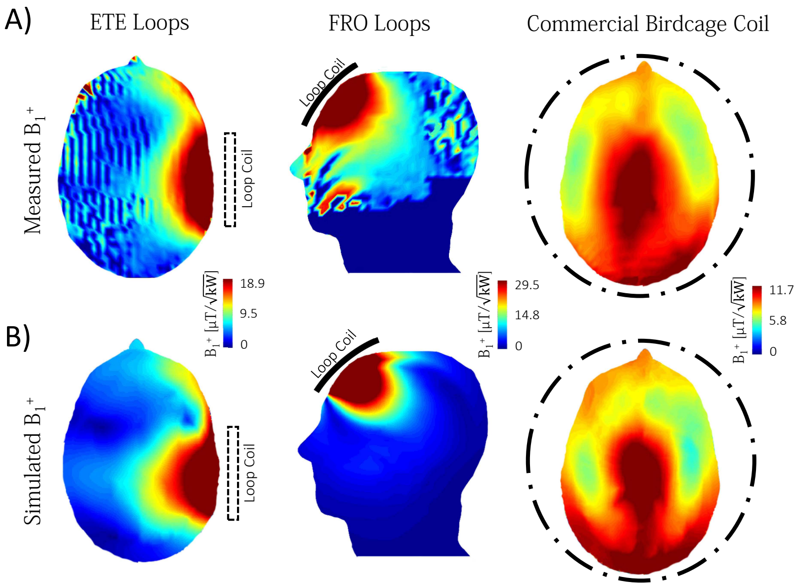
A)
ETE Loops
FRO Loops
Commercial Birdcage Coil
Measured B_1^+
Loop Coil
Loop Coil
B_1^+ [μT/√kW]
18.9
9.5
0
29.5
14.8
0
11.7
5.8
0
B)
Simulated B_1^+
Loop Coil
Loop Coil

Figure 5.10: *A) Experimentally measured and B) Simulated transmit field maps for the ETE and FRO loops, and the commercial birdcage coil, normalized to 1 kW total input peak-power.*

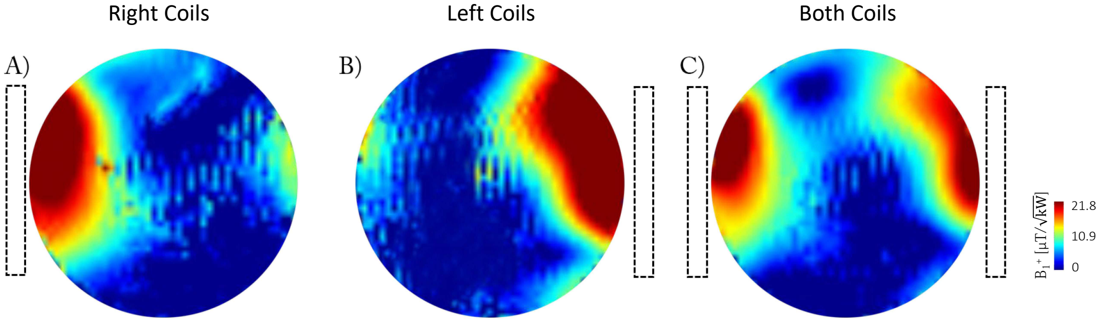

Figure 5.11: *Experimentally measured B_1^+ maps, normalized to 1 kW input peak-power, with the quadrature ETE loops and for: A) the unilateral quadrature right mode, B) the unilateral quadrature left mode and C) the bilateral quadrature mode. The measurements were acquired on a spherical phantom (⌀ ≈ 180 mm, Siemens D165-10606820).*

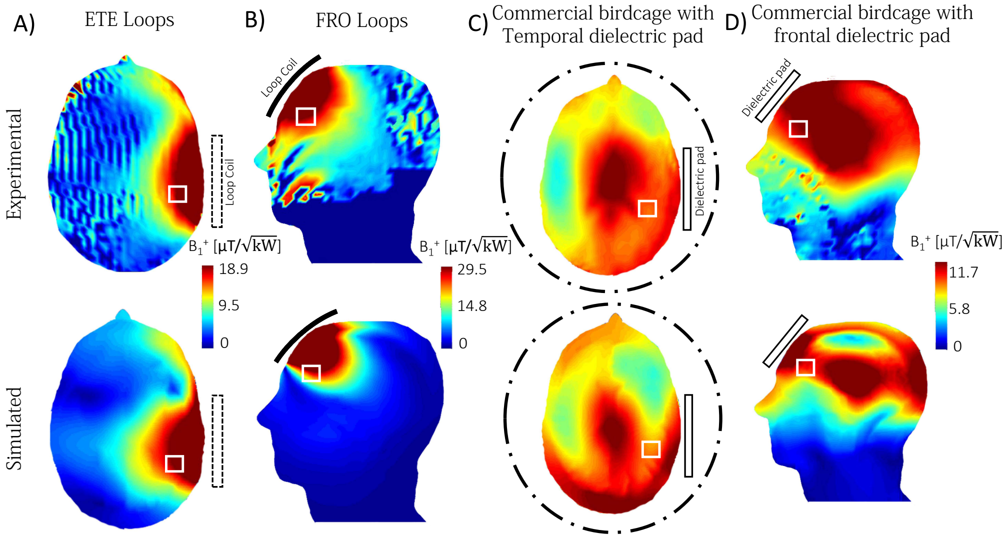
A)
ETE Loops
B)
FRO Loops
C) Commercial birdcage with Temporal dielectric pad
D) Commercial birdcage with frontal dielectric pad
Experimental
Simulated
Loop Coil
Loop Coil
Dielectric pad
Dielectric pad
B1+ [μT/√kW]
18.9
9.5
0
B1+ [μT/√kW]
29.5
14.8
0
B1+ [μT/√kW]
11.7
5.8
0

Figure 5.12: *Experimentally measured (upper row) and simulated (bottom row) transmit field maps for A) the ETE loops, B) the FRO loops, C) the commercial birdcage coil with the dielectric pad placed on temporal lobe, and D) the commercial birdcage with the dielectric pad placed on the frontal lobe.*

The $\mathrm{SAR}_{10g,max}$ value was increased by 11% for the birdcage coil when the dielectric pad was placed on frontal lobe, and located close to the pad (Figure 5.13D), while no variation was found when the pad was placed on temporal lobe (Figure 5.13C). Maximum SAR_{10g} values of 1.44 W/kg and 3.67 W/kg were calculated for the ETE and FRO loops, respectively (Figure 5.13A-B).

The MR spectra acquired with the FRO loops and the commercial birdcage coil demonstrated similar profiles. However, a 11% increase in SNR was measured for the NAA (N-acetylaspartate) peak when using the FRO loops. The measured concentrations in metabolites were consistent with the results obtained on the commercial birdcage coil (Figure 5.15).

While with the ETE loop an MR spectra could be acquired in the temporal lobe (Figure 5.16A), the commercial birdcage coil exceeded the RF power limits with the dielectric pad in-place. No MR spectra could therefore be acquired for comparison. The high-resolution (0.6 mm-iso) MR images demonstrated a large coverage of the temporal lobes in bilateral and unilateral transmit modes (Figure 5.16B).

5.4 Discussion

In this study, two different coil setups were built and evaluated. The Ear-to-Ear (ETE) loops aimed to improved the RF signal in the temporal lobes of the brain while the frontal-region-operating (FRO) loops covered the frontal lobe. The spectroscopy results were compared to a commercial birdcage coil using a dielectric pad to enhance the transmit field in the areas of interest.

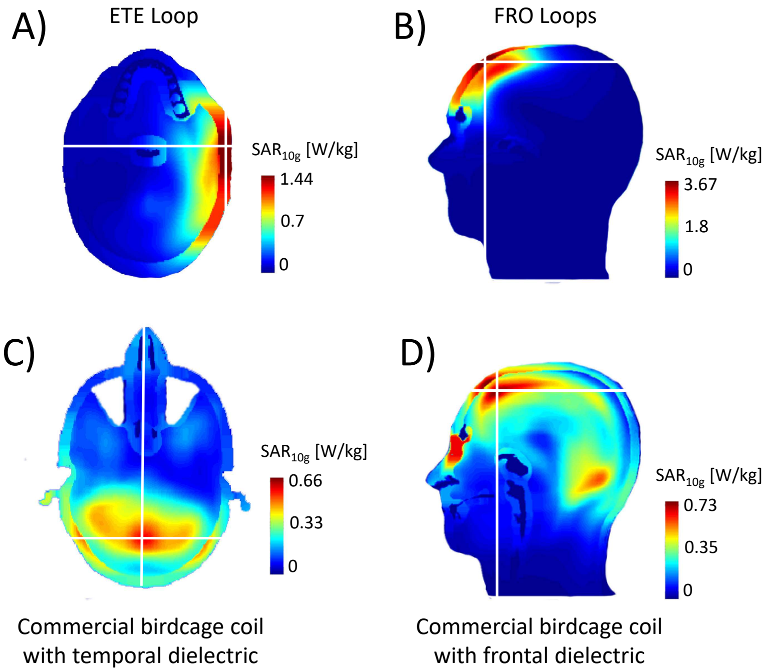
A)
ETE Loop
SAR10g [W/kg]
1.44
0.7
0
B)
FRO Loops
SAR10g [W/kg]
3.67
1.8
0
C)
SAR10g [W/kg]
0.66
0.33
0
D)
SAR10g [W/kg]
0.73
0.35
0
Commercial birdcage coil with temporal dielectric
Commercial birdcage coil with frontal dielectric

Figure 5.13: *SAR_{10g} maps shown for A) the ETE loops, B) the FRO loops, C) and D) the commercial birdcage coil with the dielectric pad placed on temporal and frontal lobe, respectively. The maps were scaled to the maximum SAR_{10g} value, and the white cross indicate the position of the maximum.*

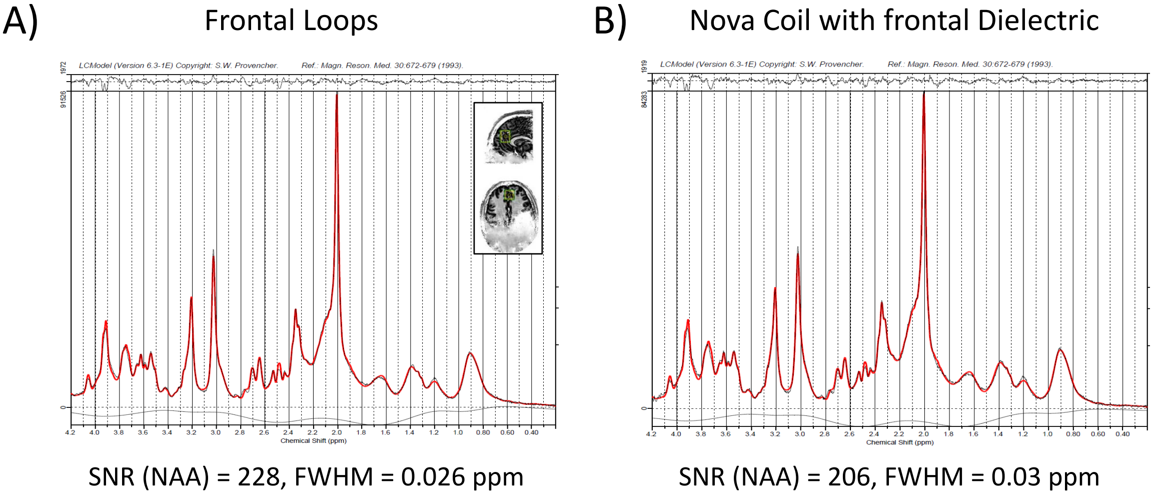

Figure 5.14: *For the FRO loops and the commercial birdcage coil: MR spectra acquired in the VOI.*

The presence of the dielectric pads inside the commercial birdcage coil improved the transmit-field efficiency in the temporal and frontal lobes, respectively. However, in the

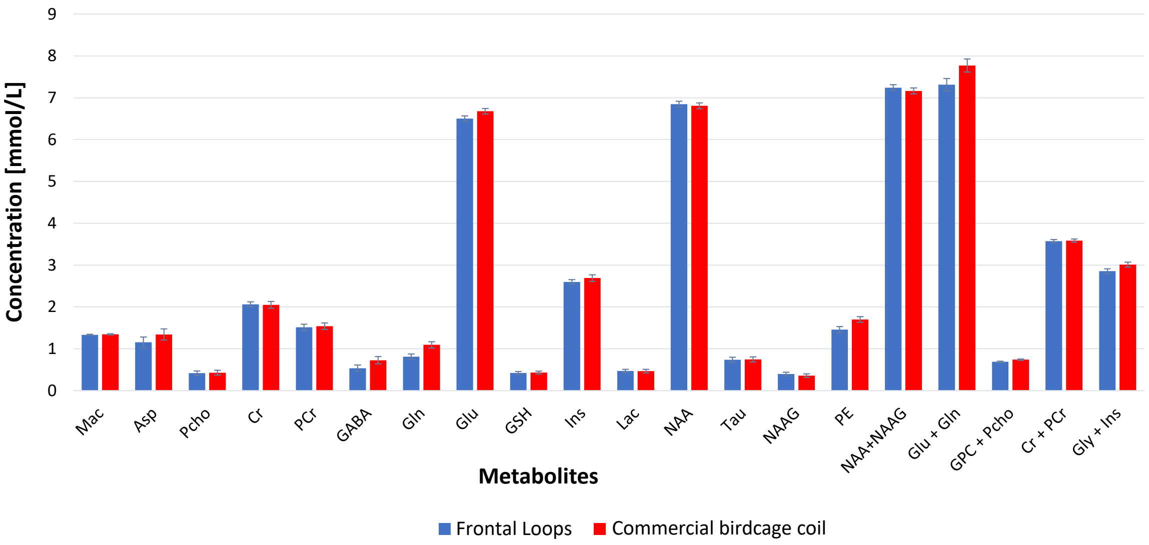

Figure 5.15: *For the FRO loops and the commercial birdcage coil: Metabolites concentration measured in the VOI.*

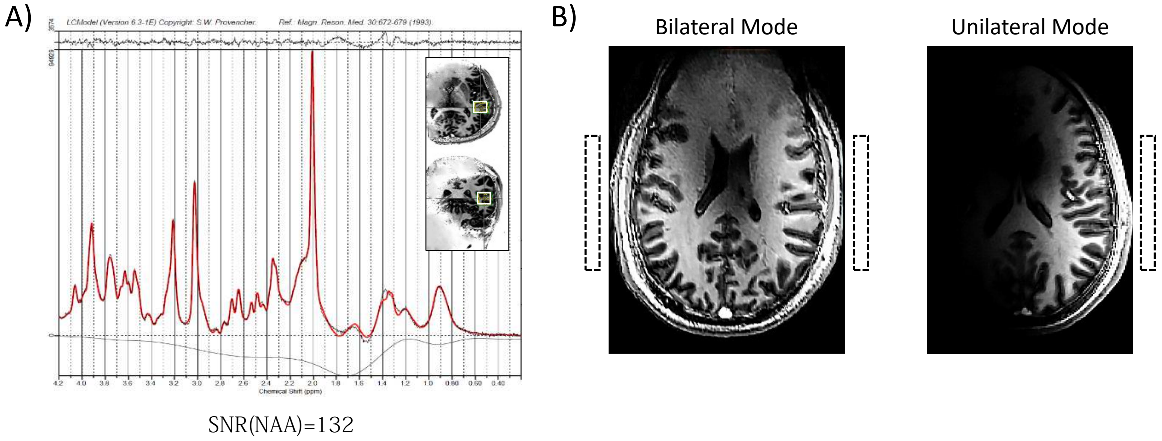
A)
LCModel (Version 6.3-1E) Copyright: S.W. Provencher.
Ref.: Magn. Reson. Med. 30:672-679 (1993).
4.2
4.0
3.8
3.6
3.4
3.2
3.0
2.8
2.6
2.4
2.2
2.0
1.8
1.6
1.4
1.2
1.0
0.80
0.60
0.40
Chemical Shift (ppm)
SNR(NAA)=132
B)
Bilateral Mode
Unilateral Mode

Figure 5.16: *For the ETE loops: A) MR spectrum acquired in unilateral right mode and B) MP2RAGE images shown in transverse and coronal orientations*

frontal lobe, the B_1^+ field efficiency measured with the FRO loops was largely superior compared to the commercial birdcage coil (Figure 5.12B-D). The high transmit field efficiency lead to a high $SAR_{10g,max}$ value for the FRO loops (40% stronger compared to the commercial birdcage coil). Nevertheless, MR spectra were acquired with both the FRO and the commercial birdcage coil. Only a slight increase in SNR was measured with the FRO loops in the voxel-of-interest, which was expected since 32-channel receive-only loop coils are used in combination with the commercial birdcage coil. The metabolite concentrations were consistent between the two coils.

With the ETE loops, a net increase of the transmit field efficiency was measured in the temporal lobes compared to the commercial birdcage coil with dielectric pad. Moreover, while a MR spectrum could be acquired with the ETE loops, the commercial birdcage coil did not achieve sufficient B_1^+ field without exceeding the RF safety limits. The improvements observed with the dielectric pad are sensitive to the placement of the pad and the exact position of the voxel-of-interest. Moreover, the compounds could be modified to get higher efficiency, and enable MR spectroscopy in the temporal lobes with the commercial birdcage coil. The B_1^+-field asymmetry observed with the ETE loops (Figure 5.10A) was addressed by using two loop coils on each side which were fed in quadrature.

The remotely-controlled TR switch enabled unilateral/bilateral operation modes for the ETE-loops. Each mode could be selected by switching on the corresponding PIN-diodes through the bed DC-lines and the exam card. In unilateral mode, the RF losses were limited to 40% of the input power while in bilateral mode, large RF losses were measured. This may originate from an inadequate RF circuit or a non-optimal impedance matching of the line from the input to the RF coils. However, the use of the quadrature hybrid couplers to feed the quadrature ETE loops did not generate significant additional RF losses. This circuit design enables an automated and user-friendly switching controlled directly by the MR exam card for unilateral/bilateral MR acquisitions; therefore, coil structure and patient positions can stay fixed during the MR examination.

5.5 Conclusion

In the present study two different coil setups were investigated for enhanced MR spectroscopy in the temporal and frontal lobes of the human brain at 7T. The ETE and FRO loops were built and the performances were evaluated in comparison with a commercial birdcage including 32-channel receivers. A slight increase in SNR was measured for the FRO loops in comparison with the commercial birdcage coil. In the temporal lobes, the commercial birdcage coil lacked transmit field efficiency. Therefore, no MR spectrum could be acquired while the ETE loops demonstrated robust results in this area. We conclude that the construction of dedicated surface loop coils is a valuable alternative to the birdcage coil with dielectric pads for 7T MR applications in the human brain.

6

General conclusion and outlook

6.1 Main conclusions

This thesis was dedicated to investigate innovative radio-frequency coil designs for parallel-transmit whole-brain magnetic resonance (MR) at 7T.

It was demonstrated that center-shortened dipoles represent an efficient approach to address the challenges at ultra-high fields. When they were combined into a tight-fitted array for the human head imaging, a large coverage was achieved including highly-challenging regions as the cerebellum. A high decoupling between the closely placed dipoles was demonstrated when using a passive scatterer approach (Chapter 2). The transmit field efficiency achieved with the dipole coil array was comparable to previously reported RF coil array designs at 7T human head magnetic resonance (see Chapter 1 section 1.5.6 and Chapter 2).

The construction of a 32-channel receive loop coil array to be combined with the transmit dipole coil array represents one of the most challenging achievement of this thesis (Chapter 3). Both arrays could be combined within dimensions constrained by the head-only MR system. Particularly, the geometrical arrangement of the receivers and cable management was optimized with respect to the center-shortened dipoles. It was demonstrated that the transmit field efficiency is not substantially decreased by the presence of receivers, while higher SNR levels could be achieved compared to the 8-channel transmit/receive dipole coil array. The noise correlation coefficients demonstrated the appropriate decoupling between all the receivers. Compared to a commercial 32-channel receive array, higher performances were achieved in the cerebellum in terms of SNR while comparable results were obtain in the cerebral cortex.

To get an high and homogeneous B_1^+-field over the human brain, an efficient optimization tool for the individual RF fields was required. In this thesis, the particle-swarm optimization (PSO) algorithm was investigated and implemented into a user-friendly graphical interface (Chapter 4). It was demonstrated that the PSO algorithm was efficient to optimize the RF phases over large regions in the human brain whereas a mathematical approach failed to provide homogeneous coverage. Moreover, further investigations demonstrated that the variability in terms of transmit field distribution between different subjects was limited when a reference set of RF phases was applied.

It was demonstrated in this thesis that dedicated RF coils are a valuable alternative to a birdcage coil with dielectric pads in the aim to address the lack of transmit field in regions as the temporal and frontal lobes of the human brain (Chapter 5). A significantly higher transmit field efficiency was achieved with the surface coils, while in the temporal lobes a birdcage coil with dielectric pads could not achieve sufficient B_1^+-field to perform spectroscopy acquisitions. Moreover, the dedicated TR-switch designed for the temporal surface loop coils (ETE-loops) enabled three different transmission modes which could limit the presence of lipid contamination in the MR spectra acquired on only one of the temporal lobes.

In conclusion, this thesis provides an in-depth view on MR engineering of RF coils at ultra-high field. It includes the development and clear description of transmit and receive coil arrays, RF phase shimming methods and dedicated RF coils for MR spectroscopy in highly-challenging regions of the human brain at 7T.

6.2 Outlook

What is next ? There is nowadays an increasing interest into pushing the MRI research into stronger magnetic fields. The 7T Magnetom Terra (Siemens, Erlangen, Germany) MR scanner is now approved in Europe [159] and United States [160] for clinical use but limited to examinations of the head, arms and legs. In the next years, it is foreseeable that public and private institutions will invest in these systems to benefit from the advantages offered by 7T MR scanners. However, whole-body 9.4T and 10.5T human MR scanner already exist and even higher magnetic fields strengths are envisaged. The increased SNR would contribute to the visualization of previously unseen structures and could enable sub-millimeter BOLD fMRI. Nevertheless, there are consequent challenges. The shorter wavelength in human body tissues results in stronger signal inhomogeneities. The safety of patients is also a main concern since with higher RF frequencies the power deposition in the tissues is increased. In this context, parallel-transmit methods and RF coils array engineering are crucial for the future of magnetic resonance at ultra-high field in clinical routine. While in research it is common to develop and use the RF coils on healthy subjects, clinical applications cannot be restrained to this. Therefore, RF coil designs and safety evaluation must consider situations where the subjects may have implants or cardio-vascular impairments. We believe the opportunities in terms of RF field shimming offered by individual transmit elements combined into an array will contribute to address the new challenges and provide the medical staff with robust and reliable tools to exploit the potential of ultra-high field. The transmit RF fields could be e.g tailored to exclude precisely the regions presenting an implant or could be optimized such that power deposition is strictly controlled when non-healthy subjects are scanned. In this context, the RF coil developed during this thesis may represent only a small step but it provides an insight of the possibilities in terms of RF coil design at ultra-high field parallel-transmit ; whose methods (RF phase shimming, RF pulse optimization etc.) represent the future of magnetic resonance in clinical applications. Dedicated RF coils could be optimal to get ultra-high resolution (lower than 0.5 mm-iso) anatomical images of local regions as it was demonstrated in this thesis that high SNR and transmit field efficiency were achievable. Combined tight-fitted multi-channel transmit and receive arrays may offer the possibility to perform fast acquisitions over the whole-brain without significant loss of SNR and with homogeneous B_1^+ field coverage.

MR imaging applications The 8-channel transmit/32-channel receive dipole coil array presented in this thesis allows a full coverage of the human brain at 7T MR imaging. Notably, the cerebellum can be imaged at high-resolution without visible drops in signal or inhomogeneities. It is known that the cerebellum plays a crucial role in the motor control system. Having the possibility to acquire robust results in the cerebellum is therefore of the utmost interest to get a better understanding of all the functionalities related with this structure of the human brain. Nevertheless, the strength of this RF coil array design is not limited to the cerebellum region. It was demonstrated that all the regions of the human brain could be covered simultaneously. Moreover, the additional receive sensitivity provided by the 32-channel loop coil array over the entire human brain volume could contribute to enhanced performances in the lower areas of the brain. Combined to the high capabilities in RF phase shimming, the possibility to image very small structures at high resolution is a possible outcome of the thesis work. One application is e.g to get high-resolution structural information about the inner ear. This crucial part of the auditory pathway is located at the cerebellum-level, and surrounded by air. By optimizing the RF phases specifically on this region high transmit field efficiency could be achieved.

RF safety improvements The particle-swarm algorithm demonstrated high performances in RF phases optimization. However, the RF safety limits were set according to the worst-case local SAR for all the data acquired with the 8-channel transmit/32-channel receive dipole coil array. Therefore, the power used to perform MR imaging or functional MRI in the human brain was decreased to ensure subject's safety. The adaptability of parallel-transmit methods to clinical routine strongly depends on the possibility to estimate accurately the

RF safety limits when using a RF coil array. It is a very actual field of investigations since the first 7T clinical MR scanners are coming out. By deriving the RF power limits from the optimized RF phases, more applications as MR spectroscopy or diffusion could be available. In this thesis, the possibility to use the same set of optimized RF phases with subjects presenting variations in head shape and size was demonstrated. This represents a valuable step for clinical routine since the RF-phase optimization procedure is time-consuming and could require some prior-knowledge or expertise about the RF coil array design. According to the results shown in this thesis a database of RF phase settings could be created, specific to the RF coil array, but applicable in any situation.

List of Symbols

Symbol	Description
B_0	Main magnetic field
ω_0	Larmor frequency
γ	Gyromagnetic ratio
h	Planck's constant
B_1	RF magnetic field
B_1^+	Component of B_1 rotating in the counter-clockwise direction
B_1^-	Component of B_1 rotating in the clockwise direction
B_{eff}	Effective magnetic field
$\vec{M}$	Magnetization vector
$N_\uparrow, N_\downarrow$	Spin populations on states up and down (^1H atom)
T	Temperature
T_1	Longitudinal relaxation time
T_2	Transverse relaxation time
T_2^*	Transverse relaxation time affected by B_0 non-uniformities
$\Delta B_0(\vec{r})$	B_0 field non-uniformities
α	Flip angle amplitude
$\vec{S}$	Nuclear spin
$\vec{\mu}$	Magnetic dipole moment
k_B	Boltzmann's constant
M_0	Magnetization at thermal equilibrium
ρ	Number of protons per unit volume
$\vec{e}_x, \vec{e}_y, \vec{e}_z$	Unit vectors in the lab frame
$\vec{e}_{x'}, \vec{e}_{y'}, \vec{e}_{z'}$	Unit vectors in the rotating frame
ζ	Electromotive force
g_ρ	g-factor
$\vec{E}$	Electric field
$\sigma(\vec{r})$	Electric conductivity distribution
λ	RF wavelength
c	Speed of light
ϵ_r	Relative permittivity
M_{xy}	Magnetization in the transverse plane
M_z	Longitudinal magnetization

List of Abbreviations

Acronym	Meaning
NMR	Nuclear Magnetic Resonance
MRI	Magnetic Resonance Imaging
fMRI	functional MRI
SNR	Signal to Noise Ratio
RF	Radio Frequency
TSE	Turbo Spin Echo
T	Tesla
FID	Free Induction Decay
WM	White Matter
GM	Gray Matter
GRE	Gradient-recall Echo
FOV	Field Of View
TR	Repetition Time
TE	Echo Time
TA	Acquisition Time
TALES	Transmit Antenna LEvel Sensor
SAR	Specific Absorption Rate
PTx	Parallel Transmission
SENSE	SENSitivity Encoding
FWHM	Full Width at Half Maximum
SA2RAGE	SAturation prepared with 2 RApid Gradient Echoes
PSO	Particle-Swarm Optimization
FA	Flip Angle
Rx	Receiver
Tx	Transmitter
VNA	Vector Network Analyzer
TR-switch	Transmit-Receive switch
FDTD	Finite-Difference Time-Domain
VOP	Virtual Observation Points
PALI	Power Absorption LImiter
DICO	DIrectional COupler

Bibliography

[1] I. I. Rabi, J. R. Zacharias, S. Millman, and P. Kusch. A New Method of Measuring Nuclear Magnetic Moment. *Physical Review*, 53(4):318–318, February 1938. 1.1

[2] Walther Gerlach and Otto Stern. Der experimentelle Nachweis der Richtungsquantelung im Magnetfeld. *Zeitschrift für Physik*, 9(1):349–352, December 1922. 1.1

[3] W. Pauli. Zur Quantenmechanik des magnetischen Elektrons. *Zeitschrift für Physik*, 43(9):601–623, September 1927. 1.1

[4] F. Bloch. Nuclear Induction. *Physical Review*, 70(7-8):460–474, October 1946. 1.1

[5] E. M. Purcell, H. C. Torrey, and R. V. Pound. Resonance Absorption by Nuclear Magnetic Moments in a Solid. *Physical Review*, 69(1-2):37–38, January 1946. 1.1

[6] E. L. Hahn. Nuclear Induction Due to Free Larmor Precession. *Physical Review*, 77(2):297–298, January 1950. 1.1

[7] E. L. Hahn. Spin Echoes. *Physical Review*, 80(4):580–594, November 1950. 1.1

[8] P. C. Lauterbur. Image Formation by Induced Local Interactions: Examples Employing Nuclear Magnetic Resonance. *Nature*, 242(5394):190, March 1973. 1.1

[9] R. R. Ernst and W. A. Anderson. Application of Fourier Transform Spectroscopy to Magnetic Resonance. *Review of Scientific Instruments*, 37(1):93–102, January 1966. 1.2.2.5

[10] D. I Hoult and R. E Richards. The signal-to-noise ratio of the nuclear magnetic resonance experiment. *Journal of Magnetic Resonance (1969)*, 24(1):71–85, October 1976. 1.3.1, 1.3.1.1

[11] John D. Kraus and Ronald J. Marhefka. *Antennas for All Applications*. Tata McGraw-Hill, second edition edition, 1997. 1.3.1.1

[12] A. J. E. Raaijmakers, O. Ipek, D. W. J. Klomp, C. Possanzini, P. R. Harvey, J. J. W. Lagendijk, and C. A. T. van den Berg. Design of a radiative surface coil array element at 7 T: The single-side adapted dipole antenna. *Magnetic Resonance in Medicine*, 66(5):1488–1497, November 2011. 1.3.3.1, 1.3.3.2, 1.5.6, 2.1, 3.1

[13] A. J. E. Raaijmakers, P. R. Luijten, and C. A. T. van den Berg. Dipole antennas for ultrahigh-field body imaging: A comparison with loop coils. *NMR in Biomedicine*, 29(9):1122–1130, September 2016. 1.3.3.1, 1.3.3.1, 1.3.3.3

[14] Xiaoliang Zhang, Kamil Ugurbil, and Wei Chen. Microstrip RF surface coil design for extremely high-field MRI and spectroscopy. *Magnetic Resonance in Medicine*, 46(3):443–450, September 2001. 1.3.3.2, 1.3.3.2, 1.3.3.2, 1.3.3.2

[15] Jérémie D. Clément, Rolf Gruetter, and Özlem Ipek. A human cerebral and cerebellar 8-channel transceive RF dipole coil array at 7T. *Magnetic Resonance in Medicine*, 0(0). 1.3.3.3, 1.5.6, 3.1, 3.2.2, 3.3

[16] Gregor Adriany, Edward J. Auerbach, Carl J. Snyder, Ark Gözübüyük, Steen Moeller, Johannes Ritter, Pierre-François Van de Moortele, Tommy Vaughan, and Kâmil Uğurbil. A 32-channel lattice transmission line array for parallel transmit and receive MRI at 7 tesla. *Magnetic Resonance in Medicine*, 63(6):1478–1485, June 2010. 1.3.3.3, 1.6.4.1, 1.6.4.1, 3.1

[17] T W Redpath. Signal-to-noise ratio in MRI. *T he British Journal of Radiology*, page 4, 1998. 1.3.3.4

[18] J.T. Vaughan, G. Adriany, M. Garwood, E. Yacoub, T. Duong, L. DelaBarre, P. Andersen, and K. Ugurbil. Detunable transverse electromagnetic (TEM) volume coil for high-field NMR. *Magnetic Resonance in Medicine*, 47(5):990–1000, 2002. 1.3.3.4, 1.3.3.4, 1.3.3.4, 1.3.4.2, 2.1, 3.1

[19] P. Röschmann. Radiofrequency penetration and absorption in the human body: Limitations to high-field whole-body nuclear magnetic resonance imaging. *Medical Physics*, 14(6):922–931, 1987. 1.3.3.4

[20] J. B. Johnson. Thermal Agitation of Electricity in Conductors. *Physical Review*, 32(1):97–109, July 1928. 1.3.3.4

[21] H. Nyquist. Thermal Agitation of Electric Charge in Conductors. *Physical Review*, 32(1):110–113, July 1928. 1.3.3.4

[22] Andrew G. Webb and Christopher M. Collins. Parallel transmit and receive technology in high-field magnetic resonance neuroimaging. *International Journal of Imaging Systems and Technology*, 20(1):2–13, March 2010. 1.3.4, 1.3.4.1, 2.1, 3.1

[23] CE Hayes, WA Edelstein, JF Schenck, OM Mueller, and M. Eash. An Efficient, Highly Homogeneous Radiofrequency Coil for Whole-Body NMR Imaging at 1.5T. *J Magn Reson*, 63:622–628, 1985. 1.3.4.1, 2.1, 3.1, 5.1

[24] H. Barfuss, H. Fischer, D. Hentschel, R. Ladebeck, A. Oppelt, R. Wittig, W. Duerr, and R. Oppelt. In vivo magnetic resonance imaging and spectroscopy of humans with a 4 t whole-body magnet. *NMR in Biomedicine*, 3(1):31–45, February 1990. 1.3.4.1

[25] Christopher M. Collins, Wanzhan Liu, Weston Schreiber, Qing X. Yang, and Michael B. Smith. Central brightening due to constructive interference with, without, and despite dielectric resonance. *Journal of Magnetic Resonance Imaging*, 21(2):192–196, February 2005. 1.3.4.1, 2.1, 3.1, 5.1

[26] Tamer S Ibrahim, Robert Lee, Brian A Baertlein, Amir M Abduljalil, Hui Zhu, and Pierre-Marie L Robitaille. Effect of RF coil excitation on field inhomogeneity at ultra high fields: A field optimized TEM resonator. *Magnetic Resonance Imaging*, 19(10):1339–1347, December 2001. 1.3.4.2

[27] Chunsheng Wang and Gary X. Shen. B1 field, SAR, and SNR comparisons for birdcage, TEM, and microstrip coils at 7T. *Journal of Magnetic Resonance Imaging*, 24(2):439–443, 2006. 1.3.4.2

[28] Yee Kane. Numerical solution of initial boundary value problems involving maxwell's equations in isotropic media. *IEEE Transactions on Antennas and Propagation*, 14(3):302–307, May 1966. 1.4.1

[29] Ozlem Ipek, Alexander J. Raaijmakers, Jan J. Lagendijk, Peter R. Luijten, and Cornelis A. T. van den Berg. Intersubject local SAR variation for 7T prostate MR imaging with an eight-channel single-side adapted dipole antenna array. *Magnetic Resonance in Medicine*, 71(4):1559–1567, 2014. 1.4.2, 2.2.5.3, 3.2.3

[30] Tongning Wu, Liwen Tan, Qing Shao, Chen Zhang, Chen Zhao, Ying Li, Emmanuelle Conil, Abdelhamid Hadjem, Joe Wiart, Bingsong Lu, Li Xiao, Nan Wang, Yi Xie, and Shaoxiang Zhang. Chinese adult anatomical models and the application in evaluation of RF exposures. *Physics in Medicine and Biology*, 56(7):2075–2089, March 2011. 1.4.2

[31] Tomoaki Nagaoka, Soichi Watanabe, Kiyoko Sakurai, Etsuo Kunieda, Satoshi Watanabe, Masao Taki, and Yukio Yamanaka. Development of realistic high-resolution whole-body voxel models of Japanese adult males and females of average height and weight, and application of models to radio-frequency electromagnetic-field dosimetry. *Physics in Medicine and Biology*, 49(1):1–15, December 2003.

[32] Chan Hyeong Kim, Sang Hyoun Choi, Jong Hwi Jeong, Choonsik Lee, and Min Suk Chung. HDRK-Man: A whole-body voxel model based on high-resolution color slice images of a Korean adult male cadaver. *Physics in Medicine and Biology*, 53(15):4093–4106, July 2008.

[33] J. Gao, I. Munteanu, W. F. O. Müller, and T. Weiland. Generation of postured voxel-based human models for the study of step voltage excited by lightning current. *Advances in Radio Science*, 9:99–105, July 2011.

[34] G. M. Noetscher, A. T. Htet, N. D. Maino, and P. A. Lacroix. The Visible Human Project male CAD based computational phantom and its use in bioelectromagnetic simulations. In *2017 39th Annual International Conference of the IEEE Engineering in Medicine and Biology Society (EMBC)*, pages 4227–4230, July 2017.

[35] MC Gosselin, E Neufeld, and H et al. Moser. Development of a new generation of high-resolution anatomical models for medical device evaluation: The Virtual Population 3.0. *Physics in Medicine and Biology*, 59(18):5287, 2014. 1.4.2, 2.2.3, 3.2.3, 5.2.3

[36] E. Zastrow, S. K. Davis, M. Lazebnik, F. Kelcz, B. D. V. Veen, and S. C. Hagness. Development of Anatomically Realistic Numerical Breast Phantoms With Accurate Dielectric Properties for Modeling Microwave Interactions With the Human Breast. *IEEE Transactions on Biomedical Engineering*, 55(12):2792–2800, December 2008. 1.4.2

[37] P. C. Miranda, R. Salvador, C. Wenger, and S. R. Fernandes. Computational models of non-invasive brain and spinal cord stimulation. In *2016 38th Annual International Conference of the IEEE Engineering in Medicine and Biology Society (EMBC)*, pages 6457–6460, August 2016.

[38] Nikos Makris, Leonardo Angelone, Seann Tulloch, Scott Sorg, Jonathan Kaiser, David Kennedy, and Giorgio Bonmassar. MRI-based anatomical model of the human head for specific absorption rate mapping. *Medical & Biological Engineering & Computing*, 46(12):1239–1251, December 2008. 1.4.2

[39] F. Bardati, A. Borrani, A. Gerardino, and G. A. Lovisolo. SAR optimization in a phased array radiofrequency hyperthermia system. *IEEE Transactions on Biomedical Engineering*, 42(12):1201–1207, December 1995. 1.4.2.2

[40] Gabriele Eichfelder and Matthias Gebhardt. Local specific absorption rate control for parallel transmission by virtual observation points. *Magnetic Resonance in Medicine*, 66(5):1468–1476, November 2011. 1.4.2.2, 1.4.2.2, 1.5.2, 4.4

[41] P. B. Roemer, W. A. Edelstein, C. E. Hayes, S. P. Souza, and O. M. Mueller. The NMR phased array. *Magnetic Resonance in Medicine*, 16(2):192–225, November 1990. 1.5.5, 1.6, 1.6.1, 1.6.2, 3.1, 3.1

[42] Xiaozhong Zhang and Andrew Webb. Design of a capacitively decoupled transmit/receive NMR phased array for high field microscopy at 14.1T. *Journal of Magnetic Resonance*, 170(1):149–155, September 2004. 1.5.5

[43] Takayuki Nabeshima, Tetsuhiko Takahashi, Yoshikuni Matsunaga, Etsuji Yamamoto, and Kageyoshi Katakura. RF probe for MRI, 1996. US Patent 5,489,847. 1.5.5

[44] Nikolai I. Avdievich. Transceiver-Phased Arrays for Human Brain Studies at 7 T. *Applied magnetic resonance*, 41(2-4):483–506, December 2011. 1.5.5, 1.5.6, 2.1, 2.4

[45] Kyle M. Gilbert, Andrew T. Curtis, Joseph S. Gati, L. Martyn Klassen, Lauren E. Villemaire, and Ravi S. Menon. Transmit/receive radiofrequency coil with individually shielded elements. *Magnetic Resonance in Medicine*, 64(6):1640–1651, 2010. 1.5.5

[46] Ye Li, Zhentian Xie, Yong Pang, Daniel Vigneron, and Xiaoliang Zhang. ICE decoupling technique for RF coil array designs. *Medical Physics*, 38(7):4086–4093, July 2011. 1.5.5

[47] Xinqiang Yan, Long Wei, Suoda Chu, Rong Xue, and Xiaoliang Zhang. Eight-Channel Monopole Array Using ICE Decoupling for Human Head MR Imaging at 7 T. *Applied Magnetic Resonance*, 47(5):527–538, May 2016.

[48] X. Yan, X. Zhang, B. Feng, C. Ma, L. Wei, and R. Xue. 7T Transmit/Receive Arrays Using ICE Decoupling for Human Head MR Imaging. *IEEE Transactions on Medical Imaging*, 33(9):1781–1787, September 2014. 1.5.5, 5.1

[49] Xinqiang Yan, Xiaoliang Zhang, Long Wei, and Rong Xue. Magnetic wall decoupling method for monopole coil array in ultrahigh field MRI: A feasibility test. *Quantitative Imaging in Medicine and Surgery*, 4(2):79–86, April 2014. 1.5.5

[50] Xinqiang Yan, Xiaoliang Zhang, Long Wei, and Rong Xue. Design and Test of Magnetic Wall Decoupling for Dipole Transmit/Receive Array for MR Imaging at the Ultrahigh Field of 7T. *Applied Magnetic Resonance*, 46(1):59–66, 2015. 1.5.5, 2.2.4

[51] Masoud Sharifian Mazraeh Mollaei, Anna Hurshkainen, Sergei Kurdjumov, Stanislav Glybovski, and Constantin Simovski. Passive Decoupling of Two Closely Located Dipole Antennas. *arXiv:1802.07500 [physics]*, February 2018. 1.5.5, 1.5.5

[52] Xinqiang Yan, John C. Gore, and William A. Grissom. Self-decoupled radiofrequency coils for magnetic resonance imaging. *Nature Communications*, 9(1):3481, August 2018. 1.5.5

[53] Gregor Adriany, Pierre-Francois Van de Moortele, Florian Wiesinger, Steen Moeller, John P. Strupp, Peter Andersen, Carl Snyder, Xiaoliang Zhang, Wei Chen, Klaas P. Pruessmann, Peter Boesiger, Tommy Vaughan, and Kāmil Uğurbil. Transmit and receive transmission line arrays for 7 Tesla parallel imaging. *Magnetic Resonance in Medicine*, 53(2):434–445, 2005. 1.5.6, 2.1, 2.4

[54] Gregor Adriany, Pierre-Francois Van de Moortele, Johannes Ritter, Steen Moeller, Edward J. Auerbach, Can Akgün, Carl J. Snyder, Thomas Vaughan, and Kâmil Uğurbil. A geometrically adjustable 16-channel transmit/receive transmission line array for improved RF efficiency and parallel imaging performance at 7 Tesla. *Magnetic Resonance in Medicine*, 59(3):590–597, March 2008. 1.5.6

[55] N. I. Avdievich, J. W. Pan, J. M. Baehring, D. D. Spencer, and H. P. Hetherington. Short echo spectroscopic imaging of the human brain at 7T using transceiver arrays. *Magnetic Resonance in Medicine*, 62(1):17–25, July 2009. 1.5.6, 2.4, 4.1

[56] Kyle M. Gilbert, Andrew T. Curtis, Joseph S. Gati, L. Martyn Klassen, and Ravi S. Menon. A radiofrequency coil to facilitate B shimming and parallel imaging acceleration in three dimensions at 7 T. *NMR in Biomedicine*, 24(7):815–823, December 2010. 1.5.6

[57] Kyle M. Gilbert, Jean-Guy Belliveau, Andrew T. Curtis, Joseph S. Gati, L. Martyn Klassen, and Ravi S. Menon. A conformal transceive array for 7 T neuroimaging. *Magnetic Resonance in Medicine*, 67(5):1487–1496, May 2012. 1.5.6, 2.4

[58] O Ipek, AJE Raaijmakers, DWJ Klomp, JJW Lagendijk, PR Luijten, and CAT Van den Berg. Characterization of transceive surface elements designs for 7 tesla magnetic resonance imaging of the prostate: Radiative antenna and microstrip. *Physics in Medicine and Biology*, 57(2), 2012. 1.5.6, 2.1, 3.1

[59] G Chen, M Cloos, D Sodickson, and G Wiggins. A 7T 8 channel transmit-receive dipole array for head imaging: Dipole element and coil evaluation. In *Proceedings of the 22nd Annual Meeting of ISMRM, Milan, Italy*, number 621, 2014. 1.5.6, 2.1, 3.1

[60] Bei Zhang, Martijn Cloos, Gang Chen, and Graham Wiggins. A size-adaptable electric dipole array for 7T body imaging. page 3508, Singapore, 2016. 1.5.6, 1.6.4.1

[61] B. Zhang, G. Chen, M. Cloos, Z. Yu, J. Walczyk, C. Collins, R. Brown, R. Lattanzi, D. Sodickson, and G. Wiggins. 29-Channel receive-only dense dipole head array for 7T MRI. In *2017 International Conference on Electromagnetics in Advanced Applications (ICEAA)*, pages 1624–1627, September 2017. 1.5.6, 1.6.4.1, 1.6.4.1

[62] Klaas P. Pruessmann, Markus Weiger, Markus B. Scheidegger, and Peter Boesiger. SENSE: Sensitivity encoding for fast MRI. *Magnetic Resonance in Medicine*, 42(5):952–962, November 1999. 1.6, 1.6.3, 1.6.3, 1.6.4, 1.6.4, 3.1, 3.2.4

[63] H. Nyquist. Thermal Agitation of Electric Charge in Conductors. *Physical Review*, 32(1):110–113, July 1928. 1.6.2

[64] E M Tunnicliffe, M J Graves, and M D Robson. Use of the noise covariance matrix in array coil quality assurance. In *Proceedings of the 19th Annual Meeting of ISMRM, MontrÃľal, Canada*. 1.6.2

[65] Chris D. Constantinides, Ergin Atalar, and Elliot R. McVeigh. Signal-to-noise measurements in magnitude images from NMR phased arrays. *Magnetic Resonance in Medicine*, 38(5):852–857, 1997. 1.6.4

[66] R. Mark Henkelman. Measurement of signal intensities in the presence of noise in MR images. *Medical Physics*, 12(2):232–233, 1985. 1.6.4

[67] J. Sijbers, A. J. den Dekker, J. Van Audekerke, M. Verhoye, and D. Van Dyck. Estimation of the Noise in Magnitude MR Images. *Magnetic Resonance Imaging*, 16(1):87–90, January 1998. 1.6.4

[68] Peter Kellman and Elliot R. McVeigh. Image reconstruction in SNR units: A general method for SNR measurement†. *Magnetic Resonance in Medicine*, 54(6):1439–1447, December 2005. 1.6.4, 1.6.4, 1.6.4, 3.2.4

[69] G. C. Wiggins, C. Triantafyllou, A. Potthast, A. Reykowski, M. Nittka, and L. L. Wald. 32-channel 3 Tesla receive-only phased-array head coil with soccer-ball element geometry. *Magnetic Resonance in Medicine*, 56(1):216–223, July 2006. 1.6.4.1, 1.6.4.1, 3.1

[70] Yudong Zhu, Christopher J. Hardy, Daniel K. Sodickson, Randy O. Giaquinto, Charles L. Dumoulin, Gontran Kenwood, Thoralf Niendorf, Hubert Lejay, Charles A. McKenzie, Michael A. Ohliger, and Neil M. Rofsky. Highly parallel volumetric imaging with a 32-element RF coil array. *Magnetic Resonance in Medicine*, 52(4):869–877, October 2004.

[71] Boris Keil, Vijay Alagappan, Azma Mareyam, Jennifer A. McNab, Kyoko Fujimoto, Veneta Tountcheva, Christina Triantafyllou, Daniel D. Dilks, Nancy Kanwisher, Weili Lin, P. Ellen Grant, and Lawrence L. Wald. Size-optimized 32-channel brain arrays for 3 T pediatric imaging. *Magnetic Resonance in Medicine*, 66(6):1777–1787, December 2011.

[72] Jacco A. de Zwart, Patrick J. Ledden, Peter van Gelderen, Jerzy Bodurka, Renxin Chu, and Jeff H. Duyn. Signal-to-noise ratio and parallel imaging performance of a 16-channel receive-only brain coil array at 3.0 Tesla. *Magnetic Resonance in Medicine*, 51(1):22–26, January 2004. 1.6.4.1, 3.1

[73] Shajan Gunamony, Jens Hoffmann, Gregor Adriany, Kamil Ugurbil, and Klaus Scheffler. A 7T head coil with 16-channel dual-row transmit and 32-channel receive array for pTx applications and high SNR. In *Proceedings of the 24th Annual Meeting of ISMRM, Singapore*, number 2132, 2016. 1.6.4.1, 1.6.4.1

[74] Kyle M. Gilbert, Joseph S. Gati, Esther Kho, L. Martyn Klassen, Peter Zeman, and Ravi S. Menon. An parallel-transmit, parallel-receive coil for routine scanning on a 7T head-only scanner. In *Proceedings of the 23th Annual Meeting of ISMRM, Toronto, Canada*. 1.6.4.1, 1.6.4.1, 3.1

[75] José P. Marques, Tobias Kober, Gunnar Krueger, Wietske van der Zwaag, Pierre-François Van de Moortele, and Rolf Gruetter. MP2RAGE, a self bias-field corrected sequence for improved segmentation and T1-mapping at high field. *NeuroImage*, 49(2):1271–1281, January 2010. 1.6.4.1, 2.2.5.3, 3.2.4, 5.2.4

[76] G. Shajan, Mikhail Kozlov, Jens Hoffmann, Robert Turner, Klaus Scheffler, and Rolf Pohmann. A 16-channel dual-row transmit array in combination with a 31-element receive array for human brain imaging at 9.4 T. *Magnetic Resonance in Medicine*, 71(2):870–879, February 2014. 1.6.4.1, 2.1, 2.4, 3.1

[77] Riccardo Lattanzi, Graham C. Wiggins, Bei Zhang, Qi Duan, Ryan Brown, and Daniel K. Sodickson. Approaching ultimate intrinsic signal-to-noise ratio with loop and dipole antennas. *Magnetic Resonance in Medicine*, 79(3):1789–1803, March 2018. 1.6.4.1, 3.4

[78] D. I. Hoult and R. E. Richards. The signal-to-noise ratio of the nuclear magnetic resonance experiment. *Journal of Magnetic Resonance*, 213(2):329–343, December 2011. 2.1, 3.1

[79] J. T. Vaughan, M. Garwood, C. M. Collins, W. Liu, L. DelaBarre, G. Adriany, P. Andersen, H. Merkle, R. Goebel, M. B. Smith, and K. Ugurbil. 7T vs. 4T: RF power, homogeneity, and signal-to-noise comparison in head images. *Magnetic Resonance in Medicine*, 46(1):24–30, July 2001. 2.1, 3.1

[80] Rolf Gruetter, Sally A. Weisdorf, Vasantham Rajanayagan, Melissa Terpstra, Hellmut Merkle, Charles L. Truwit, Michael Garwood, Scott L. Nyberg, and Kâmil Ugurbil. Resolution Improvements inin Vivo1H NMR Spectra with Increased Magnetic Field Strength. *Journal of Magnetic Resonance*, 135(1):260–264, November 1998. 2.1, 3.1

[81] David I. Hoult. Sensitivity and Power Deposition in a High-Field Imaging Experiment. *Journal of Magnetic Resonance Imaging*, 12(1):46–67, July 2000. 2.1

[82] Christopher M. Collins, Wanzhan Liu, Jinghua Wang, Rolf Gruetter, J. Thomas Vaughan, Kamil Ugurbil, and Michael B. Smith. Temperature and SAR calculations for a human head within volume and surface coils at 64 and 300 MHz. *Journal of Magnetic Resonance Imaging*, 19(5):650–656, May 2004.

[83] Matthias J. P. van Osch and Andrew G. Webb. Safety of Ultra-High Field MRI: What are the Specific Risks? *Current Radiology Reports*, 2(8):61, July 2014. 2.1

[84] G. C. Wiggins, A. Potthast, C. Triantafyllou, C. J. Wiggins, and L. L. Wald. Eight-channel phased array coil and detunable TEM volume coil for 7 T brain imaging. *Magnetic Resonance in Medicine*, 54(1):235–240, July 2005. 2.1, 3.1

[85] Ralf Mekle, Wietske van der Zwaag, Andreas Joosten, and Rolf Gruetter. Comparison of three commercially available radio frequency coils for human brain imaging at 3 Tesla. *Magnetic Resonance Materials in Physics, Biology and Medicine*, 21(1):53, 2008. 2.1, 3.1

[86] Ozlem Ipek. Radio-frequency coils for ultra-high field magnetic resonance. *Analytical Biochemistry*, 529:10–16, 2017. Introduction to in vivo Magnetic Resonance Spectroscopy (MRS): A method to non-invasively study metabolism. 2.1, 3.1, 5.1

[87] J.E.M. Snaar, W.M. Teeuwisse, M.J. Versluis, M.A. van Buchem, H.E. Kan, N.B. Smith, and A.G. Webb. Improvements in high-field localized MRS of the medial temporal lobe in humans using new deformable high-dielectric materials. *NMR in Biomedicine*, 24(7):873–879, 2011. 2.1, 5.1, 5.1

[88] Wouter M. Teeuwisse, Wyger M. Brink, and Andrew G. Webb. Quantitative assessment of the effects of high-permittivity pads in 7 Tesla MRI of the brain. *Magnetic Resonance in Medicine*, 67(5):1285–1293, 2012. 2.1, 5.1, 5.1

[89] Gregory J. Metzger, Carl Snyder, Can Akgun, Tommy Vaughan, Kamil Ugurbil, and Pierre-Francois Van de Moortele. Local B1+ shimming for prostate imaging with transceiver arrays at 7T based on subject-dependent transmit phase measurements. *Magnetic Resonance in Medicine*, 59(2):396–409, 2008. 2.1, 3.1, 4.1

[90] Xinqiang Yan, ChuangXin Ma, Lei Shi, Yan Zhuo, Xiaohong Joe Zhou, Long Wei, and Rong Xue. Optimization of an 8-Channel Loop-Array Coil for a 7 T MRI System with the Guidance of a Co-Simulation Approach. *Applied Magnetic Resonance*, 45(5):437–449, 2014. 2.1

[91] J Clement, O Ipek, F Eggenschwiler, G Donati, K Pierzchala, and R Gruetter. Eight-Channel Loop Coil Array for 7T MR Brain Imaging. In *Proceedings of the 32nd Annual Meeting of ESMRMB, Edinburgh, United Kingdom*, number 284, 2015. 2.1

[92] X Yan, JO Pedersen, L Wei, X Zhang, and R Xue. Multichannel Double-Row Transmission Line Array for Human MR Imaging at Ultrahigh Fields. *IEEE Transactions on Biomedical Engineering*, 62(6):1652–1659, 2015. 2.1

[93] Celal Oezerdem, Lukas Winter, Andreas Graessl, Katharina Paul, Antje Els, Oliver Weinberger, Jan Rieger, Andre Kuehne, Matthias Dieringer, Fabian Hezel, Dirk Voit, Jens Frahm, and Thoralf Niendorf. 16-channel bow tie antenna transceiver array for cardiac MR at 7.0 tesla. *Magnetic Resonance in Medicine*, 75(6):2553–2565, 2016. 2.1, 3.1

[94] B Steensma, AV Obando, D Klomp, N Van den Berg, P Luijten, and A Raaijmakers. Body Imaging at 7 Tesla with much lower SAR levels: An introduction of the Snake Antenna array. In *Proceedings of the 23rd Annual Meeting of ISMRM, Toronto, Canada*, number 395, 2015. 3.1

[95] GC Wiggins, K Lakshmanan, and Chen G. The Distributed Inductance Electric Dipole Antenna. In *Proceedings of the 23rd Annual Meeting of ISMRM, Toronto, Canada*, number 3100, 2015.

[96] M. Arcan Ertürk, Alexander J. E. Raaijmakers, Gregor Adriany, Kâmil Uğurbil, and Gregory J. Metzger. A 16-channel combined loop-dipole transceiver array for 7 Tesla body MRI. *Magnetic Resonance in Medicine*, 77(2):884–894, February 2017. 2.1, 3.1, 3.1

[97] Alexander J. E. Raaijmakers, Michel Italiaander, Ingmar J. Voogt, Peter R. Luijten, Johannes M. Hoogduin, Dennis W. J. Klomp, and Cornelis A. T. van den Berg. The fractionated dipole antenna: A new antenna for body imaging at 7 Tesla. *Magnetic Resonance in Medicine*, 75(3):1366–1374, March 2016. 2.4

[98] I Voogt, D Klomp, H Hoogduin, M Luttje, P Luijten, C Van den Berg, and A Raaijmakers. Combined 8-channel transceiver fractionated dipole antenna array with a 16-channel loop coil receive array for body imaging at 7 Tesla. In *Proceedings of the 23rd Annual Meeting of ISMRM, Toronto, Canada*, number 631, 2015. 2.1

[99] Gang Chen, Christopher M. Collins, Daniel K. Sodickson, and Graham C. Wiggins. A method to assess the loss of a dipole antenna for ultra-high-field MRI. *Magnetic Resonance in Medicine*, 79(3):1773–1780, March 2018. 2.2.3

[100] James Kennedy and Russell C. Eberhart. Particle swarm optimization. In *Proceedings of the 1995 IEEE International Conference on Neural Networks*, volume 4, pages 1942–1948, Perth, Australia, IEEE Service Center, Piscataway, NJ, 1995. 2.2.5.1, 3.2.4, 4.1

[101] J Clement, R Gruetter, and O Ipek. Comparison of passive RF phase shimming methods on the human brain at 7T using particle-swarm optimization. In *Proceedings of the 33rd Annual Meeting of ESMRMB, Vienna, Austria*, number 503, 2015. 2.2.5.1, 3.2.4, 4.1

[102] Florent Eggenschwiler, Tobias Kober, Arthur W. Magill, Rolf Gruetter, and José P. Marques. SA2RAGE: A new sequence for fast B1+-mapping. *Magnetic Resonance in Medicine*, 67(6):1609–1619, 2012. 2.2.5.2, 3.2.4, 4.2.3, 5.2.4

[103] Viktor Pfaffenrot, Sascha Brunheim, Stefan H. G. Rietsch, Peter J. Koopmans, Thomas M. Ernst, Oliver Kraff, Stephan Orzada, and Harald H. Quick. An 8/15-channel Tx/Rx head neck RF coil combination with region-specific B1+ shimming for whole-brain MRI focused on the cerebellum at 7T. *Magnetic Resonance in Medicine*, 80(3):1252–1265, September 2018. 2.4

[104] N. I. Avdievich, J. Hoffmann, G. Shajan, A. Pfrommer, I. A. Giapitzakis, K. Scheffler, and A. Henning. Evaluation of transmit efficiency and SAR for a tight fit transceiver human head phased array at 9.4 T. *NMR in Biomedicine*, 30(2):e3680, February 2017. 2.4

[105] N. Boulant, J.-F. Mangin, and A. Amadon. Counteracting radio frequency inhomogeneity in the human brain at 7 Tesla using strongly modulating pulses. *Magnetic Resonance in Medicine*, 61(5):1165–1172, 2009. 2.4

[106] M. A. Cloos, N. Boulant, M. Luong, G. Ferrand, E. Giacomini, D. Le Bihan, and A. Amadon. kT-points: Short three-dimensional tailored RF pulses for flip-angle homogenization over an extended volume. *Magnetic Resonance in Medicine*, 67(1):72–80, 2012. 2.4, 3.4

[107] Florent Eggenschwiler, Kieran R. O'Brien, Rolf Gruetter, and José P. Marques. Improving T2-weighted imaging at high field through the use of kT-points. *Magnetic Resonance in Medicine*, 71(4):1478–1488, 2014. 2.4, 3.4

[108] Qi Duan, Govind Nair, Natalia Gudino, Jacco A. de Zwart, Peter van Gelderen, Joe Murphy-Boesch, Daniel S. Reich, Jeff H. Duyn, and Hellmut Merkle. A 7T spine array based on electric dipole transmitters. *Magnetic Resonance in Medicine*, 74(4):1189–1197, October 2015. 2.4, 3.1

[109] Stefan HG Rietsch, Stephan Orzada, and Harald H. Quick. An 8Tx/32Rx RF Coil for 7T UHF Body MRI. In *Proceedings of the 24th Annual Meeting of ISMRM, Singapore*, number 2131, 2016. 2.4

[110] Todd B. Parrish, Darren R. Gitelman, Kevin S. LaBar, and M.-Marsel Mesulam. Impact of signal-to-noise on functional MRI. *Magnetic Resonance in Medicine*, 44(6):925–932, 2000. 2.4

[111] DS Williams, JA Detre, JS Leigh, and AP Koretsky. Magnetic resonance imaging of perfusion using spin inversion of arterial water. *Proceedings of the National Academy of Sciences of the United States of America*, 89(9), 1992. 2.4

[112] Daniel K. Sodickson and Warren J. Manning. Simultaneous acquisition of spatial harmonics (SMASH): Fast imaging with radiofrequency coil arrays. *Magnetic Resonance in Medicine*, 38(4):591–603, October 1997. 3.1

[113] Mark A. Griswold, Peter M. Jakob, Robin M. Heidemann, Mathias Nittka, Vladimir Jellus, Jianmin Wang, Berthold Kiefer, and Axel Haase. Generalized autocalibrating partially parallel acquisitions (GRAPPA). *Magnetic Resonance in Medicine*, 47(6):1202–1210, June 2002. 3.1

[114] Elfar Adalsteinsson, Murat Aksoy, David Atkinson, Roland Bammer, Philip G. Batchelor, Thomas Benner, Michael Bock, Jan Casselman, Olaf Dietrich, Randy Duensing, Roger Eibel, Marco Essig, Christian Fink, J Paul Finn, Bastian Fischer, Mark A. Griswold, Karin Herrmann, Romhild M. Hoogeveen, Armin Huber, and Christoph J. Zech. *Parallel Imaging in Clinical MR Applications*. Springer, Berlin Heidelberg New York, 01 2007. 3.1

[115] Boris Keil, James N. Blau, Stephan Biber, Philipp Hoecht, Veneta Tountcheva, Kawin Setsompop, Christina Triantafyllou, and Lawrence L. Wald. A 64-channel 3T array coil for accelerated brain MRI. *Magnetic Resonance in Medicine*, 70(1):248–258, July 2013. 3.1

[116] Mary Preston McDougall and Steven M. Wright. 64-channel array coil for single echo acquisition magnetic resonance imaging. *Magnetic Resonance in Medicine*, 54(2):386–392, August 2005. 3.1

[117] Graham C. Wiggins, Jonathan R. Polimeni, Andreas Potthast, Melanie Schmitt, Vijay Alagappan, and Lawrence L. Wald. 96-Channel receive-only head coil for 3 Tesla: Design optimization and evaluation. *Magnetic Resonance in Medicine*, 62(3):754–762, September 2009. 3.1

[118] A Potthast, G Wiggins, O Kraff, V Alagappan, C Wiggins, L Wald, and A Reykowski. A 32 channel receive-only head coil and detunable transmit birdcage coil for 7 tesla brain imaging. In *Proceedings of the 14th Annual Meeting of ISMRM, Seattle, USA*, number 415, USA, 2006. 3.1

[119] PJ Ledden, A Mareyam, S Wang, P van Gelderen, and J Duyn. 32 channel receive-only sense array for brain imaging at 7t. In *Proceedings of the 15th Annual Meeting of ISMRM, Berlin, Germany*, number 242, Germany, 2007. 3.1

[120] Ulrich Katscher, Peter Börnert, Christoph Leussler, and Johan S. van den Brink. Transmit SENSE. *Magnetic Resonance in Medicine*, 49(1):144–150, January 2003. 3.1

[121] Ozlem Ipek, Alexander Raaijmakers, Jan Lagendijk, Peter Luijten, and Cornelis van den Berg. Optimization of the radiative antenna for 7-T magnetic resonance body imaging. *Concepts in Magnetic Resonance Part B: Magnetic Resonance Engineering*, 43B(1):1–10, February 2013. 3.1

[122] GC Wiggins, K Lakshmanan, and Chen G. The distributed inductance electric dipole antenna. In *Proceedings of the 23rd Annual Meeting of ISMRM, Toronto, Canada*, number 3100, Canada, 2015. 3.1

[123] N. I. Avdievich, I. A. Giapitzakis, A. Pfrommer, T. Borbath, and A. Henning. Combination of surface and 'vertical' loop elements improves receive performance of a human head transceiver array at 9.4 T. *NMR in Biomedicine*, 31(2):e3878, February 2018. 3.1

[124] A. Avdievich, IA Giapitzakis, and A Henning. 32-channel combined surface loop vertical loop tight-fit array provides for full-brain coverage, high transmit performance, and snr improvement at 9.4t: an alternative to surface loop / dipole antenna combination. In *Proceedings of the 26th Annual Meeting of ISMRM, Paris, France*, number 140, France, 2018. 3.1

[125] Bart R. Steensma, Ingmar J. Voogt, Tim Leiner, Peter R. Luijten, Jesse Habets, Dennis W. J. Klomp, Cornelis A. T. van den Berg, and Alexander J. E. Raaijmakers. An 8-channel Tx/Rx dipole array combined with 16 Rx loops for high-resolution functional cardiac imaging at 7 T. *Magnetic Resonance Materials in Physics, Biology and Medicine*, 31(1):7–18, February 2018. 3.1

[126] Henry Dreyfuss. *The Measure of Man: Human Factors in Design*. Whitney Library of Design, 1969. 3.2.1

[127] B Keil, Charlotte Sappo, Berkin Bilgic, JR Polimeni, L Golestanirad, R Etzel, LL Wald, DA Feinberg, and K Setsompop. Sub-millimeter cortical imaging at 7t using a high-density motor-cortex 32-channel array coil. In *Proceedings of the 25th Annual Meeting of ISMRM, HawaÃŕ, USA*, number 1224, USA, 2017. 3.4

[128] W Zhao, B Keil, JR Polimeni, JN Blau, A Mareyam, T Witzel, E Adalsteinsson, and LL Wald. 16-channel tx array and 32-channel rx array for brain mri at 7t. In *Proceedings of the 21st Annual Meeting of ISMRM, Salt Lake City, USA*, number 2724, USA, 2013.

[129] Kyle M. Gilbert, Joseph S. Gati, Kevin Barker, Stefan Everling, and Ravi S. Menon. Optimized parallel transmit and receive radiofrequency coil for ultrahigh-field MRI of monkeys. *NeuroImage*, 125:153–161, January 2016. 3.4

[130] Vincent Gras, Alexandre Vignaud, Alexis Amadon, Denis Le Bihan, and Nicolas Boulant. Universal pulses: A new concept for calibration-free parallel transmission. *Magnetic Resonance in Medicine*, 77(2):635–643, February 2017. 3.4

[131] Shaihan J. Malik, Shiva Keihaninejad, Alexander Hammers, and Joseph V. Hajnal. Tailored excitation in 3D with spiral nonselective (SPINS) RF pulses. *Magnetic Resonance in Medicine*, 67(5):1303–1315, 2012. 3.4

[132] Adam C. Zelinski, Lawrence L. Wald, Kawin Setsompop, Vivek K Goyal, and Elfar Adalsteinsson. Sparsity-Enforced Slice-Selective MRI RF Excitation Pulse Design. *IEEE transactions on medical imaging*, 27(9):1213–1229, September 2008. 4.1

[133] Kawin Setsompop, Vijayanand Alagappan, Adam C. Zelinski, Andreas Potthast, Ulrich Fontius, Franz Hebrank, Franz Schmitt, Lawrence L. Wald, and Elfar Adalsteinsson. High-Flip-Angle slice-selective parallel RF transmission with 8 channels at 7 Tesla. *Journal of magnetic resonance (San Diego, Calif. : 1997)*, 195(1):76–84, November 2008. 4.1, 4.1

[134] Cem Murat Deniz, Ryan Brown, Riccardo Lattanzi, Leeor Alon, Daniel K. Sodickson, and Yudong Zhu. MAXIMUM EFFICIENCY RF SHIMMING: THEORY AND INITIAL APPLICATION FOR HIP IMAGING AT 7 TESLA. *Magnetic resonance in medicine*

: official journal of the Society of Magnetic Resonance in Medicine / Society of Magnetic Resonance in Medicine, 69(5):1379–1388, May 2013. 4.1

[135] Arian Beqiri, Anthony N. Price, Francesco Padormo, Joseph V. Hajnal, and Shaihan J. Malik. Extended RF shimming: Sequence-level parallel transmission optimization applied to steady-state free precession MRI of the heart. *Nmr in Biomedicine*, 30(6), June 2017. 4.1

[136] Tales Santini, Sossena Wood, Narayanan Krishnamurthy, Yutong Zhang, Nadim Farhat, Neilesh Vinjamuri, Minseok Koo, Howard Aizenstein, and Tamer S. Ibrahim. New optimization strategies for RF shimming at UHF MRI. In *Proceedings of the 26th Annual Meeting of ISMRM, Paris, France*, number 4406, 2018. 4.1

[137] David W. Zingg, Marian Nemec, and Thomas H. Pulliam. A comparative evaluation of genetic and gradient-based algorithms applied to aerodynamic optimization. *European Journal of Computational Mechanics*, 17(1-2):103–126, January 2008. 4.1

[138] John H. Holland. *Adaptation in Natural and Artificial Systems*. A Bradford Book, 1975. 4.1

[139] Y. Rahmat-Samii, D. Gies, and J. Robinson. Particle swarm optimization (PSO): A novel paradigm for antenna designs. *URSI Radio Science Bulletin*, 2003(306):14–22, September 2003. 4.1

[140] J. Robinson and Y. Rahmat-Samii. Particle swarm optimization in electromagnetics. *IEEE Transactions on Antennas and Propagation*, 52(2):397–407, February 2004. 4.1

[141] Riccardo Poli, James Kennedy, and Tim Blackwell. Particle swarm optimization. *Swarm Intelligence*, 1(1):33–57, June 2007. 4.1

[142] Riccardo Poli. Analysis of the Publications on the Applications of Particle Swarm Optimisation. *J. Artif. Evol. App.*, 2008:4:1–4:10, January 2008. 4.1

[143] S. Chandra, R. Bhat, and H. Singh. A PSO based method for detection of brain tumors from MRI. In *2009 World Congress on Nature Biologically Inspired Computing (NaBIC)*, pages 666–671, December 2009. 4.1

[144] Wei He, Yiyuan Cheng, Ling Xia, and Feng Liu. A New Particle Swarm Optimization-Based Method for Phase Unwrapping of MRI Data. https://www.hindawi.com/journals/cmmm/2012/475745/, 2012. 4.1

[145] Abbas El Dor, Julien Lepagnot, Amir Nakib, and Patrick Siarry. PSO-2S Optimization Algorithm for Brain MRI Segmentation. In Jeng-Shyang Pan, Pavel Krömer, and Václav Snášel, editors, *Genetic and Evolutionary Computing*, Advances in Intelligent Systems and Computing, pages 13–22. Springer International Publishing, 2014. 4.1

[146] Rania Hassan, Babak Cohanim, Olivier de Weck, and Gerhard Venter. A Comparison of Particle Swarm Optimization and the Genetic Algorithm. In *46th AIAA/ASME/ASCE/AHS/ASC Structures, Structural Dynamics and Materials Conference*, Structures, Structural Dynamics, and Materials and Co-located Conferences. American Institute of Aeronautics and Astronautics, April 2005. 4.1

[147] Alessandro Sbrizzi, Alexander J. E. Raaijmakers, Hans Hoogduin, Jan J. W. Lagendijk, Peter R. Luijten, and Cornelis A. T. van den Berg. Transmit and receive RF fields determination from a single low-tip-angle gradient-echo scan by scaling of SVD data. *Magnetic Resonance in Medicine*, 72(1):248–259, July 2014. 4.2.2, 4.2.2, 4.4

[148] Sebastian Schmitter, Gregor Adriany, Edward J Auerbach, Kamil Ugurbil, and Pierre-Francois Van de Moortele. Neither Flat Profile Nor Black Spots: A Simple Method to Achieve Acceptable CP-like Mode Transmit B1 Pattern for Whole Brain Imaging with Transmit Arrays at 7 Tesla. In *Proceedings of the 20th Annual Meeting of ISMRM, Melbourne, Australia*. 4.2.2, 4.4

[149] A.G. Webb. Dielectric materials in magnetic resonance. *Concepts in Magnetic Resonance Part A*, 38A(4):148–184, July 2011. 5.1, 5.1

[150] Qing X. Yang, Weihua Mao, Jinghua Wang, Michael B. Smith, Hao Lei, Xiaoliang Zhang, Kamil Ugurbil, and Wei Chen. Manipulation of image intensity distribution at 7.0 T: Passive RF shimming and focusing with dielectric materials. *Journal of Magnetic Resonance Imaging*, 24(1):197–202, 2006. 5.1, 5.1

[151] Carl T.A Johnk. *Engineering Electromagnetic Fields and Waves, 2nd Edition*. Wiley, 1988. 5.1

[152] Wyger M. Brink, Annerie M.A. van der Jagt, Maarten J. Versluis, Berit M. Verbist, and Andrew G. Webb. High Permittivity Dielectric Pads Improve High Spatial Resolution Magnetic Resonance Imaging of the Inner Ear at 7 T:. *Investigative Radiology*, 49(5):271–277, May 2014. 5.1

[153] M. A. van der Jagt, W. M. Brink, M. J. Versluis, S. C. A. Steens, J. J. Briaire, A. G. Webb, J. H. M. Frijns, and B. M. Verbist. Visualization of human inner ear anatomy with high-resolution MR imaging at 7T: Initial clinical assessment. *AJNR. American journal of neuroradiology*, 36(2):378–383, February 2015. 5.1

[154] Wei Luo, Michael T. Lanagan, Christopher T. Sica, YeunChul Ryu, Sukhoon Oh, Matthew Ketterman, Qing X. Yang, and Christopher M. Collins. Permittivity and Performance of Dielectric Pads with Sintered Ceramic Beads in MRI: Early Experiments and Simulations at 3 T. *Magnetic resonance in medicine : official journal of the Society of Magnetic Resonance in Medicine / Society of Magnetic Resonance in Medicine*, 70(1):269–275, July 2013. 5.1

[155] Jiaming Cui, John C. Bosshard, Joseph V. Rispoli, Ivan E. Dimitrov, Sergey Cheshkov, Mary Preston McDougall, Craig Malloy, and Steven M. Wright. A Switched-Mode Breast Coil for 7 T MRI Using Forced-Current Excitation. *IEEE transactions on biomedical engineering*, 62(7):1777–1783, July 2015. 5.1

[156] Maria Evelina Fantacci, Laura Biagi, Mirco Cosottini, Mauro Costagli, Massimo Marletta, Alessandra Retico, Riccardo Stara, Mark Symms, Gianluigi Tiberi, Virna Zampa, and Michela Tosetti. Magnetic Resonance Imaging at 7 Tesla with Dedicated Radiofrequency Coils - Application to Cervical Cord and Knee:. In *Proceedings of the 9th International Joint Conference on Biomedical Engineering Systems and Technologies*, pages 229–234, Rome, Italy, 2016. SCITEPRESS - Science and and Technology Publications. 5.1

[157] Jérémie Clément, Lijing Xin, Rolf Gruetter, and Ozlem Ipek. Dedicated surface coils for mr studies in the temporal and the frontal lobes of the human brain at 7t. In *Proceedings of the 24th Annual Meeting of ISMRM, Singapore*. 5.2.1

[158] Jérémie Clément, Maxime Aboukrat, Rolf Gruetter, and Ozlem Ipek. Unilateral/bilateral rf excitation of temporal lobes using a dc-controlled transmit/receive switch and two surface coils. In *Proceedings of the 34th Annual Meeting of ESMRMB, Barcelona*. 5.2.1

[159] K. Urmila. Siemens Healthineers receives CE mark for 7 Tesla scanner Magnetom Terra. 6.2

[160] Office of the Commissioner. Press Announcements - FDA clears first 7T magnetic resonance imaging device. https://www.fda.gov/NewsEvents/Newsroom/PressAnnouncements/ucm580154.htm. 6.2

Publications

Peer-reviewed journal articles

1. **Jérémie Clément**, Rolf Gruetter, Özlem Ipek, *A human cerebral and cerebellar 8-channel transceive RF dipole coil array at 7T*, Magnetic Resonance in Medicine 81(2), 2019
2. **Jérémie Clément**, Rolf Gruetter, Özlem Ipek, *A combined 32-channel receive-loops/8-channel transmit-dipoles coil array for whole-brain MR imaging at 7T*, Early View in Magnetic Resonance in Medicine, 2019

Peer-reviewed abstracts at international conferences

1. **Jérémie Clément**, Özlem Ipek, Florent Eggenschwiler, Guillaume Donati, Katarzyna Pierzchala, Rolf Gruetter, *Eight-channel loop coil array for 7T MR brain imaging*, Proc. ESMRMB 32nd Scientific Meeting, Edinburgh, Scotland, 2015.
2. **Jérémie Clément**, Lijing Xin, Rolf Gruetter, Özlem Ipek, *Dedicated surface coils for MR studies in the temporal and the frontal lobes of the humain brain at 7T*, Proc. ISMRM 24th Scientific Meeting, Singapore, 2016.
3. **Jérémie Clément**, Arthur Magill, Hongxia Lei, Özlem Ipek, Rolf Gruetter, *Slotted-tube-resonator design for whole-body MR imaging at 14T*, Proc. ISMRM 24th Scientific Meeting, Singapore, 2016.
4. **Jérémie Clément**, Rolf Gruetter, Özlem Ipek, *Comparison of passive RF phase shimming methods on the human brain at 7T using particle-swarm optimization*, Proc. ESMRMB 33rd Scientific Meeting, Vienna, Austria, 2016.
5. **Jérémie Clément**, Rolf Gruetter, Özlem Ipek, *Optimal array configuration for cerebral cortex MRI at 7T: six center-fed dipoles with two loops RF coil array*, Proc. ISMRM 25th Scientific Meeting, Hawaï, United States of America, 2017.
6. **Jérémie Clément**, Maxime Aboukrat, Rolf Gruetter, Özlem Ipek, *Unilateral/bilateral RF excitation of temporal lobes using a DC-controlled transmit/receive switch and two surface coils*, Proc. ESMRMB 34th Scientific Meeting, Barcelona, Spain, 2017.
7. **Jérémie Clément**, Rolf Gruetter, Özlem Ipek, *31-channel receive coil array combined with an 8-channel whole-brain dipole transmit array*, Proc. ISMRM 26th Scientific Meeting, Paris, France, 2018.
8. **Jérémie Clément**, Sandra Da Costa, Rolf Gruetter, Özlem Ipek, *8-channel whole-brain center-fed dipoles with quadrature frontal loops coil array*, Proc. ISMRM 26th Scientific Meeting, Paris, France, 2018.

9. **Jérémie Clément**, Sandra Da Costa, Rolf Gruetter, Özlem Ipek, *High-resolution human inner-ear imaging and auditory cortices fMRI at 7T parallel-transmit MRI*, Proc. ISMRM workshop on Ultrahigh Field Magnetic Resonance, Dubrovnik, Croatia, 2019.

10. Claudia Zanella, Elise Vinckenbosch, **Jérémie Clément**, Masoumeh Dehghani, Bernard Lanz, Rolf Gruetter *A custom-designed 1H saddle coil for CEST imaging at 14.1 Tesla*, Proc. ISMRM 27th Scientific Meeting, Montréal, Canada, 2019.

11. **Jérémie Clément**, Sandra Da Costa, Rolf Gruetter, Özlem Ipek, *An 8Tx dipoles/32Rx loop coil array - Evaluation of fMRI performances in auditory cortices at 7T*, Proc. ISMRM 27th Scientific Meeting, Montréal, Canada, 2019.

Jérémie Clément

PHYSICS ENGINEER

28 years (14.11.1990), Swiss-Peruvian, Single, with driving license
Chemin du Bochet 20, 1024 Ecublens, Switzerland
Phone: 00 41 78 870 62 34 // Email: jeremie.clement@alumni.epfl.ch

EDUCATION

2014 – 2019
PhD student in Physics
Ecole Polytechnique Fédérale de Lausanne, Switzerland
Development of radiofrequency (RF) coils for magnetic resonance (MR) systems at ultra-high field.

2012 - 2014
MSc in Applied Physics
Ecole Polytechnique Fédérale de Lausanne, Switzerland
Master thesis in MR Physics with a strong focus on RF engineering at ultra-high magnetic field (7T)

2008-2012
BSc in Physics
Ecole Polytechnique Fédérale de Lausanne, Switzerland

EXPERIENCES

Sept. 2010 – 2019
Teaching-assistant
Ecole Polytechnique Fédérale de Lausanne, Switzerland
Supervision of the exercise sessions in physics and grading of the exams. Teaching of experimental methods in Physics.

Feb. 2015 – June 2017
Project management
Ecole Polytechnique Fédérale de Lausanne, Switzerland Preparation of a project for two physics students, definition of the objectives and the calendar for their tasks. Supervision of their work and help to make the projects successful.

Sept. 2013-Feb. 2014
Internship in the R&D department
NTN-SNR, Annecy, France
Theoretical study and bench measurements on a new kind of magnetic sensor to characterize its properties relative to existing technologies.

MAIN PROJECTS

2016 – 2019
Whole-brain RF coil array for MR studies at 7T
A highly efficient RF antenna was developed and presented improved performances compared to existing devices. Many technical and safety constraints were addressed to make the prototype viable for human brain imaging at ultra-high magnetic field. The research results were peer-reviewed and published in journal.

2016
Comparison of optimization methods for the RF Phase shimming at 7T
Implementation of an existing algorithm into a user-friendly interface, coded in Matlab. The project required to identify the needs and how to address them such as other scientist could benefit from the work.

2015
Dedicated surface coils for MR studies in the temporal and frontal lobes of the human brain at 7T
Two separate devices were designed and built to address specific needs for brain MR studies. The project was conducted with two master students who worked under my supervision.

SKILLS

RF circuits and antenna design at ultra-high magnetic field
CAD with Solidworks and Altium Designer
Electromagnetic field simulations with Sim4Life
Latex language
Matlab programming
Adobe Photoshop and Illustrator (basics)
C++ (basics)

LANGUAGES

- Bilingual French/Spanish
- English - Level C1
- German – Level A1

OTHER ACTIVITIES

- Ancient greek and latin learned at high school
- Transverse flute
- Fitness, badminton
- Aeronautics Initiation Certificate (BIA, France)

Acknowledgments

The time has come to finish the writing of this thesis with probably one of the most important sections. Behind all scientific achievements there is never a single person and always a story. My story at EPFL started 10 years ago (slightly more now) but my PhD story started in 2014. At this time I had finished my master thesis, already at the CIBM-LIFMET.

Willing to continue with a PhD I went to the office of Professor Rolf Gruetter who gave me this day the opportunity to do my PhD at LIFMET. This is why I would like first to express my grateful thanks to him for giving me this chance. The working conditions you offer us (me and all the colleagues) are great. The freedom we have to develop our ideas, to apply them and to present our results at international conferences is something that must be underlined. Your advice and remarks about my work always challenged me to push further my understanding of physics.

All the achievements of this thesis would not have been possible without the second person I would like to thank and who is my co-supervisor Özlem Ipek. I started to work with you for my master thesis and you followed my work during all the years of my PhD. I appreciated your unconditional support when things did not work as expected and for always pushing me to be more precise in my scientific approach of the work. Thank you also for encouraging me to write and publish about the thesis and reading my manuscripts several times.

I would like also to thank my jury members Alexander Raaijmakers, Andrew Webb, Giovanni Boero, Frederic Mila, Özlem Ipek and Rolf Gruetter for participating in the private defense and for the interesting discussion and comments they had about this work.

Lillian, thank you for organizing so well the conferences' trips and for being always available to answer questions. Marc, thank you for helping me on the IT side. Yves, thank you for helping me so many times at the RF lab and your advice about RF coil designs and circuits. I would also like to thank all the people working on the 7T and who all gave me during my thesis helpful inputs on my work. Özlem, Sandra, Yohan, Joao, Eulalia, Lijing, Olivier, Bernard, Frederic and Guillaume, thank you for the fruitful comments during our meetings. To avoid threats on my life, I definitely have to thank the people I shared the office with. Claudia, Emma and Radek, thank you for your good mood and for the nice working environment you create. I did not count the number of times I went with any of you to push back the famous "dewar" but it was always funny moments. No regrets ! Radek, I am still impressed how you managed to save the orchid. All the lab was jealous of our office after this. Emma, thank you for encouraging me to follow you at body attack. The effort is worth it. Claudia, you were always smiling and full of energy. I appreciated your enthusiasm (I should be safe after this). I would also like to mention the other colleagues I spent a lot of time with. Alice, I will not forget the tasty tiramisu you prepared for each Christmas apero. It was great also to travel with you, Thanh and the others after the conferences in the different countries we went. Catarina, it was nice to meet you during the several months you spent at our lab. To all, your friendship is greatly appreciated. Thank you also to the others

PhD students and scientists who made this lab a very nice place to work.
Finally, I would like to express all my love and deepest appreciation to my family. Priscile, Etienne and Anna (my brother and sisters) you have been with me throughout the whole thesis and before. To my parents, Norbert and Lucie, thank you for your unconditional love and support to achieve this work. You always believed often more than myself on what I could accomplish and pushed me to always go further. You taught me to trust in God at every step of my PhD and of my life and for this I will always be grateful.

Ecole Polytechnique Fédérale de Lausanne Jérémie Clément

June 2019

Bless the Lord, O my soul, and forget not all His benefits.

Psalm 103:2

For great is His love toward us, and the faithfulness of the Lord endures forever.

Psalm 117: 2

Sola Gratia

Ce document a été imprimé au Centre d’impression EPFL,
imprimerie climatiquement neutre, certifiée myClimate.